Rayabilité des verres Silico-Sodo-Calciques

Vincent Le Houerou

▶ To cite this version:

Vincent Le Houerou. Rayabilité des verres Silico-Sodo-Calciques. Mechanics [physics.med-ph]. Université Rennes 1, 2005. English. NNT : . tel-00011224

HAL Id: tel-00011224
https://theses.hal.science/tel-00011224
Submitted on 16 Dec 2005

N° d'ordre: 3059

THÈSE

Présentée pour obtenir le grade de

DOCTEUR EN SCIENCES DE L'UNIVERSITÉ DE RENNES 1

et de *DOCTOR EUROPEUS*

Mention : MÉCANIQUE DES MATÉRIAUX

par

Vincent LE HOUÉROU

LAboratoire de Recherche en Mécanique Appliquée de l'Université de Rennes 1
(LARMAUR) FRE CNRS-2717
École doctorale *Sciences de la Matière*
UFR *Structure et Propriétés de la Matière*

Rayabilité des verres Silico-Sodo-Calciques

Scratchability of Soda-Lime Silica Glasses

soutenue le 18 Juillet 2005 devant la commission d'examen

Président	C. GAUTHIER	Maître de conférences HDR, Institut Charles Sadron, CNRS UPR 22, U.L.P. Strasbourg
Rapporteurs	J. MICHLER	Head of Micromechanics and Micropatterning Group, EMPA, Thun (Suisse)
	R. HAND	Senior Lecturer, Department of Engineering Materials, University of Sheffield (Angleterre)
	S. BENAYOUN	Maître de conférences HDR, LPMI, EA 1427, ENSAM d'Angers
Examinateurs	R. EL ABDI	Professeur, LARMAUR, FRE CNRS 2717, Université de Rennes 1
	T. ROUXEL	Professeur, LARMAUR, FRE CNRS 2717, Université de Rennes 1
Invité	J.-C. SANGLEBOEUF	Maître de conférences HDR, LARMAUR, FRE CNRS 2717, Université de Rennes 1

Avec l'idole de la certitude (qui inclut celle de la certitude imparfaite ou probabilité) tombe l'une des défenses de l'obscurantisme, lequel met un obstacle sur la voie du progrès scientifique. Car l'hommage rendu à cette idole non seulement réprime l'audace de nos questions, mais en outre compromet la rigueur et l'honnêteté de nos tests. La conception erronée de la science se révèle dans la soif d'exactitude. Car ce qui fait l'homme de science, ce n'est pas la possession *de connaissances, d'irréfutables vérités, mais la* quête *obstinée et audacieusement critique de la vérité. - Logique de la Découverte Scientifique*

With the idol of certainty (including that of degrees of imperfect certainty or probability) there falls one of the defences of obscurantism which bar the way of scientific advance. For the worship of this idol hampers not only the boldness of our questions, but also the rigour and the integrity of our tests. The wrong view of science betrays itself in the craving to be right; for it is not his possession *of knowledge, of irrefutable truth, that makes the man of science, but his persistent and recklessly critical* quest *for truth. - The Logic of Scientific Discovery*

Karl Popper (1902-1994).

ACKNOWLEDGMENTS

This Thesis work started in autumn 2001 and was conducted in LARMAUR, Laboratory of Applied Mechanics of the University of Rennes 1. It was subjected to a 4 months collaboration at EMPA in Thun (Switzerland) in summer 2004. This prompts the European label "Doctor Europeus" application associated to this work.

I was particularly honored that Dr. Christian Gauthier presided at the thesis defense and he can be sure that he has all my gratitude.

I also wish to express my gratitude to Dr. Russell Hand who accepted to review this manuscript and to travel in order to assist to the defense in Rennes (France) and to Dr. Stéphane Benayoun for his comments on the manuscript as reviewer and for his advices for this final version.

I am grateful to Pr. Tanguy Rouxel for giving me the opportunity to accomplish this Thesis work in LARMAUR and for giving a large autonomy to the doctoral candidates.

I am particularly grateful to Dr. Jean-Christophe Sangleboeuf who has been following my evolution since 1998 and greatly participated to my research training. I also wish to thank Pr. Rochdi El Abdi for his support.

This work should have not been possible without the help and the continuous support of Sébastien Dériano and Emmanuelle Reynaud. My friendly thoughts go to everyone I had pleasure to met in LARMAUR and in the University of Rennes 1: the list is too long, but I know you will recognize yourself and consider all the best I wish to you in these lines. I also think to all the students I had the chance to teach during the course of this thesis.

It was with great honor that I joined the Lab 126 at EMPA in Thun (Switzerland) and its research team. So, I wish to thank Dr. Johann Michler and Dr. Lukas Rohr (Director of EMPA Thun) who gave me this opportunity. Dr. Johann Michler also provided me advices and solutions for each technical problem I met and accepted to review this manuscript and to assist to the defense in Rennes. I wish to thank him also for these reasons. I am particularly grateful that I was allowed to use in complete autonomy the research equipment of the laboratory (AFM, SEM, profilometer,…).

I wish to thank Sven Stauss for his availability and for sharing with me his huge experience of the Abaqus software. I acknowledge Dr. Patrick Schwaller and Dr. Christophe Ballif for finding a special interest in this work. I am grateful to Remy Gassilloud who showed me more than one time "how to do it" and to Christian Jaeggi for his availability and his happiness. I also acknowledge Kilian Wasmer and Cédric Pouvreau for helpful discussions and their kindness. To be sure not to forget anyone, I wish to thank everybody that I met at EMPA: be sure of my sincere gratitude.

I acknowledge René Gy and Géraldine Duisit from Saint Gobain Research (Aubervilliers, France) for their support at the beginning of this study, for providing assistance for the materials and for their attention paid during the course of this work.

Finally, I wish to thank my family, as well as Antoine L. and Pierre-Yves F. and of course, last but not least, Monika.

SUMMARY

CHAPITRE 0 :

SYNTHESE DES DEMARCHES SCIENTIFIQUES ET DES RESULTATS

-

french version

SOMMAIRE DU CHAPITRE 0

0.1 Introduction

La tenue en service des céramiques et des verres (et des matériaux fragiles en général) dépend habituellement de leurs endommagements de surface qui se propagent dramatiquement jusqu'à rupture. Les types d'endommagement se trouvent essentiellement sous forme de rayures et d'abrasions. Ainsi, l'étude du procédé de rayage par une unique pointe dure apparaît appropriée pour i) comprendre, ii) prédire et ainsi iii) prévenir l'endommagement de surface des verres. Le but de ce travail de thèse est l'étude de la *rayabilité des verres silico-sodo-calciques*, soit la caractérisation de la résistance au rayage et la compréhension de l'endommagement par rayage à la lumière de considérations structurales et d'une analyse mécanique.

Concrètement, les buts de cette étude sont :

1. Identification des endommagements dus au rayage des verres considérés.
2. Compréhension et discussion des différents types d'endommagement et de leurs occurrences respectives aux vues de considérations structurales (études de verres de différentes compositions chimiques).
3. Mise en place d'un modèle mécanique et analyse des résultats pour la prédiction des endommagements.

0.2 Pré requis : comportement des verres à l'indentation

0.2.1 Introduction

D'un point de vue macroscopique ou sous de hautes contraintes localisées, il est couramment admis que les verres présentent une déformation permanente sans rupture complète de l'échantillon étudié [1, 2], qui peut être dissociée i) en une déformation permanente (abusivement nommée déformation plastique en référence à la déformation permanente relative à la plasticité des métaux) qui intervient par densification et/ou par glissements locaux et ii) en une déformation par rupture (amorce et propagation de fissures).

0.2.2 Zone plastique

0.2.2.1 Déformation par densification / déformation par cisaillement

Du fait de la structure ouverte du verre (cas d'un taux peu élevé d'ions modificateurs), la pression d'une indentation induit une compaction du réseau, augmentant ainsi sa densité [3, 4] (ce phénomène a d'abord été reporté sur la compaction des verres massifs soumis à une pression quasi-hydrostatique [3, 5]). Donc, ce procédé, dit de *densification,* est une déformation non-conservative en volume et est attribuée à la possibilité qu'ont les atomes de bouger du fait de la relative souplesse des liaisons Si–O–Si. Les ions modificateurs restreignent ces mouvements.

La déformation sous une indentation est également connue pour intervenir de manière irréversible par déformation "plastique" ou glissements locaux [1, 6]. Ainsi, le phénomène de *pile-up* (apparition de bourrelets sur les bords de l'indentation [7]) est sensé apparaître dans le cas d'une déformation principalement gouvernée par déformation plastique puisque cette dernière s'exécute idéalement à volume constant.

0.2.2.2 Comportement normal/anormal des verres

Les verres dits *normaux* sont caractérisés par l'absence ou la contribution mineure de la déformation par densification sous la zone de contact. Des essais d'indentation ont montré dans ce cas l'existence d'une déformation irréversible par réarrangement "plastique".

A l'inverse, le comportement à l'indentation et au rayage des verres dits *anormaux* est gouverné de manière prépondérante par le procédé de densification qui témoigne de la capacité des verres à haute teneur en silice à densifier sous un contact mécaniquement sévère. Ainsi, les verres peuvent se déformer par glissements locaux et/ou par densification selon leur composition chimique.

0.2.3 La fissuration des verres

Les différents types de fissures qui ont lieu lors d'une indentation sont représentés sur la Fig. 1 (traduite de [8]) et montrent la différence fondamentale entre les verres normaux et anormaux d'un point de vue de la fissuration : les fissures radiales ^{c} (parfois), médianes ^{c,d} et latérales ^{d} apparaissent dans les verres normaux alors que les fissures cônes ^{c}, médianes/radiales ^{c} (restreintes par les fissures cônes) et latérales ^{d} apparaissent dans les verres anormaux [9]. Les indices ^{c} et ^{d} représentent l'occurrence des fissures au chargement ^{c} et/ou au déchargement ^{d} de la séquence du test d'indentation.

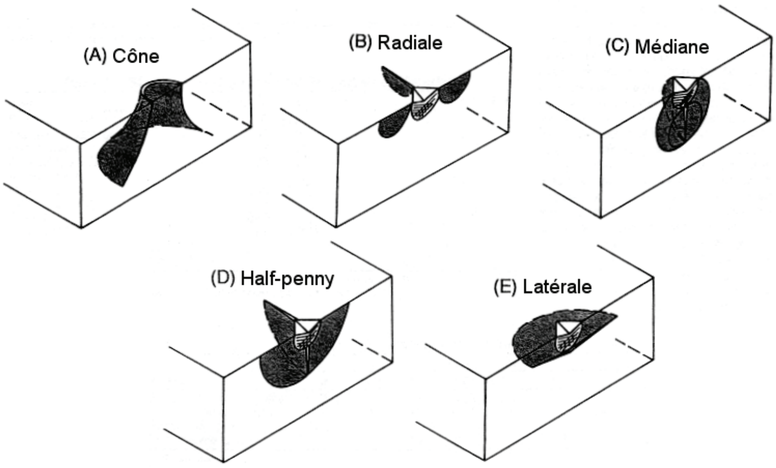

Fig. 1 [8] : Coupes isométriques des morphologies idéalisées des fissures observées pendant une indentation : (A) fissure cône et la fissure circulaire d'amorçage associée, (B) fissure radiale avec l'empreinte de contact et la zone de déformation plastique associées (indenteur Vickers), (C) fissure médiane, (D) fissure *half-penny*, et (E) fissure latérale.

0.3 Matériaux et dispositif expérimental de rayage

0.3.1 Matériaux

Les compositions chimiques des verres étudiés sont définies de telle sorte que leur comportement à l'indentation va des verres normaux aux verres anormaux [9].

Un verre silico-sodo-calcique commercial[1], une silice vitreuse et 4 différents verres synthétisés [10, 11] dans le diagramme de phase Na_2O-CaO-SiO_2 (notés SLS 1 à 4) ont été étudiés. Le détail de la composition chimique de chaque verre est donné dans la Table 1.

[mol. %]	Planilux	SLS 1	SLS 2	SLS 3	SLS 4	Silice vitreuse
SiO_2	70,8	71,0	74,0	77,0	80,00	100,00
Na_2O	12,8	17,5	15,7	13,9	12,10	-
MgO	5,9	-	-	-	-	-
CaO	10,2	11,5	10,3	9,1	7,90	-
AL_2O_3	0,4	-	-	-	-	-

Table 1 : Composition chimique des verres étudiés.

---

[1] Planilux™, Saint-Gobain

0.3.2 Le dispositif expérimental de rayage

Pendant un essai de rayage, une pointe de géométrie connue chargée d'une force normale P est déplacée sur la surface de l'échantillon testé. Les matériaux répondent différemment selon leur nature à la sollicitation compliquée résultant d'un test de rayage : déformation plastique, densification, recristallisation, fissuration,…

Un dispositif expérimental appelé machine de rayage ou scléromètre linéaire a été conçu pour ce travail et permet un chargement variable durant les essais. Pour l'étude du rôle de l'environnement, l'appareil a été placé dans une boite à gants contrôlée en humidité (de 0 % à 100 % r.h.). L'ensemble du dispositif est représenté schématiquement dans la Fig. 2.

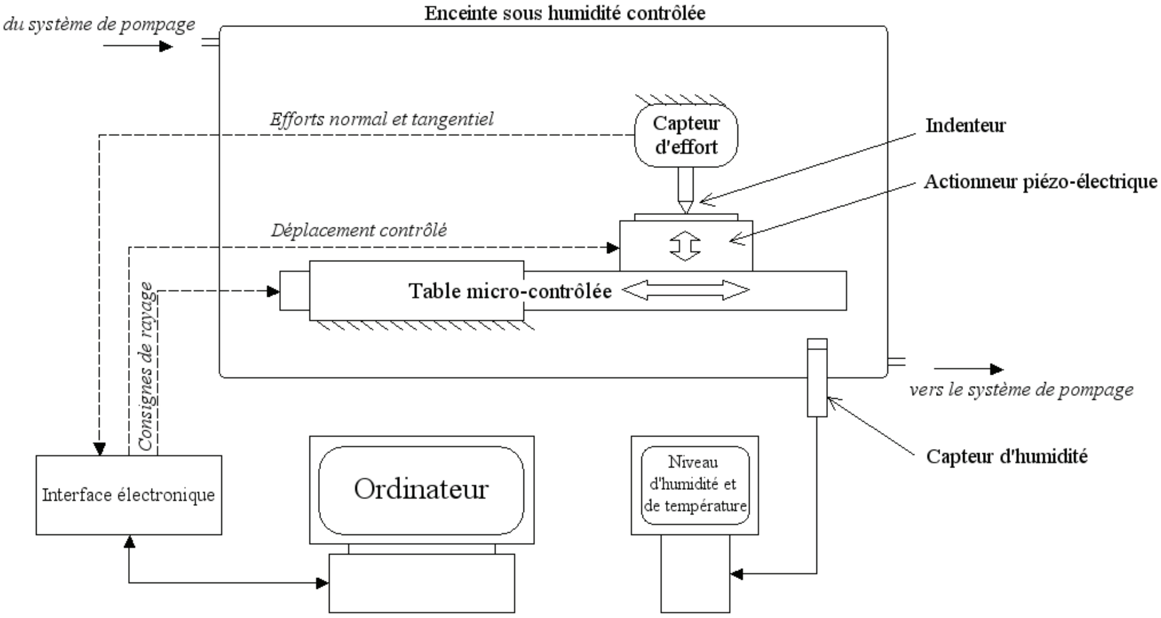

Fig. 2 : Schéma du dispositif expérimental de rayage dans l'enceinte contrôlée en humidité.

Le déplacement horizontal qui impose le mouvement de rayage est obtenu à l'aide d'une table pilotée par ordinateur, alors que le mouvement vertical qui impose la pénétration de la pointe dans le matériau est assuré par un actionneur piézo-électrique.

La pénétration ainsi que les efforts normal et tangentiel sont continuellement mesurés. Ce dispositif expérimental permet des essais de rayage effectués à charge normale constante ainsi qu'en rampe charge-décharge.

0.4 Résultats expérimentaux

0.4.1 Propriétés physiques et comportement à la sollicitation statique

Les propriétés physiques et mécaniques des verres étudiés ont été mesurées et sont rassemblées dans la Table 2.

Propriétés Verres	T_g (°C) ±2	ρ (g/cm^3) ±0.01	E (GPa) ±0.5	ν ±0.01	H (GPa) ±0.01	K_c (MPa.m$^{1/2}$) ±0.02
Verre à vitre	560	2.55	71.5	0.21	6.12	0.72
SLS 1	558	2.53	70.4	0.20	5.35	0.71
SLS 2	559	2.50	69.9	0.19	5.11	0.70
SLS 3	560	2.47	69.2	0.18	5.15	0.76
SLS 4	561	2.43	68.7	0.17	5.19	0.82
Silice vitreuse	700-1200	2.20	73.0	0.16	8.03	1.47 – 0.77*

Table 2 : Composition chimique et propriétés physiques des verres étudiés. * note une mesure de la ténacité par S.E.N.B. [12].

La dureté Meyer H et la ténacité par indentation K_c ont été déterminées par essais d'indentation avec une charge de 1 kg (maintenue pendant 15 s) et à l'aide des équations suivantes :

$$H = \frac{P}{2a^2} \qquad \textbf{Eq. 1}$$

et

$$K_c = 0.016\sqrt{\frac{E}{H}}\frac{P}{c^{3/2}} \qquad \textbf{Eq. 2}$$

avec P la charge normale, a la demi longueur moyenne des deux diagonales de l'empreinte résiduelle, E le module d'Young et c la demi longueur des deux fissures radiales (de bout en bout).

La densité des verres décroît avec l'augmentation de la proportion de silice (les ions formateurs Si^{4+} remplacent les ions modificateurs Na^+ et Ca^{2+}), du fait de la capacité du réseau siliceux à accommoder l'addition de larges proportions de cations due à sa structure ouverte. L'augmentation monotone de la masse volumique ρ provient du remplissage optimum des sites vacants du réseau tridimensionnel par les cations interstitiaux comme Na^+ et Ca^{2+}. Le module d'Young décroît légèrement avec la diminution de cations modificateurs dans le réseau : moins il y a d'ions formateurs, plus la rigidité du réseau dépend de l'orientation mutuelle des tétraèdres de silice et des angles entre chacun alors que les autres paramètres structuraux restent inchangés [4]. Le coefficient de Poisson est également gouverné par cet effet.

H et K_c présentent des évolutions non monotones en fonction de la proportion d'ions modificateurs dans le réseau et sont minimum pour le verre SLS 2. Yamane et al. [13] ont montré que plus la compacité du verre est élevée, plus la dureté et les modules élastiques le sont aussi (les présents résultats sur la silice sont à exclure). Aux vues des résultats relatés, cela suggère qu'un faible coefficient de Poisson favorise la densification (avec la diminution permanente de volume associée). La ténacité K_c mesurée par indentation augmente avec la proportion de silice dans le verre pour un pourcentage molaire supérieur à 74 % sauf pour le verre SLS 2 (voir Graph 1). Cela confirme que les verres riches en silice se déforment davantage par densification et donc ont une ténacité supérieure que les verres avec une forte proportion de modificateurs. En effet, l'énergie dissipée dans le procédé de densification ainsi que le changement relatif de fissuration des fissures médianes/radiales vers des cônes de Hertz contribuent à la limitation en taille des fissures médianes/radiales dont est déduit la ténacité qui apparaît alors d'autant plus élevée. L'exception de la ténacité de la nuance de verre SLS 2 est attribuée à sa structure supposée entrelacée de deux structures correspondantes aux phases tridymite et devitrite du diagramme de phases Na_2O-CaO-SiO_2.

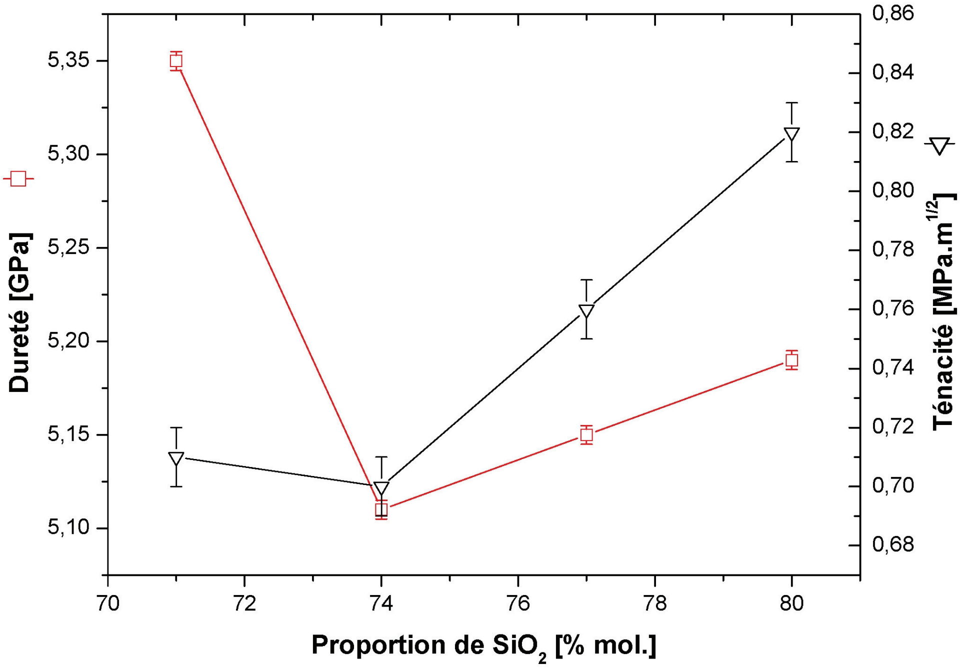

Graph 1 : La dureté H et la ténacité K_c en fonction de la proportion en silice pour les verres de la série SLS.

La fragilité B ainsi que les charges critiques expérimentales d'amorce de fissures radiales P_C^R et latérales P_C^L et théoriques (indiquées par un exposant *) ont été déterminées et reportées dans le Table 3. B, P_C^{R*}, P_C^{L*} ont été calculées à partir des équations suivantes [14-17]:

$$B = \frac{H}{K_c} \qquad \textbf{Eq. 3}$$

$$P_C^{R*} = \alpha \frac{K_C{}^4}{H^3} \qquad \textbf{Eq. 4}$$

$$P_C^{L*} = \beta E \frac{K_C{}^4}{H^4} \qquad \textbf{Eq. 5}$$

où K_c est la ténacité, H la dureté Meyer, et E le module d'Young. Les valeurs suivantes ont été obtenues dans cette étude pour α et β : α=3.9 10^5, β=4.9 10^4 dans le cas des verres de la famille SLS et α=2.2 10^4 pour le verre *float* (verre à vitre commercial standard - Planilux).

	$B = H/K_c$ ($m^{-1/2}$)	P_C^R (N)	P_C^{R*} (N)	P_C^L (N)	P_C^{L*} (N)
Verre *float*	8500	0.25 – 0.50	0.30	1 – 2	
SLS1	7550	0.10 – 0.25	0.65	0.25 – 0.50	1.07
SLS2	7300	0.10 – 0.25	0.70	0.25 – 0.50	1.20
SLS3	6800	1 – 2	0.95	2 – 3	1.59
SLS4	6350	1 – 2	1.26	2 – 3	2.09

Table 3 : Fragilité, charges d'amorces de fissures radiales expérimentales et théoriques et charges d'amorces de fissures latérales expérimentales et théoriques.

Dans le cas des verres de la série SLS, la différence entre le comportement des verres SLS 1/SLS 2 et des verres SLS 3/SLS 4 est prédit (Table 3). De plus, les verres SLS 1/2 semblent les plus sensibles à la fissuration radiale et latérale ainsi que les plus fragiles du fait de leur valeur de fragilité B. Dans le cas du verre *float*, l'ajout des ions modificateurs est responsable de changements significatifs dans le réseau vitreux.

0.4.2 Comportement au rayage

0.4.2.1 Rôle de l'effort normal appliqué sur le comportement au rayage (verre *float*)

Pendant un essai d'indentation Vickers sur un verre silico-sodo-calcique, l'occurrence des fissures dépend fortement de la charge appliquée et celles-ci peuvent apparaître durant la charge ou la décharge du test [8, 18]. Des observations similaires ont été effectuées durant des tests de rayage [11, 19] mais l'étude de la fissuration et des endommagements reste à explorer. Une analyse fractographique à l'échelle micrométrique a été menée. Par exemple, les fissures chevrons comme définies par Rice et al. [19], la propagation des fissures latérales décrite par Ahn [20] et Bulsara [21], ainsi que l'écaillage donné par Le Houérou et al. [11] méritent quelques investigations supplémentaires. Les observations des endommagements de surface décrites dans les parties à suivre renseignent sur la nature et l'occurrence des phénomènes de fissuration radiales, latérales et d'écaillage.

Pendant un test de rayage, le faciès d'endommagement dépend fortement de la charge normale appliquée et différentes fissures ont été identifiées : i) les fissures médianes, ii) les fissures radiales (chevrons) et iii) les fissures latérales.

Pendant un essai de rayure effectué avec une charge croissante monotone sur un verre, trois régimes différents d'endommagement sont typiquement observés et représentés schématiquement sur la Fig. 3 : i) le régime micro-ductile I (sillon permanent sans endommagement visible), ii) le régime fragile, de fissuration ou d'écaillage II (endommagement important sous forme de fissures : fissures latérales atteignant la surface et fissures radiales) et iii) le régime micro-abrasif III (présence de nombreux débris et éventuellement de petites fissures latérales débouchantes).

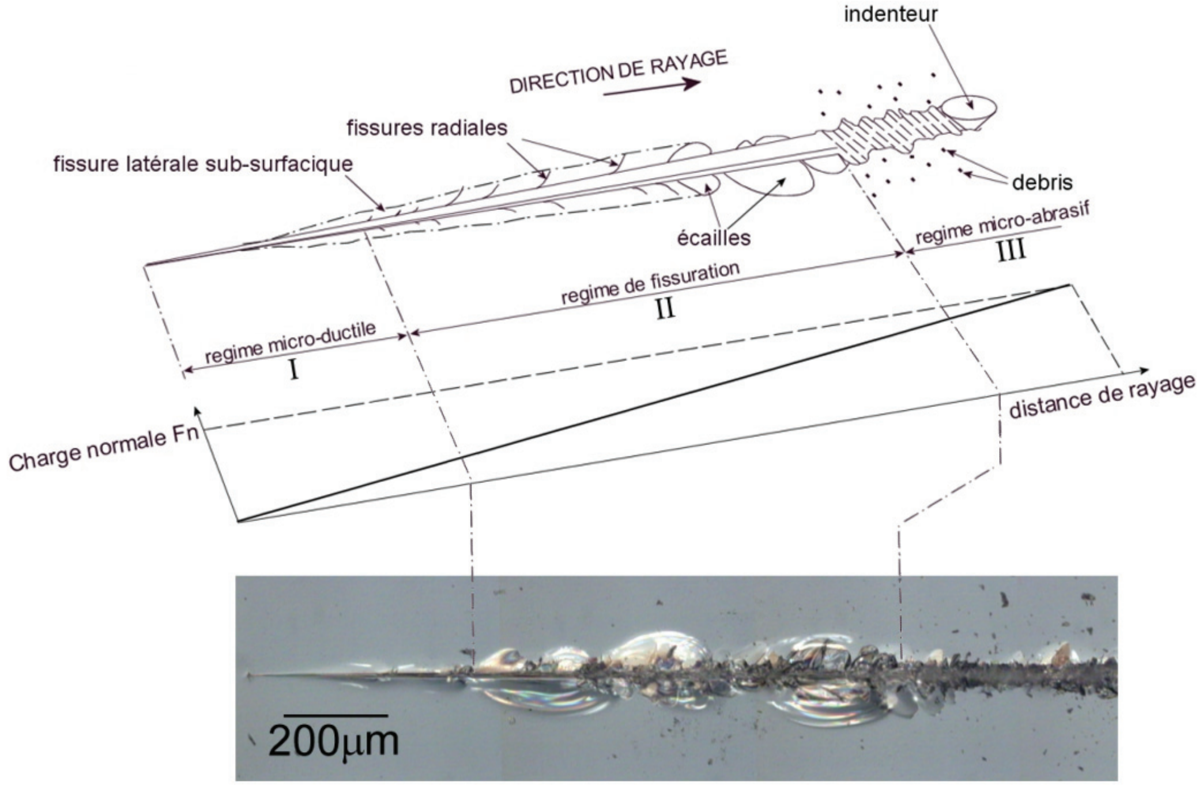

Fig. 3 : Rayure typique obtenue sur la surface d'un verre silico-sodo-calcique lors d'un chargement monotone d'un indenteur (voir le diagramme de force associé) et micrographie d'une rayure sur verre. Définition des régimes d'endommagement I, II et III.

0.4.2.2 Résultats préliminaires

L’influence de divers paramètres a été succinctement étudiée. Un effet dynamique selon l’histoire de la charge appliquée (i.e. charge croissante ou décroissante) a été noté. Par contre, aucune dépendance de la face testée (face étain ou atmosphère du verre *float*) n’a été remarquée dans la gamme de charge et de précision considérées. Les contraintes résiduelles influencent grandement la sévérité du faciès d’endommagement de la rayure (i.e. décalage des régimes d’endommagement qui apparaissent à des charges normales appliquées plus faibles en présence de contraintes résiduelles de compression). Ces résultats suggèrent que tous les verres trempés devraient montrer moins de pertes optiques et esthétiques (le régime micro-abrasif est moins dommageable de ce point de vue que le régime d'écaillage), mais davantage de pertes des propriétés mécaniques.

La géométrie de l’indenteur influence également le comportement au rayage des verres. Les résultats expérimentaux montrent clairement que plus la géométrie de l’indenteur est sévère (par exemple l’indenteur Vickers comparé à un indenteur conique ou encore un indenteur conique d’angle au sommet plus aigu qu’un autre indenteur conique), plus les régimes d’endommagement apparaissent rapidement (dans le sens de la charge appliquée). Ainsi, un décalage dans les charges de transitions a été mesuré. Mis à part, l’indenteur Vickers se révèle être un pénétrateur donnant un essai de rayage plus stable.

0.4.2.3 Rôle de l’hygrométrie (% r.h.)

La Fig. 4 montre les rayures effectuées à différents taux d’humidité (de 0 à 100 % r.h.) sur un verre *float* recuit accompagnées du diagramme de charge normale appliquée durant les essais.

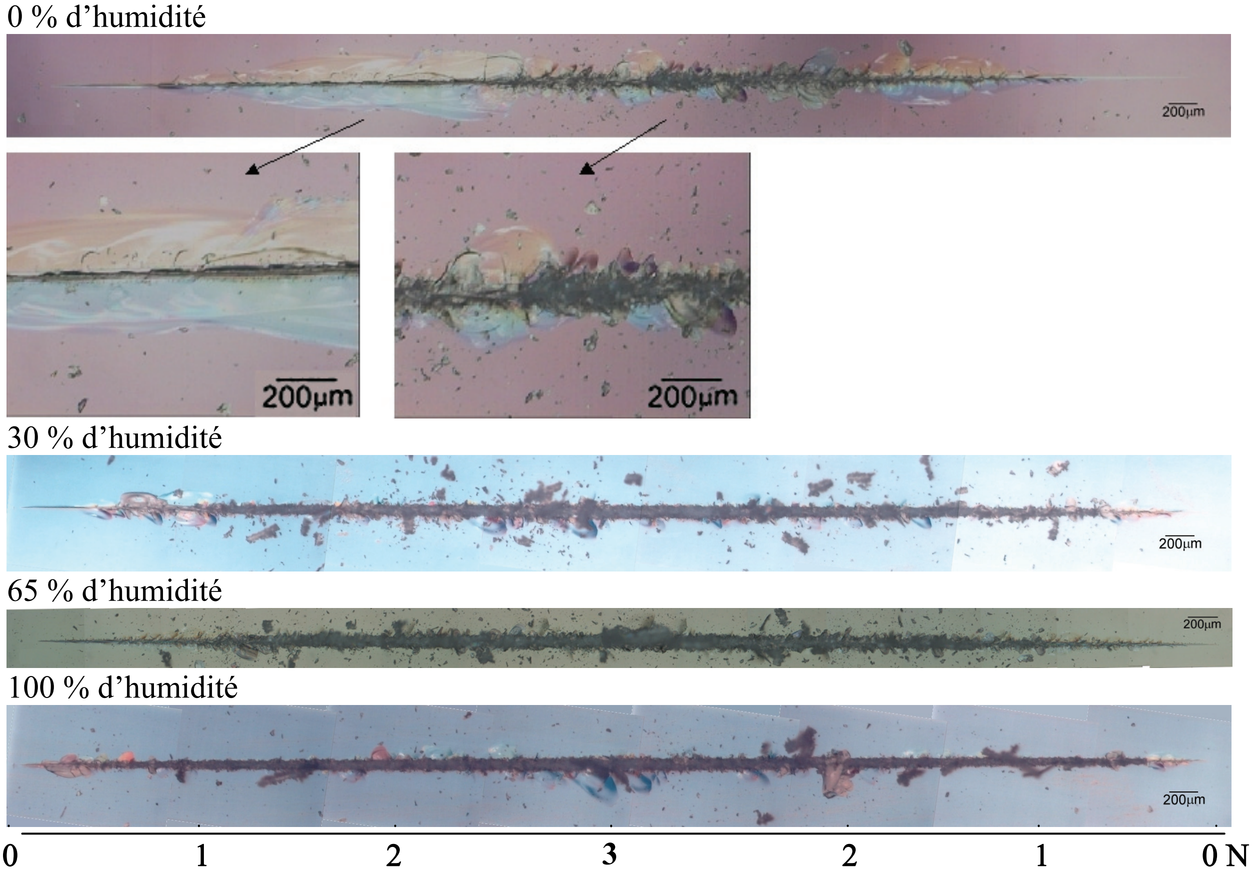

Fig. 4 : Images des rayures obtenues à différents taux d’hygrométrie avec un indenteur Vickers piloté en rampe charge-décharge.

Les charges de transition de régimes évoluent évidemment avec le taux d'hygrométrie. En effet, les régimes d'endommagement d'écaillage et micro-abrasif apparaissent à des charges normales appliquées plus élevées à mesure que le taux d'hygrométrie diminue comme il est reporté dans le Graph 2.

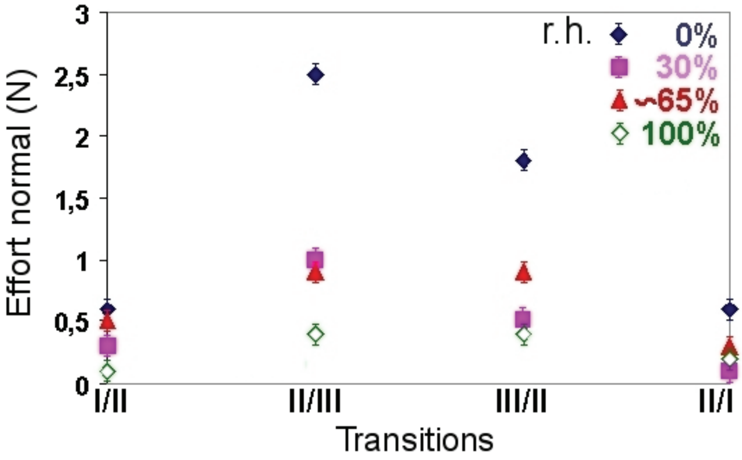

Graph 2 : Charges de transition de régime en fonction du taux d'hygrométrie.

Le faciès d'endommagement particulier obtenu à 0 % d'humidité est caractérisé par une large fissure latérale sub-surfacique (i.e. non-débouchante). Ce phénomène s'estompe rapidement à mesure que le taux d'humidité augmente. Un manque de fissure radiale est à mettre en cause dans le cas de 0 % d'humidité puisque cela empêche les fissures latérales sub-surfaciques d'atteindre la surface de l'échantillon qui se développent alors largement sous la surface au lieu de former des écailles par intersection avec les fissures radiales. Ce mécanisme de création d'écailles sera discuté en détail dans la prochaine partie. Ainsi, l'occurrence des fissures radiales est gouvernée par le taux d'hygrométrie durant l'essai de rayage.

0.4.2.4 Phénoménologie : identification et compréhension des endommagements lors du rayage

0.4.2.4.1 Le régime micro-ductile

Le régime micro-ductile présente des endommagements à l'intérieur du sillon mais également sous le sillon.

0.4.2.4.2 Le régime fragile

0.4.2.4.2.1 Apparition des fissures radiales (chevrons)

Les fissures radiales (ou chevrons) qui apparaissent pendant le rayage s'inclinent rapidement à partir du sillon créé et se propagent en suivant une forme courbe finissant habituellement perpendiculaire à la rayure comme illustré sur la Fig. 3. La Fig. 5 montre l'amorce et le début de la propagation d'une fissure radiale. L'amorce se fait clairement au contact avec l'arête menante de l'indenteur Vickers et la fissure se propage rapidement dans une direction curviligne, au départ parallèle à la rayure et qui tend vers la fin à en être perpendiculaire. La fissure émerge donc du sillon avec un angle noté θ. Cette propagation peut être qualifiée de semi-stable pour deux raisons : i) après l'amorce de la fissure, cette dernière s'incline rapidement à "gauche" ou à "droite" du sillon ; cette direction est purement statistique et constitue la partie instable de la propagation de la fissure, et ii) la vitesse de propagation de la fissure suggère alors une propagation stable.

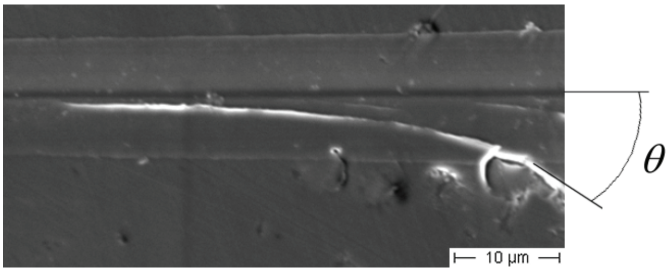

Fig. 5 : Amorce et propagation d'une fissure radiale (chevron) à la surface d'un verre *float*. (MEB)

0.4.2.4.2.2 Compréhension de la création et du développement des écailles

Deux mécanismes différents de création d'écailles ont été identifiés : i) l'écaillage peut se produire en l'absence de fissures radiales (dans le cas d'une hygrométrie limitée par exemple) si suffisamment d'énergie est mise en jeu dans la propagation de la fissure latérale afin qu'elle atteigne la surface (voir la Fig. 6), ou ii) l'écaillage peut se produire par combinaison de deux fissures radiales et d'une fissure latérale qui atteint alors la surface (voir la Fig. 7).

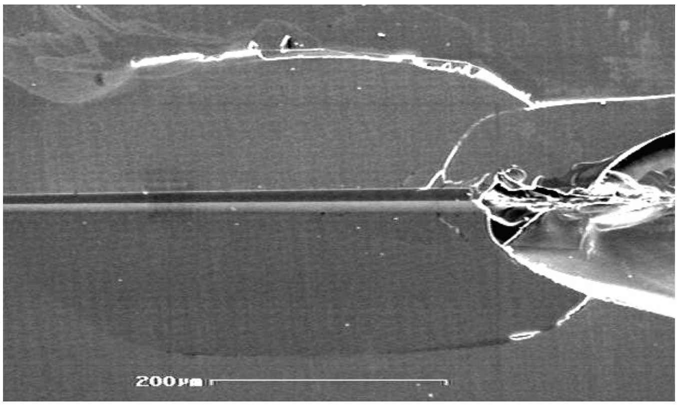

Fig. 6 : Écaillage par propagation d'une fissure latérale – absence de fissure radiale (SLS 4). (SEM)

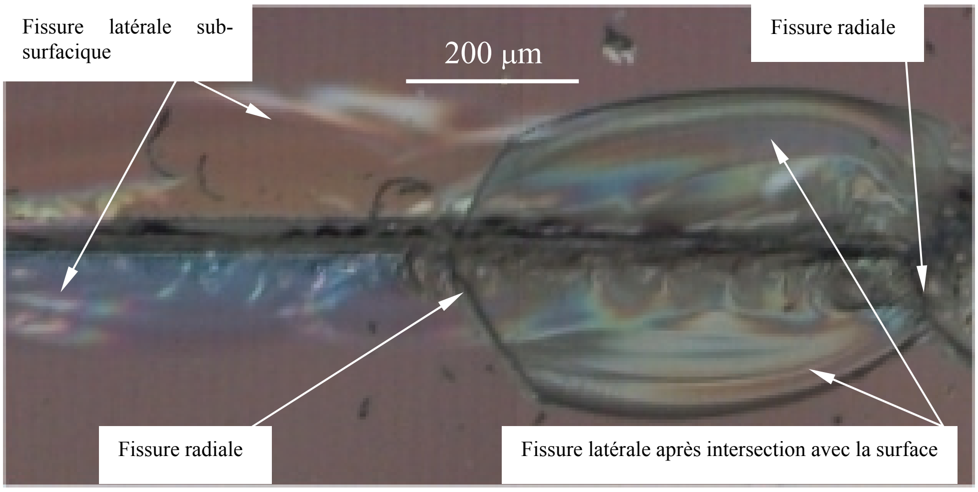

Fig. 7 : Formation d'une écaille avec les différents endommagements mis en jeu.

Un phénomène de *Twist h*ackle [22-25] a été observé sous les écailles renseignant sur la direction de propagation des écailles : elles démarrent à partir du sillon de rayage et se propagent de manière perpendiculaire à la direction de rayage.

0.4.2.5 Rôle de la composition chimique des verres

La Fig. 8 montre une rayure représentative pour chacun des six verres étudiés (obtenus pour une charge normale croissante monotone jusqu'à 4 N) et prouve que la résistance au rayage des verres dépend fortement de la composition chimique de ceux-ci. La Table 4 donne les charges de transition de régimes d'endommagement en fonction de la composition chimique des verres considérés. Ces valeurs sont des valeurs statistiques obtenues à partir de plusieurs rayures.

Verre à vitre standard :

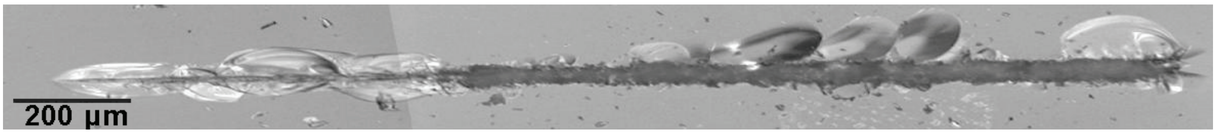

SLS 1 :

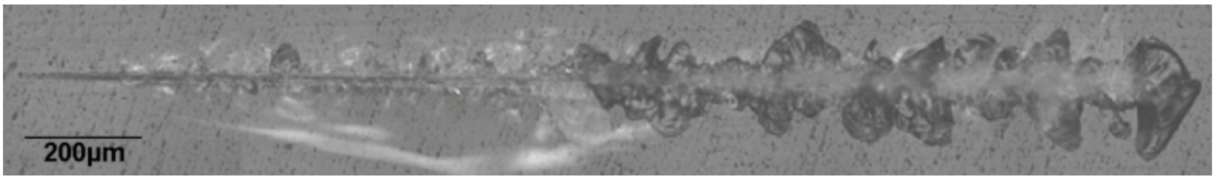

SLS 2 :

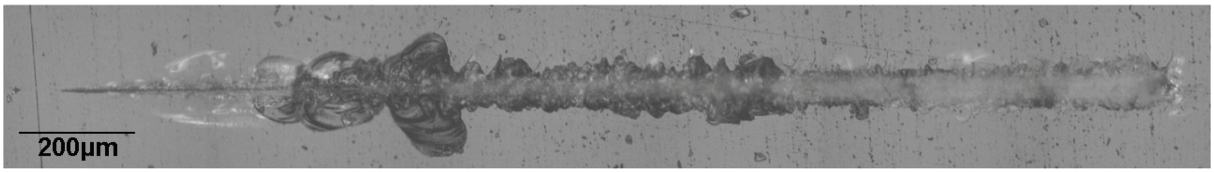

SLS 3 :

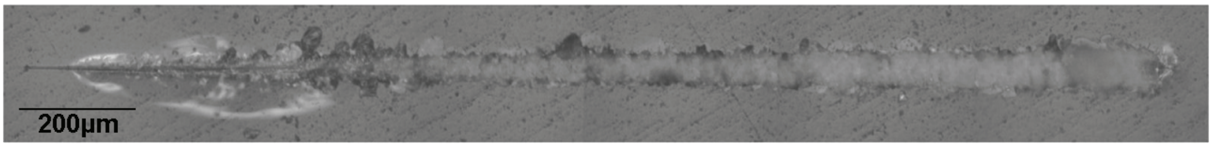

SLS 4 :

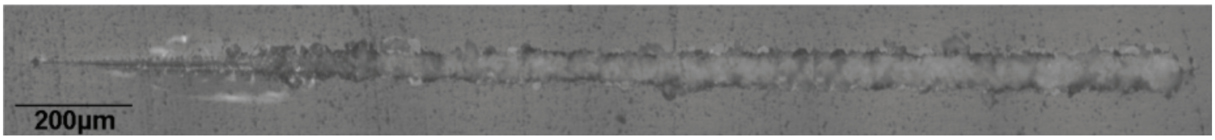

Silice vitreuse :

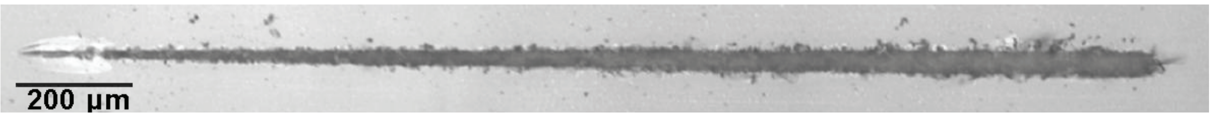

Fig. 8 : Évolution de la résistance à la rayure des six verres considérés.

Régimes d'endommagement / Verres	Micro-ductile	Micro-fragile		Micro-abrasif
		Latérales sub-surfaciques	Écailles	
Verre float standard	0 – 0.4 N	0.4 – 0.8 N	0.8 – 1.2 N	1.2 – 4 N
SLS 1	0 – 0.35 N	0.35 – 2 N	2 – 4 N →	2 – 4 N
SLS 2	0 – 0.4 N	0.4 – 0.9 N	0.9 – 1.6 N	1.6 – 4 N
SLS 3	0 – 0.35 N	0.35 – 1 N	1 – 1.1 N	1.1 – 4 N
SLS 4	0 – 0.3 N	0.3 – 0.9 N	–	0.9 – 4 N
Silice vitreuse	0 – 0.2 N	0.2 – 0.5 N	–	0.5 – 4 N

Table 4 : Charges de transition de régimes d'endommagement en fonction de la composition chimique des verres considérés. La flèche indique la difficulté à dissocier les deux différents régimes.

Les verres à vitre standard, SLS 1 et 2 apparaissent clairement sur ces photos plus sensibles à l'écaillage, ce qui est cohérent avec leur nature de verres normaux : les fissures apparaissent principalement par glissements locaux [11] dus aux chemins de percolation présents dans le réseau vitreux [26]. Les verres SLS 3, 4 et la silice vitreuse qui ont des réseaux du type de la silice sont plus résistants à la propagation de fissures et à l'écaillage durant les essais de rayage du fait de leur nature de verres anormaux [11] qui accommodent la déformation par réarrangement du réseau (densification) sans rupture de liaison inter-atomique [9]. Une étude fractographique à faible échelle confirme ces tendances aussi bien pour le régime micro-fragile que pour le régime micro-abrasif.

0.5 Modélisation mécanique

0.5.1 Introduction : extension du modèle de Ahn

La nucléation des fissures et donc l'apparition des endommagements associés requiert de considérer les contraintes locales. Comparé au modèle de Ahn [20] qui décrit le champ de contraintes pendant un essai de rayage, le modèle présenté dans le cadre de cette étude prend en compte le caractère normal/anormal des verres considérés et la singularité de la géométrie de l'indenteur Vickers. Ainsi, ce modèle consiste en l'extension du modèle de Ahn à ces deux considérations. Le modèle de Ahn (dérivé de celui de Yoffe qui traite de l'indentation conique [27]) donne l'expression complète des contraintes dans la zone du matériau restée *élastique* par superposition de deux champs de contraintes élastiques :

- un champ de contraintes de type Boussinesq qui correspond à l'idéalisation de l'indenteur chargé en deux forces concentrées à l'emplacement de l'indenteur (l'une normale, l'autre tangentielle),
- un champ de contraintes, dit de *Blister*, caractérisé par un paramètre d'intensité de champ *Blister B* et qui correspond au champ de contraintes résiduelles dans la zone élastique provoqué par l'influence de la zone plastique créée tout le long de la rayure. Il est à noter que *B* peut dépendre de la charge appliquée, du comportement du matériau à la déformation (densification/cisaillement), de la géométrie de l'indenteur ainsi que d'autres paramètres expérimentaux (effets d'environnement,…).

En conséquence, le champ de contraintes complet s'écrit :

$$\sigma = \sigma^{n}_{Bous.} + \sigma^{t}_{Bous.} + \sigma^{r}_{Blister} \qquad \textbf{Eq. 6}$$

L'exposant *n* représente le champ de contraintes dû à la charge normale ; l'exposant *t* représente le champ de contraintes dû à la force tangentielle ; l'exposant *r* représente le champ de contraintes résiduelles.

Dans cette étude, les deux extensions du modèle devront mener à l'expression suivante :

$$\sigma_{\substack{normal/anomalous\\ Vickers}} = \sigma^{n}_{Vickers} + \sigma^{t}_{Vickers} + \sigma^{r}_{\substack{Blister\ for\ scratching\\ normal/anomalous\ glasses\\ Vickers}} \qquad \textbf{Eq. 7}$$

Les termes $\sigma^{n}_{Vickers} + \sigma^{t}_{Vickers}$ correspondent à l'indenteur chargé.

Le terme $\sigma^{r}_{\substack{Blister\ for\ scratching\\ normal/anomalous\ glasses\\ Vickers}}$ correspond aux contraintes résiduelles.

L'extension concernant le caractère normal/anormal des verres sera rendue possible par l'étude de la compétition entre la densification et les glissements locaux (cisaillement) dans la déformation du matériau (considérations expérimentales). L'extension du modèle à la géométrie de l'indenteur Vickers sera menée en remplaçant le champ de Boussinesq représentant idéalement des forces concentrées par un champ plus adapté grâce à une étude par Éléments Finis portant sur la comparaison entre une indentation conique et une indentation Vickers. Le diagramme suivant résume cette approche, du modèle de départ (celui de Yoffe) au modèle final attendu en passant par le modèle de Ahn.

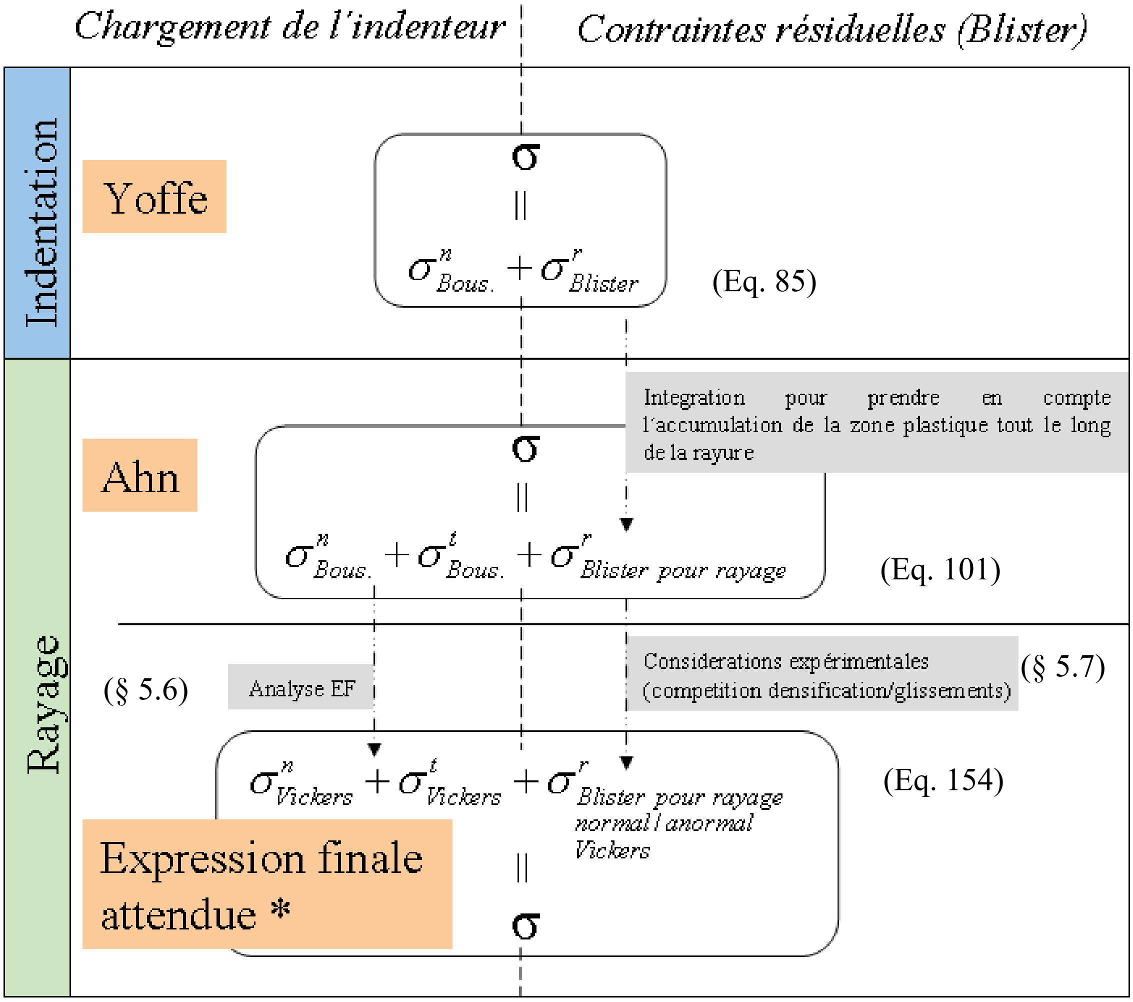

* L'expression finale approchée sera discutée dans la partie § 5.8.

Fig. 9 : Diagramme du principe d'extension des modèles de Yoffe et Ahn au caractère normal/anormal des verres considérés et à la géométrie de l'indenteur Vickers.

0.5.2 Extension du modèle à la géométrie de l'indenteur Vickers : l'étude par Éléments Finis

Un modèle 3D par éléments finis a été mis en place à l'aide du code de calcul Abaqus (version 6.2) et validé pour pouvoir analyser les champs de contraintes dans le cas de l'indentation Vickers en comparaison avec une indentation conique. Il faut noter qu'une analyse en considérant le matériau comme idéalement élastique suffit pour cette étude et que pour des raisons de symétries seulement 1/8 de l'indenteur et du solide indenté sont modélisés. L'insertion de l'indenteur (modélisé simplement par une surface définie rigide) et du solide indenté est illustrée sur la Fig. 10 sous formes maillées.

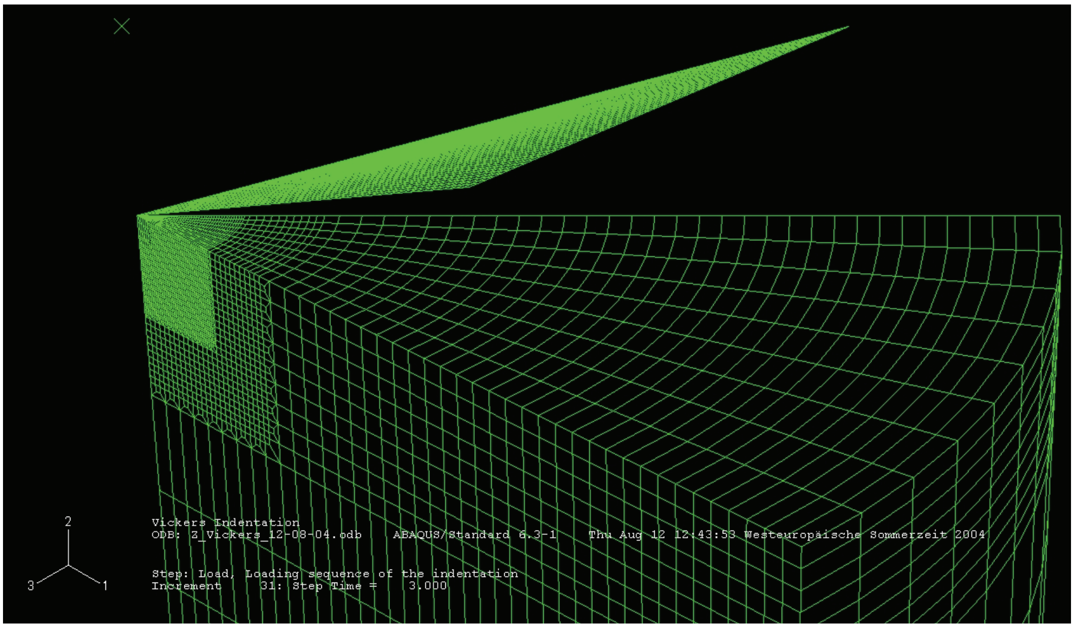

```
Vickers Indentation
ODB: Z_Vickers_12-08-04.odb    ABAQUS/Standard 6.3-1    Thu Aug 12 12:43:53 Westeuropäische Sommerzeit 2004

Step: Load, Loading sequence of the indentation
Increment     31: Step Time =     3.000
```

Fig. 10 : Le solide indenté et l'indenteur dans le module de maillage du code de calcul E.F. utilisé (Abaqus) – Vue en perspective.

La Fig. 11 montre sur une représentation schématique d'un indenteur Vickers la définition des plans *Face* (ABC) et *Arête* (ABD).

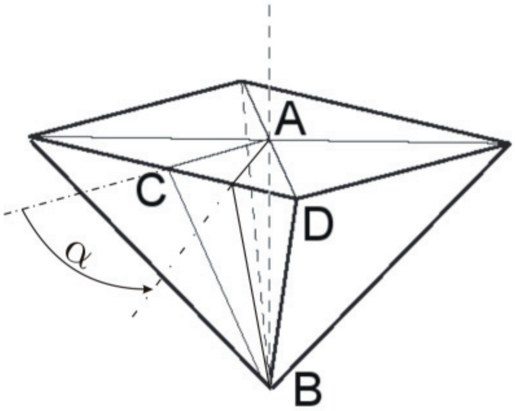

Fig. 11 : Représentation schématique d'un indenteur Vickers et définition des plans ABC et ABD.

Le Graph 3 représente le détail de la distribution des contraintes de Von Mises dans le cas d'une indentation conique (a), dans le plan de la face d'un Vickers (i.e. dans le plan ABC sur la Fig. 11) (b) et dans le plan de son arête (i.e. dans le plan ABD sur la Fig. 11) (c).

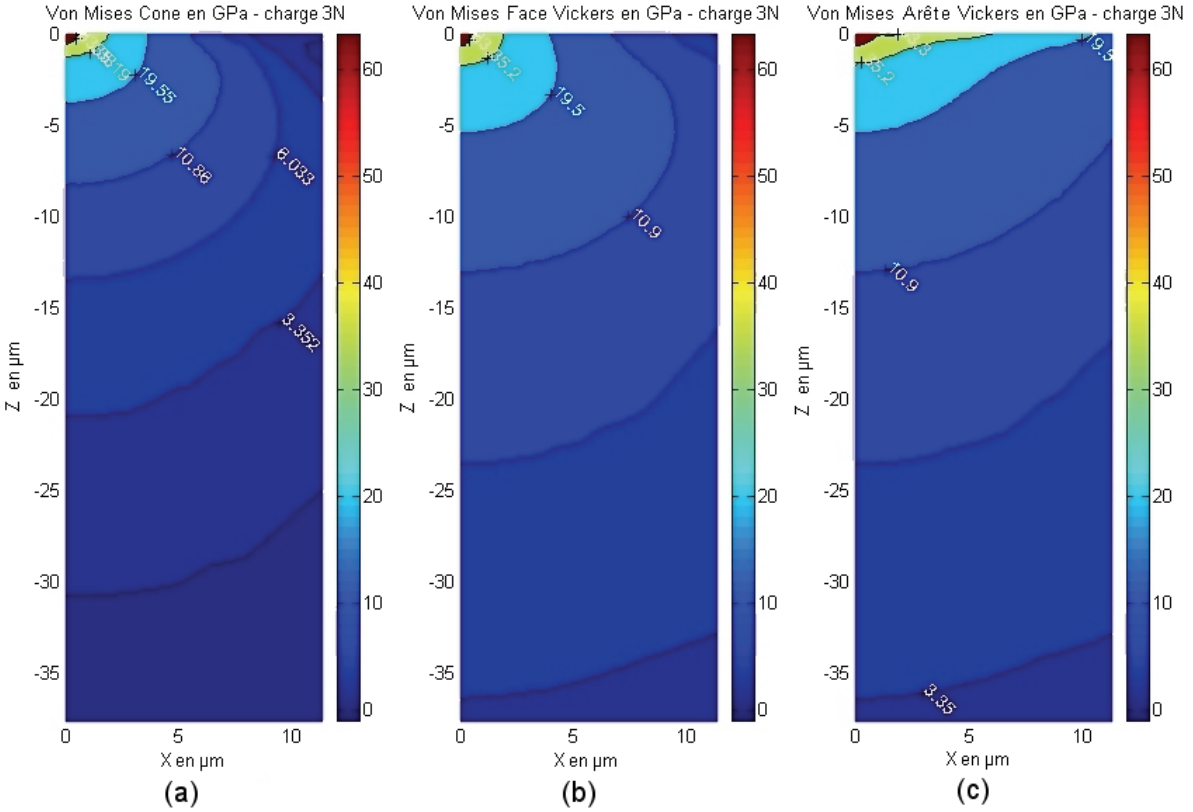

Graph 3 : Détails de la comparaison de la distribution des contraintes de Von Mises (résultats éléments finis) entre le cas (a) de l'indentation conique (cône équivalent), (b) dans le plan de la face du Vickers, et (c) dans le plan de l'arête du Vickers.

Le champ de contraintes dans le plan de la face du Vickers ressemble à celui obtenu dans le cas d'une indentation conique sur un solide purement élastique. On le modélisera donc analytiquement par les expressions des contraintes de Hanson pour une indentation conique [28, 29] (avec des coefficients correcteurs proportionnels selon la composante de contrainte considérée).

Le champ de contraintes dans le plan de l'arête du Vickers n'apparaît pas comme étant un champ de contraintes "classique". Cependant, la géométrie de l'indenteur considéré rappelle un problème simple à décrire : celui d'une ligne chargée par une pression non-uniforme sur la surface d'un solide semi-infini élastique.

De plus, la distribution de pression sur la ligne chargée est facilement accessible par le modèle éléments finis développé dans cette étude. Ainsi, la distribution de pression le long de cette ligne chargée a pu être déterminée et est illustrée sur la Fig. 12 (la symétrie du problème n'est pas représentée i.e. la pression p_0 est localisée à la pointe de l'indenteur) : elle est uniformément décroissante avec l'expression suivante pour la pression p (déterminée pour la charge normale de 3 N) selon la distance avec le centre d'indentation r :

$$p(r) = -4370,9r + 97156 \qquad \textbf{Eq. 8}$$

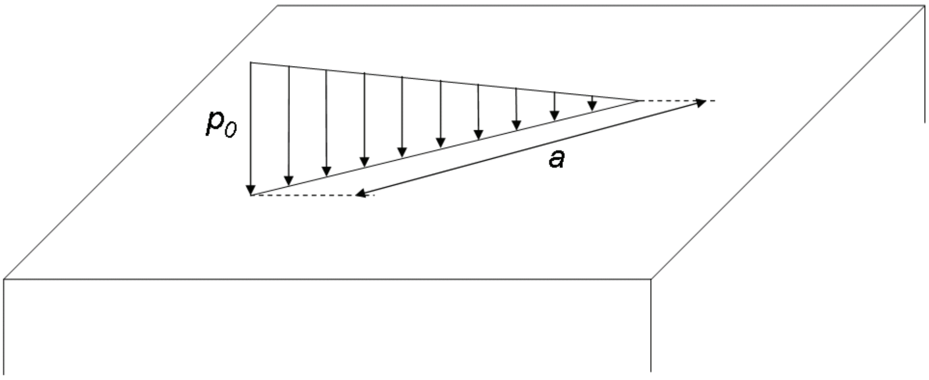

Fig. 12: Représentation schématique de la ligne chargée par une pression uniformément décroissante sur un solide élastique semi-infini.

Pour résumer, le champ de contraintes dans le plan de la face de l'indenteur Vickers peut facilement être modélisé analytiquement par un champ corrigé de contraintes de Hanson pour une indentation conique. Le champ de contraintes dans le plan de l'arête de l'indenteur Vickers pourrait être modélisé par la solution au problème d'une ligne chargée sur un solide élastique semi-infini par une pression uniformément décroissante sur la demi-longueur du contact.

Tout plan intermédiaire paramétré par un angle α (voir Fig. 11) pourrait s'exprimer par une combinaison non-linéaire de ces deux champs de contraintes fondamentaux à l'aide d'une fonction de transformation qui dépendrait de r et de α. Malheureusement, il n'existe pas encore d'expressions analytique pour modéliser le champ de contraintes dans le plan de l'arête de la pointe Vickers et toutes les tentatives dans ce but ont jusqu'alors été relativement infructueuses. Ainsi, il a été décidé de "corriger" un champ de contraintes issu d'une indentation conique par des *coefficients de correction de contraintes* déterminés par comparaison directe entre les valeurs de contraintes positives maximales pour une indentation conique et une indentation par un indenteur Vickers, et ce pour chaque composante de contraintes (voir Table 5).

Composante de contrainte	σ_{xx}	σ_{yy}	σ_{zz}	τ_{xy}
Rapport $\dfrac{\sigma^{\max}_{Vickers}}{\sigma^{\max}_{Cone}}$	0.867	1.228	1.122	0.920

Table 5: Coefficients de correction de contraintes : comparaison entre indentation Vickers/conique.

Ainsi, l'expression des contraintes pour le model semi-analytique final après intégration des spécificités de la géométrie de l'indenteur Vickers donne :

$$\sigma = \sigma^{n}_{Hanson} + \sigma^{t}_{Bous.} + \sigma^{r}_{Blister} \qquad \textbf{Eq. 9}$$

Les composantes de cette équation sont détaillées dans le chapitre 0.

0.5.3 Extension du modèle aux verres normaux/anormaux : identification de la compétition densification/cisaillement

0.5.3.1 Méthode

Les six verres considérés (verre à vitre commercial standard, verres de la série SLS et silice vitreuse) exhibent selon leur composition chimique des comportements à la déformation plus ou moins intermédiaires entre le matériau qui se déforme idéalement par pure densification et le matériau qui se déforme seulement par glissements locaux (i.e. par cisaillement ou réarrangement plastique). Ainsi, la compétition entre la densification et les glissements locaux dans la déformation des verres sera étudiée à travers l'identification du paramètre *B* (appelé intensité du champ de contraintes *Blister*) précédemment introduit.

Une nouvelle technique a été développée pour accéder au paramètre *B* du champ *Blister* : il s'agit de considérer le volume des empreintes Vickers pour discriminer les verres selon le rapport à la conservation de volume durant la déformation (au regard de leur caractère normal/anormal).

0.5.3.2 L'approche par mesures de volume d'empreintes d'indentations Vickers

A la suite des travaux de Yoffe [27] et Ahn [20], l'intensité du champ de *Blister* adapté au rayage, au caractère normal/anormal des verres et à la géométrie de l'indenteur Vickers peut s'exprimer de la façon suivante :

$$B = \frac{3Ga^2}{2\pi(1-2\nu)}\left(\frac{1}{\tan\theta} - \frac{\pi}{2}\frac{\delta Vc}{V}\right)Fpv \qquad \textbf{Eq. 10}$$

avec $\frac{\delta Vc}{V}$ le rapport de compaction pour le matériau, *G* le module de cisaillement, *ν* le coefficient de Poisson et *Fpv* le facteur de refoulement plastique en surface adapté à l'indenteur Vickers.

L'étude consistera à mesurer ce facteur de refoulement plastique en surface adapté à l'indenteur Vickers par mesure de volume d'empreinte par AFM : *Fpv*.

L'expression de *a* est donnée selon [28]:

$$a = \sqrt{2\frac{1-\nu^2}{\pi E}P\tan\alpha} \qquad \textbf{Eq. 11}$$

avec *α* le demi-angle au sommet de l'indenteur, *P* la force normale appliquée, *E* et *ν* les modules élastiques du matériau.

Par analogie au travail de Ahn [20], le facteur *Fpv* est donné par :

$$Fpv = \frac{Vupward - Vimpr}{Vtotal} \qquad \textbf{Eq. 12}$$

avec *Vupward* le volume de matière refoulé en surface (i.e. le volume des bourrelets), *Vimpr* le volume de l'empreinte (sous le plan de référence correspondant à la surface non déformée et *Vtotal*, le volume total de l'empreinte (du plus haut point – le sommet des bourrelets s'il en existe – jusqu'au point le plus profond de l'empreinte d'indentation).

0.5.3.3 Résultats

Les mesures de volumes ont été effectuées sur des empreintes d'indentations menées à différentes charges (de 0.2 N à 3 N) pour chaque verre étudié et les rapports *Fpv* ont été déterminés. Une attention particulière a été donnée pour prendre en compte la perturbation de la rugosité pour chaque échantillon.

Ainsi, le paramètre *B* (qui dépend de la charge appliquée, de son comportement au regard du caractère densification/glissement, de la géométrie de l'indenteur et d'autres paramètres expérimentaux – effet de l'environnement,…) est déterminé pour chaque verre par la méthode décrite auparavant. Les résultats après interpolation par une loi puissance sont reportés dans le Graph 4.

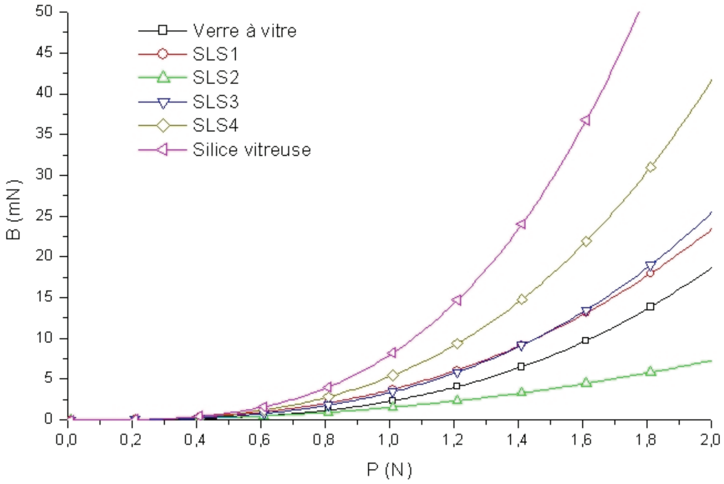

Graph 4 : Evolution des paramètres *B* (champ de *Blister*) adaptés au rayage en fonction de la force d'indentation *P* et des différents verres.

Il faut noter que les évolutions de *B* semblent cohérentes avec celle trouvée par Ahn [20]. Comme attendu dans cette gamme de charges, plus la tendance à la densification est présente, plus *B* est élevé. Le verre SLS 2 fait exception puisqu'il exhibe les valeurs de B les moins élevées pour la gamme de charge considérée.

0.5.4 Expression complète du modèle

De la même manière que Yoffe [27] et Ahn [20], l'expression complète du champ de contraintes est obtenue par superposition des trois champs préalablement introduits :

$$\sigma = \sigma^{n}_{Hanson} + \sigma^{t}_{Bous.} + \sigma^{r}_{\substack{Blister \\ normal/anomalous \\ Vickers}} \qquad \textbf{Eq. 13}$$

et

$$\tau = \tau^{n}_{Hanson} + \tau^{t}_{Bous.} + \tau^{r}_{\substack{Blister \\ normal/anomalous \\ Vickers}} \qquad \textbf{Eq. 14}$$

L'exposant *n* renvoie au champ de contraintes de Hanson (correspondant à la charge normale durant le rayage) ; l'exposant *t* renvoie au champ de contraintes dû au chargement tangentiel modélisé par l'approche de Boussinesq ; l'exposant *r* correspond aux contraintes résiduelles produites par la présence de la zone plastique.

D'après le choix du système de coordonnées lié au modèle, l'indenteur raye suivant l'axe *x*, de $x=-\infty$ à sa position actuelle en $x=0$.

0.5.5 Résultats du modèle semi-analytique

0.5.5.1 Phénoménologie

0.5.5.1.1 Prédiction de l'occurrence des fissures médianes/radiales

Le terme de contraintes dans le modèle considéré qui correspond au chargement de l'indenteur durant le rayage (i.e. $\sigma^{n}_{yy-Hanson} + \sigma^{t}_{yy-Bous.}$) domine largement la solution complète pour des valeurs faible de *P* (typiquement < 0.6 N). L'amorce des fissures médianes/radiales est gouvernée par la part positive de cette composante (tension). La valeur la plus élevée en traction de la contrainte est située proche de la surface comme illustré dans le Graph 5 (a), un peu au devant de l'indenteur sur l'axe des *x*.

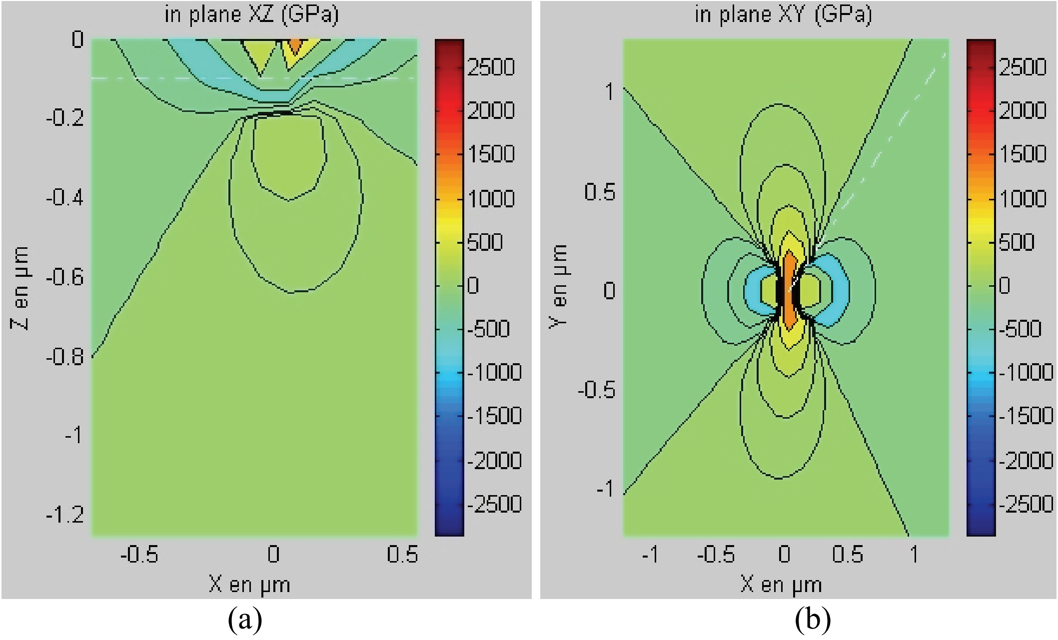

Graph 5 : Représentation de la contrainte σ_{yy} dans le plan (a) XZ et le plan (b) XY (cas de P=0.5 N).

Ainsi, l'ouverture des fissures médianes/radiales se fait en avant du pénétrateur en mouvement.

Le Graph 5 (b) montre la composante des contraintes $\sigma^{n}_{yy-Hanson}+\sigma^{t}_{yy-Bous.}$ dans le plan XY (section à z=-0.1 µm).
La fissure médiane/radiale qui a été amorcée sous l'indenteur ne se propage pas droit en avant puisqu'une contrainte de compression est présente dans cette direction mais s'incline d'un côté ou d'un autre de la rayure comme illustré par la localisation des contraintes de traction sur le Graph 5 (b). Ces résultats sont cohérents avec les résultats expérimentaux.

0.5.5.1.2 Prédiction de l'occurrence des fissures latérales

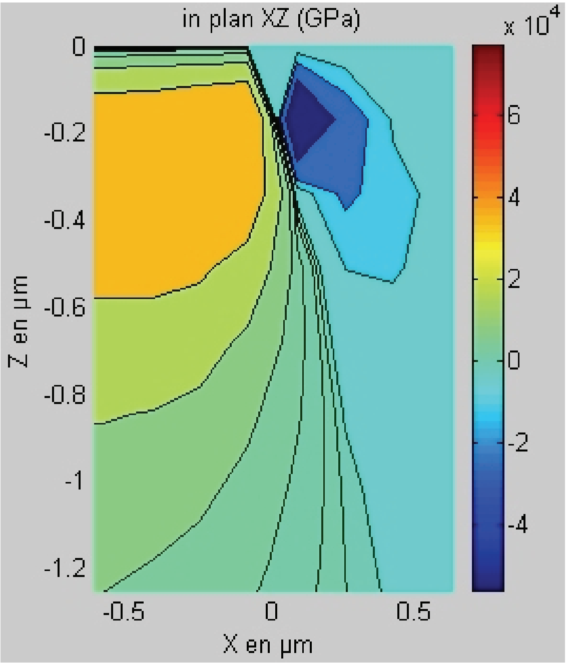

Graph 6 : Détail de la représentation de la composante de la contrainte considérée σ_{zz} dans le plan XZ (cas de P=0.8 N).

La composante résiduelle (i.e. la composante de *Blister*) domine largement la contrainte totale σ_{zz} lorsque la force normale P est suffisamment élevée (> 0.6 N). Ainsi, l'amorce des fissures latérales est gouvernée par la part positive de cette composante des contraintes. La valeur la plus élevée de cette contrainte (en traction) est située (voir Graph 6) sous la surface du verre, proche de la frontière entre la zone plastique et le matériau élastique. Sa localisation précise est un peu en arrière de l'indenteur sur l'axe des x comme il a été observé pendant les essais expérimentaux.
Les valeurs de cette composante restent élevées sur toute la longueur de la rayure, même si l'indenteur s'est largement éloigné. La composante compressive de cette contrainte au devant de l'indenteur (i.e. pour $x>0$) empêche la fissure latérale de précéder la pointe.

0.5.5.2 Prédiction de l'occurrence des endommagements selon la composition chimique

Des considérations similaires sur les champs de contraintes obtenus pour chaque verre sont cohérentes avec les résultats expérimentaux présentés auparavant dans le cadre de la phénoménologie des endommagements et de l'influence de la composition chimique sur ces endommagements : du verre *float* à la silice vitreuse (i.e. à proportion de silice croissante), les contraintes augmentent.
Les fissures médianes/radiales (gouvernées par la contrainte $\sigma_{yy} = \sigma^{n}_{yy-Hanson} + \sigma^{t}_{yy-Bous.} + \sigma^{r}_{yy-Blister}$) apparaissent *avant* (au sens de la charge normale appliquée) lorsque la proportion de silice augmente. Le verre SLS 2 constitue l'exception qui vient clôturer cette analyse : il présente la plus basse des valeurs maximales de la contrainte considérée.
Il est également clairement établi que les fissures latérales (gouvernées par la contrainte $\sigma_{zz} = \sigma^{n}_{zz-Hanson} + \sigma^{t}_{zz-Bous.} + \sigma^{r}_{zz-Blister}$) apparaissent à des charges plus faibles dans la silice vitreuse que dans le verre *float*, suivant le même ordre dans les verres à proportion de silice intermédiaire. Le verre SLS 2 est encore une fois l'exception puisqu'il présente la plus basse des valeurs maximales de la contrainte considérée. Ces conclusions sont cohérentes avec les résultats expérimentaux présentés précédemment.
Tous les tests de rayure effectués semblent révéler que l'évolution des régimes micro-abrasifs dans le cas de l'étude du rôle de la composition chimique suit l'évolution des autres régimes d'endommagement, i.e. si le régime fragile apparaît à plus faible charge dans le cas d'un verre, le régime micro-abrasif apparaîtra également à plus faible charge. Il semblerait qu'une contrainte locale critique serait alors atteinte ce qui est cohérent avec les charges critiques nécessaires pour déclencher les autres régimes d'endommagement observées expérimentalement. Cette conclusion semble donc cohérente, même s'il est préférable de s'abstenir d'énoncer des interprétations supplémentaires par faute de certitudes établies.

0.5.5.3 Remarque finale concernant le modèle semi-analytique

Une analyse quantitative n'est pas encore raisonnable dans le cadre de ce modèle. Entre autres, certaines hypothèses ainsi que d'autres paramètres divers sont encore trop restrictifs dans cette étude pour mener rigoureusement à un modèle qui serait validé quantitativement.

CHAPTER 0:

SUMMARY OF THE SCIENTIFIC APPROACH USED AND RESULTS OBTAINED

-

version anglaise

SUMMARY OF CHAPTER 0

0.1 Introduction

The resistance of glasses and ceramics (and brittle material in general) depends usually on surface damage that dramatically grows until complete rupture of the material. The damage types are essentially in the form of surface scratches and abrasions. Thus, the study of single-scratch process on considered glass appears appropriate to i) understand, ii) predict and then iii) prevent surface damage on glasses. The goal of this study deals with the *scratchability of soda-lime silica glasses*, i.e. the resistance characterization and the understanding of the damage occurring during scratching with material structure considerations and mechanical analysis.

Concrete goals can be listed as follows:

1. to identify the damage during scratching of considered glasses.
2. to understand and explain the damage types and occurrences in the light of structural considerations (study of different chemical composition of glasses).
3. to build a mechanical model and to analyze the results for damage predictions.

0.2 Required knowledge: indentation behavior of glasses

0.2.1 Introduction

From a microscopic point of view or under high punctual stresses, it is admitted that glasses can undergo a permanent deformation without completely breaking [1, 2], that can be dissociated into: i) a permanent deformation (abusively named *plastic deformation* in reference of permanent deformation occurring in metals plasticity) that occurs by densification and/or by local shearing, and ii) a deformation by damage (cracks initiation and propagation).

0.2.2 Plastic zone

0.2.2.1 Deformation by densification / deformation by shear

Due to the open structure of the glass (case of low content of modifiers), the effect of an indentation pressure is to compact this network, increasing its density [3, 4] (firstly reported in bulk glasses under nearly hydrostatic pressure [3, 5]). Then, this process known as *densification* is a non-conservative deformation in volume and is attributed to the movements of atoms due to the relative compliance of the Si–O–Si linkages. Modifiers are considered to restrict these movements.

It is also shown that irreversible deformation may occur by “plastic” deformation, or shear flow [1, 6]. Then, pile-up [7] may appear since this deformation type is ideally volume conservative.

0.2.2.2 Normal/anomalous aspect

Normal glasses are characterized by the absence or a minor contribution of densification process in the area beneath the applied contact stress. Indentation experiments showed that in this case, irreversible deformation occurs by "plastic" deformation. On the contrary, a flow-densification process shows up in anomalous glasses, and the ability of glasses with relatively high silica content to densify under sharp contact loading has a great influence on the indentation and on the scratch damage features. Then, glasses can deform by shear and/or densification depending on their chemical composition.

0.2.3 Cracking in glass

The different cracks that occur during an indentation test can be seen in Fig. 13 [8] and show the fundamental difference between the normal and the anomalous behavior from the cracking point of view: radial ^{l} (sometimes), median ^{l,u} and lateral ^{u} cracks occur in the normal glasses while cone ^{l}, median/radial ^{l} (restricted by the cone crack) and lateral ^{u} cracks occur in the anomalous glasses [9]. The superscripts ^{l} and ^{u} denote that the occurrence of the cracks is during the loading ^{l} and/or the unloading ^{u} sequence during the indentation test.

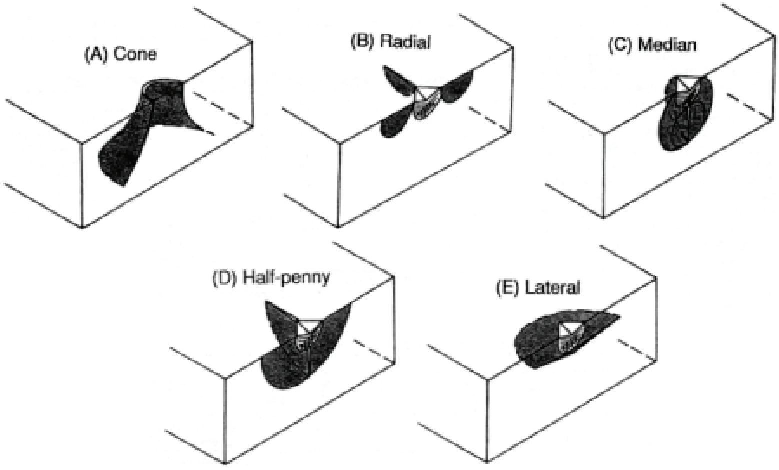

Fig. 13 [8]: Isometric sections of idealized crack morphologies observed at indentation contacts: (A) cone crack and associated nucleating ring crack, (B) radial crack and associated contact impression and plastic deformation zone (Vickers indenter), (C) median crack, (D) half-penny crack, and (E) lateral crack.

0.3 Materials and experimental scratching device

0.3.1 Materials

The chemical compositions of the studied glasses were defined in such a way that with regard to their indentation behavior, the studied glasses cover the range from typical normal glasses to near anomalous glasses [9].

A commercially available soda-lime silica glass[2], a fused silica and 4 different glasses synthesized [10, 11] in the Na_2O-CaO-SiO_2 phase diagram (referred as SLS 1 to 4) were studied. The glass compositions are given in the Table 6.

[mol. %]	Planilux	SLS 1	SLS 2	SLS 3	SLS 4	Fused Silica
SiO_2	70,8	71,0	74,0	77,0	80,00	100,00
Na_2O	12,8	17,5	15,7	13,9	12,10	-
MgO	5,9	-	-	-	-	-
CaO	10,2	11,5	10,3	9,1	7,90	-
AL_2O_3	0,4	-	-	-	-	-

Table 6: Chemical composition of studied glasses.

0.3.2 The scratch tester

During a scratch test, a well-defined tip is drawn over the surface of a sample while applying a particular normal load *P*. The complicated loading stress field induced by scratch test generates material response in various forms depending on the material nature: plastic deformation, densification, re-crystallization, cracking,…

---

[2] Planilux™, Saint-Gobain

An apparatus, named *scratch tester* also known as *linear sclerometer*, allowing for a variable loading cycle during a single experiment, was designed for the present work. This device was placed into a glove box in order to achieve a good moisture control in the range 0 % - 100 %, so as to study the effect of the environment (see Fig. 14).

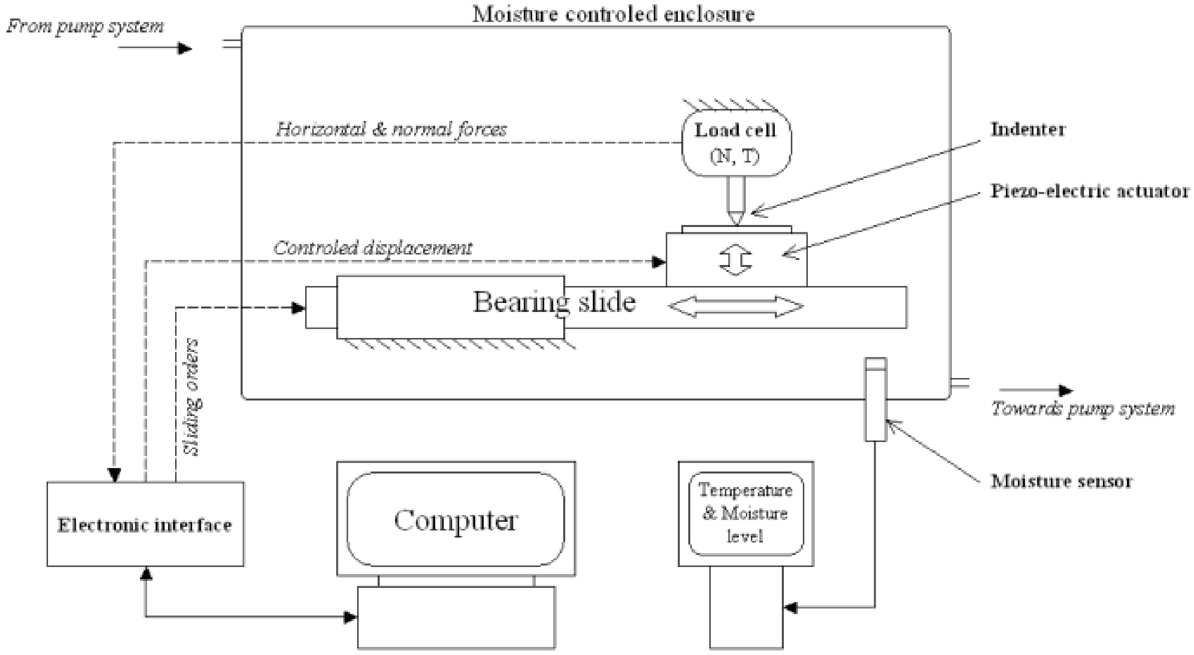

Fig. 14: Principle diagram of the experimental setup designed for variable loading scratch tests in a moisture and temperature controlled atmosphere.

The indenter horizontal displacement (to produce a groove) is obtained through a bearing slide (computer controlled), while the vertical movement is controlled by a piezo-electric actuator. Both the penetration and the forces are continuously monitored. This device allows constant load or monotonic loading-unloading slope load scratch processes.

0.4 Experimental results

0.4.1 Physical properties and static behavior

The physical and mechanical properties of the studied glasses were measured and are summarized in Table 7.

Properties Glasses	T_g (°C) ±2	ρ (g/cm^3) ±0.01	E (GPa) ±0.5	ν ±0.01	H (GPa) ±0.01	K_c (MPa.m$^{1/2}$) ±0.02
Float glass	560	2.55	71.5	0.21	6.12	0.72
SLS 1	558	2.53	70.4	0.20	5.35	0.71
SLS 2	559	2.50	69.9	0.19	5.11	0.70
SLS 3	560	2.47	69.2	0.18	5.15	0.76
SLS 4	561	2.43	68.7	0.17	5.19	0.82
Fused silica	700-1200	2.20	73.0	0.16	8.03	1.47 – 0.77*

Table 7: Composition and physical properties of glasses. * denotes a S.E.N.B. measurement of the toughness [12].

Meyer's hardness H and indentation fracture toughness K_c were determined by indentation tests with a load of 1 kg (15 s of dwell time) and by means of the following equations:

$$H = \frac{P}{2a^2} \qquad \textbf{Eq. 15}$$

and

$$K_c = 0.016\sqrt{\frac{E}{H}}\frac{P}{c^{3/2}} \qquad \textbf{Eq. 16}$$

where P is the load, a is half the mean size of the two diagonals of the residual imprint, E is the Young's modulus, and c is half the mean length of the two radial cracks (tip to tip).

The density decreases with rising silica content as Si^{4+} former ions replace modifiers (Na^+ and Ca^{2+}), because of the ability of the silica network to accommodate interstitial cations in a large proportion due to its open structure. The monotonic increase of ρ is explained by the filling of the empty sites of the three dimensional network by the interstitial cations such as Na^+ and Ca^{2+}. Young's modulus decreases slightly when the amount of modifiers decreases: the more the amount of network modifying cations decreases, the more the network stiffness is controlled by the variations of the Si–O–Si inter-tetrahedral angles and by the mutual orientation of SiO_4 tetrahedra, whereas the other structural parameters do not appreciably change [4]. This effect also governs the Poisson's ratio.

H and K_c present a non-monotonic trend as silica replaces modifiers and show a minimum for the SLS 2 glass. Yamane et al. [13] showed that the higher the glass compacity and the hardness and the elastic moduli (present results about the fused silica glass have to be excluded). Combined with the present results, it strongly suggests that a low Poisson's ratio also favors densification (with an irreversible volume decrease as a consequence). The indentation–derived fracture toughness K_c increases with the silica content for $SiO_2 \geq 74$ mol. % except for the specific SLS 2 composition (see Graph 7). It confirms that high silica content glasses mainly deform through densification and hence possess higher indentation toughness than typical soda-lime silicate glasses with high amount of modifiers. In fact, the energy dissipation in flow-densification process and the shift toward Hertzian cone cracks for high silica content glasses contribute to the shortening of the radial-median cracks, so as the indentation derived toughness increases. The exception of the toughness value of the SLS 2 grade is attributed to a particular structure supposed to be interpenetrated tridymite and devitrite phase field networks.

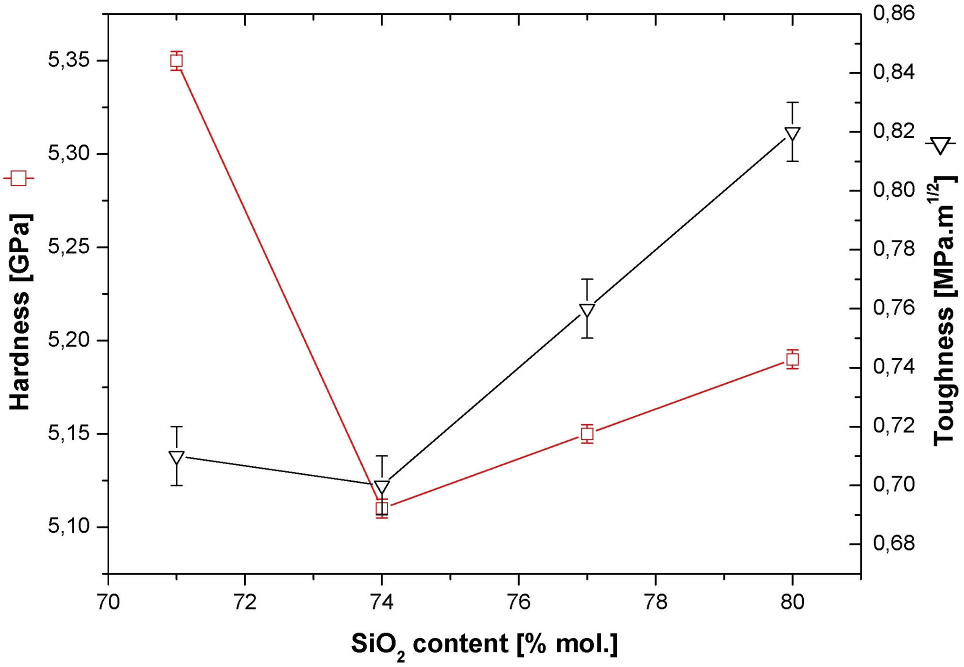

Graph 7: Hardness *H* and fracture toughness K_c with regard to silica content for the SLS series.

The brittleness B as well as the measured and theoretical (superscripted by *) radial P_C^R and lateral P_C^L critical loads were determined and reported in Table 8. B, P_C^{R*}, P_C^{L*} were calculated from the following equations [14-17]:

$$B = \frac{H}{K_c} \qquad \textbf{Eq. 17}$$

$$P_C^{R*} = \alpha \frac{{K_C}^4}{H^3} \qquad \textbf{Eq. 18}$$

$$P_C^{L*} = \beta E \frac{{K_C}^4}{H^4} \qquad \textbf{Eq. 19}$$

where K_c is the fracture toughness, H is the Meyer's hardness, and E is the Young's modulus. The following values were obtained in the present study for α and β: α=3.9 10^5, β=4.9 10^4 for the SLS series and α=2.2 10^4 for the float glass.

	$B = H/K_c$ ($m^{-1/2}$)	P_C^R (N)	P_C^{R*} (N)	P_C^L (N)	P_C^{L*} (N)
Float glass	8500	0.25 – 0.50	0.30	1 – 2	
SLS1	7550	0.10 – 0.25	0.65	0.25 – 0.50	1.07
SLS2	7300	0.10 – 0.25	0.70	0.25 – 0.50	1.20
SLS3	6800	1 – 2	0.95	2 – 3	1.59
SLS4	6350	1 – 2	1.26	2 – 3	2.09

Table 8: Brittleness, experimental and theoretical radial crack critical loads and experimental and theoretical lateral crack critical loads.

In the case of the SLS glass series, the gap between the behaviors of SLS 1/SLS 2 and SLS 3/SLS 4 is predicted (see Table 8). Furthermore, the SLS 1/2 glasses seem to be the most sensitive to radial/lateral cracking and also the most brittle regarding the so called brittleness parameter B. In the case of the commercial float glass, the addition of modifiers is responsible for significant changes in the glass network.

0.4.2 Scratch behavior

0.4.2.1 Load dependence of the scratch behavior (standard float glass)

During an indentation experiment performed with a Vickers indenter on a soda-lime silica glass, cracks are known to occur during loading or unloading, and depend strongly on the load level [8, 18]. Similar observations have been carried out in the case of scratching [11, 19] but this field remains to be explored further. The fractography analysis in a micro-scale has been carried out. For example, the chevron cracks as defined by Rice et al. [19], the lateral cracks propagation described by Ahn [20] and Bulsara [21] and the chipping process given by Le Houérou et al. [11] need some more investigations. Observations of the surface damage lead to detailed results about the radial cracking, lateral cracking and chip formation and are given in the following parts.

During a scratch experiment, the scratch pattern strongly depends on the level of the normal load and different micro-cracks form: i) the median cracks, ii) the radial (chevron) cracks and iii) the lateral cracks.

During a monotonic loading scratch process on a glass, three different regimes are typically observed and are schematically drawn in Fig. 15: i) the micro-ductile regime I (permanent groove with no damage visible), ii) the cracking regime II (important damage by micro-cracking: lateral cracks intersecting the surface and radial cracks) and iii) the micro-abrasive regime III (presence of many debris and eventually small lateral cracks).

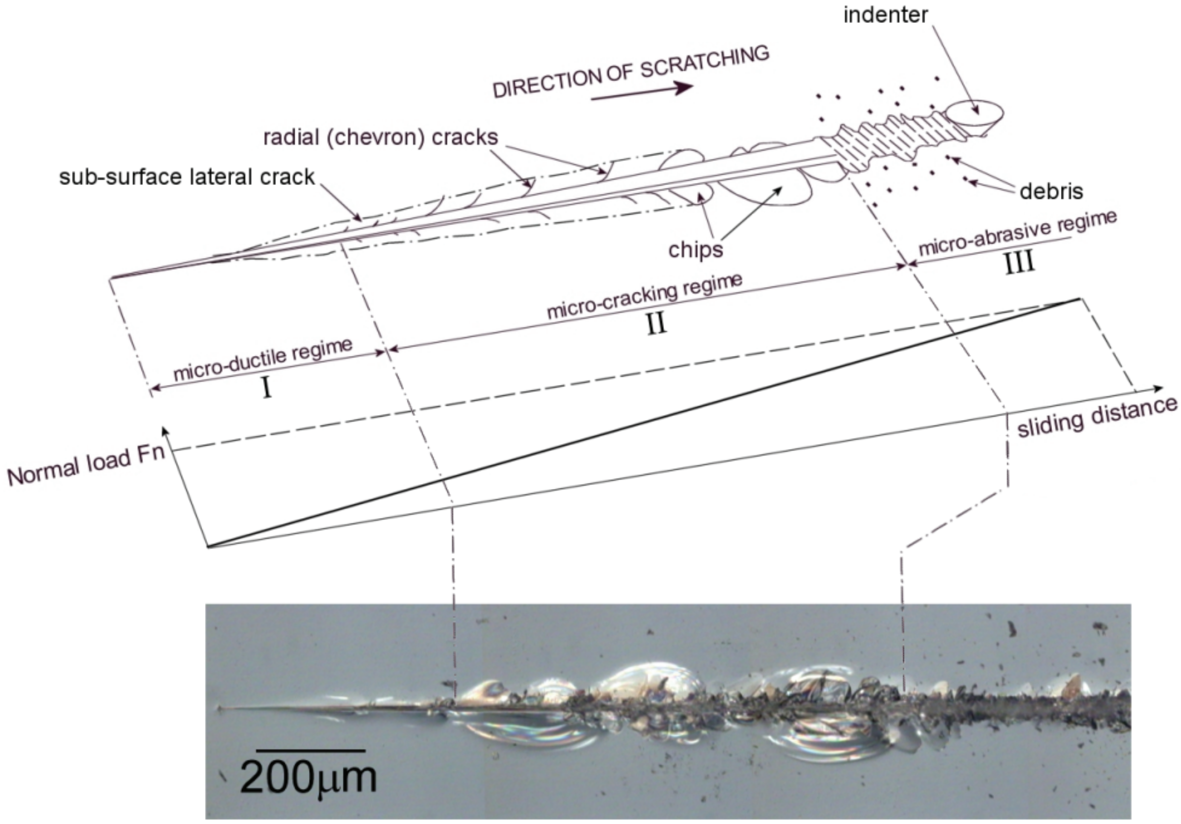

Fig. 15: Typical scratch pattern obtained on the surface of a soda-lime silica (SLS) glass when scratched by an indenter during a monotonic loading cycle (see associated load diagram) and micrograph of a scratch performed on a glass. Definition of the damage regimes I, II and III.

0.4.2.2 Preliminary results

The influence of various parameters was shortly studied. A dynamical effect due to the load history (loading/unloading scratch process) have been noticed. No dependence of the face of the float glass (tin or air) was shown in the load range of this study. The residual stresses were found to strongly influence the severity of the scratch pattern (i.e. shift of the severe damage regimes towards lower normal loads in the presence of compressive residual stresses). It suggests that all the quenched glasses should exhibit less optical and aspect losses (the micro-abrasive regime is less optically severe than the micro-cracking regime), but also lower mechanical properties.

The indenter geometry plays a great role in the scratch process. It appears that the more severe the indenter shape is (a Vickers compared to a conical indenter or a conical indenter compared to another one with a higher apex angle), the more early (in a load sense) the damage regimes appear. Thus, a shift in the transition loads is measured. By the way, the Vickers indenter reveals a more stable scratch process.

0.4.2.3 Dependence on humidity (% r.h.) and other environmental effects

The Fig. 16 shows the scratches together with the normal load recorded during the experiments at different humidity levels (0 to 100 % r.h.) on an annealed standard float glass.

0 % humidity

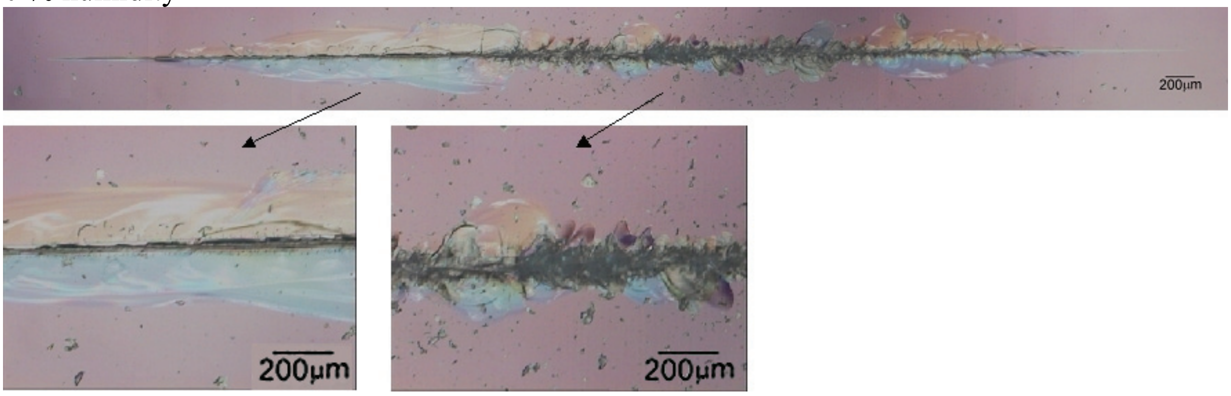

30 % humidity

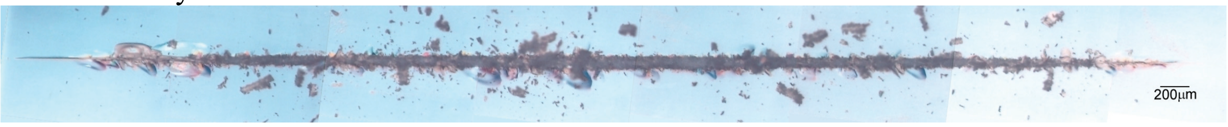

65 % humidity

100 % humidity

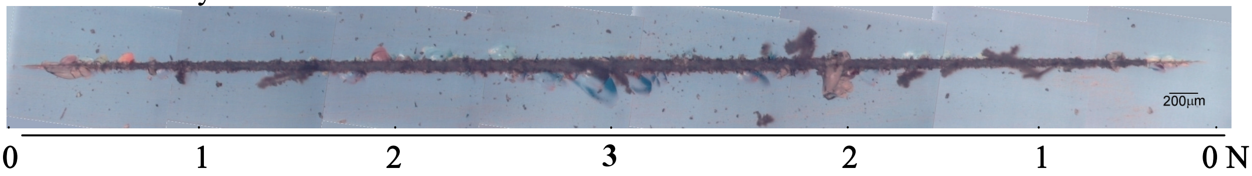

Fig. 16: Pictures of scratches conducted under different humidity levels with a Vickers penetrator following a slope load-unload process.

The transition loads between the different regimes of damage obviously evolve with the humidity level: the cracking and abrasive regimes tend to develop at higher loads when the moisture decreases as reported in Graph 8.

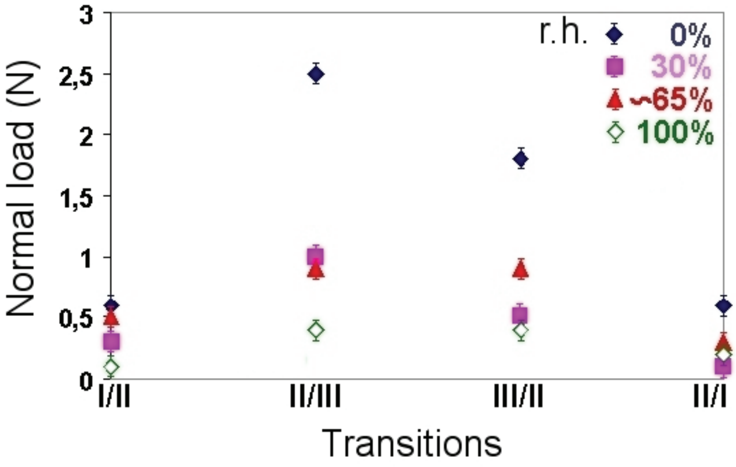

Graph 8: Transition loads vs. the humidity level.

The particular damage obtained with 0 % of humidity is characterized by a large lateral crack which remains under the surface of the sample. This phenomenon fades rapidly as the humidity level is raised. In the case of 0 % of humidity, a lack of radial cracks is observed and avoids that the lateral crack reaches out to the surface so as it largely extends under the surface instead of forming chip. The mechanism of chip creation will be discussed in detail in next part. Then, the occurrence of radial cracks is governed by the humidity level (directly exposed to ambient air).

0.4.2.4 Phenomenology: identification and understanding of scratching damage

0.4.2.4.1 The micro-ductile regime

The micro-ductile regime has been shown to exhibit the presence of damage i) inside the track, and ii) under the track.

0.4.2.4.2 The cracking regime

0.4.2.4.2.1 Radial (chevron) cracks events

The radial cracks occurring during the cracking regime significantly inclined toward the sliding direction, and propagate in a curved shape usually ending perpendicular to the scratch direction as illustrated in Fig. 15. The Fig. 17 shows the initiation and the beginning of the propagation of a radial crack. It clearly initiates at the leading edge of the Vickers indenter and soon propagates from a direction parallel to the scratch track to a curved shape that tends to get perpendicular to the track. The crack reaches out from the track with an angle noted *θ*. This propagation can be qualified as semi-stable: i) after the initiation, it rapidly curves either on the right or on the left of the track; this choice is purely statistic and constitutes the unstable part of the crack propagation, and ii) the advance speed of the crack suggests a stable propagation.

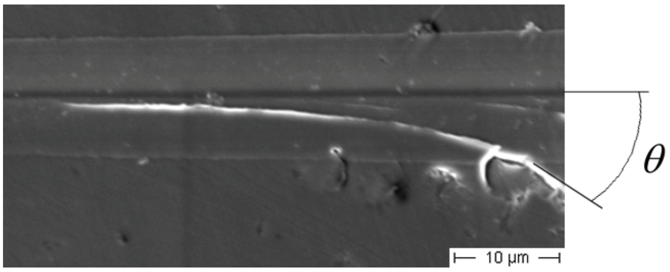

Fig. 17: Initiation and propagation of a radial (chevron) crack on the surface of a standard float glass. (SEM)

0.4.2.4.2.2 Understanding of the creation and development of chips

Two different mechanisms of chipping process were identified: i) in the case of non-existent radial crack (case of low humidity level for example), chipping can occur if there is enough spent energy to make the lateral crack reach out toward the surface (see Fig. 18), or ii) a chip is the combination of two radial cracks and a lateral one which then intersects the specimen surface (see Fig. 19).

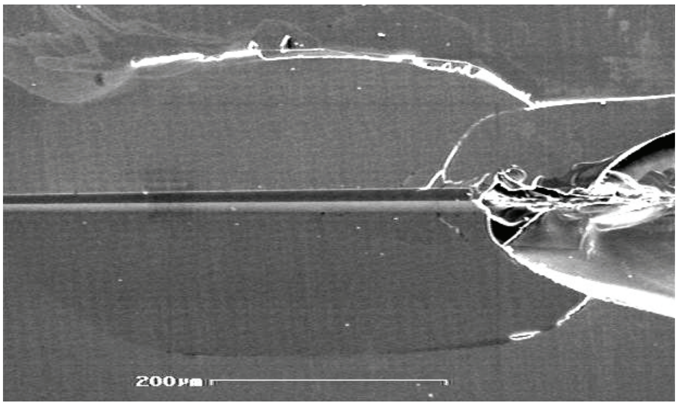

Fig. 18: Chipping by propagation of a lateral crack – absence of radial crack (SLS 4). (SEM)

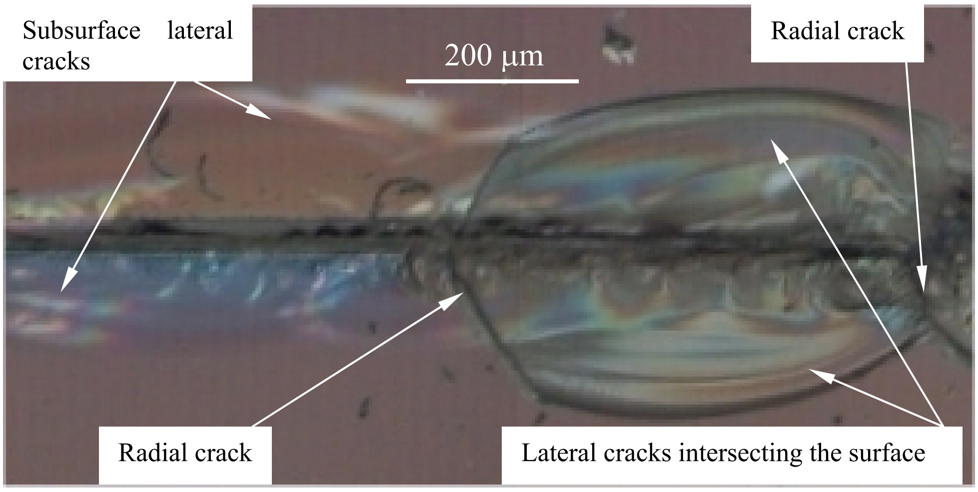

Fig. 19: Chip formation with the different involved damage.

Twist hackle [22-25] was observed below the chips and indicates the direction of propagation of the fracture: it starts from the track with a direction perpendicular to the scratching direction.

0.4.2.5 Dependence on the chemical composition of the glass

Fig. 20 shows a representative scratch groove of each of the six studied glasses (obtained with a monotonically increasing normal load up to 4 N) and proves that the scratchability is greatly affected by the chemical composition. The Table 9 gives the transition loads between the damage regimes with regard to the chemical composition. Note that these values are statistical values and are obtained on numerous scratches.

Standard float glass:

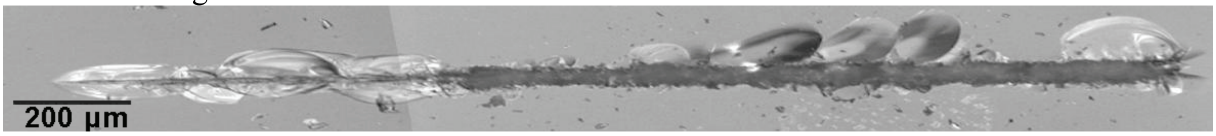

SLS 1:

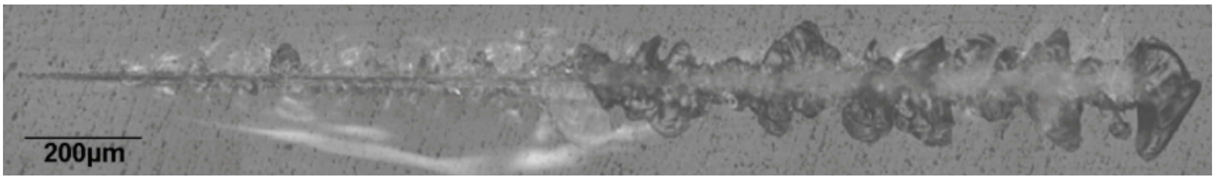

SLS 2:

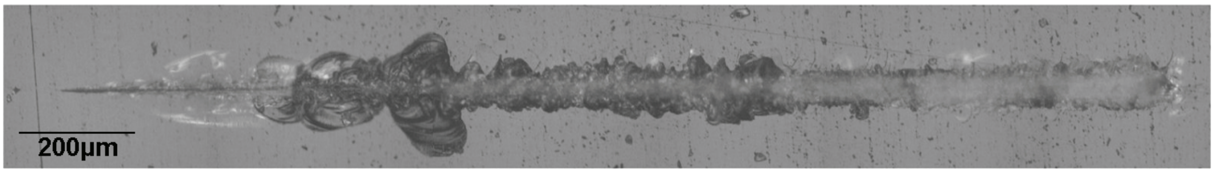

SLS 3:

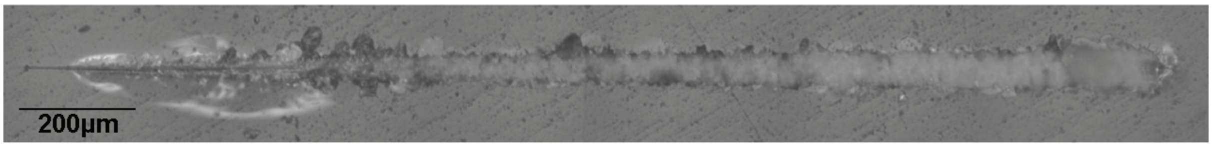

SLS 4:

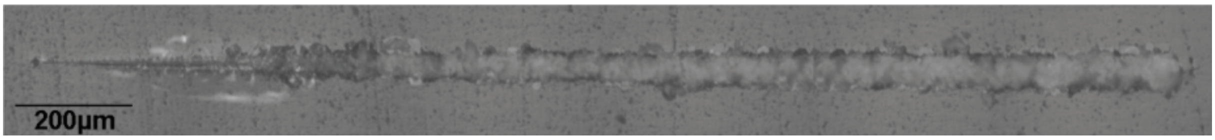

Fused silica:

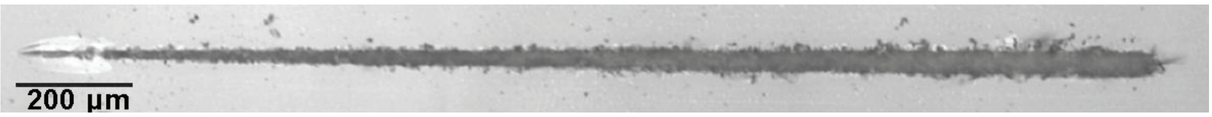

Fig. 20: Evolution of scratch resistance for the six considered glasses.

Damage regimes Glasses	Micro-ductile	Micro-cracking		Micro-abrasive
		Sub-surface laterals	Chips	
Standard float glass	0 – 0.4 N	0.4 – 0.8 N	0.8 – 1.2 N	1.2 – 4 N
SLS 1	0 – 0.35 N	0.35 – 2 N	2 – 4 N →	2 – 4 N
SLS 2	0 – 0.4 N	0.4 – 0.9 N	0.9 – 1.6 N	1.6 – 4 N
SLS 3	0 – 0.35 N	0.35 – 1 N	1 – 1.1 N	1.1 – 4 N
SLS 4	0 – 0.3 N	0.3 – 0.9 N	–	0.9 – 4 N
Fused silica	0 – 0.2 N	0.2 – 0.5 N	–	0.5 – 4 N

Table 9: Transition loads associated with changes in the scratch regimes. The arrow indicates the difficulty to dissociate the two considered regimes.

From direct analysis of the photos reported in Fig. 20, standard float glass, SLS 1 and 2 appear sensitive to chipping as a direct consequence of their normal character that mainly allows cracks to form by local shearing [11] due to weak percolation paths in the vitreous network [26]. SLS 3, 4 and fused silica with silica-like networks appear to be more resistant to both crack propagation and chipping during scratch experiments as a consequence of their anomalous character [11] that accommodates the deformation by network rearrangement (densification) without breaking bond [9]. A fractographic study at low scale confirms these trends for both micro-cracking and micro-abrasive regimes.

0.5 Mechanical modeling

0.5.1 Introduction: extension of Ahn's model

The nucleation of cracks and then the appearance of associated damage can't be studied without considering the local stresses. Compared to the model of Ahn [20] which describes the stress field during a scratch test, the model proposed in this study takes into account the normal/anomalous character of the considered glasses and the Vickers indenter geometry. Then, the model consists to extend Ahn's model to these two considerations. Ahn's model (derived from Yoffe's model about conical indentation [27]) gives the distribution of the stresses in the *elastic* zone that is obtained by superposing two different *elastic* stress fields:

- a Boussinesq stress field corresponding to stress field due to the loading indenter simplified in this case as a point loading,
- a stress field called *Blister* field characterized by a *Blister* strength parameter *B* and corresponding to the residual stress field in the elastic zone due to the presence of the plastic zone all along the scratch track. Note that *B* can depend on the load, the densification/shear behavior of the material, the geometry of the indenter and other experimental parameters (environmental effect,…).

Then, the complete stress field is given by:

$$\sigma = \sigma^{n}_{Bous.} + \sigma^{t}_{Bous.} + \sigma^{r}_{Blister} \qquad \textbf{Eq. 20}$$

The superscript *n* denotes the stress field due to the normal load; the superscript *t* denotes the stress field due to the tangential load; the superscript *r* denotes the residual stress field.
In this study, the extension of this model may lead to:

$$\sigma_{\substack{normal/anomalous\\ Vickers}} = \sigma^{n}_{Vickers} + \sigma^{t}_{Vickers} + \sigma^{r}_{\substack{Blister\ for\ scratching\\ normal/anomalous\ glasses\\ Vickers}} \qquad \textbf{Eq. 21}$$

The terms $\sigma^{n}_{Vickers} + \sigma^{t}_{Vickers}$ correspond to the indenter loading.

The term $\sigma^{r}_{\substack{Blister\ for\ scratching\\ normal/anomalous\ glasses\\ Vickers}}$ corresponds to residual stresses.

The extension to the normal/anomalous glasses will be achieved by the study of the densification/shearing competition (experimental considerations). The extension to the Vickers indenter geometry will be achieved by enhancing the *Point loading* stress field with the help of the Finite Elements study dealing with the difference between a conical and a Vickers indentation. The following organization chart summarizes the specific approach from Yoffe's model to the expected final model.

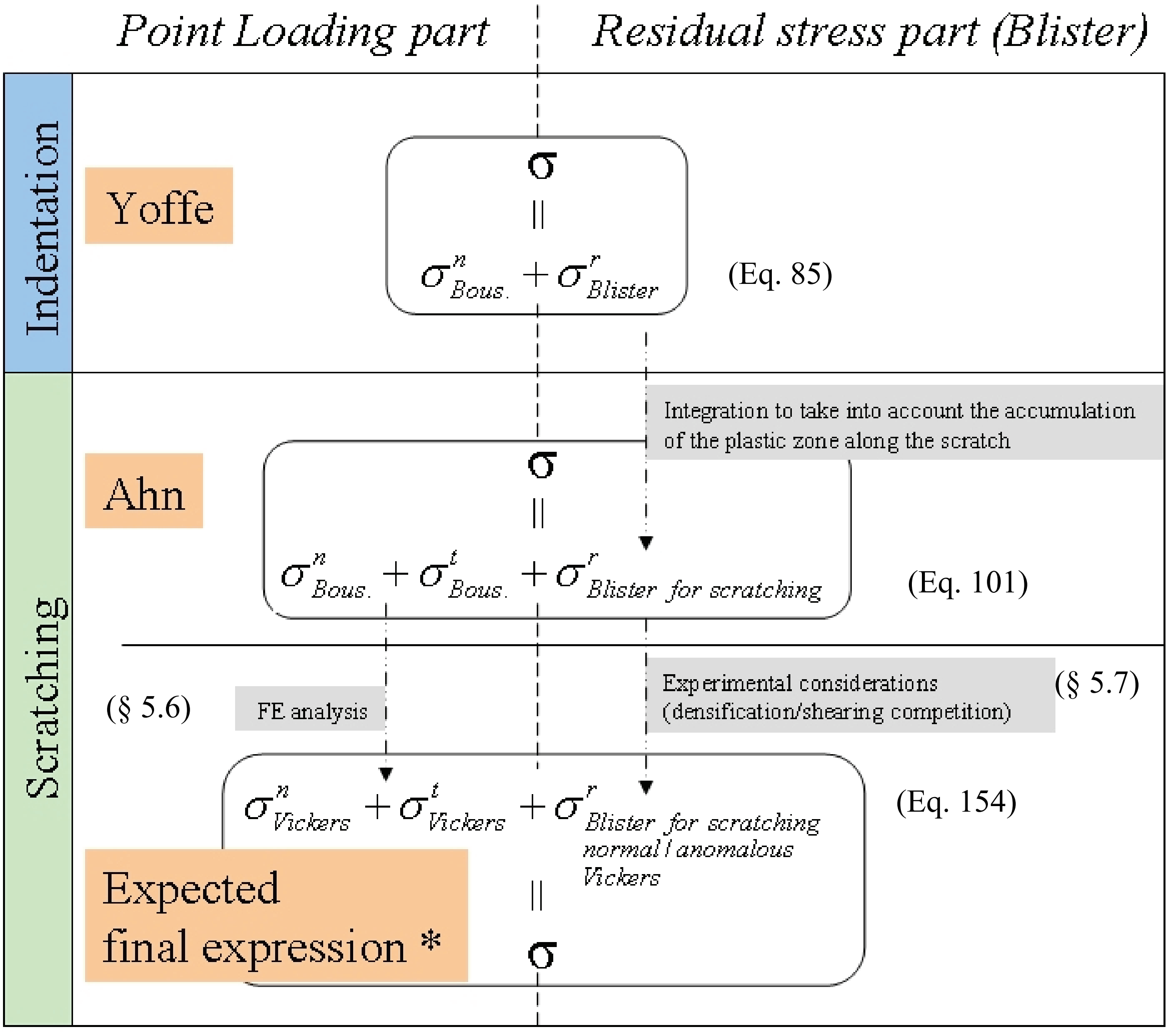

* The approximated final expression will be discussed in § 5.8.

Fig. 21: Organization chart to extend the model to normal/anomalous glasses and Vickers indenter.

0.5.2 Extension of the model to the Vickers indenter geometry: the Finite Elements study

A 3D Finite Elements model was designed with the help of the Abaqus FE code (version 6.2) and validated to analyze the stress field due to a Vickers indentation in comparison with a conical indentation. Note that an elastic analysis is sufficient in this study and that for symmetry considerations, only 1/8 of the geometry had been meshed. The insertion of the indenter (shaded) and the indented body is shown in Fig. 22.

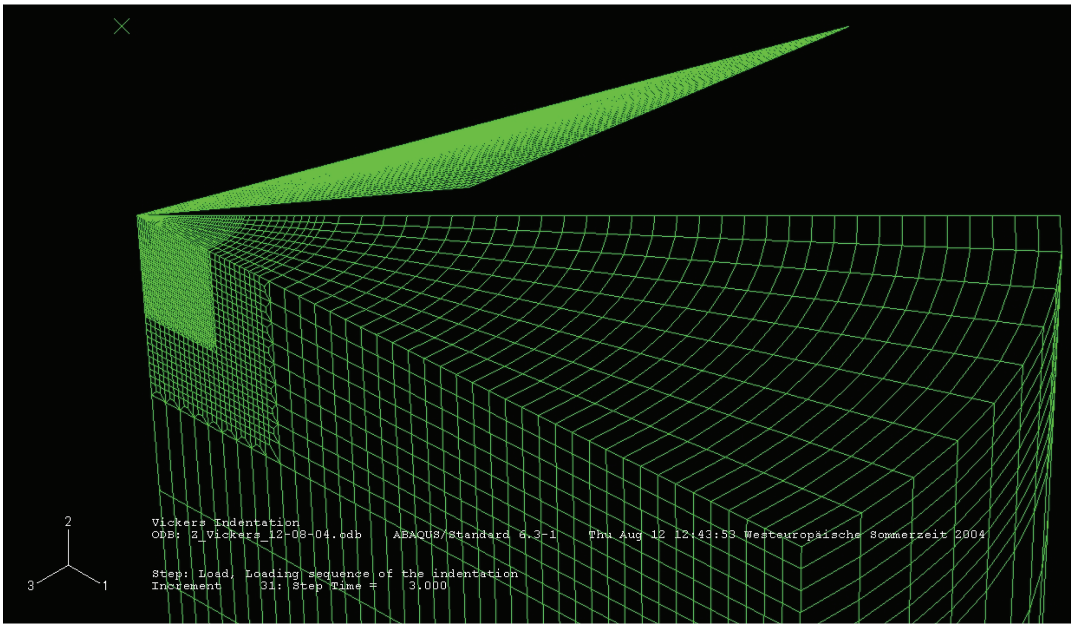

Fig. 22: The body and the indenter in the mesh module of Abaqus - Perspective view.

The Fig. 23 shows a Vickers representation with the definition of the *Face* plane (ABC) and the *Edge* plane (ABD).

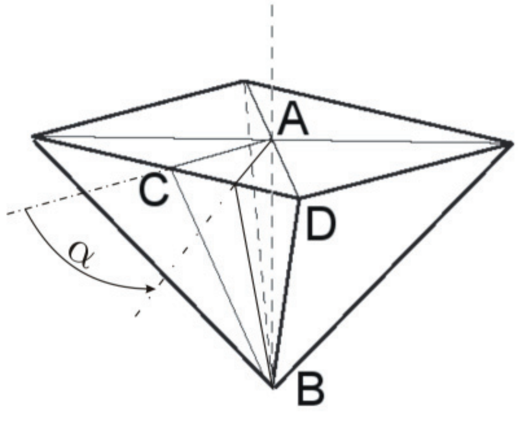

Fig. 23: Vickers representation with definition of ABC and ABD planes.

The Graph 9 represents the detail of the Von Mises distribution in a conical 2D model (a), in the plane of the Vickers face (i.e. ABC plane in Fig. 23) (b) and in the plane of Vickers edge (i.e. ABD plane in Fig. 23) (c).

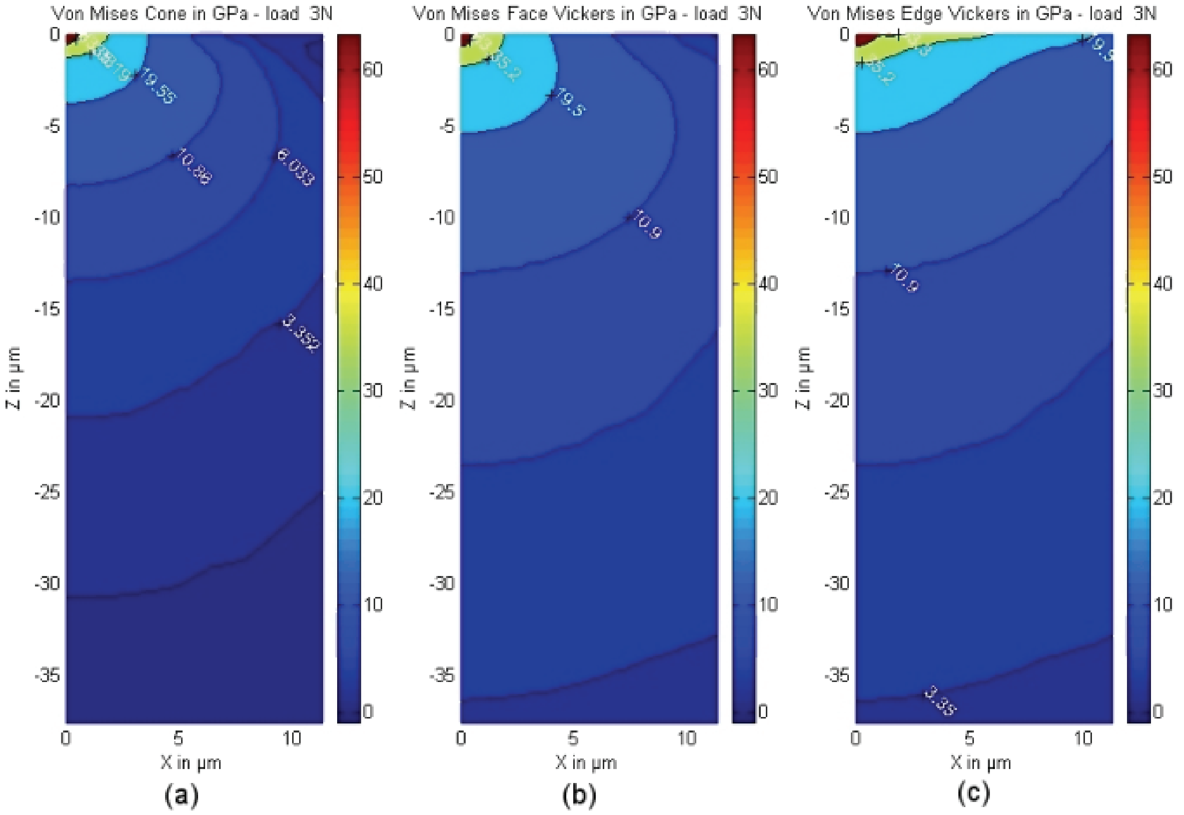

Graph 9: Details of the F.E. comparison of Von Mises distribution between (a) conical case (equivalent cone), (b) Vickers face case and (c) Vickers edge case.

The Vickers face's stress field plane *looks like* the one produced by the conical indentation of the elastic body and will be analytically modeled in the final model by the Hanson's expression of the stresses for a conical indentation [28, 29] (with proportional correction coefficients depending on the concerned stress component).

The field in the edge plane does not appear like one of the solution of a "classical" analytical problem. However, the geometry of the indenter reminds a problem that could be designed as follows: a line loading on an infinite elastic half body, applying a non-uniform pressure along its axis.

Moreover, this distribution of the pressure on the line loading is easily available by the F.E. developed model. Then the idealized case of the line loading on an elastic body is reduced to the distribution of pressure illustrated in Fig. 24 (the symmetry of the problem is not represented i.e. the p_0 pressure is located on the very-close point to the tip) with the following expression for the pressure p (determined for the normal load of 3 N) depending on the contact radius r:

$$p(r) = -4370,9r + 97156 \qquad \textbf{Eq. 22}$$

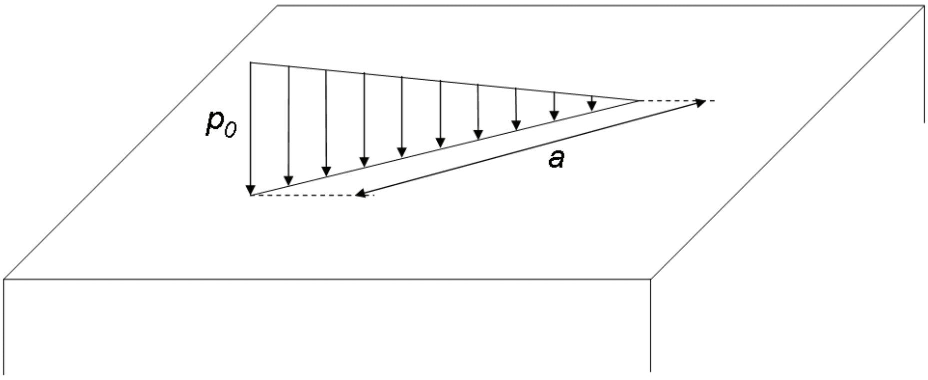

Fig. 24: Representation of a line loading on an infinite elastic half body, applying a uniform pressure.

To summarize, the stress field in the face plane of the Vickers indenter can easily be modeled in analytical form by the field designed by Hanson for conical indentation. The stress field in the edge plane of the Vickers indenter should be modeled by the field corresponding of a progressively line-loading on an elastic half body.

Any intermediate plane's stress field noted by an angle α (see Fig. 23) should be expressed by a non-linear combination of these two fundamentals stress field with the help of a transformation function that would depends on r and α. Unfortunately, no expression to model the edge plane's stress field is available yet and the different attempts in this aim failed. Then, it was decided to "correct" a conical stress field by applying *stress correction coefficients* determined by direct comparison between highest tensile stresses of conical and Vickers edge stress field for each stress component (see Table 10).

Stress component	σ_{xx}	σ_{yy}	σ_{zz}	τ_{xy}
Ratio $\frac{\sigma^{\max}_{Vickers}}{\sigma^{\max}_{Cone}}$	0.867	1.228	1.122	0.920

Table 10: Stress correction coefficients: Vickers-conical indentation comparison.

Thus, the expression of the stresses for the final semi-analytical model after integration of the geometry of the indenter gives:

$$\sigma = \sigma^{n}_{Hanson} + \sigma^{t}_{Bous.} + \sigma^{r}_{Blister} \qquad \textbf{Eq. 23}$$

The components of this equation are fully detailed in chapter 0.

0.5.3 Extension of the model to normal/anomalous glasses: identification of the densification/shear competition

0.5.3.1 Method

The six considered glasses (standard float glass, SLS series and fused silica) exhibit a deformation behavior under stress that is more or less intermediate between an "ideally-pure" densifying or shearing glass, depending on each glass composition. Thus, the competition between densification and shearing in the deformation of the glasses will be studied through the identification of the parameter B (called strength of the *Blister* field) introduced previously.

The choice in this work had been to investigate a new technique to assess the parameter of the *Blister* field B: it is to consider the volume of the Vickers imprints due to more or less (with regard to the normal/anomalous character) volume conservative deformation.

0.5.3.2 Volume measurements approach

Considering the work of Yoffe [27] and Ahn [20], the scratching *Blister* strength adapted to the present case (Vickers indenter, normal/anomalous glasses) is given by:

$$B = \frac{3Ga^2}{2\pi(1-2\nu)}\left(\frac{1}{\tan\theta} - \frac{\pi}{2}\frac{\delta Vc}{V}\right)Fpv \qquad \textbf{Eq. 24}$$

where $\frac{\delta Vc}{V}$ is the compaction ratio for glass, G the shear modulus, ν the Poisson ratio of the material and Fpv is the upward plastic flow factor adapted to the Vickers indenter.

The study will deal with the measurement of the upward flow factor adapted to the Vickers indenter by volume measurements by the AFM technique: Fpv.

The expression for a is chosen as [28]:

$$a = \sqrt{2\frac{1-\nu^2}{\pi E}P\tan\alpha} \qquad \textbf{Eq. 25}$$

with α the semi-apex angle of the indenter, P the normal load, E and ν the elastic properties of the material.

By analogy to Ahn [20], the Fpv factor is given by:

$$Fpv = \frac{Vupward - Vimpr}{Vtotal} \qquad \textbf{Eq. 26}$$

with *Vupward* the volume of the upward flow, *Vimpr* the volume within the imprint (under the undeformed plane) and *Vtotal*, the total imprint volume (from the upper point – the top of pile-up if it occurs – to the deepest point of the indentation).

0.5.3.3 Results

The volume measurements had been carried out on indentations (from 0.2 N up to 3 N) for each studied glass and the ratios *Fpv* had been determined. Particular attention was paid to take into account the disturbance of the roughness for each sample.

Then, the parameter *B* (depending on the load, the densification/shear behavior of the material, the geometry of the indenter and other experimental parameters – environmental effect,…) is assessed for each glass by the method described previously. After fitted by a power law, the results are summarized in Graph 10.

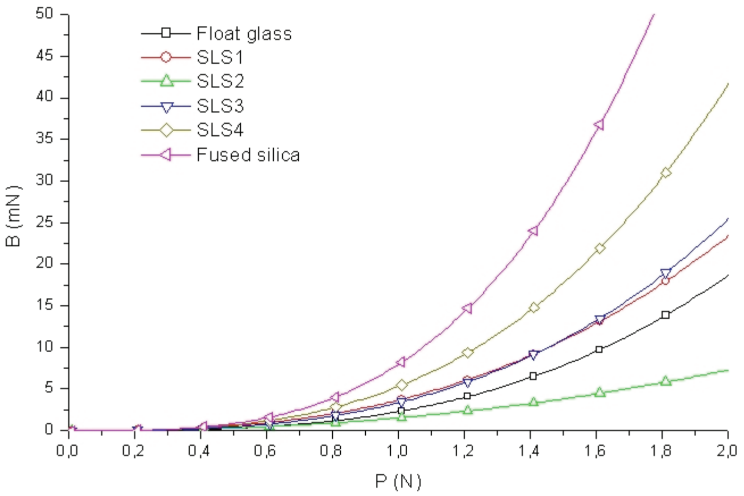

Graph 10: The evolution of the sliding indentation *Blister* field constant *B* with the indentation load *P* and the different glasses.

Note that the evolutions of *B* make sense compared to Ahn's one [20].
As expected in this load range, the more the densifying tendency is, the highest *B* appears. The exception must be noted for the SLS 2 glass which exhibits the lowest *B* in this load range.

0.5.4 Complete expression of the model

As for Yoffe [27] and Ahn [20], The complete stress field is obtained by direct superposition of the three different stress fields:

$$\sigma = \sigma^{n}_{Hanson} + \sigma^{t}_{Bous.} + \sigma^{r}_{\substack{Blister \\ normal/anomalous \\ Vickers}} \qquad \textbf{Eq. 27}$$

and

$$\tau = \tau^{n}_{Hanson} + \tau^{t}_{Bous.} + \tau^{r}_{\substack{Blister \\ normal/anomalous \\ Vickers}} \qquad \textbf{Eq. 28}$$

The superscript *n* denotes the stress field due to the normal loading and uses the Hanson's equations; the superscript *t* denotes the stress field due to the tangential loading and uses the Boussinesq's equations; the superscript *t* denotes the residual stress field due to the plastic zone.
Note that because of the chosen coordinate system linked to the model, the indenter is considered to scratch the material along the *x*-axis, from - x=-∞ to its current position at x=0.

0.5.5 Results of the semi-analytical model

0.5.5.1 Phenomenology

0.5.5.1.1 Prediction of the median/radial crack occurrence

The component corresponding to the cone loading (i.e. $\sigma^{n}_{yy-Hanson} + \sigma^{t}_{yy-Bous.}$) largely dominates the complete stress σ_{yy} for low values of *P* (typically < 0.6 N). The initiation of the median/radial cracks is driven by the tensile part of this component. The highest tensile stress is located close to the surface as shown in Graph 11 (a), just under and a bit in front of the indenter on the *x* axis.

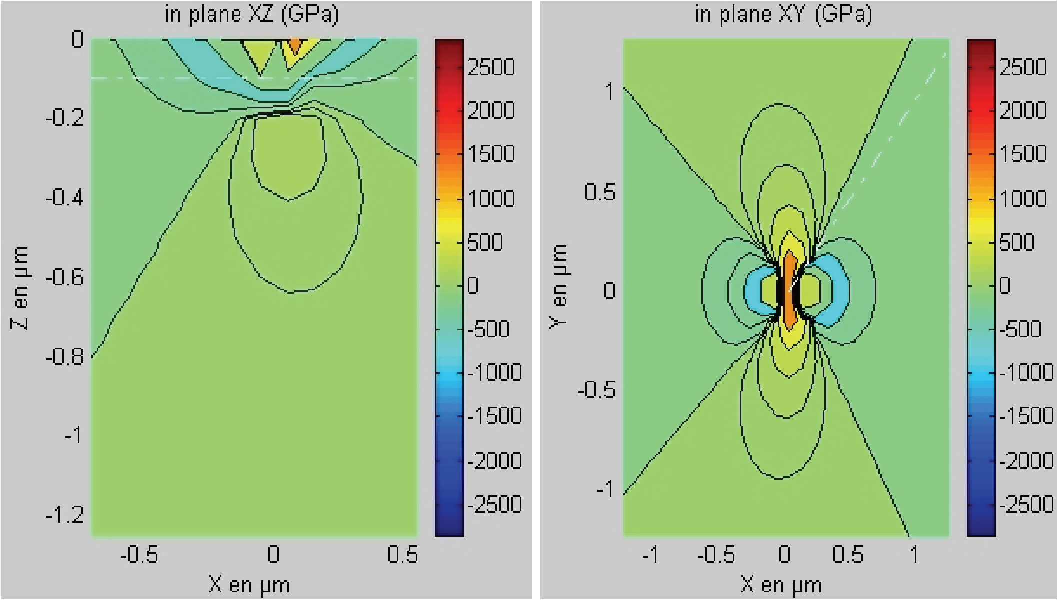

(a) (b)

Graph 11: Representation of the considered part of the stress σ_{yy} in the XZ plane (a) and XY plane (b) (case of P=0.5 N).

Then, the opening of the median/radial crack occurs in front of the moving penetrator.

The Graph 11 (b) shows the component $\sigma^{n}_{yy-Hanson} + \sigma^{t}_{yy-Bous.}$ in the plane XY (section at z=-0.1 µm).

The median/radial crack that just initiates under the indenter does not propagate straight due to a compressive stress component in the x direction as shown on Graph 11 (b). Then, as the indenter moves, the crack tends to propagate by inclining either on the left or the right as observed in experiments.

0.5.5.1.2 Prediction of the lateral crack occurrence

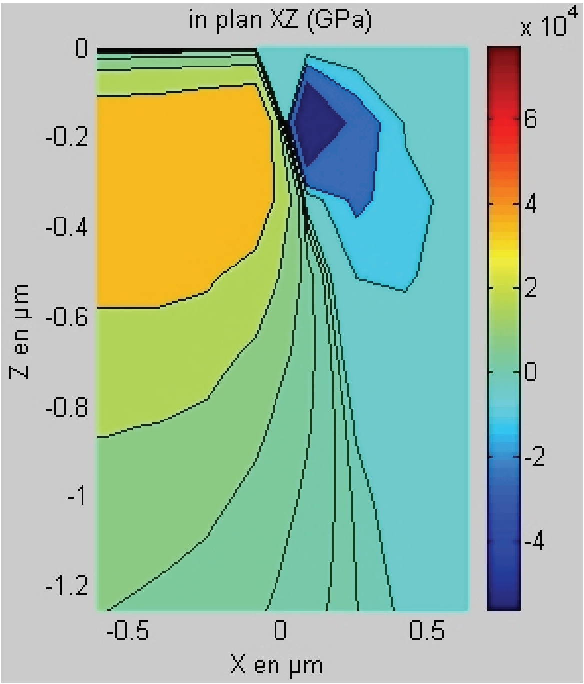

Graph 12: Detail of the representation of the considered stress σ_{zz} in the XZ plane (case of P=0.8 N).

The residual component (i.e. the *Blister* component) largely dominates the complete stress σ_{zz} when the normal load P is high enough (> 0.6 N). Then, the initiation of the lateral crack is expected to be driven by the tensile part of this component. The highest tensile stress is located (see Graph 12) in the depth of the body close to the boundary between the plastic zone and the elastic body). Its precise location is a bit behind the indenter on the x axis as observed in experiments.

High values of this component stay all along the scratch, even if the indenter passes far away. The compressive component in the x>0 prevents the propagation of the lateral crack in front of the indenter.

0.5.5.2 Prediction of the damage occurrence with regard to the chemical composition

Equivalent considerations on the stress fields obtained for each glass are consistent with the experiments achieved for the phenomenology and chemical composition dependence studies previously treated: from the standard float glass to the fused silica following the increase of silica content, the highest stress increases.

The median/radial cracking (governed by $\sigma_{yy} = \sigma^{n}_{yy-Hanson} + \sigma^{t}_{yy-Bous.} + \sigma^{r}_{yy-Blister}$ stresses) appears "earlier" as the silica content increases. The exception of the SLS 2 completes this analysis: it exhibits the lowest "highest" stress.

It is clearly established that the lateral cracking (governed by $\sigma_{zz} = \sigma^{n}_{zz-Hanson} + \sigma^{t}_{zz-Bous.} + \sigma^{r}_{zz-Blister}$ stresses) appears at lowest normal load in the fused silica than in the standard float glass, following the same order in the intermediate glasses. The SLS 2 is again the exception: it exhibits the lowest "highest" stress. These conclusions are consistent with experimental results previously reported.

All the scratch tests seem to reveal that the micro-abrasive regimes follow the same evolution than the rest of the scratch, i.e. if the micro-cracking regime appears early (i.e. at low normal load), the micro-abrasive regime appears early as well. It seems that the local stresses involved in the scratching just reach critical values for the micro-abrasive regime to occur that is consistent with the critical local stresses needed for the other damage events (i.e. micro-cracking regime appearance for example), which were experimentally observed. Then it seems that this conclusion is consistent but calls for caution for further interpretation.

0.5.5.3 Final remark about the semi-analytical model

No quantitative analysis is today reasonable with this model. There are still some parameters and hypothesis pointed out in this work that are too restrictive to lead to a quantitative model in the case of this study.

CHAPTER 1:
INTRODUCTION

SUMMARY OF CHAPTER 1

1.1 Thesis remarks

The goal of this thesis is to provide a scientific work of research in the field of interest but also to give complete details and as pedagogic as possible explanations for involved problems that belong to direct surrounding topics. Thus, the author's will is to give details in every fields of work which are treated in this thesis, from purely research considerations as analytical mechanical modeling of stress distribution under an indentation to engineering considerations as development of a scratching and instrumented indentation tester. The details will sometimes be reported in appendix for reading convenience.

1.2 Context

Nowadays, glasses are more and more used as load-bearing parts: windows in buildings, windscreens of cars, pathways made in glass,... Then the resistance in use is of prior interest and is closely linked to the way the glass piece is elaborated (machining, floating, extrusion, blowing,...). In fact, the resistance of glasses (and brittle materials in general) depends usually in surface damage that dramatically grows until complete rupture of the material. Thus, the industrial challenges for glass makers for instance lie in two main points: i) to control damage during producing, stocking and handling processes; ii) to provide a glass with the appropriate behavior for its expected given use. Because glasses are essentially used for optical and/or structural properties, the latter point considers what the worse damage could be: the larger damage (large chips for example) for optical losses and the more severe damage (deep and/or sharp crack for example) for mechanical losses. The ultimate goal on this point of view may be to avoid in part or completely both quoted types of damage.

Cutting, machining, handling, manufacturing, transportation, glazing, inappropriate storing, handling, and cleaning are some of the numerous mechanical sources of glass surface damage. The types of damage are usually in the form of surface scratches and abrasions which could be enhanced by thermal stresses. Thus, the study of the scratch process on glass appears to be appropriate i) to understand, ii) to predict and then iii) to prevent surface damage on glasses. Grinding and abrasion can be considered as multi-scratch process on the surface of glasses but will not be studied here. Static indentation is a convenient test to study damage occurrence but remains far from the reality of glasses in their "everyday life" use.

1.3 Research goals

In this context, this work is not focused on scratch-resistant glass making. Numerous studies in chemistry and material science (see [10, 17, 30, 31] among others) already deals with this point. The goal of this study deals with the *scratchability of soda-lime silica glasses*, i.e. the resistance characterization and the understanding of the damage occurring during scratching with material structure considerations and mechanical analysis.

Precise goals can be listed as follows:

1. to identify the damage during scratching of considered glasses.
2. to understand and explain the damage types and their occurrences in the light of structural considerations (study of different chemical compositions of glasses).
3. to build a mechanical model and to analyze the results in terms of damage predictions.

CHAPTER 2:
LITERATURE REVIEW

SUMMARY OF CHAPTER 2

2.1 Materials

2.1.1 Context

2.1.1.1 Generalities about glass & ceramic

The word *ceramic* comes from the Greek *keramos* that refers to “burnt stuff” or “burned earth”. Then, it designates a product obtained through the action of fire upon earthy materials. Ceramics is one of the three classes of solid materials that also include metals and polymers. They can be defined as inorganic, non-metallic materials that are typically produced using clays and other minerals from the earth or chemically processed powders. Ceramics are compounds formed between metallic and non-metallic elements such as aluminum and oxygen (alumina – Al_2O_3), silicon and nitrogen (silicon nitride – Si_3N_4) and silicon and carbon (silicon carbide – SiC), and usually found in crystalline form in nature [32]. “Classical” ceramic applications go from traditional products (potteries, bricks...) to advanced ceramics (artificial bones and teeth, electronic applications, space shuttle tiles, engine components, cutting tools,...), also known as *technical ceramics.*

Glasses are part of ceramics. Their main singularity, and also interest, is that they are amorphous, i.e. they exhibit no long range crystalline order. It can be compared in structure to certain liquids in which the atoms assume a temporary arrangement. The only difference being that in glass the temporary structure has been frozen into place by quenching.

The field of applications of the glasses is large (windows, electronic applications, computer and television’s screens, nuclear waste encapsulation,...) and growing as they continue to replace more traditional materials in many applications. Let’s notice some outstanding and historical applications: uses of glass in the construction industry include various types of windows of course, but also fibers for use in insulation, ceiling panels and roofing tiles instead of traditional materials. In 1879, Sir Thomas Edison invented the incandescent light bulb that changed the lives of millions of people all around the world. This is a typical application that would not be possible without the use of glass because of its necessary properties: hard, transparent, able to hold vacuum and withstand high temperatures at the same time. Another revolutionary application of glass is the optic fibers in the area of telecommunications. Information is being carried through transparent silica glass fibers instead of copper wires. The volume and speed information has greatly increased as well as the reliability of the transmission.

Even if today the wide spread field of applications of glass is a reality, its history shows that this field had tend to stay dramatically narrow for a long time early on.

2.1.1.2 History of glass

The first glasses can be found in many parts of the earth due to their volcanic origin and were used by the early man. In this time, this volcanic material called *obsidian* (a dark translucent glass – see Fig. 25) has been broken into sharp tools, chipped into decorations and later melted and form different kind of recipients. Note that *tektites* objects, probably of extra-terrestrial origin, are other examples of naturally occurring glasses.

Fig. 25: Photo of a piece of obsidian glass.

Archaeological findings indicate that it's around 3500 B.C. that the first glass objects were manufactured, in the Middle East. Glass bottles were found in the tomb of Thutmose I (1507-1497 B.C.) of Egypt. Surviving Cuneiform texts, engraved in tablet fragments and documenting the process for making glass in the Mesopotamian region, were found in the library of Assyrian's King Assurbanipal (668-627 B.C.). Glasses were still considered as luxury because of their cost due to the technical difficulties to produce them. Since these ancient times, the technology and the applications of glasses had almost not evolved up to 300 B.C.: the Greeks learned to use a blowpipe to make larger and more useful vessels. In the 1st century A.D., the Romans who acquired the glass technique forming from Greek by initiation, manufactured glasses for windows by splitting and flattening blown cylinders. Around 1000 A.D., the Grand Council of Venice moved all glassmaking to keep their trade secrets (and avoid fire in the city...) to the island of Murano where Soda-Lime Silica glass, that represents nowadays 90 % of the global glass production, called *cristallo* was soon developed. When these trade secrets were lost, the glass manufacturing rise rapidly in France, Germany, England and in the rest of Europe. In 1590, glass telescope and microscope lenses were developed in Netherlands and used for the first time. In the late 1890's, the better understanding of forming glass science enabled to considerably develop the uses and manufacturing of this material. In the early 1950's, Sir Alastair Pilkington [33] introduced a new revolutionary production method to obtain flat glass: the float process, by which 90 % of flat glass is still manufactured today. The following part introduces this process and gives details about the obtained material.

2.1.1.3 Float glass

Several techniques were invented to provide flat glasses (mainly for windows applications). Among all of these techniques that remain rarely used today (the Romans' one in the 1st century A.D. is part of them), let's mentioned some ways of giving a flat distortion free glass: i) one way was to squeeze semi-molten glass between two metals rollers (still use for glass with patterned surfaces), ii) a second one was to grind and polish both surfaces after it had cooled down. It was obviously terribly slow and costly. A more effective technique was required. In 1952, Alastair Pilkington invented the float process [33] which allows for the production of flat glass with an excellent surface finishing and that is processed continuously with no extra processing steps required.

The process is illustrated in Fig. 26. The main components of soda-lime silica glass are: silica sand (73 %), calcium oxide (9 %), soda ash (13 %), magnesium (4 %) and various other added materials in small quantity. These materials are weighted and mixed (usually also with recycled glass) before been introduced into a furnace where they are melted at 1500°C. A continuous ribbon of glass flows from the furnace at 1050°C to a bath of molten tin. The glass which is highly viscous and the tin which is very fluid do not mix. Because of the dead flat surface of the tin and the time of this operation, the glass cools down to around 600°C as it goes continuously along the tin bath. It becomes flat and both sides get parallel. The glass is then cooled down sufficiently to pass to an annealing chamber called *lehr* where it is precisely cooled down to 200°C. At the exit of the lehr, cross cutters cut the ribbon into panes of glass that have a uniform thickness and bright polished surfaces without the need for further processing. This float line is approximately half a kilometer long.

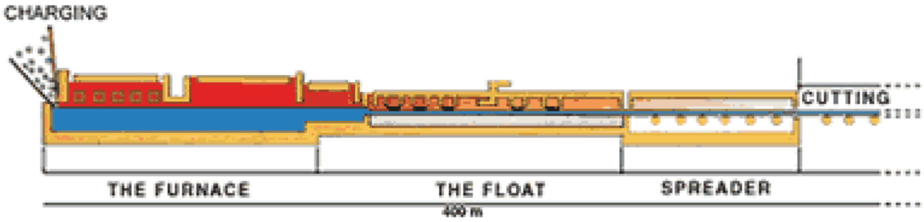

Fig. 26: Float process of glass manufacturing.

2.1.2 Definition of a glass & thermodynamic considerations

The theoretical understanding which suggested that practically all liquids could be rendered into glassy state if crystal growth could be suppressed [34] raised some forty years ago. The *glass* term consists of a non crystalline solid obtained by quenching an over-cooled liquid. Then, it exists a vitreous state in certain material whose viscosity progressively increases as the temperature goes down becoming solid without crystallizing [35]. The capacity to form a glass does not only depend on the chemical nature of the material but also on the cooling rate.

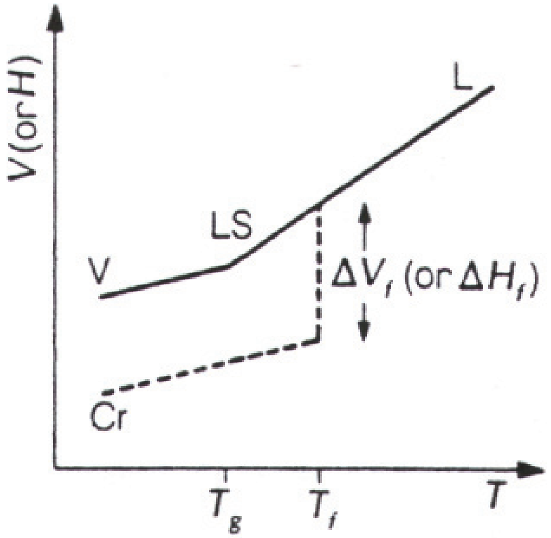

Graph 13 [35-37]: Variation of the specific volume *V* or the enthalpy *H* with respect to the temperature.

To illustrate the difference between crystallization and vitrification, let's take the Graph 13 [35-37]. The specific volume V (or the enthalpy H) evolves with the decrease of the temperature. A material crystallizes at the temperature T_f with usually a contraction of volume ΔV_f (or ΔH_f) and then continues to contract until totally cooled down. In the case of glass forming, the material linearly contracts down to the temperature T_g, called glass transition temperature, lower than T_f. Then the glass contracts a bit less than for the crystal solid and the change in the slope of the curve occurs at T_g, that corresponds to a viscosity of 10^{13} P (1

Poise=1 P=0.1 Pa.s). The solid has a short-range order similar to the "corresponding" crystal but has no long-range order [38].

2.1.3 Oxide glasses

Only the oxide glasses will be developed here because the glasses of this study belong to this amorphous family. Silica SiO_2 is the base of this kind of glasses. The structure is a 3-Dimensional tetrahedral (SiO_4) network. Each top of a tetrahedron is linked to one top of another tetrahedron as illustrated in Fig. 27 [39].

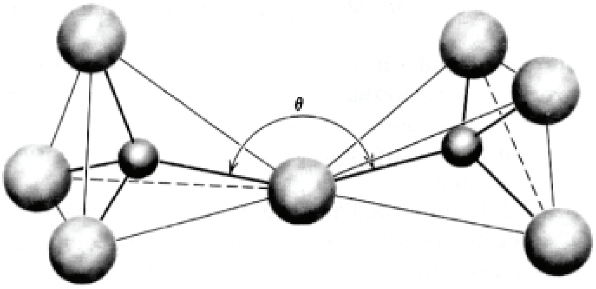

Fig. 27 [39]: Schematic representation of adjacent SiO_4 tetrahedra showing Si–O–Si bonds angle. Small spheres = Si; big spheres = O.

Most of the oxide glasses are obtained from the fusion of SiO_2 with addition of some modifiers that make a significantly decrease in the melting temperature (from ~1800°C to less than 1400-1500°C). The ternary glasses SiO_2-Na_2O-CaO, called Soda-Lime Silica glasses, are the base of the plate glass industry. For information, the Table 11 [36] gathers the chemical composition of common glass applications.

Glasses / Components	SiO_2	B_2O_3	Al_2O_3	P_2O_5	Li_2O	Na_2O	K_2O	CaO	BaO	MgO	PbO	ZnO	Fe_2O_3
Soda-lime silica glass (plate glass)	72,5	-	1,5	-	-	13	0,3	9,3	-	3	-	-	0,1
Bottle glass	73	-	1	-	-	15	-	10	-	-	-	-	0,05
Light-bulb glass	73	-	1	-	-	16	0,6	5,2	-	3,6	-	-	-
Boro-silicate glass (*Pyrex*)	80,6	12,6	2,2	-	-	4,2	-	0,1	-	0,05	-	-	0,05
Alumino-silicate glass (*E* glass)	54,6	8,0	14,8	-	-	0,6	0,6	17,4	-	4,5	-	-	-
Crystal glass	55,5	-	-	-	-	-	11,0	-	-	-	33	-	-
Optical glass (flint)	28	-	-	-	-	1	1	-	-	-	70	-	-
Glass for Sodium lamp	-	36	27	-	-	-	-	-	27	10	-	-	-
Radiation protecting glass	29	-	-	-	-	-	-	-	9	-	62	-	-
Hydrofluoric acid resistant glass	-	-	18	72	-	-	-	-	-	-	-	10	-
Base glass for nuclear waste vitrification (French composition)	58,2	17,9	6,3	-	2,5	6,8	-	5,1	-	-	-	3,2	-

Table 11 [36]: Chemical composition (in % of weight) of some industrial glasses.

2.1.4 Notions of glassification

Many chemical studies tried to explain the formation or non-formation of glasses. In this part, the work of Zachariasen [38], who established some correlations between structure and glassification aptitude, will be presented and limited to oxide glasses.

Some oxides are liable to form a glass and are called *glass formers* which involve either covalent or ionic chemical bonds. When adding a non-former oxide to a former oxide, the supplementary oxygens break some bonds of the original glassy network. For instance, if adding Na_2O in SiO_2, one bond of the Si–O–Si group is broken and give one $Si–\bar{O}$ radical composed of an atom of silicon and a so-called *non-bridging* oxygen. The negative charges of two non-bridging oxygens are compensated by a couple of cations Na^+ making the whole structure electrostatically neutral. These kinds of oxides are called *modifiers* (already quoted in the previous part). *Intermediates* oxides can behave like formers as well as modifiers, depending on the chemical composition of the glass.

The Table 12 gives the main former, modifier and intermediate oxides, classified by Zachariasen [38]. Readers can find more details in Kingery et al. [39].

Formers	Modifiers	Intermediates
SiO_2, GeO_2, B_2O_3, P_2O_5, As_2O_3, As_2O_5, V_2O_5	Li_2O, Na_2O, K_2O, MgO, CaO, SrO, BaO	Al_2O_3, PbO, ZnO, CdO, TiO_2

Table 12 [38]: Main formers, modifiers and intermediates in glass making.

2.1.5 Structural considerations

There has been a large amount of work published on this topic concerning the soda-lime silica glasses (see [6, 31, 38] among others) since the 1930's. From these early years, great steps where made in the understanding on how the chemical composition, that influences the network at an atomic scale, also modifies the macro-properties of the glasses. The chemical changes are usually rather simple: it consists in adding modifiers in precise proportions to the amount of silica when preparing the glass. These modifiers are supposed to change the basic SiO_2 structure and Zachariasen was the first to propose a model for the glass structure: the Continuous Random Network (CRN), modeling a disordered structure. Unlike a crystalline structure, in which the atoms are located at regular intervals in the three directions of space (depicted in Fig. 28 (a) [39] in schematic planar view), a disordered structure can only be defined in a statistical manner. Then an order can be described in short scale, but not in intermediate nor long scale. This kind of structure is illustrated in Fig. 28 (b) [36, 39]. Non bridging oxygens were envisaged as just being singly coordinated to the network and only loosely bound to modifying. Conversely modifying cations were envisaged as occupying occasional sites or voids in the disordered network cations as illustrated in Fig. 28 (c) [36]. Moreover, cations and non-bridging oxygens have important structural roles, as they often dictate the morphology of the network.

The work of Greaves [26] is of great interest to understand the effect of this adding of modifiers in the vitreous network. Greaves introduced a Modified Random Network model (MRN) for the glasses. The bonds between modifiers and the structural units of the original "polymerized" network (tetrahedra of SiO_4 in the case of the SLS glasses), were found to be ionic because of the non-bridging oxygens, whereas the others are covalent. Such a structure, as proposed by Greaves, is 2-Dimensionally drawn in the Fig. 28 (d) [26]. The shaded parts, that represent the original network regions, are defined by the boundary that runs through the non-bridging oxygens. The highlight places are then the conducting channels of modifiers, called percolation channels. As the modifier concentration is raised, the ionic regions become increasingly prevalent [26].

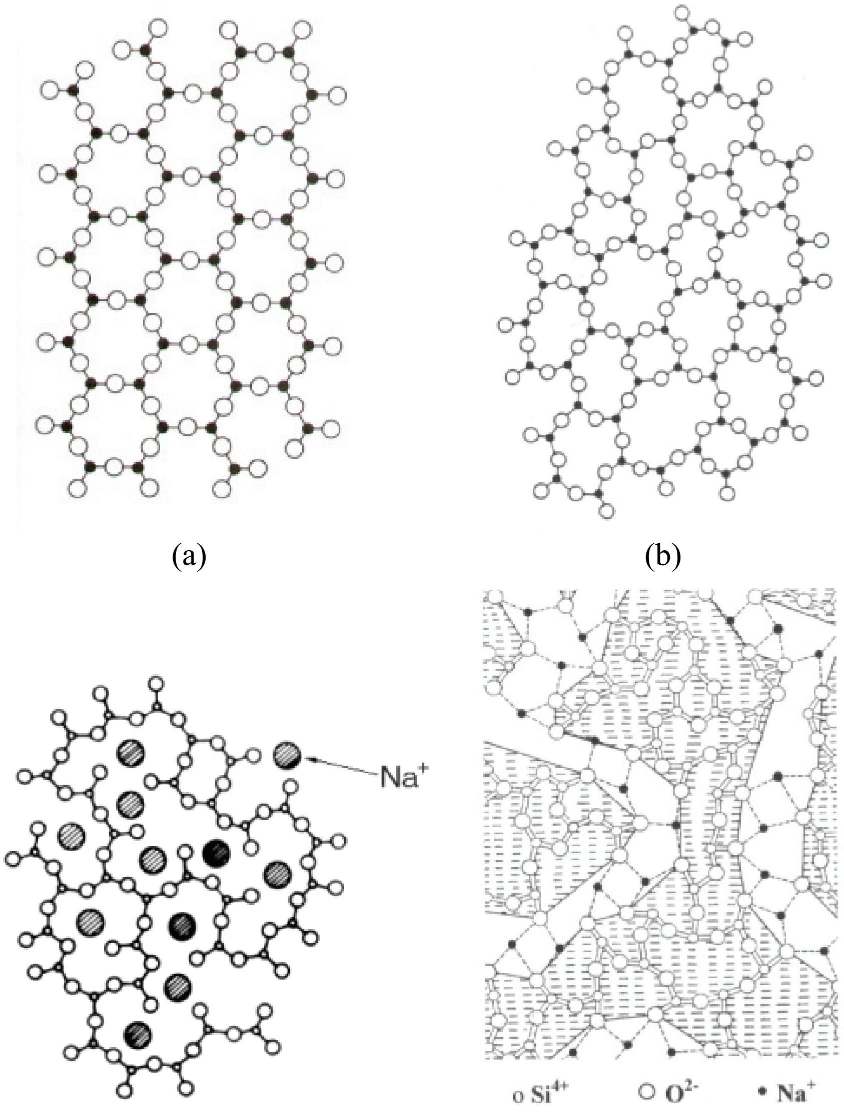

(a) (b)

(c) (d)

Fig. 28: Schematic planar representation of (a) ordered crystalline form [39]; (b) Continuous Random Network (CRN) of the glass [36, 39]; (c) glassy network with included modifiers [36]; (d) Modified Random Network (MRN) of the glass [26].

The relationships between chemical composition, structure and properties are still far from being precisely understood [34].

2.1.6 General properties

In this part, the main general properties of a standard float glass are reported:

- Chemical composition: mainly SiO_2 (71 %), Na_2O (13 %) and CaO (10 %),
- Melting temperature: T_f~800-850 °C,
- Glass transition temperature: T_g~550 °C,
- Coefficient of thermal expansion: α=10.10^{-6} °C^{-1},
- Volumic weight: ρ~2-3.10^3 kg.m^{-3},
- Young's modulus: E~60-80 GPa,
- Poisson's ratio: ν~0.2-0.25,
- Hardness ~600 H_V,
- Fracture toughness: K_C~0.7-0.8 $\mathrm{MPa}\sqrt{\mathrm{m}}$,
- Stress birefringence (applicability to photo-elasticity).

2.1.7 Subcritical crack growth of silica-based glasses

The interaction between water and glass can be sometimes not negligible at all. Actually, environment can influence greatly the physico-chemical or mechanical properties like strength, toughness [40], hardness [41],... A first possible reaction can occur when water stays on the glass surface: it exchanges hydrogen atoms with the sodium ions of the material. The result is a stained glass. Another possible reaction with water that can damage the glass is the chemical dissociation that breaks a Si–O bond and creates two –OH radicals. This is the notion of *static creep*. Then, a molecule of water enters and reaches the tip of a crack, makes it grow by a chemical reaction called *dissociative chemisorption*. Note that only the defects that are located on the surface are subject to this phenomenon. The Fig. 29 [42] illustrates this reaction: i) the molecule of water reaches the tip of the crack (see Fig. 29 (a)); ii) the atom of oxygen gets linked with a silicon atom of the vitreous network while his oxygen neighbor gets linked to one of the atom of hydrogen of the water molecule (see Fig. 29 (b)); iii) The original bonds break and give place to two silently groups at the (new) surface of the glass (see Fig. 29 (c)).

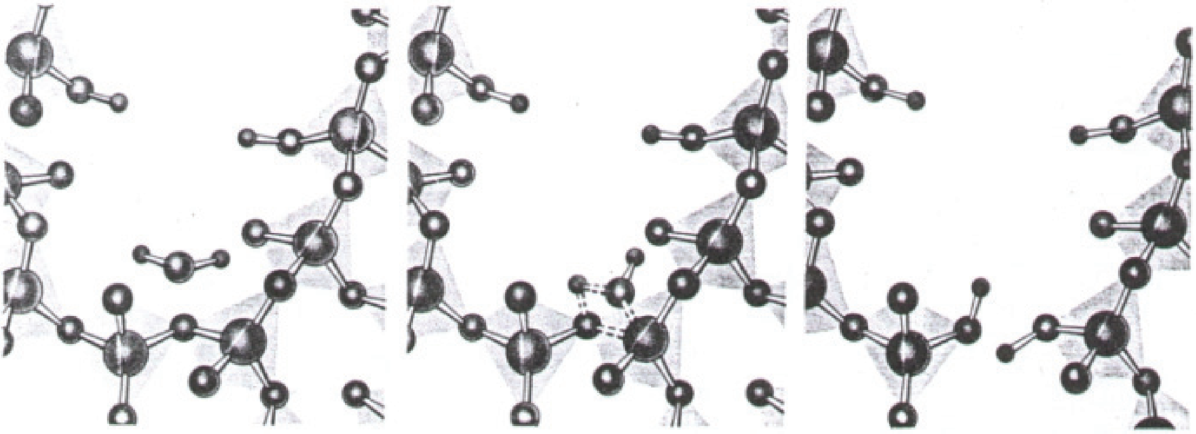

(a) (b) (c)

Fig. 29 [42]: Dissociative chemisorption: (a) the molecule of water reaches the tip of the crack, (b) the Si–O bond breaks, (c) the two –OH radicals are created.

Then, the simple equation of this reaction is:

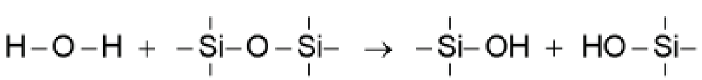

$$H-O-H + -\overset{|}{\underset{|}{Si}}-O-\overset{|}{\underset{|}{Si}}- \rightarrow -\overset{|}{\underset{|}{Si}}-OH + HO-\overset{|}{\underset{|}{Si}}-$$

Eq. 29

This chemical reaction is very slow: the crack growth speed is around 10^{-17} m.s^{-1} [42]. But, adding stress makes this reaction goes faster: it can go up to more than 1 mm.s^{-1} [42]. The mechanism of this enhancement of the crack growth is rather simple: the extreme stresses that occur near the tip of the crack, due to the stress concentration effect, deform the network. Then the atom of silicon can react more easily with the molecules of the environment. Obviously, the effectiveness of the reaction depends on the size and the nature of the molecules of the environment that reach the tip of the crack. For example, water (size of molecule: 0.26 nm) reacts more easily than methanol (0.36 nm), which also reacts more easily than aniline (0.42 nm) [42]. This phenomenon points out the importance of the molecular diffusion process close to the tip of a crack [41]. One common way in the industry to avoid the occurrence of this phenomenon is to apply a polymeric layer on the glass that will protect it to direct interaction with the environment.

This phenomenon of growth of a crack is called *subcritical crack growth* or *stress corrosion cracking* [43, 44]. This can lead to failure when the length of the crack validates the Griffith

[45] criterion. Note that the curvature of the crack tip is usually increased by this phenomenon, which increases the glass strength in some cases [40].

2.1.8 Notion of global densification in glasses

It has been well established that glasses subjected to high pressure can display significant permanent increases in density. This irreversible compaction is known as a *densification* process. Due to the opened structure of the glass (especially in the case of low content of modifiers), it is generally accepted that the effect of pressure is to compact this network, increasing its density [3, 4].

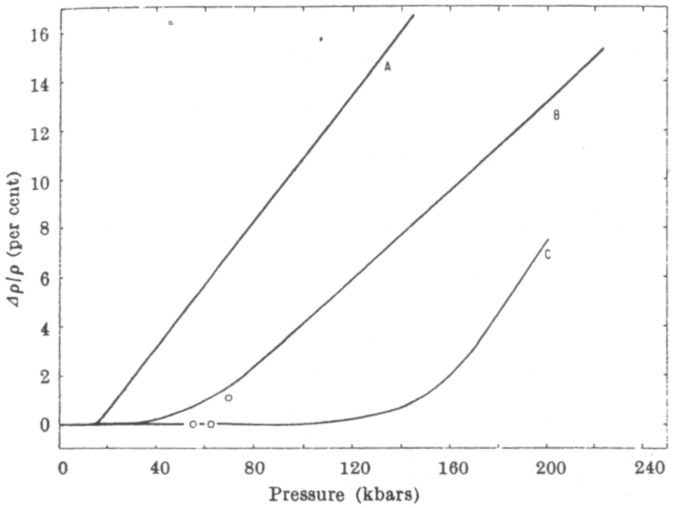

Fig. 30 [5]: Increase of density with applied pressure at room temperature for silica glass. A, Roy and Cohen [46]; B, Christiansen et al. [47]; C, Bridgman and Simon [3]; o, Mackenzie and Laforce [5].

Fig. 30 [5] reports results of global densification on vitreous silica from studies of Roy et al. [46], Bridgman et al. [3], Christiansen et al. [47] and Mackenzie et al. [5]. A threshold pressure is observed for silica-based glasses under which no more permanent densification takes place [5]. The large disparity between the results is explained to come from the shear proportion of the solicitation that is greatly affected by the experimental setup and procedure. Actually, numerous studies [3, 4, 48] dealing with global densification of glass report that the densification is much greater when large shear stress is superposed to hydrostatic pressure.

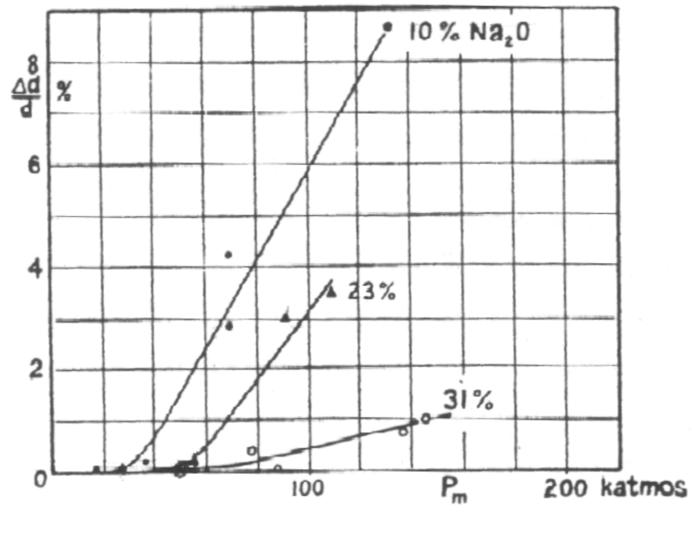

Fig. 31 [3]: Relative increase of density with applied pressure for three silicate glasses with 10, 23, and 31 molar percent Na_2O.

Fig. 31 [3] reports the densification of three silicate glasses with 10, 23 and 31 molar percent of Na_20 with regard to the applied pressure. Densification is affected by the amount of modifiers (Na^+) which fill the interstices into the silica network. Actually, the compressibility of the glass generally decreases with increasing alkali ions in the network: a permanent densification becomes more difficult.

2.1.9 Indentation behavior of glasses

2.1.9.1 Introduction

From a macroscopic point of view, glasses exhibit an elastic/brittle behavior. However, from a microscopic point of view, or under high punctual stresses, it is admitted that glasses can undergo a permanent deformation without completely breaking [1, 2]. Two main deformation phenomena can be distinguished:

- a permanent deformation (abusively named *plastic deformation* in reference to permanent deformation occurring in metals plasticity) that occurs by densification and/or by local shearing,
- a deformation by damage (cracks initiation and propagation).

The next parts deal with these different deformation phenomena.

2.1.9.2 Plastic zone

2.1.9.2.1 General

It is usual to speak about a *plastic zone* beneath the indenter in a glass during an indentation test, even when performed at low loads [1, 2, 49]. This term, taken from the material science about metals, deals with the fact that even at low load, a permanent deformation is observed beneath the indenter, without occurrence of macro-cracking phenomena. It is usually accepted that its shape is hemispherical and extends from the free surface to the depth of the material [2]. In crystallized metals, in fact especially in the ideal plastic materials, the origin of this permanent deformation under the load has been determined as plasticity due to nucleations and movements of dislocations [50, 51]. The reader would find details of the plasticity theory in metals elsewhere (see [51] for example). In the case of the soda-lime silica glasses, the notion of dislocations can't obviously be introduced due to the amorphous character of their structure. Then, the question can be formulated as the following one: what is the deformation behavior in the plastic zone in our glasses? Several authors have been discussing this topic since the 1960's.

2.1.9.2.2 Deformation by densification

It has been clear for a long time that densification process described in § 2.1.8 can also occur during indentation on glasses. This irreversible compaction of the network due to the complicated inhomogeneous stress field increases locally the density of the material. Then, this process is a non-conservative deformation in volume. This process has been pointed out by Infra-Red interferometric technique [52] or refractive index measurement [1].

Like in the global densification case (see § 2.1.8), it is generally accepted that the explanation of anomalous behavior lies in the tetrahedral bond structure of the basic silica network. The relative freedom of the atoms due to the Si–O–Si linkages (see Fig. 27) enables relatively free motions of the elementary tetrahedra of the amorphous structure. Modifiers are considered to restrict these movements.

2.1.9.2.3 Deformation by shear

Indentation experiments show that irreversible deformation may occur by shear flow (sometimes abusively named *plastic deformation*) as suggested by the presence of slip lines in the plastic zone [6]. This fact has also been pointed out by Peter [1] as pile-up appears at the surface surrounding the contact boundary (see Fig. 32 [1]) as it should happen on St. Venant bodies (ideal volume-conservative deformation). The same author shows a system of curved lines that are developed during the last stage of the indentation sequence as reported in Fig. 33 [1]. It looks like the "rosette" pattern of slip lines occurring in theoretically well-known problems of plasticity in metals as illustrated in Fig. 34 [1]. Then, introducing a yield point is justified like in classical plasticity theory.

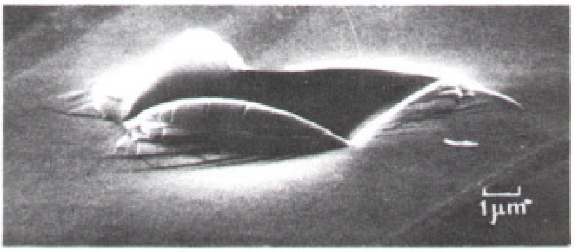

Fig. 32 [1]: Indentation on plate glass with a 70° pyramid. SEM.

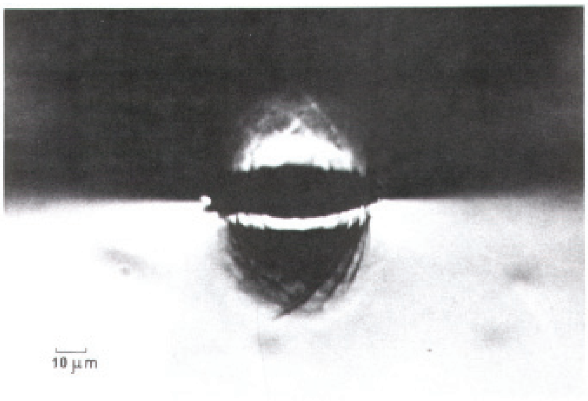

Fig. 33 [1]: Ball indentation on plate glass. Observation during indentation parallel to the surface and perpendicular to the applied outer force; the doubling of the line system is produced by total reflection on the surface. Light microscope.

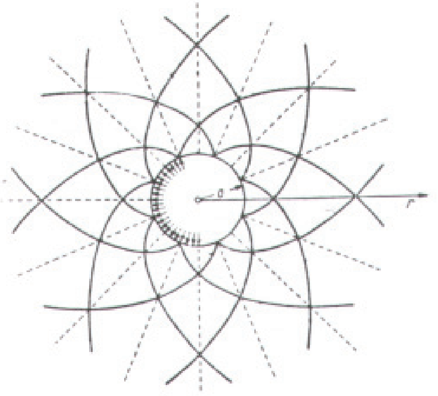

Fig. 34 [1]: Slip line system (τmax=const.) around a circular cylindrical tube inside a plastic body caused by normal pressure on the wall.

2.1.9.2.4 Normal/anomalous aspect

Normal glasses are characterized by the absence or a minor contribution of densification process in the area beneath the applied contact stress. Indentation experiments showed that in this case, irreversible deformation occurs by shear flow, as suggested by the presence of "slip" lines in the elastic-plastic contact zone [53] as reported in § 2.1.9.2.3. On the contrary, a flow-densification process shows up in anomalous glasses, and the ability of glasses with relatively high silica content to densify under sharp contact loading has a great influence on the indentation as reported in § 2.1.9.2.2 and on the scratch damage features. The densification was found to occur as soon as a permanent impression is formed [54]. Thus, these phenomena are of primary interest. For instance, the Table 13 gathers the deformation processes depending on the considered glass (from Peter [1]).

Glass Phenomenon	Plate glass	SiO_2 76 % Na_2O 14 % CaO 10 %	SiO_2 85 % Na_2O 15 %	SiO_2 100 % (Homosil ; Fa. Heraeus)
Densification	+	+	+	+
Piling-up	+	+	-	-
"Slip lines" below the indentation	+	+	-	-

Table 13: Deformation processes depending on the considered glass. The + and – signs stand for the occurrence or non-occurrence of the considered event respectively. (from Peter [1])

Peter [1] also pointed out an interesting result: the blunter the indenter is, the more the deformation occurs by densification and the less by shear flow. In the same scheme, Hagan et al. [53] found similar trends when changing the apex angle of the indenter, or the chemical composition of the glass. Kurkjian et al. [55] studied the role of the temperature on the silica glass behavior and concluded that in liquid nitrogen the silica glass behaves normal.

To summarize, glasses can deform by shear and/or densification depending on their chemical composition. This leads to the classical normal/anomalous behaviors illustrated in Fig. 35 (from [9]). Fig. 36 [7] shows schematically the pile-up (case of normal glasses) and sink-in (case of anomalous glasses) phenomena that occur during an indentation test depending on the considered glass.

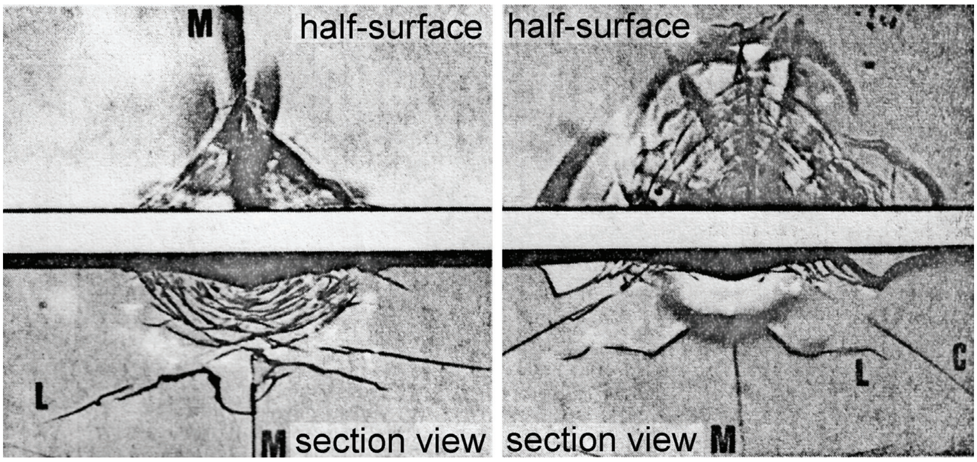

(a) (b)

Fig. 35: Vickers indentations (normal load: 30 N). Soda-lime (left) and silica (right) glasses. M, L and C denote median, lateral and cone cracks respectively. (from [9])

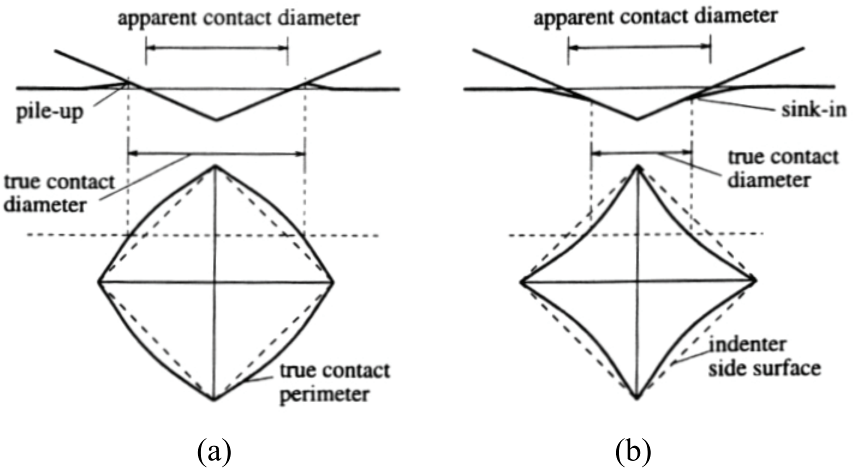

Fig. 36 [7]: Schematic diagram showing indentation of a material with a pyramidal indenter. (a) Pile-up formation, (b) sink-in pattern. Top: cross view; bottom: surface view.

2.1.9.3 Cracking in glass

Many studies deal with the cracking in glass. Among them, Cook et al. [8] summarized the cracking occurrence in glasses during indentation tests. The main ones are the cone cracks, radial cracks, median cracks, half-penny cracks and lateral cracks and are illustrated in Fig. 37 [8]. Note that half-penny cracks are usually a combination of radial and median cracks that intersect each other.

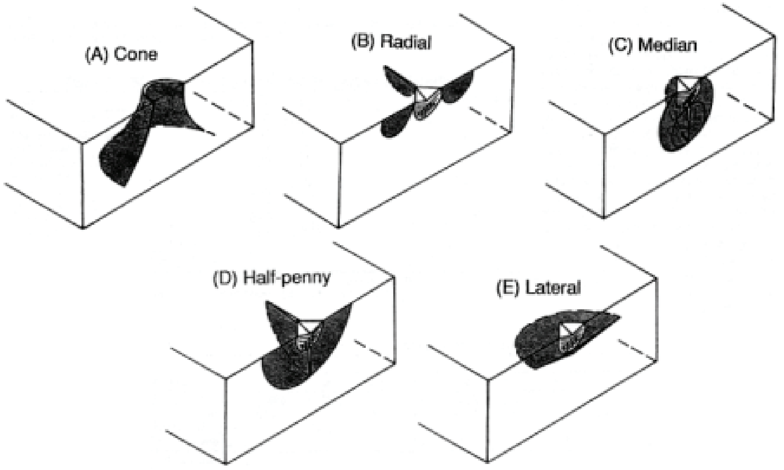

Fig. 37 [8]: Isometric sections of idealized crack morphologies observed at indentation contacts: (A) cone crack and associated nucleating ring crack, (B) radial crack and associated contact impression and plastic deformation zone (Vickers indenter), (C) median crack, (D) half-penny crack, and (E) lateral crack.

These different cracks can be seen in Fig. 35 and show the fundamental difference between the normal and the anomalous behavior from the cracking point of view: radial ^{l} (sometimes), median ^{l,u} and lateral ^{u} cracks occur in the normal glasses while cone ^{l}, median/radial ^{l} (restricted by the cone crack) and lateral ^{u} cracks occur in the anomalous glasses [9]. The superscripts ^{l} and ^{u} denote that the occurrence of the cracks is during the loading ^{l} and/or unloading ^{u} sequence during the indentation test.

It has been proved [6] that the cracks can initiate because of the slip bands that can be observed in the surrounding area of the indenter in the bulk material (i.e. out of the plastic zone). Because it seems to be non systematic [6], the comprehension of the damage in glass need to understand first the deformation of the glass in the direct surrounding of the indenter.

2.1.10 Scratching behavior of glasses

The scratch process is still far less studied in the literature than the quasi-static indentation process. Two main directions were historically followed to study the scratch process. The first one deals with the friction coefficient measurement and hence the force ratios to discuss the material removal during scratching, grinding or machining. The second one focuses on the cracking occurrences, which are particularly of interest in this study. Since the 80's, the study of scratching on brittle materials, from the cracking point of view, can be summarized as an extension of the indentation concepts [14, 49, 56]. In fact, Swain [57] found out that the microfracturing occurrence during scratching of brittle materials is very similar to the one happening under quasi-static indentation but with tangential load provided by the sliding movement. Swain defined three damage regions depending on the normal applied load: i) between 0 and 0.1 N, the scratching track remains fully plastic, ii) between 0.1 and 1 N, median and lateral cracks occur, and iii) at higher loads median cracks and poorly developed lateral cracks are observed combined with a crushing track. The phenomena appear similar in the different brittle materials that were tested (soda-lime silica glass, alumina,...) with some variability in the load values.

Ahn [20] reported the summary of the cracks occurrence in the second damage region defined by Swain as illustrated in the drawing in Fig. 38. Chevron cracks were also observed with their typical inclination toward the scratching direction.

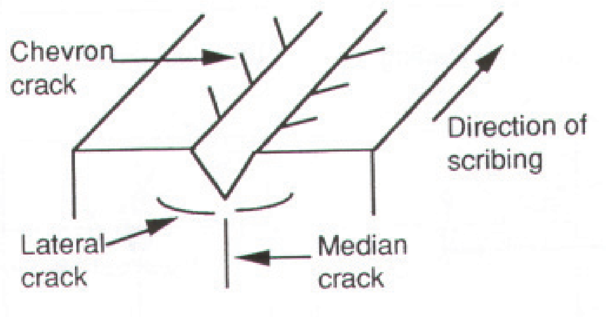

Fig. 38 [20]: Schematic view of the cracking around a scratch in brittle solid with a sharp indenter.

Bulsara [21, 58] carried a detailed work by identifying the different cracks occurring during a scratch test. His results are in agreement with the results previously given, and he went further in the observation of the lateral crack phenomenon. He found that subsurface lateral cracks appear only after the indenter lift off from the sample surface during a constant-load test. Then, the lateral crack propagates from the indenter place to the beginning of the scratch. Evans et al. [59] reported that the lateral cracking dominates the material removal in brittle material and is then of major interest for machining process understanding.

Marshall et al. [60] pointed out a dynamical phenomenon during scratching reported in Fig. 39 (section view along the scratch). It shows that the median crack does not propagate like one long and unique median crack but like successive median cracks that are created all along the scratch.

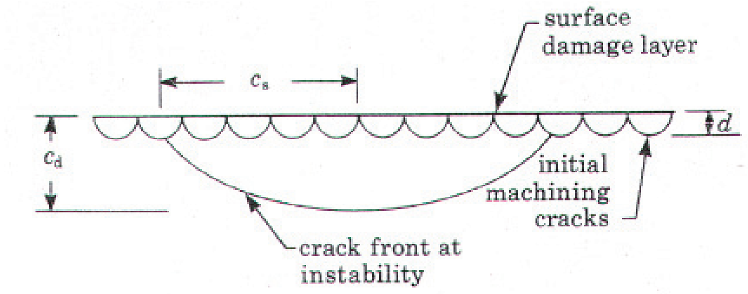

Fig. 39 [60]: Schematic representation of the crack configurations generated by linear damage processes and the crack front at failure.

As for the indentation, there could be a size effect of the tip of the indenter if the load is very low or if the indenter is seriously damaged as it has been clearly shown by Li [61]. The same authors [61] performed also few tests under water lubrication on the standard soda-lime silica glass that exhibit stick-slip phenomenon with a spherical indenter. Nevertheless, no study of the scratching damage dependence on the environment was performed up to now.

2.2 Mechanical models in indentation

2.2.1 Introduction

Even if they are usually convenient to perform, indentation tests which will be fully described in § 3.2.1 (as well as scratch tests) are complicated experiments for several reasons: many different indenters are available, the test greatly deals with the contact mechanic, the loading sequence can play an important role as well as the environment or the lubricating conditions, different materials can response in a wide range of behavior and the loading stress field is a complicated inhomogeneous state of stress within the sample. As a consequence, the mechanical models of indentation tests are multiple. Even the approaches differ considerably in certain cases. The main approaches can be quoted: i) the micro-mechanical models, ii) the analytical models, iii) the numerical models like the F.E.M. and iv) the cracking models. There are also mixed approaches (reverse-analysis,…) that deal with different methods "mixed" with others in order to get rid of some obstacles.

2.2.2 Micro-mechanical models

The first approach that was chosen in mechanical modeling of indentation is so-called *micro-mechanical* modeling. It has been built to attempt to characterize the average pressure, the stresses, the displacement and/or the strain that occur during an indentation test. These models have often different hypothesis as basis, sometimes different ways to treat the considered problem, and usually deal with different materials. In the next part, a non-exhausted list of micro-mechanical models is drawn up, from the most basic to the most complicated.

Tabor [50] formulates the mean pressure in a perfectly plastic material under an indentation by a conical indenter of apex angle ϕ:

$$p_m = C \times Y \qquad \textbf{Eq. 30}$$

with Y the yield stress and C a constant (C~2.8-3 for a wide range of isotropic metals).

Sneddon [62] gives also the mean pressure under an indentation by a conical indenter of half apex angle ϕ but in the case of a perfectly elastic material:

$$p_m = \frac{E \cot\phi}{2\left(1-\nu^2\right)} \qquad \textbf{Eq. 31}$$

Stillwell et al. [63] derived the previous equation to assess the total vertical displacement y of the indenter:

$$y = \frac{\pi p_m a\left(1-\nu^2\right)}{E} \qquad \textbf{Eq. 32}$$

where a is the contact radius of the indentation.

Theoretically, Hill [64] developed the expanding cavity in an elastic perfectly-plastic material model and found out for ν=0.5:

$$\frac{p_m}{Y} \approx 0.40 + \frac{2}{3}\ln\left(\frac{E}{Y}\right) \qquad \textbf{Eq. 33}$$

As suggested by Bishop et al. [65], Marsh [2] found with experimental considerations (various materials with a Vickers indenter) the following expression:

$$\frac{p_m}{Y} \approx 0.07 + 0.6 \ln\left(\frac{E}{Y}\right) \qquad \textbf{Eq. 34}$$

The difference between Hill's expression and this last one illustrates the discrepancy between the expanding cavity model and the experimental process as reported by Tabor [66]. Hill treated the problem as the expansion of a cavity that is different from the experimental reality measured by Marsh (probably because of the use of a Vickers indenter).

Sneddon [62] had interest in finding the pressure distribution in contact during a conical indentation performed on a purely elastic material. The pressure distribution on the indenter depending on the abscissa r, $p(r)$ is given by Eq. 35 and $p(r)/p_m$ is plotted on half of the indenter ($r/a \in [0,1]$) in Graph 14.

$$p(r) = \frac{E \cot \alpha}{2\left(1-\nu^2\right)} \cosh^{-1}\left(\frac{a}{r}\right) \qquad \textbf{Eq. 35}$$

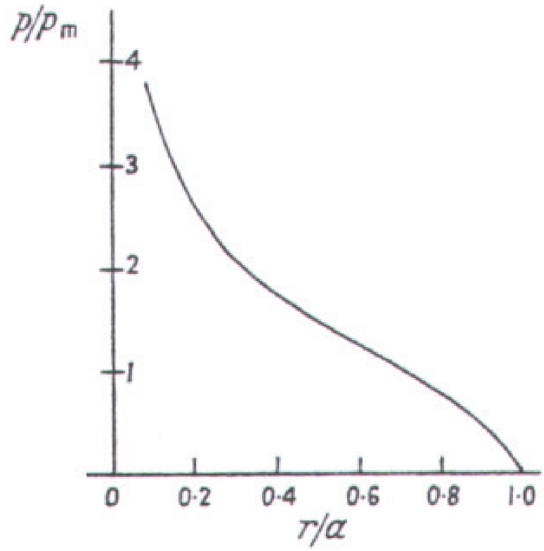

Graph 14: Distribution of the pressure under a conical indenter loading on a semi infinite purely elastic material.

Johnson [67] studied the strain under a conical indenter. He found out that the strain is constant under a conical or a Vickers indenter. It can be illustrated by:

$$\varepsilon\left(\frac{x}{a}, \frac{y}{a}\right) = f\left(\frac{h}{a}\right) = const. \qquad \textbf{Eq. 36}$$

The friction influence can also be taken into account. Numerous studies (see Johnson [68] for instance) deal with this problem. However, in the present study, the same test conditions will be always used in order to get rid of this parameter.

2.2.3 Stress field models

2.2.3.1 Notation remark

Following Johnson [68], Yoffe [27], Gladwell [69], Maugis [70], Ahn et al. [20, 71, 72], Cook et al. [8] among others, analytical expressions of stress fields will be given in the complete form of their equations. In this way, convenience of reading will be a bit altered because of complicated equations. However, for readers interested in computing these equations for building new models or verifying some results, this choice of notation is *immeasurably precious* as is illustrated in the *Description and new computation of Ahn's Model* part (§ 5.2).

2.2.3.2 Context

Micro-mechanical models give interesting results about mean pressure, strain, macroscopic displacement and profile considerations through simple models. However, the expression of the stress field (in a complete or partial form) in the indented material is often required when the problem involves complicated geometries or if the goal is to obtain the local stresses (for crack initiation for instance).

Then the direct mechanical approach of the problem lies on assumptions regarding the displacement field, the boundary conditions of the system and the knowledge of the precise material parameters (the adapted constitutive laws of the studied glasses for the considered loading conditions). Thus the problem appears complicated because of the number of variables. Moreover, finding the constitutive laws of the studied glasses raises important problems because of their complicated behavior to indentation and scratching.

This part presents the different existing models depending on the solicitation type or/and the behavior of the material to indentation test. This part will be divided in two parts: the analytical approach and the Finite Elements approach.

2.2.3.3 Analytical approach

2.2.3.3.1 Introduction

Main contributions into the understanding of the contact of elastic solids have been made by Hertz, Boussinesq and Sneddon. Then, plastic or elasto-plastic models were developed (Hill, Chiang, Yoffe,...). This part will present the main models.

In a first step, existing analytical models about perfectly elastic materials will be reported (Boussinesq, Hertz). Then, a model about conical indentation that takes into account an elasto-plastic behavior of the indented material will be reported (Yoffe). This model can represent the behavior of the considered studied materials in some cases that will be discussed later.

2.2.3.3.2 Boussinesq's model

The goal of this model is to study the stresses in a perfectly elastic semi-infinite solid loaded by a point force which is concentrated on a surface that tends to zero. Then, the force is considered to be concentrated on one point.

The coordinate system is a classical Cartesian system with the *x-y* plane corresponding to the surface of the indented material and the *z* axis oriented toward the depth of the solid.

After preliminary assumptions on the displacement and the definition of the Boussinesq and Cerruti's potentials, the stress field for a normal concentrated force *P* located on the origin of the coordinate system is given by Eq. 37 to Eq. 42 [68, 72]:

$$\sigma_x^n = \frac{P}{2\pi}\left[\frac{1-2\nu}{r^2}\left\{\left(1-\frac{z}{\rho}\right)\frac{x^2-y^2}{r^2}+\frac{zy^2}{\rho^3}\right\}-\frac{3zx^2}{\rho^5}\right]$$ **Eq. 37**

$$\sigma_y^n = \frac{P}{2\pi}\left[\frac{1-2\nu}{r^2}\left\{\left(1-\frac{z}{\rho}\right)\frac{y^2-x^2}{r^2}+\frac{zx^2}{\rho^3}\right\}-\frac{3zy^2}{\rho^5}\right]$$ **Eq. 38**

$$\sigma_z^n = -\frac{3P}{2\pi}\frac{z^3}{\rho^5}$$ **Eq. 39**

$$\tau_{xy}^{n}=\frac{P}{2\pi}\left[\frac{1-2\nu}{r^2}\left\{\left(1-\frac{z}{\rho}\right)\frac{xy}{r^2}-\frac{xyz}{\rho^3}\right\}-\frac{3xyz}{\rho^5}\right]$$ **Eq. 40**

$$\tau_{yz}^{n}=-\frac{3P}{2\pi}\frac{yz^2}{\rho^5}$$ **Eq. 41**

$$\tau_{zx}^{n}=-\frac{3P}{2\pi}\frac{xz^2}{\rho^5}$$ **Eq. 42**

with

$\rho=\sqrt{x^2+y^2+z^2}$ **Eq. 43**

and

$r=\sqrt{x^2+y^2}$ **Eq. 44**

The superscript n denotes the stress field due to the normal load.

2.2.3.3.3 Hertz's model

2.2.3.3.3.1 General problem

The problem of the Hertz's contact is formulated in the same manner as the one of Boussinesq. However it differs from Boussinesq model on the assumption of the concentrated force on an area of the surface that tends to zero. A surface area different to zero is obviously justified by the real consideration of the contact surface between two solids. Hertz also makes the hypothesis that this area of surface has an ellipsoidal shape with negligible dimensions compared to the ones of the two perfectly elastic bodies. The solids are considered without roughness.

The coordinate system is cylindrical with the *z* axis passing through the centre of each solid and the polar plane passing through the contact plane.

The expression of the mean pressure p_m is determined by Eq. 45.

$$p_m\propto\frac{a\left(\frac{1}{R_1}+\frac{1}{R_2}\right)}{\frac{1}{E_1}+\frac{1}{E_2}}$$ **Eq. 45**

with a the contact radius between the two solids, R_1 and R_2 the radius of curvature of the solids and E_1 and E_2 their Young's modulus respectively.

2.2.3.3.3.2 Case of solids of revolution shape

First of all, equivalent notations have to be introduced:

$$\frac{1}{E^*}=\frac{1-{\nu_1}^2}{E_1}+\frac{1-{\nu_2}^2}{E_2}$$ **Eq. 46**

and

$$\frac{1}{R}=\frac{1}{R_1}+\frac{1}{R_2}$$ **Eq. 47**

with ν_1 and ν_2 the Poisson's ratios of the solids in contact.

The complete stresses provided by a Hertzian contact were determined by Hüber [73]. They are reported in their corrected form (from Love [74]) in Eq. 48 to Eq. 51.

$$\frac{\sigma_r}{p_0}=\frac{1-2\nu}{3\rho^2}\left[1-\left(\frac{\zeta}{\sqrt{u}}\right)^3\right]+\frac{\zeta}{\sqrt{u}}\left[(1+\nu)\sqrt{u}\tan^{-1}\frac{1}{\sqrt{u}}+(1-\nu)\frac{u}{1+u}+\frac{\zeta^2}{u^2+\zeta^2}-2\right] \quad \textbf{Eq. 48}$$

$$\frac{\sigma_\theta}{p_0}=-\frac{1-2\nu}{3\rho^2}\left[1-\left(\frac{\zeta}{\sqrt{u}}\right)^3\right]+\frac{\zeta}{\sqrt{u}}\left[(1+\nu)\sqrt{u}\tan^{-1}\frac{1}{\sqrt{u}}-(1-\nu)\frac{u}{1+u}-2\nu\right] \quad \textbf{Eq. 49}$$

$$\frac{\sigma_z}{p_0}=-\frac{1}{s}\left(\frac{\zeta}{\sqrt{u}}\right)^3 \quad \textbf{Eq. 50}$$

$$\frac{\tau_{rz}}{p_0}=-\frac{\zeta}{\sqrt{u}}\frac{\rho\zeta}{s(1+u)} \quad \textbf{Eq. 51}$$

with

$$u=\frac{1}{2}\left(\rho^2+\zeta^2-1+s\right) \quad \textbf{Eq. 52}$$

$$s=\sqrt{\left(\rho^2+\zeta^2+1\right)^2-4\rho^2} \quad \textbf{Eq. 53}$$

$$p_0=\frac{3P}{2\pi a^2} \quad \textbf{Eq. 54}$$

$$\rho=\frac{r}{a} \quad \textbf{Eq. 55}$$

$$\zeta=z/a \quad \textbf{Eq. 56}$$

2.2.3.3.3.3 Case of the solids of general shape

Solids of general shape are accommodated by the Hertz theory if they are considered as perfectly elastic and if the contact shape can be approximated by an ellipse.

2.2.3.3.4 Hanson's model for conical indentation

The work of Hanson [28, 29], derived from Fabrikant's one [75], agrees with the solutions of Sneddon on the problem of the conical indentation on a purely elastic material [76]. However, the expressions of Hanson are in an easier form to compute. The development principle is rather simple but it is complicated to calculate the expressions of the solutions due to mathematical obstacles: Hanson found potential functions from the expression of the σ_{zz} stress component of Sneddon [76] that he derived to obtain the expressions of the complete stress field. In fact, in Hanson's equations that are given in Eq. 57 to Eq. 65, only two length parameters $l_1(a)$ and $l_2(a)$ need to be introduced, and the resulting expressions are given in simple forms.

$$l_1(a)=\frac{1}{2}\left(\sqrt{(\rho+a)^2+z^2}-\sqrt{(\rho-a)^2+z^2}\right) \quad \textbf{Eq. 57}$$

$$l_2(a)=\frac{1}{2}\left(\sqrt{(\rho+a)^2+z^2}+\sqrt{(\rho-a)^2+z^2}\right) \quad \textbf{Eq. 58}$$

$$\sigma_1 = -\frac{E\varepsilon}{2a\left(1-\nu^2\right)}\left[\left(1+2\nu\right)\left(\ln\left[l_2\left(a\right)+\sqrt{l_2^2\left(a\right)-\rho^2}\right]-\ln\left[z+\sqrt{\rho^2+z^2}\right]\right)\right.$$
$$\left.+z\left(\frac{\sqrt{l_2^2\left(a\right)-a^2}}{\left(l_2^2\left(a\right)-l_1^2\left(a\right)\right)}-\frac{1}{\sqrt{\rho^2+z^2}}\right)\right] \qquad \textbf{Eq. 59}$$

$$\sigma_2 = -\frac{E\varepsilon}{2a\left(1-\nu^2\right)}e^{2i\theta}\left[\left(1-2\nu\right)\left(\frac{1}{a\rho^2}\left(2a^2-l_2^2\left(a\right)\right)\sqrt{a^2-l_1^2\left(a\right)}+\frac{z\sqrt{\rho^2+z^2}}{\rho^2}-\frac{a^2}{\rho^2}\right)+\right.$$
$$\left.+\frac{z^2a\left[\rho^2+2l_1^2\left(a\right)-2l_2^2\left(a\right)\right]}{\rho^2\sqrt{a^2-l_1^2\left(a\right)}\left[l_2^2\left(a\right)-l_1^2\left(a\right)\right]}+\frac{z\left(\rho^2+2z^2\right)}{\rho^2\sqrt{\rho^2+z^2}}\right] \qquad \textbf{Eq. 60}$$

$$\sigma_{zz} = -\frac{E\varepsilon}{2a\left(1-\nu^2\right)}\left[\ln\left[l_2\left(a\right)+\sqrt{l_2^2\left(a\right)-\rho^2}\right]-\ln\left[z+\sqrt{\rho^2+z^2}\right]-\frac{z^2l_2\left(a\right)}{\sqrt{l_2^2\left(a\right)-\rho^2}\left[l_2^2\left(a\right)-l_1^2\left(a\right)\right]}\right.$$
$$\left.+\frac{z}{\sqrt{\rho^2+z^2}}\right] \qquad \textbf{Eq. 61}$$

$$\tau_z = -\frac{E\varepsilon}{2a\left(1-\nu^2\right)}e^{i\theta}\frac{1}{\rho}\left[\frac{zl_2\left(a\right)\sqrt{l_2^2\left(a\right)-\rho^2}}{\left[l_2^2\left(a\right)-l_1^2\left(a\right)\right]}-\frac{z^2}{\sqrt{\rho^2+z^2}}\right] \qquad \textbf{Eq. 62}$$

with a the contact radius, $\varepsilon = a\cot\left(\alpha\right)$ and ρ defined in Eq. 44.

The notations will not be explained further here. The stresses σ_{xx}, σ_{yy}, σ_{zz}, τ_{xy}, τ_{xz} and τ_{yz} are directly derived from the previous expressions with the help of Eq. 63 to Eq. 65. The reader should report to [28, 29] for more details.

$$\sigma_1 = \sigma_{xx} + \sigma_{yy} \qquad \textbf{Eq. 63}$$

$$\sigma_2 = \sigma_{xx} - \sigma_{yy} + 2i\tau_{xy} \qquad \textbf{Eq. 64}$$

$$\tau_z = \tau_{xz} + i\tau_{yz} \qquad \textbf{Eq. 65}$$

2.2.3.3.5 Direct plotting of some analytical models and possible application to material considerations

These analytical models are devoted to their own application: concentrated force for the Boussinesq's model, spherical contact for the Hertz's model and conical contact for the Sneddon/Hanson's model. However, a direct comparison between these models can be justified through material considerations. Actually, in the frame of this study, one can wonder what differentiate these three models on the densification initiation in the glass for instance. This part attempts to illustrate through this example of application how results from these analytical models can be analyzed.

As reported in § 2.1.9.2, densification is admitted to occur in glass (in bulk material or locally due to an indentation test for example) and the process is mainly related to high hydrostatic pressure. Plotting the hydrostatic stress of the different previously introduced elastic analytical models can help to locate the first point that is supposed to densify. Then, Fig. 40 represents the hydrostatic stresses distribution (normalized by the mean pressure) through the depth of the material (normalized by the contact radius *a*) of (a) the Boussinesq's model, (b) the Hertz's model, and (c) the Sneddon/Hanson's model.

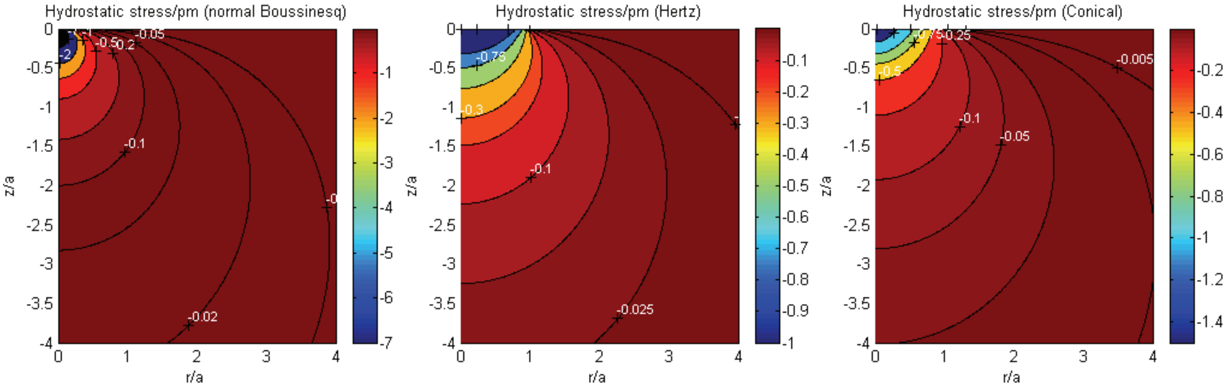

(a) (b) (c)

Fig. 40: Hydrostatic stresses in the depth of the material for (a) the Boussinesq's model, (b) the Hertz's model, and (c) the Sneddon/Hanson's model.

Then, the zone that is expected to firstly densify is:

a) of spherical shape and located right under the indentation for the concentrated normal force,
b) of flatten portion of sphere shape located on the full contact area,
c) of flatten portion of sphere shape under the contact but the highest hydrostatic stresses are located right under the tip of the penetrator (not represented here).

However, due to the elastic character of these models in contrast with the permanent character of the densification process, these results must be limited to the approximation of the location of the first zone expected to densify. Actually, these elastic models do not represent the elasto-plastic behavior of the material, and a second limitation lies in the influence of the shear stress on the densification process. Actually, as reported in § 2.1.8, shear stresses are admitted to enhance the densification. Then, to take into account only the hydrostatic part of the loading is insufficient, especially during indentation that produces shear stress in large proportion.

2.2.3.3.6 Yoffe's approach [27]

2.2.3.3.6.1 Assumptions of Yoffe's model

Peter showed [1] that the contact pressure between the indenter and the material can be considered as constant and relatively independent of the geometry of the penetrator. This hypothesis enabled Yoffe to build a model that gives the complete elastic stress field within the indented body. This model is adapted to brittle materials and for conical indenters.

To achieve this model, a hypothesis on the permanent deformed zone was assumed: the plastic zone appears under the indenter and is finally assumed to be of hemi-spherical shape. It spreads with regard to the load. This deformation can be due to both densification and/or shear deformation during the penetration of the indenter.

2.2.3.3.6.2 Principle

The distribution of the stresses in the *elastic* zone is obtained by superposing two different *elastic* stress fields:

- a Boussinesq stress field corresponding to a stress field due to the loading indenter simplified in this case as a point loading,
- a stress field called *Blister* field corresponding to the stress field that idealize the residual stresses in the *elastic* zone due to the influence of the *plastic* zone.

Then, the complete stress field is given by:

$$\sigma = \sigma^{n}_{Bous.} + \sigma^{t}_{Bous.} + \sigma^{r}_{Blister} \qquad \textbf{Eq. 66}$$

The superscript *n* denotes the stress field due to the normal load; the superscript *t* denotes the stress field due to the tangential load; the superscript *r* denotes the residual stress field.

2.2.3.3.6.3 Detail of the *Blister* field

2.2.3.3.6.3.1 Principle

The inelastic zone located under the indenter behaves like a nucleus of strain located on a free surface as reported in the Fig. 41.

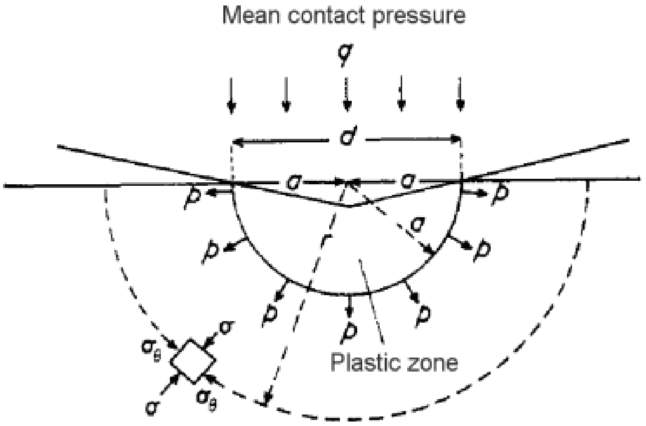

Fig. 41: Schematic representation of the inelastic zone located under the indenter as a nucleus of strain.

Then the stress field outside the plastic zone is the combination of a symmetrical centre of pressure with a double force in the *z* direction [77]. Fig. 42 (a-e) illustrates the approach which allows calculating the stress state through some simple drawings that represent the procedure ensuring the boundary conditions of a free surface with the help of an inward double force. Note that this kind of approach dealing with the boundary conditions has been also used by Chiang et al. [78, 79] in a similar model (Hill's cavity-based).

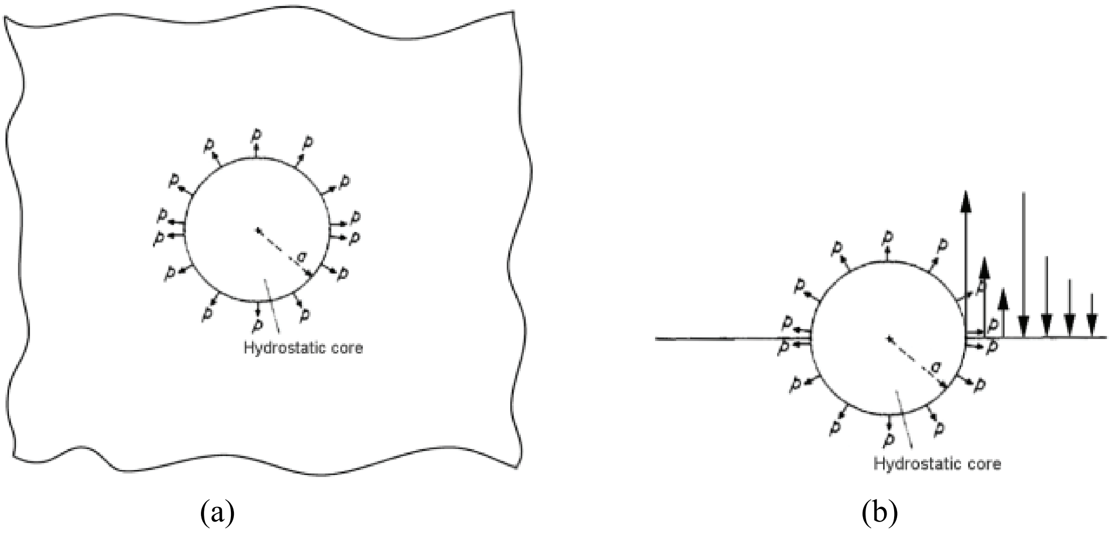

(a) (b)

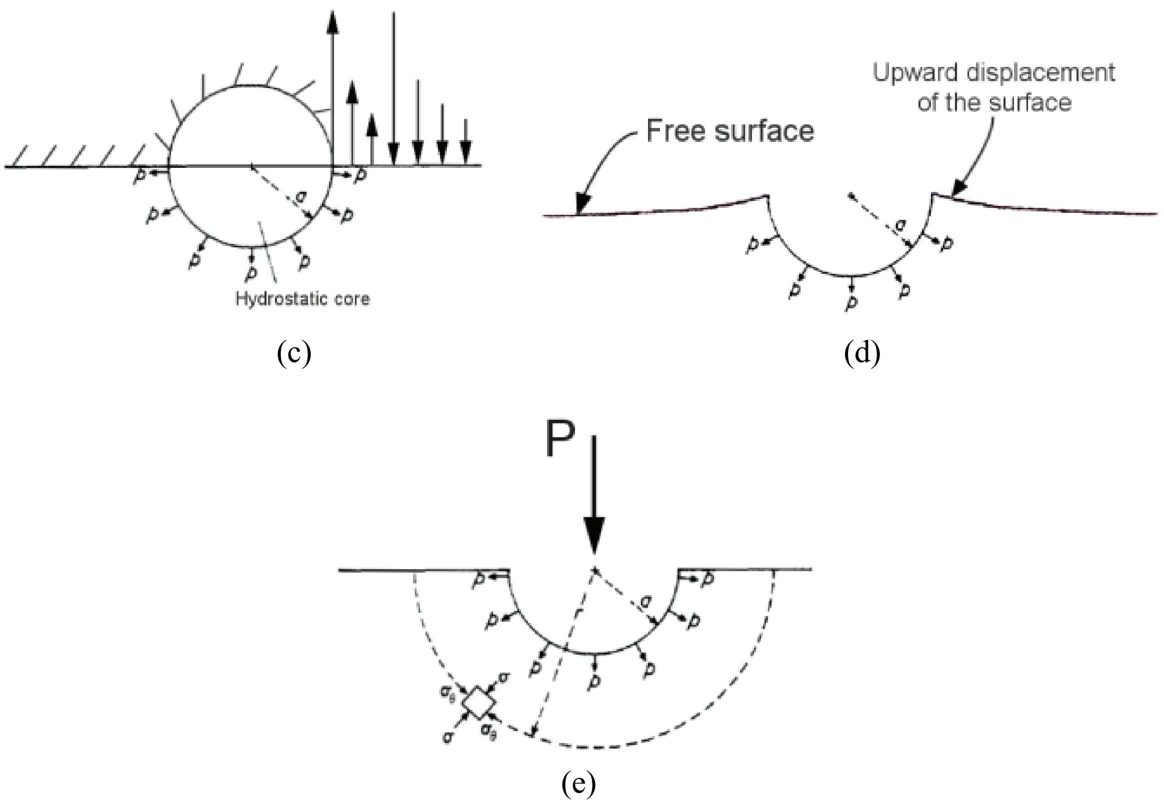

(c) (d)

(e)

Fig. 42: Procedure ensuring the boundary condition of a free surface in the model of a nucleus of strain. (a) the centre of pressure, (b) the creation of a surface plane, (c) the cutting into a half-space with the distribution of stresses in the interface, (d) the creation of the free surface with the upward displacement as a consequence, (e) the addition of the inward force P to compensate the upward displacement.

Then, Yoffe [27] models the *Blister* field as equivalent to two outward double forces in the surface plane and an inward double force of equal magnitude normal to it (see Fig. 43) using the solutions proposed by Love [77]. This combination leaves the surface free of stress as required by the boundary conditions of the indentation problem. The elastic stresses in the indented body decrease as $\frac{1}{r^3}$, with *r* the distance to the loading point.

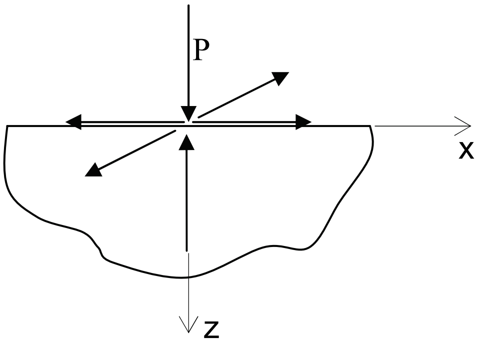

Fig. 43: The outward double forces and the inward double forces model used by Yoffe [27].

The corresponding stresses are given by Yoffe [27]:

$$\sigma_r^r = \frac{B}{r^3} 4\left[\left(5-\nu\right)\cos^2\theta - \left(2-\nu\right)\right] \qquad \textbf{Eq. 67}$$

$$\sigma_\theta^r = -\frac{B}{r^3} 2\left(1-2\nu\right)\cos^2\theta \qquad \textbf{Eq. 68}$$

$$\sigma_{\phi}^{r} = \frac{B}{r^3} 2(1-2\nu)(2-3\cos^2\theta) \quad \textbf{Eq. 69}$$

$$\tau_{r\theta}^{r} = \frac{B}{r^3} 4(1+\nu)\sin\theta\cos\theta \quad \textbf{Eq. 70}$$

where B is the strength of the *Blister* field.
The superscript r denotes the *residual* stress field as the *Blister* field.

2.2.3.3.6.3.2 Determination of the strength B of the *Blister* field

2.2.3.3.6.3.2.1 Introduction

Several studies deal with the determination of the strength of the *Blister* field that represents the difficulty of this model. This part shows the approach of each author to assess the parameter B.

2.2.3.3.6.3.2.2 Continuous stresses condition approach

Yoffe [27] considered the location of the maximum tensile stresses (i.e. where the cracks are expected to initiate). This position is a function of B, which depends on the densification and the apex angle of the indenter. The direct consequence is that the value the *Blister* field changes as a consequence of the densification of the tested material (this is what differs in the series of glasses of this study), and with the geometry of the considered indenter. Then this model seems to be adaptable to the present study as it will be discussed in Chapter 5. Theoretically, the conditions of continuous stresses at the frontier between the elastic and the plastic zones lead to a unique solution for the value of B that is reported in Eq. 71 [27].

$$B = 0.006 p.a^3 \quad \textbf{Eq. 71}$$

2.2.3.3.6.3.2.3 Created plastic volume approach

Cook et al. [8] and Wagner [80] considered the increase of plastic volume as defined by Eq. 72 (with ν=0.25).

$$\Delta V = \frac{5}{6}\frac{\pi B}{E} \quad \textbf{Eq. 72}$$

This increase of plastic volume can be equal to the volume of the contact impression during the indentation that is given for a Vickers indenter with regard to the hardness H and the load P by Eq. 73.

$$\Delta V = 0.068 f \left(\frac{P}{H}\right)^{\frac{3}{2}} \quad \textbf{Eq. 73}$$

with f an arbitrary constant of densification equal to 0 in the case of a complete accommodation (purely idealized densifying material) and 1 in the case of no densification (deformation with volume conservation).
Combining Eq. 72 and Eq. 73 leads to Eq. 74.

$$B = 0.026 fE \left(\frac{P}{H}\right)^{\frac{3}{2}} \quad \textbf{Eq. 74}$$

Moreover, H can be determined with the help of Eq. 75 [80].

$$H = 1.8544\frac{P}{4a^2} \qquad \textbf{Eq. 75}$$

with $P=P_{max}$ and $a=a_{max}$. In this model, B varies in function of P during the indentation loading and H is considered constant.

2.2.3.3.6.3.2.4 Energy conservation approach

Bobji et al. [48] determined B by considering the energy conservation during indentation as defined in Eq. 76.

$$E_i = E_c + E_h \qquad \textbf{Eq. 76}$$

with E_i the input energy to the system, E_c the core energy (i.e. the energy dissipated in the plastic zone) and E_h the energy stocked in the elastic hinterland (i.e. the elastic zone).

- E_i is determined considering the work of the normal load at the estimated maximum depth through Eq. 77 with the stiffness of the material [81]

  $$k = \frac{P}{h^2} \qquad \textbf{Eq. 77}$$

  with a simple model of two springs in series representing the elastic and the plastic behaviors that leads to Eq. 78.

  $$k = \left(\frac{1}{\sqrt{k_{elastic}}} + \frac{1}{\sqrt{k_{plastic}}}\right)^{-2} \qquad \textbf{Eq. 78}$$

  $k_{plastic}$ is given by Loubet et al. [81] as:

  $$k_{plastic} = \pi H \tan^2 \alpha \qquad \textbf{Eq. 79}$$

  $k_{elastic}$ is given for a flat punch by Sneddon [82] as:

  $$k_{elastic} = \frac{16G^2}{\pi H (1-\nu)^2} \qquad \textbf{Eq. 80}$$

  This leads to the final expression of E_i reported in Eq. 81.

  $$E_i = \frac{a^3}{3}\left(\pi^2 H^2 \frac{(1-\nu)}{4G} + \frac{\pi H}{\tan \alpha}\right) \qquad \textbf{Eq. 81}$$

- E_c is determined with the help of Yoffe's calculations [27]. They lead to Eq. 82.

  $$E_c = f_1 (2 - \mathrm{cotan}\alpha)\frac{H^2 a^3}{G} \qquad \textbf{Eq. 82}$$

  with f_1 a constant given by Bobji et al. [48].
- E_h is directly determined by:

  $$E_h = \frac{1}{2}\int_s (u_r \sigma_{rr} + u_\theta \sigma_{r\theta}) ds \qquad \textbf{Eq. 83}$$

  With the help of the calculations of Yoffe [27], it leads to Eq. 84.

  $$E_h = f_2 \frac{Ha^3}{G} - f_3 \frac{HB}{G} - f_4 \frac{HB^2}{Ga^3} \qquad \textbf{Eq. 84}$$

where f_2, f_3, f_4 are constants given by Bobji et al. [48].
Then the Eq. 76 gives an equation with B as a variable that can be solved for a considered material.

2.2.3.3.6.4 The results of Yoffe's model

As reported in § 2.2.3.3.6.2, the global stress field of the Yoffe's model is obtained by superposing the two different *elastic* stress fields (see Eq. 85): the Boussinesq's one that represents the normal load point and the *Blister* one that represents the influence of the plastic zone on the elastic zone of the indented solid.

$$\sigma = \sigma^{n}_{Bous.} + \sigma^{r}_{Blister} \qquad \textbf{Eq. 85}$$

with the common notations defined previously.
The results are the predictions of the location of the initiation of cracks. Actually, the radial crack initiations is governed by the $\sigma_{\phi\phi}\left(\phi = \frac{\pi}{2}\right)$ component. The occurrence of the conical cracks is governed by the $\sigma_{rr}\left(\theta = \frac{\pi}{2}\right)$ component. The occurrence of the median cracks is governed by the $\sigma_{\theta\theta}\left(\theta = 0\right)$ component. Finally, The occurrence of the lateral cracks is governed by the $\sigma_{rr}\left(\theta = 0\right)$ component. The different occurrences will be analyzed further in the case of Ahn's model and the mechanical modeling developed in the present work.

2.2.3.3.6.5 Limitations of Yoffe's model

Yoffe's model is restricted by some limitations: i) the quantification is not reasonable compared to experimental data probably because of the strength B that is theoretically assessed in Yoffe's work, ii) adjustment of the different parameters, iii) the model was built for the conical indenter and iv) the other basic assumptions of the model (the shape of the plastic zone for instance).

2.2.3.4 Finite Elements approach

2.2.3.4.1 Introduction / field of study

The stress field models provide precious results (especially for the local stresses in the direct surrounding of the indentation) that are not assessable with the micro-mechanical models. Nevertheless, theoretical limitations are often brakes for the use and the development of analytical stress field models for obvious reasons. Since 20 years, the numerical capabilities of computers provide powerful tools to treat numerous kinds of problems. This method remains of course limited in time cost, convergence of solution and validation of the different models but allows researchers to treat problems with involved complicated geometries which are totally impossible to treat with the two other previously mentioned approaches. This method can also "help" another mechanical approach when numerical solutions are partially required to solve the whole problem as it will be demonstrated in this present work.
In this part devoted to a literature review of finite elements studies, the presentation of the work of different authors does not have the pretension to be exhaustive, but provide an explanation for the choice taken in the numerical approach of the problem: software, mesh, boundary conditions, constitutive laws, friction coefficient,... The choices were guided by the results of the different works quoted in this part, and the ones expected in our study.

2.2.3.4.2 The Finite Elements softwares

The modeling by Finite Elements first calls for a software that is adapted to the problem. The most widely used is surely the Abaqus software [83-86]. Note that Forge 3 was successfully used for the 3-D modeling of the scratch process by an axi-symmetric indenter on polymers [87]. The reasons of the use of this software in this special case are i) its technical availability for the author and, ii) its accessibility for specific conditions (automatic re-meshing of the deformable body, movable mesh block,…).

2.2.3.4.3 The mesh

2.2.3.4.3.1 Mesh of the indented body

The mesh of the indented body is surely the key of the indentation and scratching model. Actually, only an optimized mesh can lead to precise results without being too slow in calculations.

First, let's review the 2-D meshes that are used to model indentation in axi-symmetric conditions (conical indenters and flat punch). The choices about the elements type and the refinement of the mesh vary from one author to another.

Carlsson et al. [86] used the mesh (conical indentation) reported Fig. 44 (treatment of the Vickers and the Berkovich indenters by an equivalent cone), which is composed of 5094 nodes and 4798 4-noded elements with bilinear-approximation for the displacement and a constant value for the hydrostatic pressure in each element (advantage: improve the convergence in strain in the incompressible case).

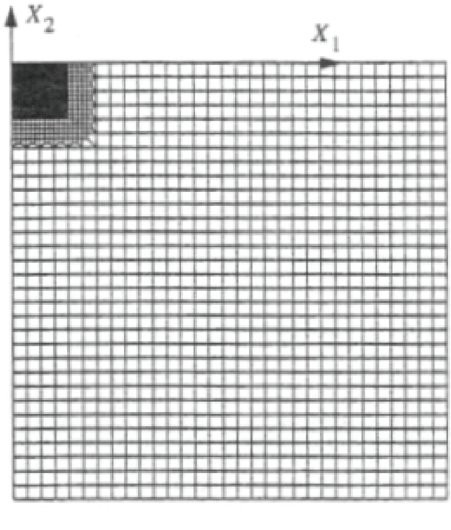

Fig. 44: Complete Finite Elements mesh used for the numerical calculations in the analysis of the cone indentation test by Carlsson et al.[86]. A prescribed indentation depth was applied in the negative X_2-direction.

The mesh used by Bucaille et al. [83] is composed of 1700 quadrilateral elements (4-noded). Close to the indenter, the elements are refined so that their size is 1.25x3 μm². The maximum depth of penetration of the indenter is 15 μm and at least 20 elements are in contact with the indenter (conical indentation model).

Finally (flat punch indentation model), Giannakopoulos et al. [85] proposed the mesh represented in Fig. 45 (before and after deformation). It is composed of 24 elements are allowed to come into contact with the indented body in order to obtain a good resolution in the calculations in the direct surrounding of the indenter. The indented body is modeled by a solid 50 times bigger than the contact size (noted *a*) to satisfy the boundary conditions of a semi-infinite body.

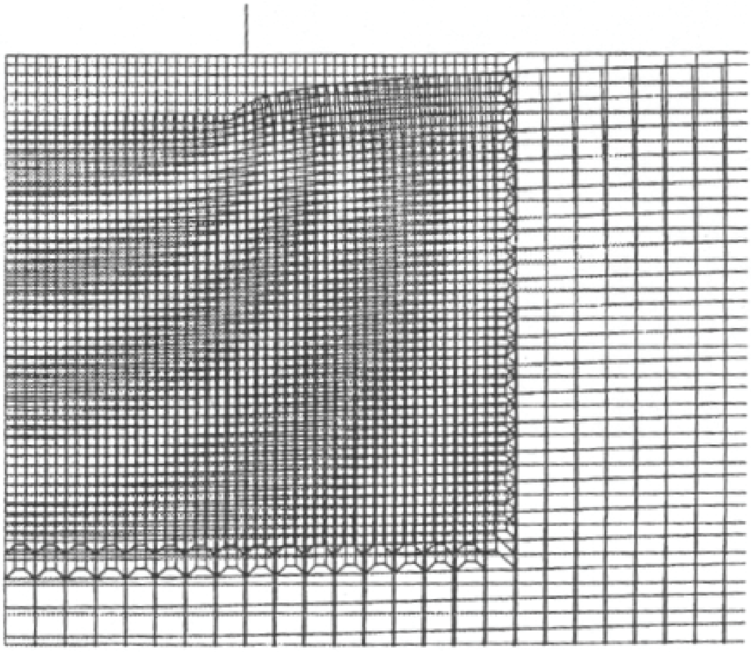

Fig. 45: The deformation under a flat circular punch. Homogeneous case, *k*=0, *ν*=0.25, w_0/a=0.005, with w_0 the penetration depth. Displacements are magnified. (from [85])

The 3-D meshes, mainly used to model indentation tests performed by a Vickers indenter, are of course far more imposing than the 2-D ones. Due to symmetry considerations of the Vickers indentation problem, only 1/8 of the indented body and indenter is generally meshed as justified by Giannakopoulos et al. [84]. Carlsson et al. [86] obtained a mesh with 14055 iso-parametric 8-noded elements and 16527 nodes. The displacements are interpolated by tri-linear functions and the hydrostatic pressure is kept constant in each element (like in the 2-D model presented previously from the same authors). A detail of this mesh is shown in Fig. 46. The complete mesh is shown in Fig. 47 reported by Giannakopoulos et al. [84] who used the same mesh.

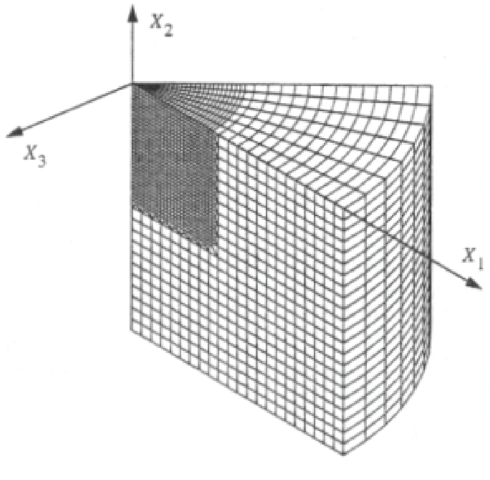

Fig. 46: Detail of the mesh close to the region used for the numerical calculations in the Vickers indentation test by Carlsson et al. [86]. A prescribed indentation depth was applied in the negative X_2-direction.

Other tests were performed by the same authors with meshes that include fewer elements in order to study the influence of this parameter on the result accuracy with respect to the mesh limits. Using the final mesh previously described is justified this way.

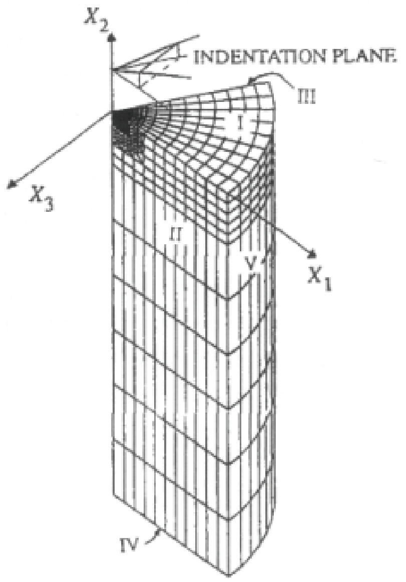

Fig. 47: General view of the F.E.M. Vickers mesh used in the numerical calculation by Giannakopoulos et al. [84] (14055 eight-noded elements).

Finally, Bucaille [87] modeled the scratch process with a conical indenter in 3 dimensions: the mesh represents 1/4 of the body only (35x220 mm² by 25 mm of depth to obtain a negligible edge effect – depth of penetration: 3 mm). Note that such a model requires an automatic remeshing procedure during the calculation. A special command of Forge 3 is used for this aim: a mesh box of the indented body “follows” the indenter all along the scratch. The obtained mesh is illustrated in Fig. 48 [87] with 13000 tetrahedral elements that are 4 noded.

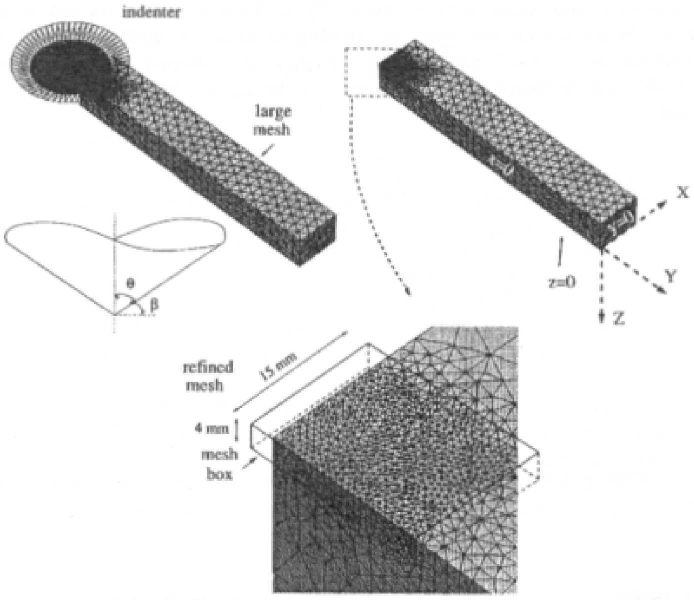

Fig. 48: Three dimensional view of the indenter and the meshed body for the scratch simulations by Bucaille [87].

2.2.3.4.3.2 The indenter

In almost all cases, the indenter is considered as infinitely rigid. Bucaille et al. [83] modeled this way the conical indenters of half apex angle of 42.3° (conical indenter equivalent to the cube-corner indenter), 50°, 60° et 70.3° (conical indenter equivalent to the Vickers and Berkovich indenters), while Giannakopoulos et al. [84] modeled only 1/8 of the Vickers indenter as illustrated in Fig. 49 (shaded region), because of the previously mentioned symmetry reasons.

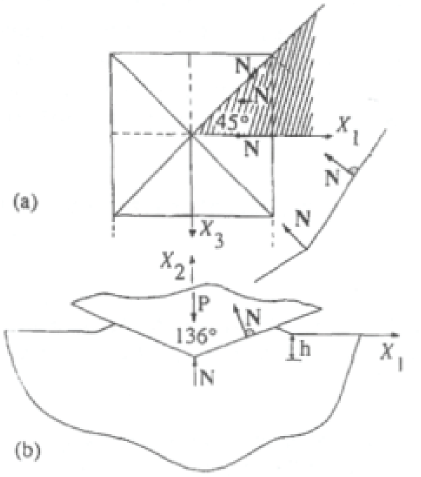

Fig. 49 [84]: Schematic view of the geometry of the Vickers indenter: (a) top view, (b) side view.

In this last case, the indenter geometry is considered perfect. Thus the edges are "sharp" as well as the tip; it is obvious that these parameters have no experimental reality. Nevertheless, the values of hardness are unchanged for penetration depth above 1/4 of the radius of the tip (numerical results).

2.2.3.4.4 Boundary conditions

This part summarizes the boundary conditions imposed to the different models by their authors.

Carlsson et al. [86] considered that the displacements are constrained to be equi-biaxial at the extreme boundaries of the body in order to simulate residual stresses. This is for example illustrated in Fig. 50 [86].

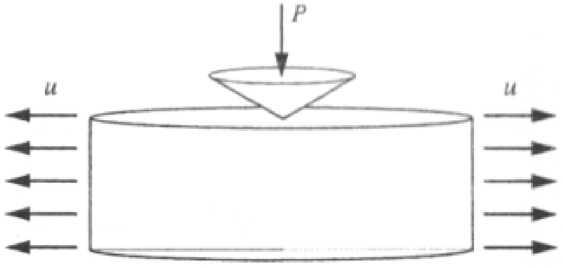

Fig. 50 [86]: Schematic of the loading. *u* is the prescribed radial displacement at the outer surface generating applied stresses and strains.

Due to the symmetry reasons that are previously reported, Giannakopoulos et al. [84] considered that i) the nodes of the faces II & III (see corresponding figure of the mesh from these authors in Fig. 47 in the § 2.2.3.4.3.1) can only move in these two planes, ii) the plane IV undergoes vertical displacement and iii) the plane I and the surface V are free of stress.

The boundary conditions are usually not more detailed in the literature, being almost trivial.

2.2.3.4.5 Constitutive laws

The constitutive laws are often different for the quoted authors. Indeed, the goal of their studies are usually rather different from one to the other (different materials, study of different test parameters and their influence on the model, presence of a residual stress field,...), that leads to the choice of special and different constitutive laws adapted to each case.

Thus, Carlsson et al. [86] modeled a perfectly elasto-plastic material, a hardening-plastic material and a non-regular hardening plastic material. In details, the constitutive laws, which are integrated in the simulations, are reported in Table 14 and Table 15, with regard to Eq. 86:

Mat no.	E	v	σ_Y	σ_0	m
1	200 GPa	0.3	200 MPa	Elastic-perfectly plastic material	
2	200 GPa	0.3	50 MPa	1000 MPa	3.3
3	70 GPa	0.28	*	*	
* Material 3: irregular behavior according to Table 15					

Table 14: Materials investigated by Carlsson et al. [86].

$$\sigma\left(\varepsilon_p\right)=\sigma_Y+\sigma_0\varepsilon_p^{\frac{1}{m}} \qquad \textbf{Eq. 86}$$

ε_p	$\sigma(\varepsilon_p)$ [MPa]
0.0	175
0.0025	197.5
0.005	210
0.0075	220
0.0175	240
0.0325	260
0.04	270
0.2	377
No hardening when ε_p>0.2	

Table 15: Details of coefficients used by Carlsson et al. [86] for constitutive laws represented by Eq. 86 for the considered glasses.

Giannakopoulos et al. [85] treated the problem of indentation with a *flat punch* in the perfectly elastic material case. But, the constitutive law has the particularity to exhibit a gradient of the elastic properties in the depth direction. Two different laws were studied: the power law $E=E_0z^k$ and the exponential law $E=E_0e^{\alpha z}$.

Giannakopoulos et al. [84] modeled precisely the indentation behavior through the indentation of materials that are sensitive to hydrostatic pressure. Thus, the chosen constitutive law in this case is:

$$\sigma=\sigma_Y+\beta H\varepsilon \qquad \textbf{Eq. 87}$$

with

$$\beta=\frac{2\frac{a_0}{3}+1}{\frac{a_0}{3}-1} \qquad \textbf{Eq. 88}$$

(properties of the studied material: E=205 GPa, v=0.3, σ_Y=350 MPa, H/E=1/40 and 1/3, a_0=-6/5, 0, 3/5, 6/5).

Lastly, Bucaille et al. [83] used an elasto-plastic constitutive law as:

$$\sigma=K\varepsilon^n \qquad \textbf{Eq. 89}$$

(the simulations had been performed with a large strain formulation).

2.2.3.4.6 Results

2.2.3.4.6.1 Preliminary remark

As for the constitutive laws, the aims of the different studies reported in the literature are often far from each other. Hence, the results are rather different, even if the technical basis of the different models is similar. This fact illustrates the reason for using such a numerical technique (i.e. the Finite Elements Method), allowing treating different problems and being effective in each case. The results reported in this part are multiple and more or less of interest in the context of the present study.

2.2.3.4.6.2 Friction coefficient

The influence of the friction coefficient is well known to be negligible on the results of Finite Elements calculations in standard cases (Carlsson et al. [86] found out maximum 10 % of deviation between the different results). Giannakopoulos et al. [84, 85] modeled the indentation test as frictionless.

However, Bucaille et al. [83] studied precisely the influence of the contact friction and of the indenter geometry on the indentation problem. These authors withdrew from the standard models in which the friction is neglected. The friction coefficient is modeled by a Coulomb's friction coefficient and this formula is proposed:

$$F = \pi p R_c^{\,2}\left(1 + \frac{\mu}{\tan\theta}\right) \qquad \textbf{Eq. 90}$$

with R_c the radius of contact and μ the true friction coefficient, θ the half apex angle and p the contact pressure assumed to be constant on the surface.

For μ>0 and θ high enough, $\frac{\mu}{\tan\theta}$ is negligible compared to 1. The results of the model are given in part § 2.2.3.4.6.

Bucaille [87] also took a standard Coulomb's friction coefficient to model the friction at the interface between the indenter and the body.

2.2.3.4.6.3 Other various results

Carlsson et al. [86] explored the hardness $H = \frac{P}{A}$ and the area ratio $c^2 = \frac{A}{A_{nom}}$

with $A_{nom} = \frac{\pi h^2}{(\tan\beta)^2}$ for a conical indenter (β being the angle between the surface and the edge) and $A_{nom} = \frac{4h^2}{(\tan\beta)^2}$ for a Vickers indenter; h is the depth (initial surface-depth under load).

The results show three important facts (see Graph 15 reported by Carlsson et al. [86]): H and c^2 rise as the material harden; this influence is not very important on H contrary to c^2; the Eq. 91 fits these results well.

$$H = C\sigma(\varepsilon_{representative} + \varepsilon_{residual}) \qquad \textbf{Eq. 91}$$

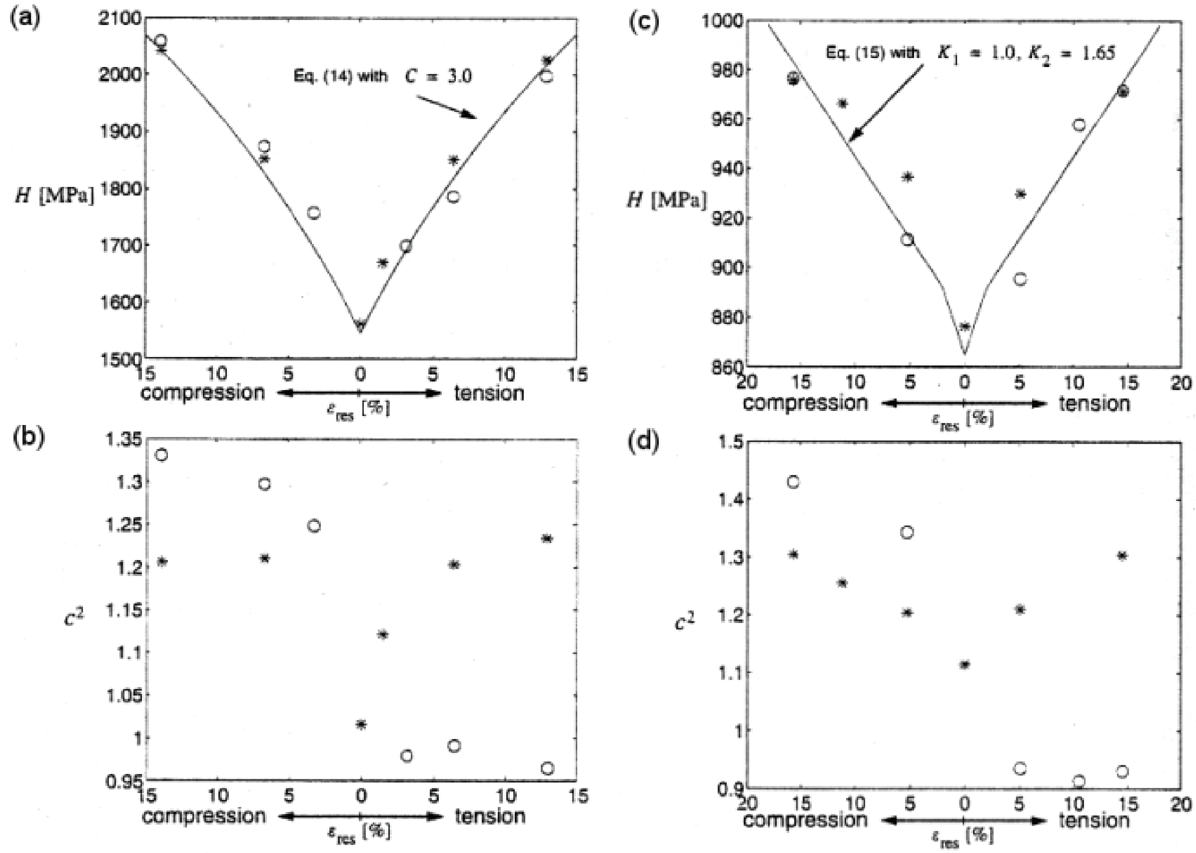

Graph 15 [86]: Influence of stress and strain on hardness and area ratio for a power-law hardening material no. 2 (resp. for an irregularly hardening material no. 3) in Table 14 – details (a) and (b) (resp. details (c) and (d) –. In all cases, the sign of stress and strain coincide. (a) (resp. (c)) Hardness *H*. (b) (resp. (d)) Area ratio c^2. (*) Cone indentation. No applied stress, (O) Cone indentation, the Von Mises effective stress due to applied stress equals $\sigma(\varepsilon_p=\varepsilon_{res})$.

Note that this study does not present any criterion of validation for the Finite Elements model: there are no test of convergence with the main parameters, no comparison with experimental values of *H*, no extraction of load-displacement curves *P-h*, no determination of long scale effect; these criteria are only reported from the existing literature [88].
The hardness *H* of the non-regular hardening material can be expressed by:

$$H = K_1\sigma_1 + K_2\sigma_h \qquad \text{Eq. 92}$$

with $\left.\begin{array}{l}\sigma_1 = \sigma(0.02)\\ \sigma_h = \sigma(0.35)\end{array}\right\}$ and K_1=1; K_2=1.55 for a conical indenter (β=22°) and K_1=K_2=1.4 for a Vickers indenter. These results are in good agreement with the Finite Elements results.

The influence of the Poisson's ratio was studied by Giannakopoulos et al. [85] and it was found out that the influence is small on the stress fields inside the indented body beneath the indenter because the singularity of the indenter dominates the solution. The results close to the contact singularity are obviously wrong but become consistent and close to the analytical values when moving of 1 or 2 element(s). The F.E.M. was only used here to confirm the analytical development proposed by their authors.
The F.E. method enabled to study the real projected area of contact as illustrated in Fig. 51 reported by Giannakopoulos et al. [84].

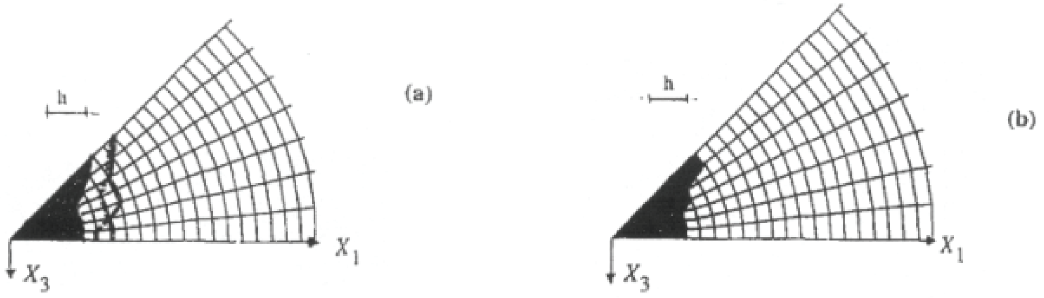

Fig. 51 [84]: Projected true contact area, *A*. The common indentation depth is also shown. (Eq. 87 et Eq. 88) (a) a_0=0, H/E=1/3, Vickers; identical to a_0=-6/5, H/E=1/3 (the contact areas for *H/E*=0 and 1/40 are also shown with continuous and dashed lines, respectively). (b) a_0=3/5, *H/E*=1/3, Vickers.

The same authors also extracted the load-displacement curves from the simulations. The comparison with hard metals or glasses on which experimental tests were performed show a good correlation for the first modeled material. But, the results show a relatively bad agreement with the second material because of the constitutive law that does not take into account the cracking phenomena that occur in glass.

Finally, Bucaille [83] reported results about the extraction of stress-strain curves by reverse analysis. The original data for the reverse analysis are instrumented indentation tests performed (numerically) on elasto-plastic materials. Interesting results are the influence of the friction coefficient on the simulations. The contact friction can be neglected when using a conical indenter with half apex angle higher than 60° (then the friction effect on the Vickers or Berkovich indentation seems to be negligible). On the other hand, the influence of the friction coefficient cannot be neglected for indenters with half apex angle less than 60° as illustrated on Graph 16 [83]. For the equivalent cone of the cube corner indenter (θ=42.3°) and μ=0.15 (typical for a metal-diamond contact), F increases by 16 %. The friction is not negligible in this case and has to be taken into account in such simulations.

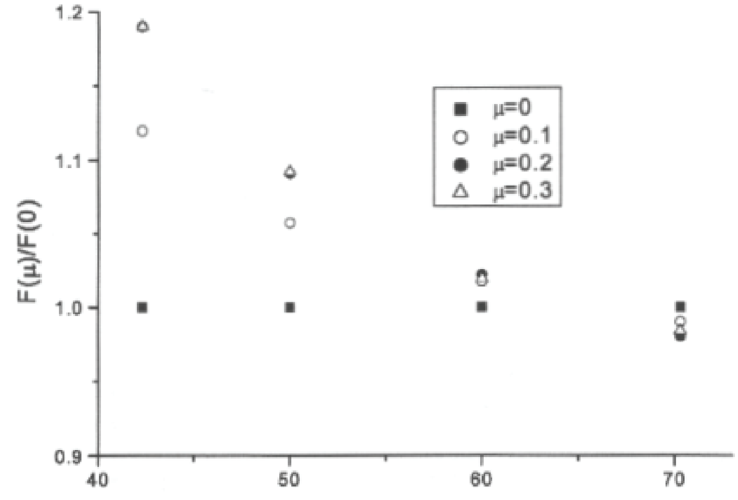

Graph 16 [83]: Influence of the friction coefficient on the normal force in indentation as a function of the included angle, *θ*. Results obtained in simulations on an aluminum alloy. For $\theta \leq 60°$, an increase in μ increases the normal load.

The complete depth of penetration h_c is also influenced by the friction coefficient. The more the friction coefficient is, the more h_c decreases. Graph 17 shows the profiles obtained for half apex angles of θ=70.3 and 42.3°:

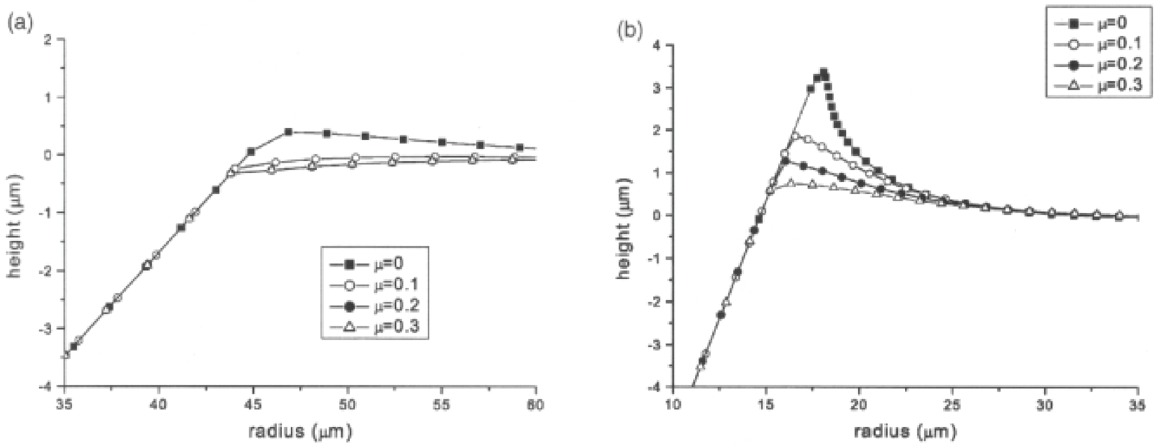

Graph 17 [83]: Indentation profiles for four values of the friction coefficient for an aluminum alloy for (a) θ=70.3° and (b) θ=42.3° conical indenters (half apex angle): the height of the pile-up is larger for a frictionless contact.

2.2.4 Cracking models

The materials, which are studied in this work, exhibit complex deformations as reported earlier. In addition to the plastic deformation composed of the combination of densification phenomenon and plastic flow deformation, performing indentation or scratch tests induces damage in the form of cracks. Several models attempt to treat directly the phenomena of initiation or/and propagation of the cracks. Thus, Lawn et al. [14] proposed for instance a model based on stress intensity factors to predict the propagation of median/radial cracks. The principle is based on the assumption that the studied materials are elasto-plastic. Then, to superpose two different stress fields, the first elastic and the second plastic, is fully justified. The elastic stress field is a Boussinesq point-loading stress field. The plastic stress field is based on the solution of the cavity problem of Hill. For each stress field, one expression of the intensity factor is given: K_e and K_r depending on experimental coefficients that are independent of the indenter/material couple.

The toughness is equal to the sum of the two stress intensity factors as reported in Eq. 93.

$$K_e + K_r = K_c \qquad \textbf{Eq. 93}$$

The Eq. 94 is derived and represents the equilibrium equation of the propagation of median cracks during the loading cycle.

$$X_e \frac{P}{c^{\frac{3}{2}}} + X_r \frac{P}{c^{\frac{3}{2}}} = K_c \qquad \textbf{Eq. 94}$$

with P the normal load, X_e and X_r the elastic and the residual stress factors respectively, c the crack mean length and K_c the material toughness. Following the same procedure, similar equations are obtained for the unloading cycle.

Similar models were developed for the sub-surface lateral crack system [15]. Equivalent considerations were also developed to model not only the propagation but also the initiation of cracks (see [16] among others).

2.3 Mechanical models in scratching

2.3.1 Principle and development

The extension of Yoffe's model [27] (adapted to a conical indentation) to a quasi-static scratch model (i.e. with a negligible scratch speed) following the coordinate system depicted in Fig. 52 [20, 71, 72] was developed.

Let's remind that the principle of Yoffe's model is to superpose two different *elastic* stress fields to model the stress field due to the normal loading indenter and the presence of the plastic zone in the indented solid.

Two fundamental points have to be taken into account to adapt Yoffe's model to scratching:

- the elastic stresses due to friction during the motion,
- the effect of the loading history due to the accumulation of plastic deformation behind the indenter.

This model has been developed by Ahn [20, 71, 72].

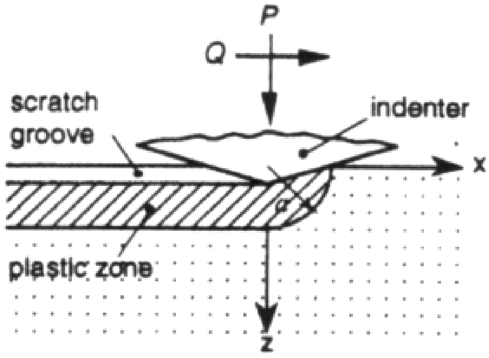

Fig. 52 [20, 71, 72]: Schematic side view of the sliding indentation showing the applied loads, the coordinate system and the plastic zone boundary.

In order to take into account the elastic stresses due to friction during the indenter motion, Ahn introduced the Boussinesq's stress field corresponding to an applied tangential force concentrated on the surface at the indenter position. Thus, this stress field concentrated in the origin of the coordinate system is given by Eq. 95 to Eq. 100 [20, 71].

$$\sigma_x^t = -\frac{Q}{2\pi}\left[\frac{3x^3}{\rho^5} - (1-2\nu)\left\{\frac{x}{\rho^3} - \frac{3x}{\rho(\rho+z)^2} + \frac{x^3}{\rho^3(\rho+z)^2} + \frac{2x^3}{\rho^2(\rho+z)^3}\right\}\right] \quad \textbf{Eq. 95}$$

$$\sigma_y^t = -\frac{Q}{2\pi}\left[\frac{3xy^2}{\rho^5} - (1-2\nu)\left\{\frac{x}{\rho^3} - \frac{x}{\rho(\rho+z)^2} + \frac{xy^2}{\rho^3(\rho+z)^2} + \frac{2xy^2}{\rho^2(\rho+z)^3}\right\}\right] \quad \textbf{Eq. 96}$$

$$\sigma_z^t = -\frac{Q}{2\pi}\frac{3xz^2}{\rho^5} \quad \textbf{Eq. 97}$$

$$\tau_{yz}^t = -\frac{Q}{2\pi}\frac{3xyz}{\rho^5} \quad \textbf{Eq. 98}$$

$$\tau_{yz}^t = -\frac{Q}{2\pi}\frac{3x^2z}{\rho^5} \quad \textbf{Eq. 99}$$

$$\tau_{xy}^t = -\frac{Q}{2\pi}\left[\frac{3xy^2}{\rho^5} + (1-2\nu)\left\{\frac{y}{\rho(\rho+z)^2} - \frac{x^2y}{\rho^3(\rho+z)^2} - \frac{2x^2y}{\rho^2(\rho+z)^3}\right\}\right] \quad \textbf{Eq. 100}$$

with Q the concentrated tangential load (see Fig. 52).

The required sliding *Blister* stress field models the local residual stress field accumulated in the elastic zone behind the indenter all along the scratch and has to be taken into account. Normal and tangential Boussinesq stress fields are not concerned by accumulation as they pass with the moving indenter. Then the accumulation of the residual stresses is done by integrating the *Blister* field all along the scratch. The detailed procedure and the complete expression of the stress fields will be integrally given in § 5.2 for the required new calculation of Ahn's model. The global expression of the stress field is given in Eq. 101.

$$\sigma = \sigma^{n}_{Bous.} + \sigma^{t}_{Bous.} + \sigma^{r}_{Blister} \qquad \textbf{Eq. 101}$$

The superscript n denotes the stress field due to the normal load; the superscript t denotes the stress field due to the tangential load; the superscript r denotes the residual stress field.

2.3.2 Determination of the strength *B* of the sliding *Blister* field: Experimental considerations approach

The residual stress field given in Eq. 101 represents the sliding *Blister* field characterized by a strength B. Ahn et al. [20, 71, 72] determined B adapted to the scratching case by experimental considerations considering the increase of plastic volume given by Eq. 102.

$$\Delta V = \frac{2}{3}\frac{\pi A\left(1-2\nu\right)}{G} \qquad \textbf{Eq. 102}$$

Two experimental parameters are introduced: the upward plastic flow factor defined in Eq. 102 with the help of Fig. 53 [20] and the compaction ratio $\delta V_c/V$ given by Chen et al. [89].

$$F_p = \frac{Area\,OAD - \left(Area\,ABC + Area\,DEF\right)}{Area\,OBE} \qquad \textbf{Eq. 103}$$

The final expression of B with regard to the upward flow factor, the compaction ratio and the contact radius a is given by Eq. 104.

$$B = \frac{3}{2}\frac{Ga^2\left(\frac{1}{\tan\theta} - \frac{1}{2}\frac{\pi\Delta V_c}{V}\right)F_p}{\pi\left(1-2\nu\right)} \qquad \textbf{Eq. 104}$$

Finally, the contact radius a is found by profilometry measurements and leads to Eq. 105.

$$a = 0.679P^{0.57} \qquad \textbf{Eq. 105}$$

Then, B is given in function of P in Graph 18 [20].

Finally, note that this procedure to assess B was designed only for the sliding case. That means that the obtained value of B is the strength of the sliding *Blister* field that will be defined later in § 2.3.1. However, this procedure can be used directly to assess the value B of the "static" *Blister* field with almost no need for adaptation to the static problem. This will be discussed in Chapter 5.

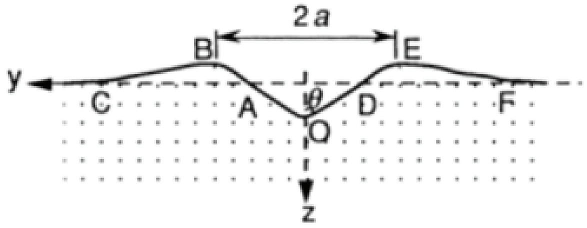

Fig. 53 [20]: Schematic of the profile of a typical scratch track made with a sliding Vickers indenter in soda-lime glass (load 5-50 gm). The ratio of vertical magnification to horizontal is 5:1.

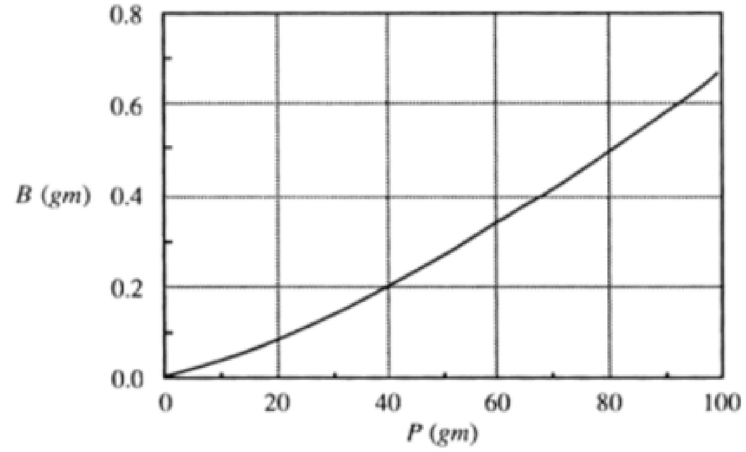

Graph 18 [20]: The variation of the sliding indentation Blister field constant *B* with indentation *P* for the soda-lime silica glass.

2.3.3 Results of Ahn's model [20]

The magnitudes of the different stresses previously found are now compared to predict which crack patterns are most likely to occur at a given load.

The $\sigma_z^r(x,0,a)$ component governs (see Fig. 52) the initiation of lateral cracks and is plotted in Graph 19. This residual stress is tensile below the scratch with its maximum value just behind the indenter. Thus, lateral cracking is supposed to occur at this location.

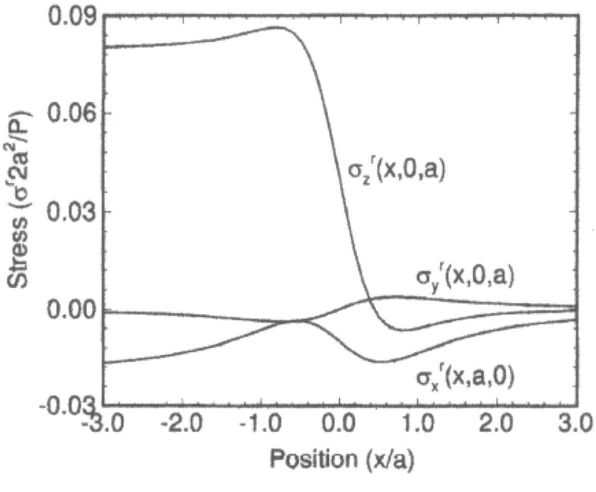

Graph 19 [20]: Residual stress distribution at the edge of the inelastic zone (B/P=0.005).

The $\sigma_y(x,0,a)$ component governs the initiation of median cracks and is plotted in Graph 20. This stress is maximal in tension right below the indenter. Thus, median cracking is supposed to occur at this location.

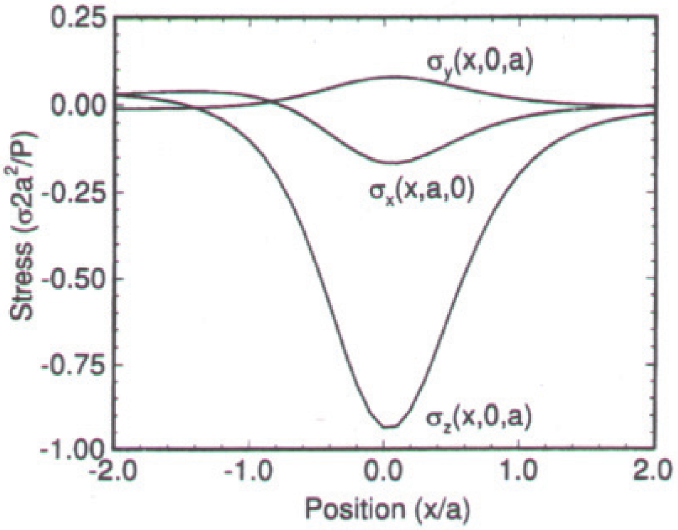

Graph 20 [20]: Complete normal stress distribution at the edge of the *inelastic* zone (B/P=0.0025).

The $\sigma_x\left(x,a,0\right)$ component governs the initiation of radial cracks and is plotted in Graph 20. This stress is maximal in tension for *x*~-1.3*a* below the indenter. Thus, radial cracking is supposed to likely occur at this location.

CHAPTER 3:
MATERIALS & EXPERIMENTAL TECHNIQUES

SUMMARY OF CHAPTER 3

3.1 Materials

The glass compositions were defined in such a way that with regard to their indentation behavior, the studied glasses cover the range from typical normal glasses to near anomalous glasses [9]. According to Peter [1], oxide glasses become normal when the modifier content exceeds 15-20 mol. %.

A commercially available soda-lime silica glass[3] was studied. 40x15x4 mm^3 specimens were cut using diamond-type cutting tools from a pane annealed at 560 °C (i.e. at T_g + 15 °C) in air during 1 hour and cooled at 2 °C.min^{-1}. In addition, different glasses were synthesized by S. Dériano (see [10, 11] for further details) in the Na_2O-CaO-SiO_2 phase diagram given in Graph 21 [90]. These glasses are referred as SLS (1 to 4), and were obtained by substituting SiO_2 for (Na_2O+CaO) while keeping Na_2O/CaO ratio constant and equal to 1.52. A fused silica glass was also studied. The glass compositions are given in the Table 16.

[mol. %]	Planilux	SLS 1 (①)	SLS 2 (②)	SLS 3 (③)	SLS 4 (④)	Fused Silica
SiO_2	70,8	71,0	74,0	77,0	80,00	100,00
Na_2O	12,8	17,5	15,7	13,9	12,10	-
MgO	5,9	-	-	-	-	-
CaO	10,2	11,5	10,3	9,1	7,90	-
AL_2O_3	0,4	-	-	-	-	-

Table 16: Chemical composition of the studied glasses.

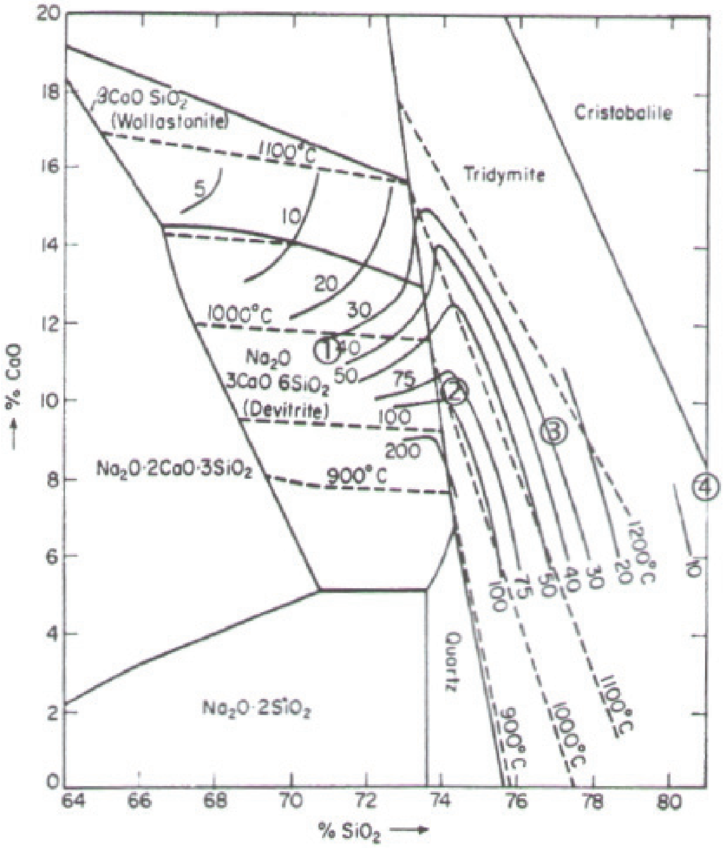

Graph 21 [90]: Na_2O-CaO-SiO_2 phase diagram in mol. %, with the four SLS glasses synthesized for this study.

---

[3] Planilux™, Saint-Gobain

Glasses through the SLS series were synthesized starting from pure and dried SiO_2, $CaCO_3$, $NaHCO_3$ powders. Small quantities (in a total proportion of less than 0.5 mol. %) of fluxing agents, such as ZnO, $BaCO_3$, $SrCO_3$ and As_2O_3 were added to ensure a good homogeneity of the glasses. Batches were then melted at 1600 °C in a platinum (Pt/Rh 10 %) crucible in air during few hours and stirred with a platinum stirrer for one hour to refine the melt. Approximately 200 g of glass melt were finally poured into a carbon mould, preheated at 550 °C, and slowly cooled to room temperature by cutting off the furnace. After determination of their T_g (located between 558 and 561 °C) by calorimetric measurement (DSC), glasses were annealed for half an hour at T_g and slowly cooled at a rate equal to 1 $°C.min^{-1}$ (see [10] for further details).

Note that the same samples were used for all measurements. Glasses from the SLS series were cut and their surfaces were polished carefully up to 1 µm grid. Glass specimens were kept in a dried atmosphere to avoid moisture pollution before testing.

3.2 Mechanical characteristics and Measurement devices

3.2.1 Instrumented indentation

It is today common to instrument a classical hardness tester [91]. A conventional hardness test consists in a classical indentation test, i.e. it consists in loading a hard penetrator called indenter with a normal load *P* on the surface of a sample. It results in a penetration of the indenter into the material by a depth noted *h* as illustrated in Fig. 54 [92].

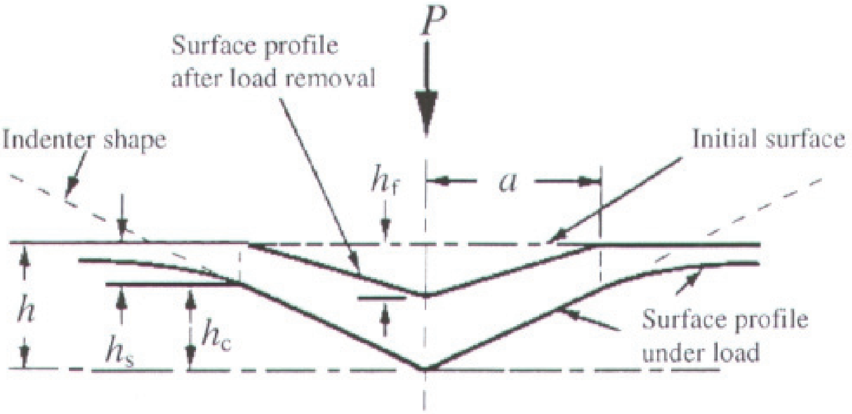

Fig. 54 [92]: Schematic representation of a section through an indentation using a conical indenter.

During an *instrumented* indentation, experiment consisting usually in a single loading-unloading cycle, the load *P* and the penetration depth *h* are recorded as a function of time. The different characteristics measured during an instrumented indentation experiment are reported in Fig. 54: h_f is the *final depth* of indentation after unloading (i.e. after elastic recovery of the matter); h_c is the *contact depth*, *a* is named the *contact radius* and represents a characteristic length of the post-experimental indentation imprint (equal to the contact radius for spherical or conical indenters and usually half the diagonal of the indenter edge for Vickers).

The different indenters used for indentation are schematically illustrated in Fig. 55 and some geometric details are reported in Table 17 [50, 93]. Among all the existing type of indenters, mostly pyramid indenters are used, but spheres of various diameter and conical indenters are also sometimes specifically used. Berkovich indenters depicted in Fig. 55 (b) (three-sided pyramidal diamond) are preferred for very low-load indentation, i.e. nano-indentation (to assess properties of thin coatings for instance) because they can have a tip radius in the order of 50-100 nm due to fabrication considerations. Thus, the four-sided pyramidal Vickers indenters drawn in Fig. 55 (a), difficult to obtain with such small tip radius, are usually used for higher load indentation, i.e. micro-indentation, and for conventional measurements.

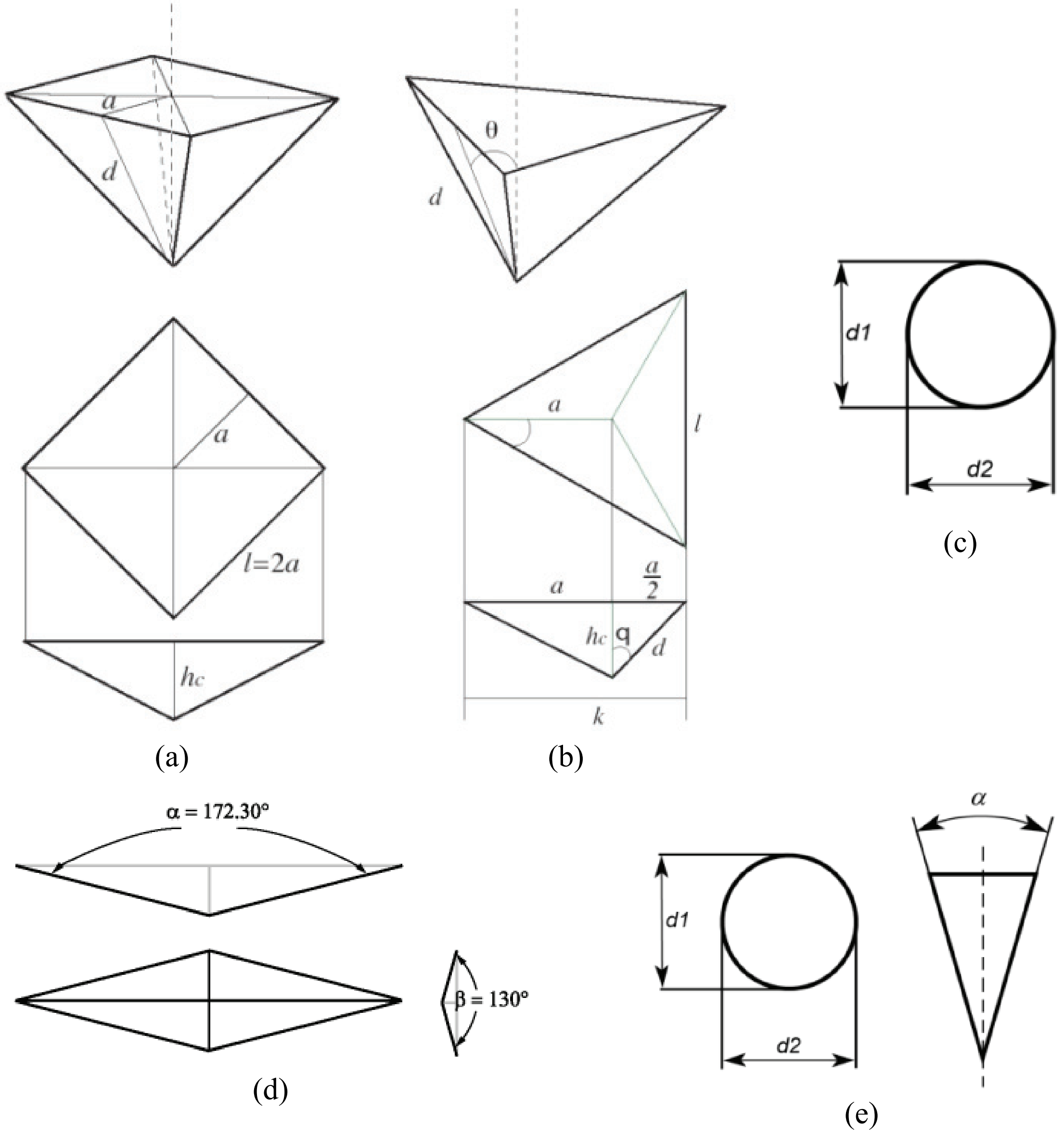

(a) (b) (c) (d) (e)

Fig. 55: Indenter geometries – (a) Vickers indenter; (b) Berkovich or cube corner indenter; (c) Brinell indenter (sphere); (d) Knoop indenter; (e) conical indenter. Characteristic dimensions are not respected.

Angle from axis to	Vickers	Berkovich	Cube corner	Knoop
edge	74	77	54.7	86.2/75
face	68	65.3	35.3	-

Table 17: Summary of angle data for the four most commonly used indenter geometries.

Graph 22 (inspired from Malzbender et al. [92]) reports a typical load-displacement (*P*-*h*) curve of an instrumented indentation experiment on an elasto-plastic material (the same curve is followed for loading and unloading sequence in the purely elastic case).

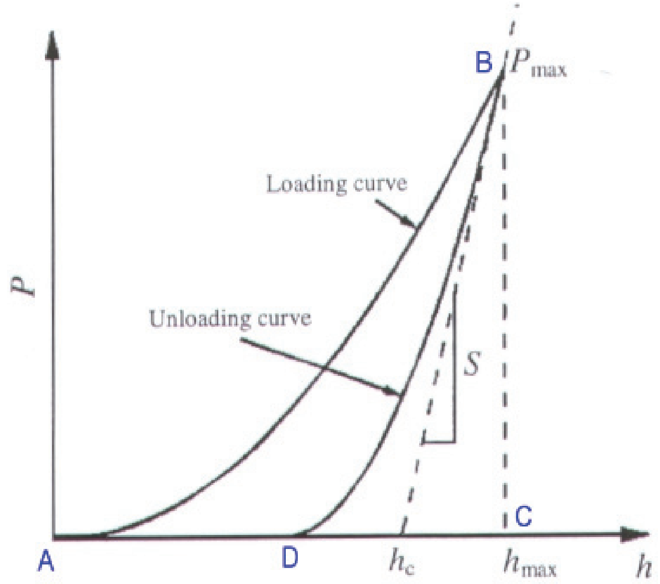

Graph 22: Schematic representation of a typical indentation load-displacement curve.

Finally, the *P-h* curves can be investigated in the energy approach [81, 94]. Actually, the surface defined by ABCA on Graph 22 represents the necessary work for the creation of the indentation, W_T. The BCDB surface corresponds to the work released by the specimen, W_E. Lastly, ABDA corresponds to the retained work, W_R. Thus it comes:

$$W_T = W_E + W_R \quad \textbf{Eq. 106}$$

3.2.2 Scratch test

3.2.2.1 Introduction

The scratch test could be summarized as dragging a hard point (indenter) on the sample surface. The first scratch test in order to assess material properties is historically the procedure to get the Mohs's hardness for mineralogists (1824): it consists in scratching or abrading a material with a harder one [66, 95]. Thus, this test appeared chronologically before the indentation test. Then, the scratch test has been naturally used for metals, in order to investigate the resistance of metals to scratch process and to study the scratch test as well in a more simplified case than with minerals. The first theories and models about friction, sliding hardness or wear were built on the basis of dead-load experiments or single scratch pendulum tests. One can note the work of Challen et al. [96, 97] who showed interesting results on the occurrence of sliding, wave pushing or chip removal depending on the friction coefficient and the penetrator angle. These three deformation modes are reported bellow in Fig. 56 [96].

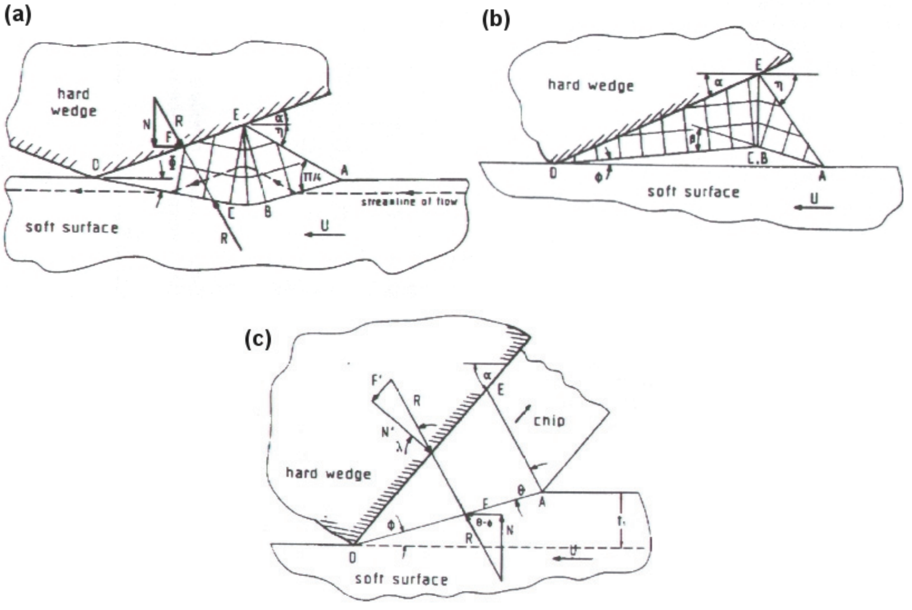

Fig. 56 [96]: Two-dimensional deformation models of scratching by a hard wedge. (a) the *rubbing* model, (b) the *wear* model and (c) the *restricted contact cutting* model.

As reported earlier, the scratch test is nowadays used to study the resistance of brittle materials, glasses and many kinds of coatings. It is used either for qualitative scratch resistance or for material properties assessment and this test is more than ever of great research interest.

3.2.2.2 General principle

During a scratch test, a well-defined tip is drawn over the surface of a sample while applying a particular normal load *P*. This normal load may be constant during the experiment as it may be stepwise or even it may monotonically increase (resp. decrease) from an initial value (resp. maximum load) to a maximum load (resp. a lower value) at the end of the scratch. As for instrumented indentation treated in § 3.2.1, various different indenters may be used for scratch experiments as illustrated in Fig. 55.

The complicated loading stress field induced by scratch test generates material response in various forms depending on the material nature: plastic deformation, densification, re-crystallization, cracking,…

Indentation technique is usually preferred to the scratch experiment to assess most of the material mechanical properties. In fact, properties such as the elastic modulus, the hardness and the fracture toughness can only be relatively coarsely estimated from scratch experiments due to over simplifications [92]. However, characteristics provided by the scratching technique about scratch resistance of bulk or coated materials greatly fill the gap of contact mechanics right between quasi-static damage (indentation,…) and tribology science (grinding,...).

3.2.2.3 Parameters assessment

Aside some of the mechanical properties quoted in the previous paragraph that will not be treated in this document, some convenient results are usually collected, measured or calculated from scratch experiments and are shortly presented in this part.

Scratch testers are usually instrumented with a 2-axis load cell that enables to measure the normal load F_n and the tangential load F_t simultaneously. Then, the apparent friction coefficient is simply given by:

$$\mu = \frac{F_t}{F_n} \qquad \textbf{Eq. 107}$$

It is sometimes convenient to introduce the apparent friction coefficient as the superposition of adhesion and ploughing contributions [95]. Thus it gives:

$$\mu = \mu_a + \mu_p \qquad \textbf{Eq. 108}$$

where μ_a is the adhesion component of the friction and μ_p is the ploughing component of the friction. One can also see Lafaye et al. [98] for further development to assess the local friction coefficient.

Hardness expressions specific to scratch experiments but related to indentation values are derived as reported in Eq. 109 and Eq. 110 [95].

$$H_s = \frac{F_n}{A_{LB}} \qquad \textbf{Eq. 109}$$

where A_{LB} is the projected load bearing area and F_n the normal load.

$$H_P = \frac{F_t}{A_P} \qquad \textbf{Eq. 110}$$

where A_p is the projected contact area seen in the direction normal to the relative motion of the indenter and F_t the tangential load.

H_s and H_p are named *scratch hardness* and *ploughing hardness* respectively. Both lead to consistent values with the indentation hardness of the considered materials [95, 99, 100].

3.2.2.4 The scratch tester

An apparatus, named *scratch tester* also known as *linear sclerometer*, allowing for a variable loading cycle during a single experiment was designed for the present work. This device was placed into a glove box in order to achieve a good moisture control in the range 0 % - 100 % r.h., so as to study the effect of the environment (see Fig. 57).

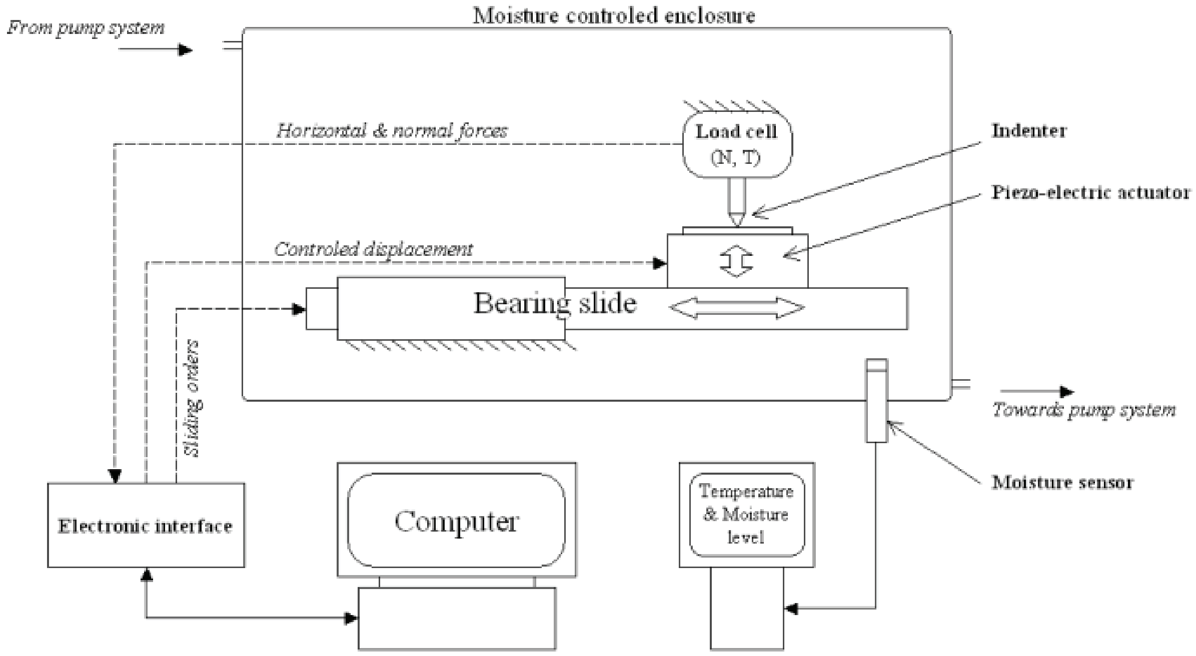

Fig. 57: Principle diagram of the experimental setup designed for variable loading scratch test in a moisture and temperature controlled atmosphere.

The horizontal displacement of the indenter (to produce a groove) is obtained through a bearing slide, while the vertical movement is controlled by a piezo-electric actuator. Both the penetration and the forces are continuously monitored. The main characteristics of the apparatus are a maximal normal load of less than 5 N with an accuracy of 0.02 N, a vertical penetration displacement limited to 100 μm, and a scratch displacement accuracy better than 1 μm and a maximum speed of 5 mm/s. The displacement of the bearing slide is computer controlled, and both displacements (horizontal and vertical) and environmental parameters are continuously monitored with the help of a computer and Labview programs. The different loading programs that were designed for the purpose of this study are: i) a constant loading scratch, ii) a uniform slope of loading scratch and iii) a uniform slope of loading-unloading scratch.

The solution adopted for the study of the influence of the environment was a classical "glove box" with a pumping system that allows to precisely control the humidity level (% r.h.) inside the enclosure (< 3 % of deviation in r.h. during a whole test). The rubber gloves enable the manipulation of the samples inside the box and to set-up the different parameters before each test that are not computer controlled.

Several details about *conception, building, instrumentation and testing* of the scratch tester are given in Appendix 1.

3.2.3 Material properties measurements devices

3.2.3.1 Density

The density of the samples is usually found by determining the mass of a determined volume of the samples. The various types of materials with different structure required different methods of density measurement. The density is typically measured using buoyancy and liquid or gas pycnometry techniques.

Pycnometer is used worldwide to obtain material density measurements. This method provides a more rapid and more accurate measurement of the true density than the Archimedean technique. The resolution of the method is 0.0001 g/cc. Helium, under precisely-known pressure, is used to fill small voids within a specimen. The volume change of helium in a constant volume chamber allows determination of the solid volume. The ratio of sample mass to its true volume for materials without closed porosity gives the true density. For materials with closed porosity, this result is the apparent density.

3.2.3.2 Elastic parameters - ultrasonic device

At room temperature the vast majority of brittle materials are linearly elastic up to their fracture stress. Basic elastic material properties such as Young's modulus E and Poisson's ratio ν (as well as derived parameters: shear modulus G and bulk modulus K), which are of interest in many manufacturing and research applications, can be determined quickly and easily through computations based on sound velocities. The sound velocity can be easily measured using ultrasonic pulse-echo techniques where an ultrasound transducer generates an ultrasonic pulse and receives its "echo". The ultrasonic transducer operates as both transmitter and receiver in one unit. Two transducers: a longitudinal wave transducer and a normal incidence shear wave transducer are required for pulse-echo sound velocity measurement in longitudinal and shear modes. The test samples may be of any geometry that permits clean pulse-echo measurement of sound transit time through a section of known thickness. Ideally this would be a slug or bar at least 12.5 mm thick with smooth parallel surfaces. The diameter on cross-section must exceed about five longitudinal wavelengths. The elastic modulus is determined from the acoustic velocities of the longitudinal and transverse elastic waves and from the density because the deformation in the acoustic case is believed to be purely elastic.

The elastic moduli E and G are deduced from the measured velocities V_L and V_T of the propagation of the longitudinal and transversal waves respectively, with help of the Eq. 111 and Eq. 112:

$$E = d\frac{3V_L^{\ 2} - 4V_T^{\ 2}}{\left(\frac{V_L}{V_T}\right)^2 - 1}$$ **Eq. 111**

and

$$G = dV_T^{\ 2}$$ **Eq. 112**

with d the density of the material. The accuracy is usually accepted to be ±1 %, even if in most cases, it is limited by the density measure. It is then of the order of the GPa.
The Poisson's ratio is derived through:

$$\nu = \frac{E}{2G} - 1$$ **Eq. 113**

The accuracy on the Poisson's ratio is about ± 0.01.

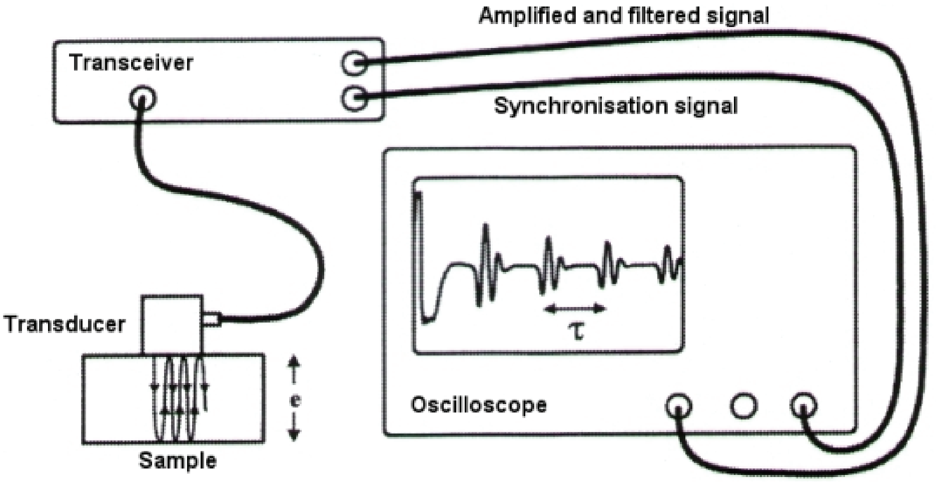

Fig. 58: Ultrasonic method by reflection with a contact transducer

3.3 Imaging Tools

3.3.1 Optical microscope

3.3.1.1 Classical optical microscope

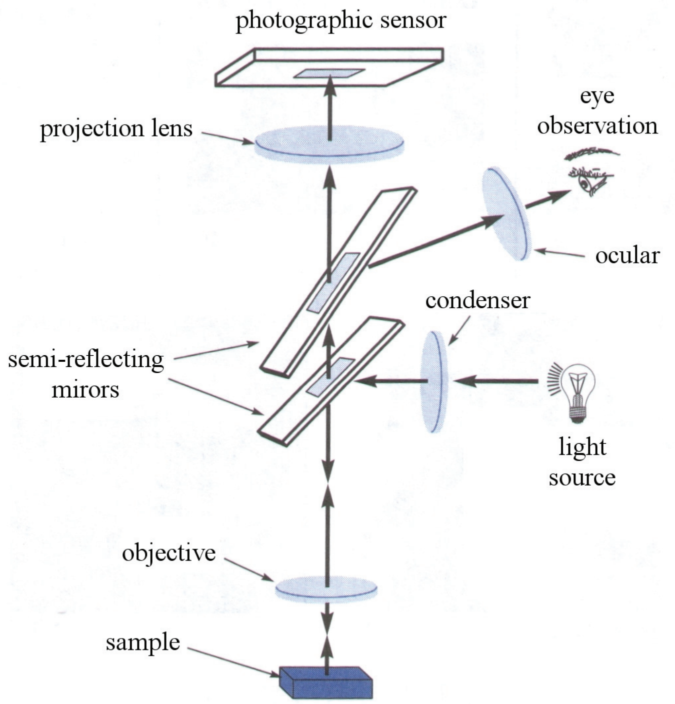

Fig. 59: Schematic principle of a classical optical microscope. (from [101])

The optical microscope is used to create an enlarged view of an object typically in the magnification range of 5x to 1 000x. The resolution depends on the physical properties of lens and on the wavelength of light that is passed through the lens. The physical properties are summed up in a value known as the *numerical aperture* while the wavelength is determined by the light color.

Increasing the visibility of objects under the microscope has followed various routes. Several of these techniques make use of the fact that light is deflected, reflected, or diffracted at boundaries between two materials with different refractive indices. These techniques are named: Absorption, Refraction, Fluorescence, Reflection and Diffraction.

There are three modes by which optical microscopy is commonly conducted, namely, brightfield illumination, darkfield illumination, and interference contrast (Nomarski).

Brightfield illumination is the normal mode of viewing with an optical microscope. This mode provides the most uniform illumination of the sample. Under this mode, a full cone of light is focused by the objective on the sample. The observed image results from the various levels of reflectivities exhibited by the compositional and topographical differences on the surface of the sample.

Under *darkfield illumination*, the inner circle area of the light cone is blocked, such that the sample is only illuminated by light that impinges on its surface at a glancing angle. This scattered reflected light usually comes from feature edges, particulates, and other irregularities on the sample surface. Structure in the object appears bright on a dark background.). Either incident or transmitted light may be used. Darkfield illumination is therefore effective in detecting surface scratches and contamination.

The *interference contrast* (Nomarski) makes use of polarized light that is divided by a Wollaston prism into two orthogonal light rays. These slightly displaced light rays hit the specimen at two different points and return to the prism through different paths. The differences in the routes of the reflected rays will produce interference contrasts in the image when the rays are recombined by the prism upon their return. Surface defects or features such as etch pits and cracks that are difficult to see under brightfield illumination can stand out clearly under the Nomarski mode.

3.3.1.2 Long-distance microscope

Even if the principle is rather simple, Long Distance Microscope is a non-conventional microscope. The aim of this device is to make images of objects in enclosures, in hostile environments, in process and on-line. Microscopic resolution could be achieved from a longer distance without cluttering the work area with instrumentation.

It has a working range of about 50 cm to 150 cm, a 30 to 1 variability in view field, and a noteworthy depth of field, a linearity and chromatic correction. It is also equipped of a CCD video camera and a complete video acquisition computer and software. Two Barlow lenses are also available to magnify the observation: 1.5x and 2x (can be mounted simultaneously).

The optical resolution is 2.7 µm at 55.9 cm of working distance. The field of view (2/3" format) is 0.9 mm to 15 mm. Finally, the microscope can be set on axial position (horizontal) or 90 degree position (vertical).

Then, thanks to this device (Questar QM100 – see Fig. 60), images and videos of indentations and scratches can be taken in-situ due to the long working range of the microscope. This is of prior interest in this study for understanding damage processes.

Fig. 60: Views of the long-distance microscope Questar QM100.

3.3.2 Confocal microscope

Confocal microscope is a very powerful tool for the investigation of crack morphologies in transparent or translucent materials. In this case, the technique allows observing three-dimensional subsurface features and provides depth information without the need for mechanical sectioning of the samples. The arrangement of lenses and apertures in the confocal microscope allows light originating from only one focal plane within a samples to be detected, resulting in an image that is bright for those parts of the samples that are in focus, and dark for other part of the sample that are out of the focal plane.

A laser is usually used to provide intense illumination, and, because only one point at a time is illuminated, a scanning system must be used. Light from that point (which may be fluorescent) is focused on a point detector (such as a pinhole in front of a photomultiplier) and is illustrated in Fig. 61.

Layers of the object away from the point being viewed are not illuminated as brightly because the illuminating light is not on focus there, so the light coming from those layers is not focused on the detector pinhole. As a result, thin layers of relatively thick objects can be examined. This is obtained by an arrangement of diaphragms which, at optically conjugated points of the path of rays, acts as a point light source and as a point detector respectively. Rays from out-of-focus are suppressed by the detection pinhole as illustrated in Fig. 62 that depicts the principle of a confocal microscope. The depth of the focal plane is, besides the wavelength of light, determined in particular by the numerical aperture of the objective used and the diameter of the diaphragm. At a wider detection pinhole the confocal effect can be reduced. To obtain a full image, the image point is moved across the specimen by mirror scanners. The emitted/reflected light passing through the detector pinhole is transformed into electrical signals by a photomultiplier and displayed on a computer monitor.

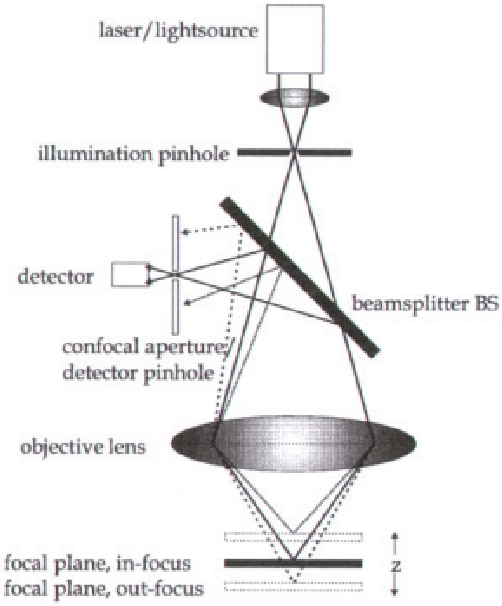

Fig. 61: Schematic principle of in plane focus with a laser or lightsource. (from [102])

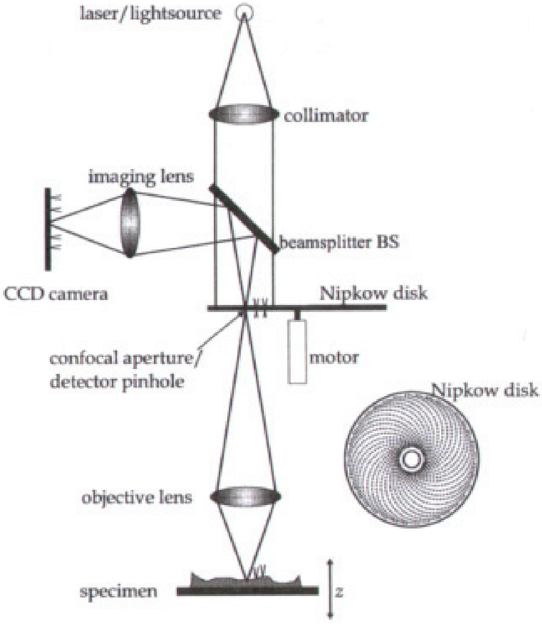

Fig. 62: Schematic principle of a confocal microscope. (from [102])

The confocal microscope used in the present study is a Leica ICM 1000.

3.3.3 Scanning Electron Microscope (S.E.M.)

SEM produces images by detecting secondary electrons which are emitted from the surface due to excitation by the primary electron beam and its principle is depicted in Fig. 63.

In a typical SEM configuration, electrons are thermally emitted from a cathode. The electron beam, which typically has an energy ranging from a few keV to 50 keV, is focused by two successive condenser lenses into a beam having a very fine spot size (~ 5 nm). Then, the beam passes through the objective lens, where pairs of scanning coils deflect the beam either linearly or in a raster fashion over a rectangular area of the sample surface. As the primary electrons strike the surface, they interact with the surface atoms which lead to the subsequent emission of electrons and x-rays, which are then detected by a scintillator-photomultiplier device to produce an image.

Because the secondary electrons come from the near surface region, the brightness of the signal depends on the surface area that is exposed to the primary beam. This surface area is relatively small for a flat surface, but increases for steep surfaces. Thus steep surfaces and edges (cliffs) tend to be brighter than flat surfaces resulting in images with good three-dimensional contrast. Using this technique, resolutions of the order of 5 nm are possible.

In addition to the secondary electrons, backscattered electrons (essentially elastically scattered primary electrons) can also be detected. Backscattered electrons may be used to detect both topological and compositional details, although due to their much higher energy (approximately the same as the primary beam). These electrons may be scattered from fairly deep within the sample. This results in a smaller topological contrast than in the case of secondary electrons. However, the probability of backscattering is a weak function of the atomic number, thus some contrast between areas of different chemical compositions can be observed especially when the average atomic number of the different regions is quite different.

The spatial resolution of the SEM depends on the size of the electron spot which in turn depends on the magnetic electron-optical system which produces the scanning beam. The resolution is also limited by the size of the interaction volume, or the extent of material which interacts with the electron beam. The magnification for a common SEM can be up to x50 000.

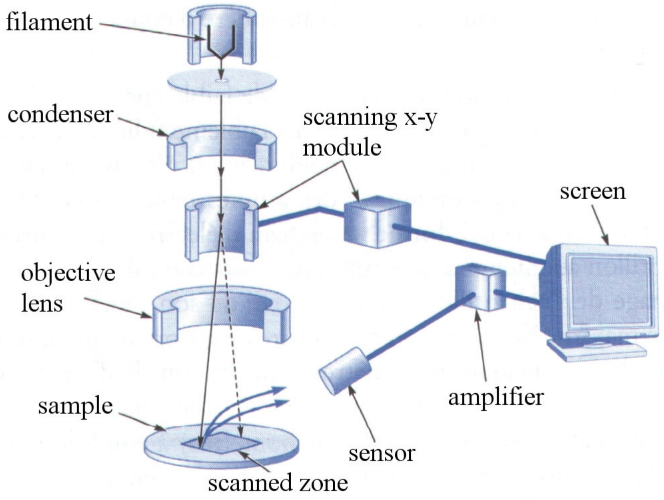

Fig. 63: Schematic principle of a SEM. (from [101])

The SEM used in the present study is a Zeiss DSM 962.

3.3.4 Atomic Force Microscope (A.F.M.)

The atomic force microscope measures a local property (such as the height, the optical absorption, or the magnetism) with a probe or "tip" placed very close to the sample. To acquire an image the microscope raster-scans the probe over the sample while measuring the local derived property. The resulting image is monitored on a screen. AFMs can achieve a resolution of 10 pm, and unlike electron microscopes, can image samples in air and samples immerged in liquids.

AFM operates by measuring attractive or repulsive forces between a tip and a sample as given on Graph 23. To do so, it uses a sharp probe moving over the sample surface in a raster scan. The probe (see Fig. 64) is a tip at the end of a cantilever which bends in response to the force between the tip and the sample. The AFM measures the vertical cantilever deflection by reflecting a laser beam off the cantilever. The angular deflection of the cantilever causes a twofold larger angular deflection of the laser beam. The reflected laser beam strikes a position-sensitive photodetector consisting of four side-by-side photodiodes as illustrated in the *principle of AFM* representation in Fig. 65. The difference between the photodiode signals indicates the position of the laser spot on the detector and thus the angular deflection of the cantilever.

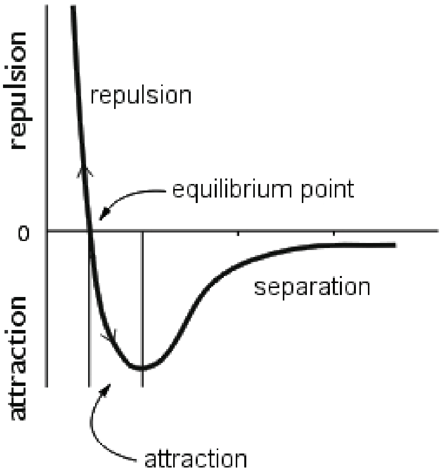

Graph 23: Inter-molecular force curve.

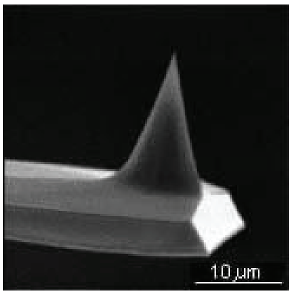

Fig. 64: The tip at the end of the cantilever that composed the AFM's probe.

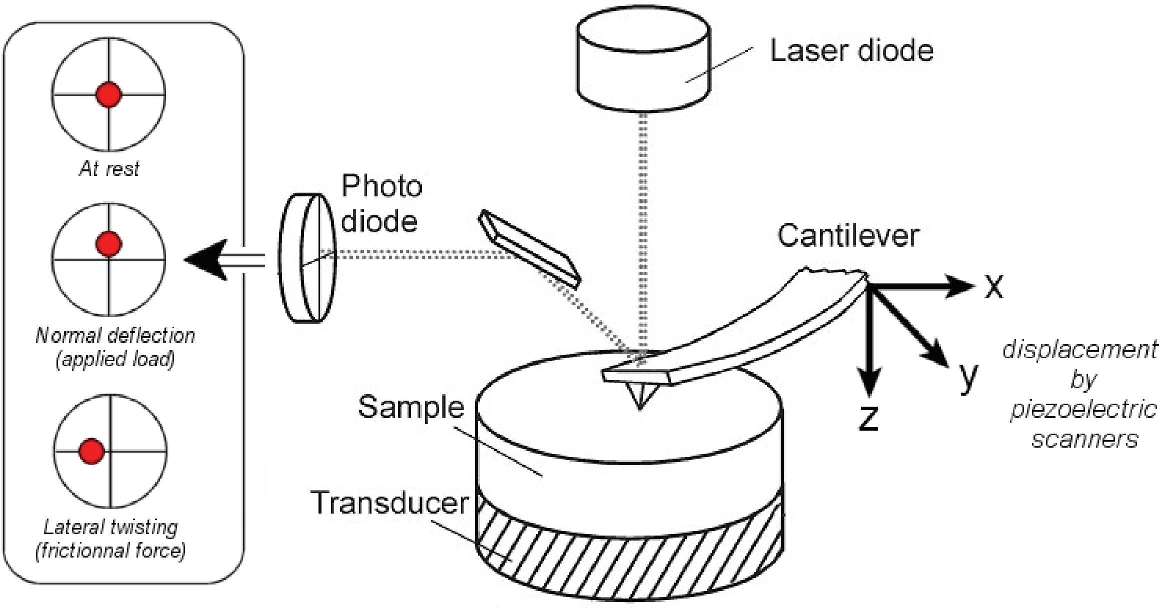

Fig. 65: Schematic principle of an A.F.M.

The three main classes of interaction used in AFM imaging are the *contact mode*, the *tapping mode* and the *non-contact mode*:

- *Contact mode*: the tip and the sample remain in close contact as the scanning proceeds. By "contact" it is meant the repulsive regime of the inter-molecular force curve (see Graph 23). The vertical deflection of the cantilever indicates the local sample height. Thus, in contact mode the AFM measures hard sphere repulsion forces between the tip and the sample.
- *Tapping mode*: when operated in air or other gases, the cantilever is oscillated at its resonant frequency using a piezo-electric crystal (often hundreds of kilohertz) and positioned above the surface so that it only lightly touches or taps the surface. During scanning, the vertically oscillating tip alternately contacts the surface and lifts off, generally at a frequency of 50 000 to 500 000 cycles per second. As the oscillating cantilever begins to intermittently contact the surface, the cantilever oscillation is necessarily reduced due to energy loss caused by the tip contacting the surface. The reduction in oscillation amplitude is used to identify and measure surface features. When imaging poorly immobilized or soft samples, tapping mode may be a far better choice than contact mode for imaging. In this mode, the AFM derives topographic images from measurements of attractive forces because the tip does not really touch the sample. This method was developed as a method to achieve high resolution without inducing destructive frictional forces both in air and fluid.
- *Non-contact*: the cantilever must be oscillating above the sample surface at such a distance that the force is no longer in the repulsive regime of the inter-molecular force curve (see Graph 23). This is a very difficult mode to operate in ambient conditions with an AFM because of the thin layer of water contamination which exists on the sample surface that causes the tip to "jump-to-contact". Even under liquids and in vacuum, jump-to-contact is difficult to avoid.

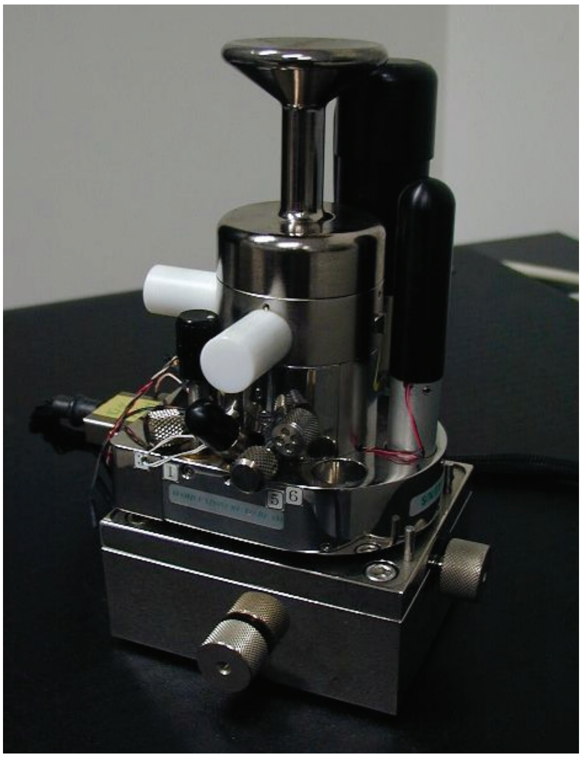

Fig. 66: The Topometrix Explorer A.F.M. used in the present study.

The A.F.M. used in the present study is a Topometrix Explorer depicted in Fig. 66.

3.3.5 White-light optical profilometer

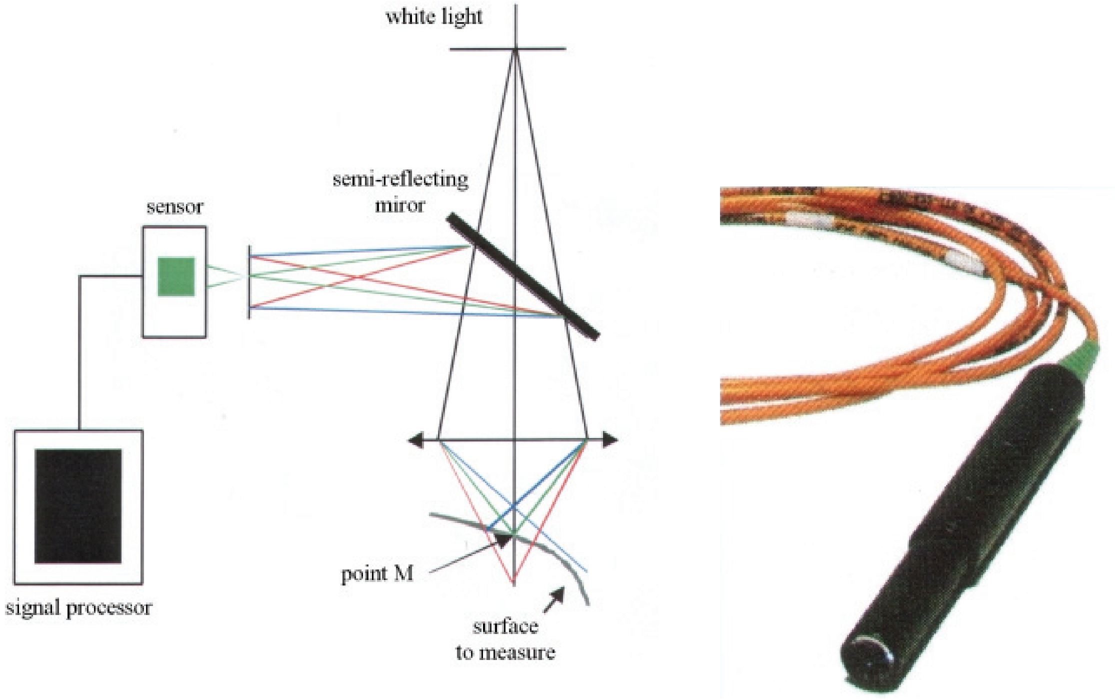

(a) (b)

Fig. 67: Principle of a white-light optical profilometer: (a) principle scheme; (b) view of the optical probe.

A lens that exhibits an axial chromatism plays the role of a prism that separates the wavelengths of a halogen whitelight in an axial direction. Each wavelength is one point of measure. The result is a spot of separated wavelengths (diameter 1 µm) that scan the sample surface. The perfect focus of a wavelength is converted through a CCD spectrometer and analyzed by the signal processor. Then, it gives the altitude corresponding to the detected wavelength for the measured point reported as M in the Fig. 67 (a).

The scan movements are produced by two bearing slides, X axis for the scanning drive and Y axis for the line-return of scan with 0.5 µm and 1 µm of resolution respectively. The maximum speed of scan is 10 500 µm/s. The Z axis is moved by a third bearing slide.

The optical probe (see Fig. 67 (b)) has a depth of measure of 300 µm with 10 nm of resolution. The working distance is 4.5 mm. The maximum acquisition speed of the probe is 1 000 Hz.

The optical profilometer used in the present study is a Cotec Altisurf 500.

3.3.6 Image analysis

Image analysis is required in this study in part § 5.7.4. The measurements performed with the A.F.M. on indentation imprints are quantitatively analyzed with regard to the volume of upward flow and the real imprints volume. Three methods are available to treat the volume of peaks and/or holes from the 3-D reconstruction data with the Mountain Altimap Universal software. Because it is difficult to discriminate the most adapted method to our case, the three methods will be used.

The first step is to delimit a hole (respectively a bump) using the mouse, to calculate its volume. After, the detail of these methods is:

- Method (a): the volume is calculated column by column as illustrated on Fig. 68 (a): for each *Cx* column of the surface, one takes the 2 points situated under the drawn contour (the edge of the hole). One traces a line segment *Sx* between these 2 points. The basic void volume for this column is the one between the segment and the bottom of the hole. When the surface is higher than the segment, the basic volume is measured between the segment and the top of the bump. This corresponds to the basic material volume. The total volume of the hole (resp. of the bump) is the sum of the basic void volumes for each column. The drawback is the sensibility to the roughness altering the hole edge.
- Method (b): similar to the previous but this method calculates per lines *Ly* as shown in Fig. 68 (b). The choice between these methods (a) and (b) depends on the shape orientation of the feature to be measured.
- Method (c) (see Fig. 68 (c)): the volume calculated is included between the bottom of the hole (resp. the top of the bump) and the *P* plane, where the *P* plane is the least squares plane calculated on all the points outside of the contour drawn. This method is applied when the outside area is sufficiently flat to be considered as the top of the hole by extrapolation (resp. the base of the bump).

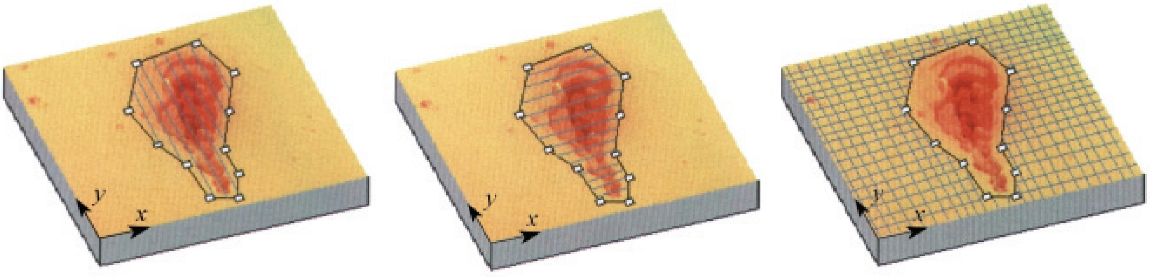

(a) (b) (c)

Fig. 68: Illustration of the methods (a), (b) and (c) of volume measurements.

3.4 Tests

3.4.1 Studied parameters

It was decided to study the influence of a wide range of parameters on the scratching behavior. They are summarized in the following list. Note that some are preliminary parameters which were studied and others were discovered to be interesting parameters during this study:

- Influence of the normal load
- Influence of the loading history (dynamical effect)
- Influence of the nature of the glass side (only for the float glass)
- Influence of the residual stresses
- Influence of the indenter geometry
- Influence of the glass chemical composition

3.4.2 Performed tests

The glass density ρ was measured on powdered samples by the pycnometry method. Young's modulus E and Poisson's ratio ν were measured by the pulse-echo technique on 4 mm thick rectangular specimen. Vickers indentations were performed with a load of 9.8 N applied during 15 s to assess both Meyer's hardness H and indentation fracture toughness K_c by means of the following equations:

$$H = \frac{P}{2a^2} \quad \textbf{Eq. 114}$$

and

$$K_c = 0.016\sqrt{\frac{E}{H}}\frac{P}{c^{3/2}} \quad \textbf{Eq. 115}$$

where P is the load, a is half the mean size of the two diagonals of the residual imprint, E is the Young's modulus, and c is half the mean length of the two radial cracks (tip to tip).

The scratch resistance (tangential load) was followed through constant normal load and low rate loading-unloading experiments (from 0 N to the maximum load and reverse to 0 N at a sliding velocity (slow regime) of 0.01 mm/s) on the 6 studied glasses. Such experiments allow first to study a wide load range within a single experiment and second, to reveal any possible dynamical effect, by studying the symmetry of the scratch pattern. Then, a commercial float glass and an annealed one (both sides), the 4 SLS grades, and a fused silica glass were scratched with a Vickers penetrator following the described loading-unloading cycle.

In order to characterize the influence of humidity on the glasses scratch resistance, experiments were conducted under humidity levels of 0 %, 30 %, 65 % and 100 % of humidity. The particular value of 100 % of humidity was obtained by placing boiling water inside the enclosure.

In order to study the influence of the indenter geometry, tests were performed on the annealed commercial float glass following the described loading-unloading cycle with three different indenters: i) a Vickers indenter, ii) a conical indenter with an apex angle of 136° and iii) a conical indenter with an apex angle of 90°.

The Vickers penetrator (inverse pyramidal, 136° face to face angle) was always used with a leading edge orientation.

If not especially mentioned, the tests were performed in a relative humidity of about 65 % r.h. (ambient humidity).

Other complementary scratching indentation experiments were occasionally performed.

3.4.3 Caution on the samples

The samples and the indenters were cleaned with ethanol before each test. At least, three different grooves were made on each glass to ensure a good reproducibility of the results.

Scratch patterns were observed by means of an optical microscope under Nomarski contrast conditions. The observations were systematically made 2 min after the mechanical testing, so that the possible incidence of stress-corrosion phenomenon is about the same for all the specimens. AFM measurements were performed (tapping mode) on the scratched samples that were stored in dry atmosphere immediately after testing. At last, the samples were observed by SEM after being coated with a thin layer of gold-palladium estimated to 12 nm of thickness.

CHAPTER 4:
EXPERIMENTAL RESULTS

SUMMARY OF CHAPTER 4

4.1 Static behavior

The physical and mechanical properties measured on glasses are summarized in Table 18.

Properties / Glasses	T_g (°C) ±2	ρ (g/cm^3) ±0.01	E (GPa) ±0.5	ν ±0.01	H (GPa) ±0.01	K_c (MPa.m$^{1/2}$) ±0.02
Float glass	560	2.55	71.5	0.21	6.12	0.72
SLS 1	558	2.53	70.4	0.20	5.35	0.71
SLS 2	559	2.50	69.9	0.19	5.11	0.70
SLS 3	560	2.47	69.2	0.18	5.15	0.76
SLS 4	561	2.43	68.7	0.17	5.19	0.82
Fused silica	700-1200	2.20	73.0	0.16	8.03	1.47 – 0.77*

Table 18: Composition and physical properties of glasses. * denotes a S.E.N.B. measurement of the toughness [12].

Some properties such as ρ, E and ν showed a monotonic trend with increasing SiO_2 content, while H and K_c exhibit minima for the SLS 2 composition (i.e. for glass containing 74 mol. % of silica).

The density decreases with rising silica content as Si^{4+} former ions replace modifiers (Na^+ and Ca^{2+}). In fact, the silica network has an open structure with a lot of vacancies, and is therefore able to accommodate interstitial cations in a large proportion. The present results are consistent with those of Doweidar [31] who showed that linear relations can be found in simple silicate systems. Young's modulus decreases slightly when the amount of modifiers decreases. Two opposite effects seem to be in competition: the increase of the bond strength ($E_{Si\text{-}O} >> E_{Ca\text{-}O} > E_{Na\text{-}O}$ [103]) and the decrease of the bond density when less and less modifiers fill the voids of the high silica content vitreous network. This latter effect leads to a more flexible network and predominates over the first effect, which is a short range one. Indeed, the less the amount of network modifying cations is, the more the network stiffness is controlled by the variations of the Si–O–Si inter-tetrahedral angles and by the mutual orientation of the SiO_4 tetrahedra, whereas the other structural parameters do not appreciably change [4]. This effect also governs the Poisson’s ratio.

More interesting are the changes of H and K_c that are plotted in Graph 24 for the four SLS glasses. In fact, these two properties present a non-monotonic trend as silica content rises and show a minimum for the SLS 2 glass. Silica has a small Poisson’s ratio equal to 0.16, reflecting a great tendency for an elastic (or reversible) volume change under stress. Yamane et al. [13] proposed a relationship between Poisson’s ratio and a parameter reflecting the glass network compacity where ν is proportional to c ($\nu \sim 1.1c - 0.3$). A detailed theoretical and experimental investigation of the hardness H and the elastic properties of glasses [13] confirmed this tendency and further showed that the higher the glass compacity, the higher the hardness and the elastic moduli. The present results about the fused silica glass have to be excluded. These previous investigations together with the present results strongly suggest that a low Poisson’s ratio also favors densification (with an irreversible volume decrease as a consequence). The maximum values obtained for the SLS 1 glass can be explained by an optimum filling of the three-dimensional network. In fact, interstitial cations, such as Na^+ and Ca^{2+}, enter into the empty sites until the network structure becomes saturated and so lead to a monotonic increase of E, ν and ρ in this range. It is anticipated however that when all these latter sites are filled, the silica network becomes disrupted and begins to weaken.

Noteworthy, hardness and indentation fracture toughness exhibit non-monotonic changes with the minima for the SLS 2 composition. In order to explain these experimental observations, the lecture of the phase diagram of the ternary SiO_2-Na_2O-CaO system is helpful [90]. In fact, one can see from Graph 21 (p. 91) that the SLS 2 grade has an intermediate composition between two different primary phase fields, namely the tridymite (SiO_2) phase field, containing SLS 3 and SLS 4 glasses, and the devitrite (Na_2O-3CaO-$6SiO_2$) phase field containing the SLS 1 composition. The hardness accounts for the resistance of a glass to a permanent deformation process. Babcock has shown that a linear relation can be drawn inside each primary phase field for Knoop's hardness values as a function of glass composition [104]. In accordance with this work, it suggests that the non-monotonic trend of the measured properties relates to a transition between both phase fields: two interpenetrated different networks may induce these particular properties as suggested by Babcock [104].

The indentation–derived fracture toughness K_c increases with the silica content for $SiO_2 \geq 74$ mol. % (see Graph 24). Again the shift toward a more and more anomalous indentation behavior has to be evoked. Indeed the energy dissipation due to the flow-densification process beneath the indenter results in a less important micro-cracking, and in shorter radial-median cracks. The progressive shift toward Hertzian cone cracks (which are typically observed in the vitreous silica) also contributes to the shortening of the radial-median cracks. However, one must keep in mind that a quantitative comparison of K_c between glasses with significantly different silica contents calls for caution, since the experimental method is based on a pure normal behavior. Here, the apparent fracture toughness has the meaning of the glasses resistance against crack propagation when subjected to a sharp surface contact. It is now well established that radial and lateral crack systems initiate and grow as the indenter is removed from the glass surface. The deformation mechanism has therefore a strong influence on the crack propagation via the residual driving forces. Let's recall that densification is an irreversible process, which spends energy by rearrangement of the tetrahedral network, while volume-conservative deformation takes place by a shear displacement of the matter under the contact zone, and involves a localized shear flow process along modifying cation rich channels. The previous results suggest that these two different processes may be combined together in the considered glasses. Nevertheless, our results confirm that high silica content glasses mainly deform through densification and hence possess higher indentation toughness than typical soda-lime silicate glasses with high amount of modifiers. What seems clear though is that a high silica content in the starting powder mixture favors flow-densification and enhances the fracture toughness, as was previously noticed by Seghal et al. [17] (Note that a fracture toughness of 0.77 MPa $m^{1/2}$ was obtained on pure vitreous silica by means of a single edge notch beam method [12]).

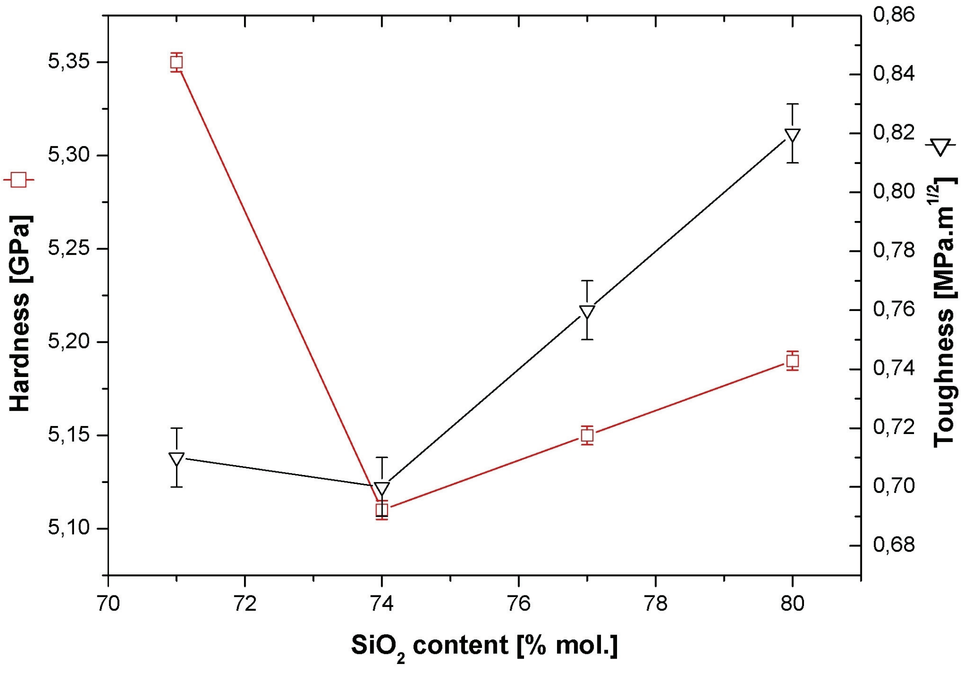

Graph 24: Hardness *H* and fracture toughness K_c for the SLS glass series.

In the aim to correlate indentation behaviors, indexes or parameters combining both flow and fracture properties are useful. Among them, the brittleness parameter *B* introduced by Lawn et al. [105] and given by Eq. 116 accounts for two competitive processes: plastic deformation and crack propagation. The higher the value for *B* is, the more “brittle” the glass is considered.

$$B = \frac{H}{K_c} \qquad \textbf{Eq. 116}$$

where K_c is the fracture toughness and *H* is Meyer’s hardness.

B values allow for a comparison of the brittleness of glasses belonging to the same family (example: SLS glasses). However, to interpret the indentation and scratch behavior, the appearance or the disappearance of the different crack systems is of paramount importance. In first attempt to characterize the sensitivity of glasses to micro-cracking, indentation experiments were made at 0.1, 0.25, 0.50, 1, 2 and 3 N. The critical load P_C^R and P_C^L for crack initiation were measured for radial and lateral cracks respectively (see Table 19). The experimental values were compared with the theoretical ones proposed by Lawn et al. [14] or Hagan [16] for radial critical load P_C^{R*} which is expressed as:

$$P_C^{R*} = \alpha \frac{{K_C}^4}{H^3} \qquad \textbf{Eq. 117}$$

and for the lateral critical load P_C^{L*} given by Marshall et al. [15]:

$$P_C^{L*} = \beta E \frac{{K_C}^4}{H^4} \qquad \textbf{Eq. 118}$$

where *E* is Young’s modulus. The following values were obtained in the present study for α and β: α=3.9 10^5, β=4.9 10^4 for the SLS series and α=2.2 10^4 for the float glass.

Parameters Glasses	$B = H/K_c$ ($m^{-1/2}$)	P_C^R (N)	P_C^{R*} (N)	P_C^L (N)	P_C^{L*} (N)
Float glass	8500	0.25 – 0.50	0.30	1 – 2	
SLS1	7550	0.10 – 0.25	0.65	0.25 – 0.50	1.07
SLS2	7300	0.10 – 0.25	0.70	0.25 – 0.50	1.20
SLS3	6800	1 – 2	0.95	2 – 3	1.59
SLS4	6350	1 – 2	1.26	2 – 3	2.09

Table 19: Brittleness, experimental and theoretical radial crack critical loads and experimental and theoretical lateral crack critical load.

Regarding the glasses, Table 19 gathers the values considered brittleness, experimental and theoretical radial crack critical loads and experimental and theoretical lateral crack critical loads. The gap between the behaviors of SLS 1/SLS 2 and SLS 3/SLS 4 is predicted. So, the SLS 1/2 glasses seem to be the most sensitive to the radial/lateral cracking and also the most brittle regarding the so called brittleness parameter *B*.

In the case of the commercial float glass, the addition of modifiers is responsible for significant changes in the glass network. More specifically, the void concentration and the flexibility of the (SiO_4) tetrahedral arrangement is assumed to be much lower than in a model glass (SLS series) of nominally identical silica content. Although the changes on the bulk properties are small, major consequences on theoretical parameters like *B*, P_C^{R*} and P_C^{L*} are noticed.

4.2 Scratching behavior

*All the micrographs of scratches (from optical microscope, SEM,...) presented in this part have been shot so that the scratching direction was from the left to the right (*Fig. 83 *excluded).*

4.2.1 Statistic remark

To mechanically test glasses calls for caution from a probabilistic point of view. In fact, because of their brittle nature, the weakest link concept introduced by Weibull (see [106]) fits well to these materials. Characterizing these glasses should require at least 10 tests to ensure a good reproducibility. It will not be the case in this study. Actually, even if the cracks, that occur during two successive scratch tests performed with similar conditions, are not exactly the same, the critical loads are almost identical and do not lead to reproducibility problems. This fact was determined to be probably due to:

- the small volume of matter involved in the test,
- the stresses undergone by the materials are mainly compressive.

Several photos of scratches performed on the studied glasses will be exposed in this chapter. Attention was paid to choose representative photos in the light of the scratching patterns. However, to avoid imprecision and misunderstandings with regard to the statistical numerical values that will be reported in tables, almost no transition loads will be reported on these photos.

4.2.2 Load dependence of the scratching behavior (standard float glass)

During an indentation experiment performed with a Vickers indenter on a soda-lime silica glass, cracks are known to occur during loading or unloading, and depend strongly on the load level [8, 18]. Similar observations have been carried out in the case of scratching [11, 19] but this field remains to be explored further. For example, the chevron cracks as defined by Rice et al. [19], the lateral cracks propagation described by Ahn [20] and Bulsara [21] and the chipping process given by Le Houérou et al. [11] need some more investigations.

Then, the fractography analysis in a micro-scale has been carried out in this work. Observations of the surface damage lead to detailed results about the radial cracking, lateral cracking and chip formation and are given in the following parts.

Then, during a scratch experiment, the scratch pattern strongly depends on the level of the normal load, and for low loads the different kinds of micro-cracks which form during the scratch process are namely: i) the median cracks, ii) the radial (chevron) cracks and iii) the lateral cracks. This last kind of crack induces chipping when it propagates toward the specimen surface and reaches out.

Monotonic loading/unloading cycles were conducted in order to screen all the possible damage events in a single scratch experiment. Following Ahn [20] and Bulsara [21, 58], three different regimes are typically observed and are schematically drawn in Fig. 69 (only the loading process is reported): i) the first one is associated with a permanent groove with eventually the formation of sub-surface lateral cracks under the plastic track, and corresponds to a micro-ductile regime I, ii) the second one, so-called cracking regime II, is characterized by an important damage by micro-cracking (lateral cracks intersecting the surface and radial cracks) and iii) the third one is a micro-abrasive regime III and gives birth to many debris, with sometimes small lateral cracks along the track.

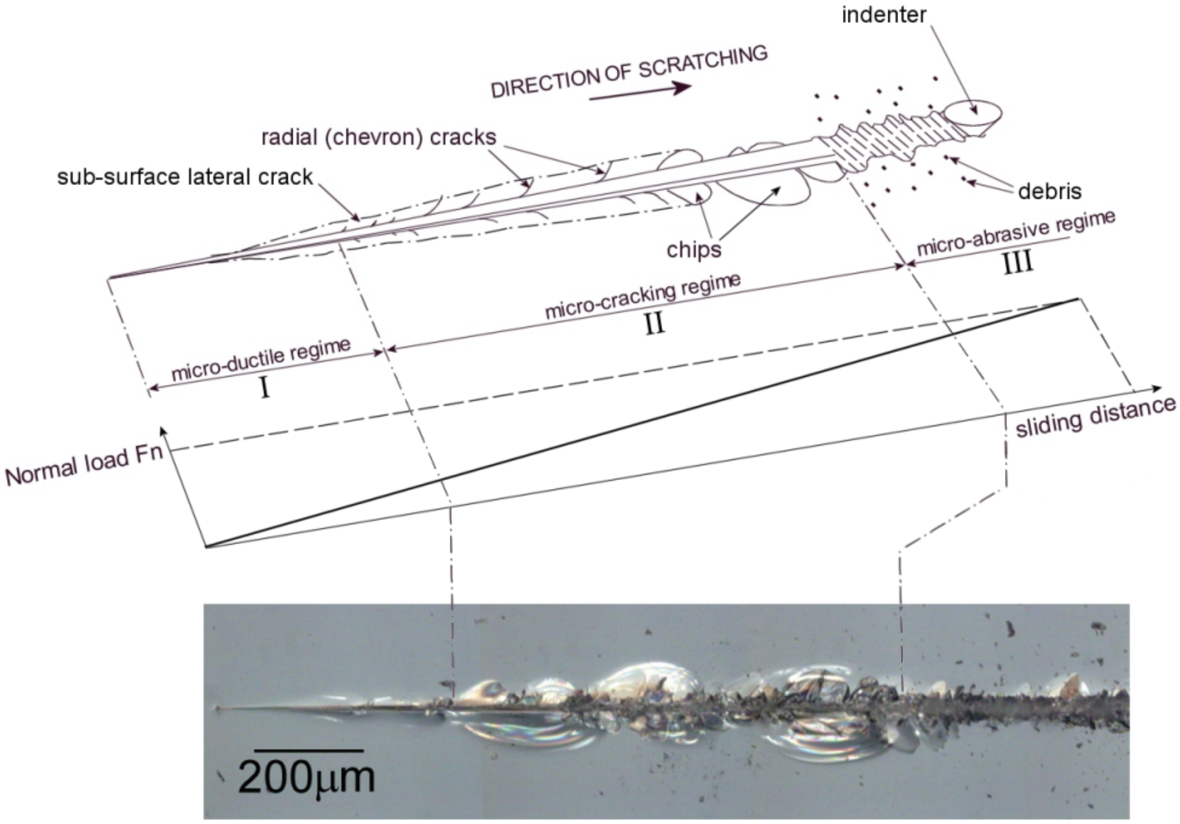

Fig. 69: Typical scratch pattern obtained on the surface of a soda-lime silica (SLS) glass when scratched by an indenter during a monotonic loading cycle (see associated load diagram) and micrograph of a scratch performed on a glass. Definition of the damage regimes I, II and III.

The transition forces between the different regimes were recorded and are summarized in Table 20. They were found to be unaffected by the load history in the sense that the application of a constant loading rate during scratching gives a coherent value (i.e. in the same range) than obtained by quasi-static steps. Note also that scratching speed in the range 0.01 mm/s to 0.1mm/s is commonly considered [20] not to influence greatly the scratching behavior of this kind of glass. So, the comparison in Table 20 is justified. The values for the critical loads are slightly lower than those found by Ahn or Bulsara, likely because of the difference between the glass compositions.

Experiment / Fracture Pattern	Constant loading experiments		Monotonic loading experiments	
	Normal load (N) (Ahn et al. [72])*	Normal load (N) this study °	Normal load (N) loading rate 0.01 N/s °	Normal load (N) Unloading rate 0.01 N/s °
No crack	~ 0 – 0.05	~ 0 – 0.3	~ 0 – 0.7	~ 0.4 – 0
Median crack	~ 0.05 – 0.8			
Median crack and lateral crack under plastic scratch	~ 0.8 – 1.5			
Median, radial cracks and lateral crack intersecting the surface	~ 1.5 – 3	~ 0.3 – 0.9	~ 0.7 – 1.1	~ 1.2 – 0.4
Median crack and crushed scratch track	~ 3 – 6	> 0.9	> 1.1	1.2 >

* scratching speed: 5mm/min~833µm/s
° scratching speed: 10µm/s

Table 20: Transition loads during scratch experiments.

The three different damage regimes defined in function of normal load are closely linked to the crack occurrences that are expected to happen. This had been systematically confirmed during the whole experimental study, by different ways and different instruments (SEM, A.F.M., profilometer, classical and long distance optical microscope,...). For instance, the Fig. 70 shows the sections of the annealed commercial float glass for the three different damage regimes (the samples were broken in liquid nitrogen in 3-points bending tests). These pictures were performed with the confocal microscope, because of its very large field depth. The crack occurrences are confirmed. Last but not least, another convenient and efficient way to investigate the scratch features is the optical profilometer. The Fig. 71 shows the detail of two cracking regime parts with large chip grooves (chips were removed by cleaning process before imaging) and a crushing track from the micro-abrasive regime with its mean profile. They illustrate that the chips can be deeper on one side of the track (Fig. 71 (a)), that the borders of chips can be straight to the depth of the matter (Fig. 71 (b)) and that the micro-abrasive regime (presented here with a large chip) is statically regular so as the mean profile (Fig. 71 (c)) makes sense.

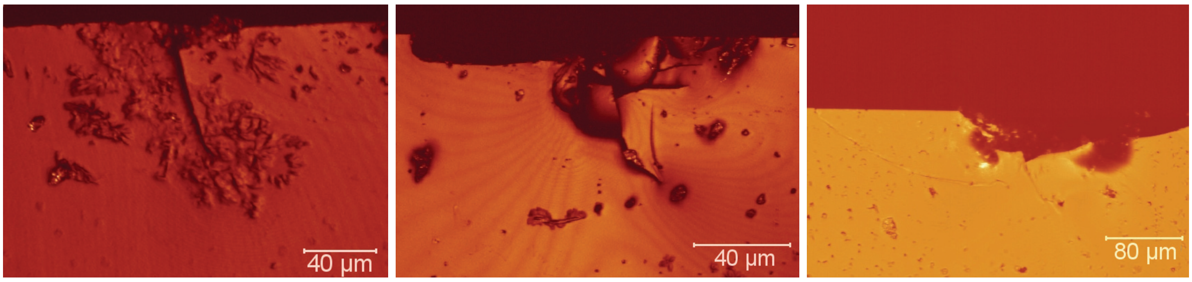

(a) (b) (c)

Fig. 70: Sections of scratches on an annealed commercial float glass: (a) micro-plastic regime, (b) micro-cracking regime, (c) micro-abrasive regime.

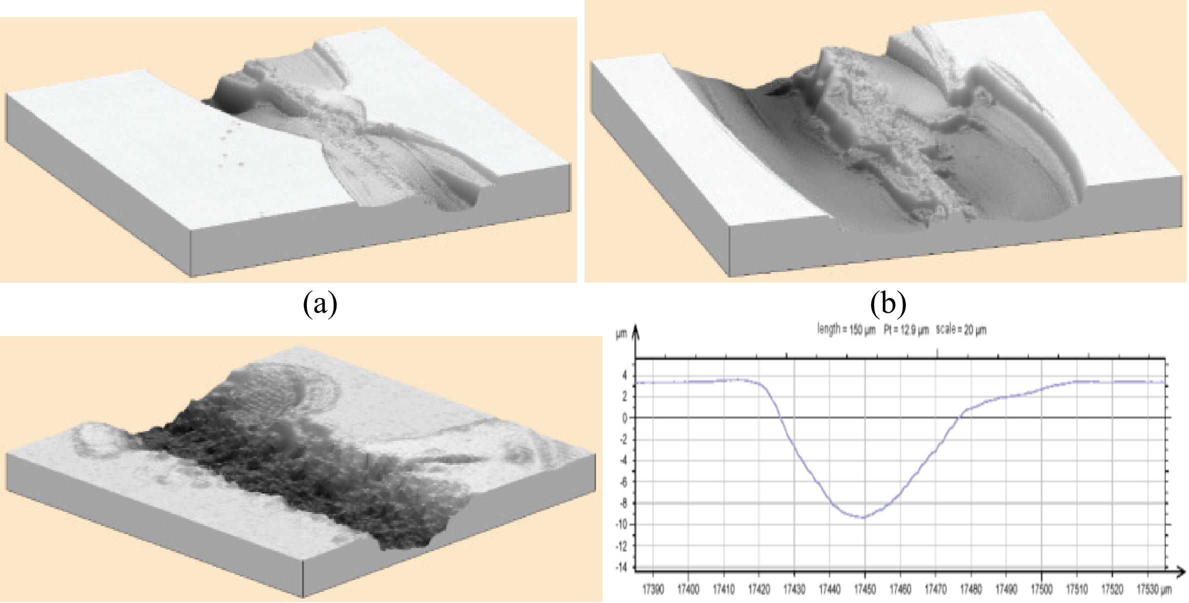

(a) (b)

(c) (d)

Fig. 71: Pictures of damage features on glass obtained by optical profilometer: (a) (full scale: 400x400x18 µm^3) and (b) (full scale: 500x500x30 µm^3) micro cracking regimes; (c) micro-abrasive regime (full scale: 150x150x18 µm^3) and its mean profile (d).

4.2.3 Preliminary results: influence of various parameters

4.2.3.1 Non-symmetry of scratches upon the load history

As shown on the picture of scratch reported in Fig. 72, that will be also studied later, the symmetry of the scratch that could have been expected between the loading and the unloading part does not appear. It seems that a dynamical effect due to the applied load influence the damage in the material during the scratch process. Though, the tangential force which is recorded all along the test is perfectly symmetrical to respect to the maximum load of 3 N as shown in Fig. 72. I/II and II/III refers to the transitions between the plastic to the cracking regimes and the cracking to the abrasive regimes respectively. II/I and III/II refer the reverse transitions.

Moreover, the transition loads on the unloading path are slightly lower, likely because crack initiation and propagation are unstable phenomena.

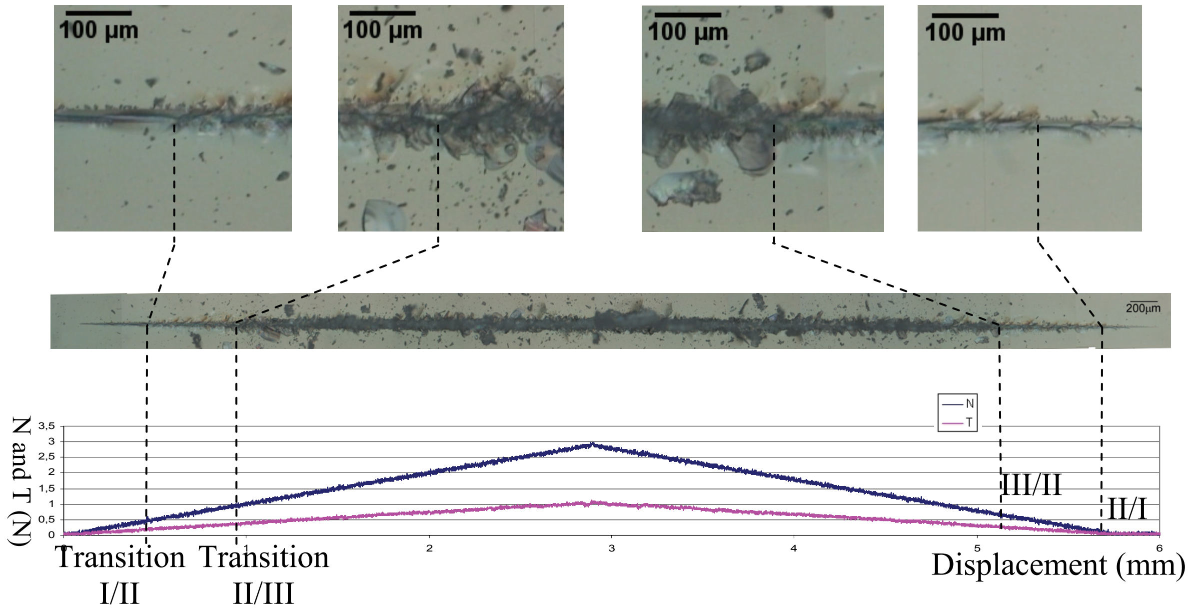

Fig. 72: Photo of a loading-unloading scratch sequence on an annealed standard float glass with graph of forces.

4.2.3.2 Dependence on tin/air face of the float glass

The float glass differs from the other glasses from its chemical composition but also because it has two different faces. The face that was in contact with the tin bath during the cooling is called *tin face*, and the other one *air face* because of its contact with air during the float process. The influence of this parameter must be studied before investigating other parameters.

The corresponding pictures of the scratches accompanying the load scale are represented in Fig. 73. No significant difference was observed in the behavior of both faces of the float glass: the damage regimes appear at the same loads; the cracks and chips have the same size. Similar results were obtained with different humidity levels (0 %, 30 % and 100 %), as well as with the conical indenter of 136° of apex angle. Then, it concludes to a similar behavior in scratching between the tin face and the air face of the glass, within the considered load range.

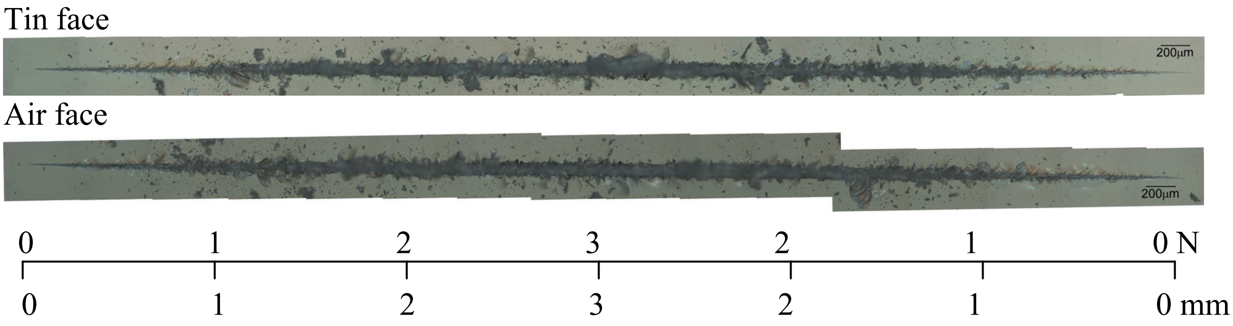

Fig. 73: Photos of loading-unloading scratching sequences on both sides of an annealed standard float glass (tin and air faces).

4.2.3.3 Dependence on the residual thermal stresses

The photos reported in Fig. 74 show scratches performed on an as-received standard commercial float glass and on an annealed one. The provider claims that the residual stresses that exist on the surface and in few micro-meters deep (due to partial quenching during industrial process) was estimated to 7 MPa and rapidly decreases with rising depth. On the contrary, the annealed sample is *a priori* free of residual stress.

Commercial standard float glass

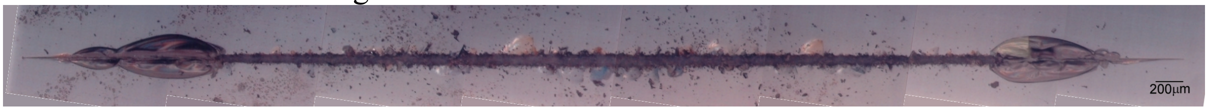

Annealed commercial standard float glass

Fig. 74: Scratches (loading-unloading sequence with 3 N maximum) on a standard float glass and an annealed one.

The first remark deals with the shift of the transition loads between the different damage regimes with rising residual stresses. This shift follows the apparition of damage regimes at lower load when the residual stresses increase. The morphologies of the scratches on the two glasses differ in few points: the morphology of the scratch performed on the annealed specimen show only few cracks and chips in the cracking regime and are very limited in their size. The transition load for the micro-abrasive regime is slightly higher than in the standard float glass case. The fact that the damage is size-limited in the case of the annealed glass indicates that the lateral cracks are small.

The transition loads shift of damage regimes is explained by local stress considerations in the surrounding of the indenter/material interface. Actually, the larger the residual thermal stresses in the material, the larger the local stresses in the direct surrounding of the indenter. This is rather obvious when assuming that the surface of contact is the same in both cases: the residual thermal stresses are compressive stresses close to the surface and the triaxial stress loading of an indentation is greatly dominated by a high compressive component. Then, these two added components give higher compressive local stresses than in the case of the annealed standard float glass. That explains naturally the described phenomenon.

The study of the dependence of the residual thermal stresses on the behavior of the glasses to scratch process seems to be of prior interest and it is pertinent to try to predict the behavior of the industrial glasses. It is clear that in the case of quenched glasses, sometimes commercially-called *securit* glasses, the damage corresponding to one precise applied normal load will be more severe than in a standard float glass or for an annealed standard float glass. The problem is to define here what “the damage (...) will be more severe” means in this case. For instance, a relatively slight scratch (in the load sense) will produce a cracking regime in a standard float glass and then will leave big chips that will considerably alter optical and aspect properties. At the same load, the *securit* glass may exhibit a micro-abrasive regime that leads to less optical and aspect losses. But, and this is the conclusion of the use of such quenched glasses, the abrasive regime provides deeper cracks that alter the mechanical properties of the material more than the cracking regime does. Then, the optical and aspect losses may be less important in quenched glasses, but the mechanical properties may be certainly decreased.

4.2.3.4 Dependence on the indenter geometry

Like explained in § 4.1, the cracks initiation and the associated damage can’t be studied without considering the local stresses. This fully justifies the following study on the influence of the indenter geometry as a preliminary study.

Three geometries of indenters were used for scratch tests:

- a Vickers indenter,
- a conical indenter of 136° of apex angle,
- a conical indenter of 90° of apex angle.

The photos of scratches with the graph of apparent friction coefficient (i.e. the value of the tangential force on the value of the normal one) during the tests with the different involved indenter geometries are reported in Fig. 75, Fig. 76 and Fig. 77. Note that the imposed normal load was a loading-unloading slope with 3 N as maximum.

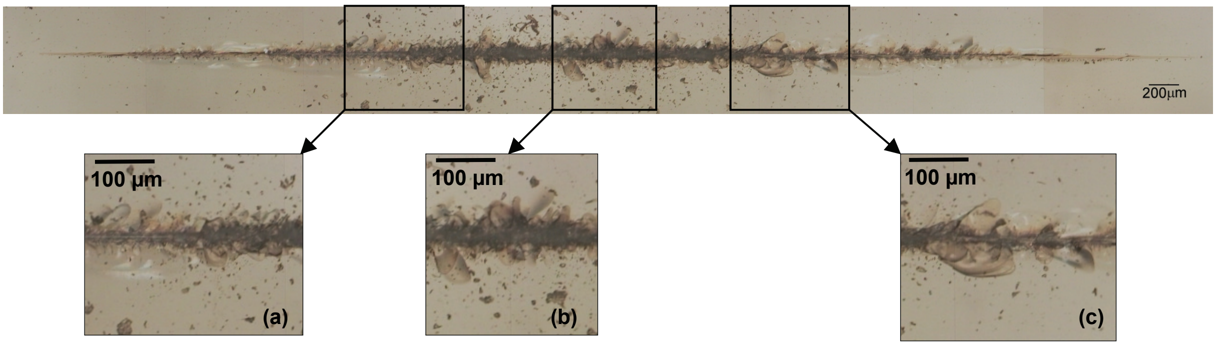

Fig. 75: Loading-unloading scratching sequence (3 N max) on an annealed standard float glass with a 136° conical indenter.

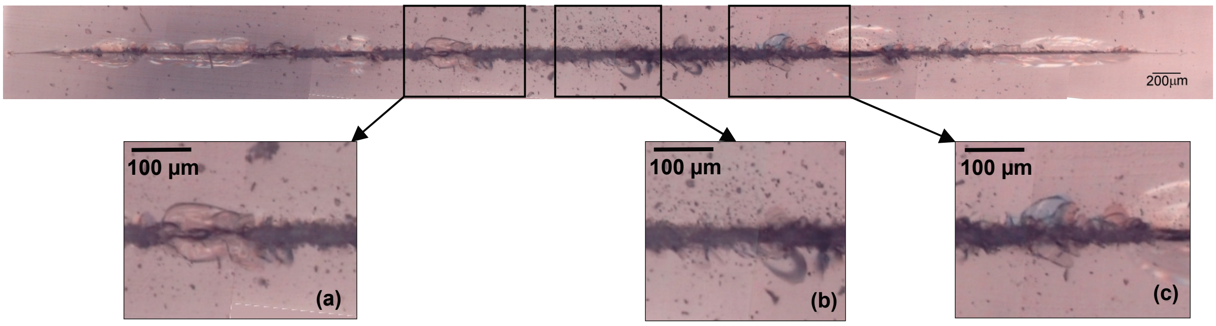

Fig. 76: Loading-unloading scratching sequence (3 N max) on an annealed standard float glass with a 90° conical indenter.

Fig. 77: Loading-unloading scratching sequence (3 N max) on an annealed standard float glass with a Vickers indenter.

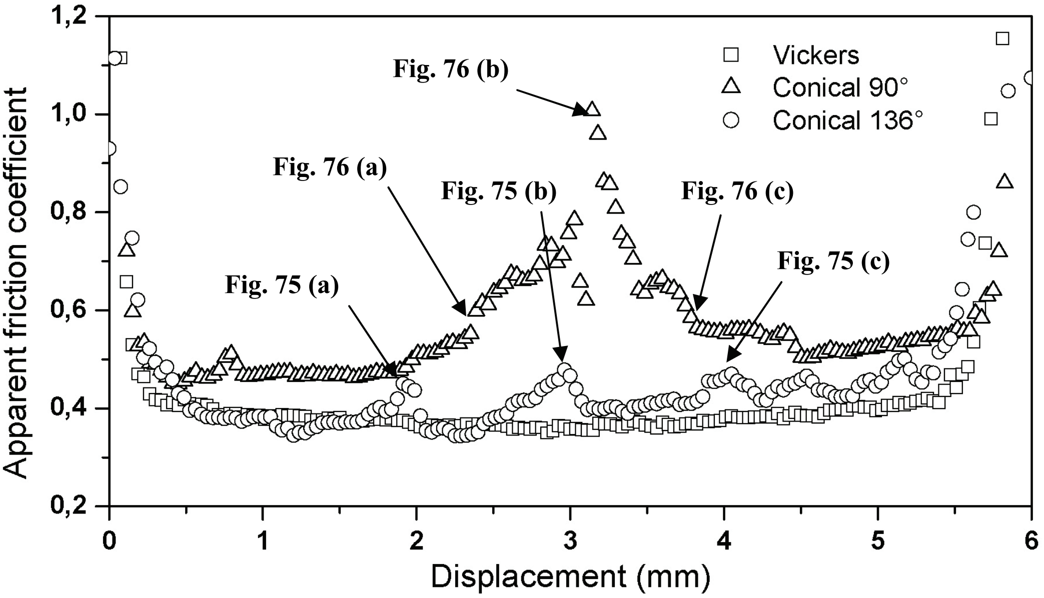

Graph 25: Apparent friction coefficient evolutions during the scratch tests for the three considered indenter geometries. Correspondence to micrograph figures.

The first remark about these results deals with the evolution of the apparent friction coefficient (see Graph 25). First, for small values of the tangential loads (case of small values of the normal load), the ratio $\frac{F_t}{F_n}$ varies greatly. Then, the values of this ratio are not representative for a normal load less than 0.3 N (i.e. both borders of the Graph 25). In the Vickers case, the evolution of the friction coefficient is almost constant, witnessing that the evolution of the tangential force rigorously follows the normal force one, whereas the curves followed by the two conical cases exhibit *accidents*. In addition, the average value of the friction coefficient is not the same as well. Actually, the apparent friction coefficient corresponding to the 90° conical indenter is higher (in average on the stable parts of the curve) than in the case of the 136° conical and Vickers indenters. This result is in agreement with the work of Li et al. [61] who reported that the friction coefficient increases with the sharpness of the indenter.

The accidents on the curves are probably due to material instabilities under the indenter (that will be discussed further in the light of micrographs reported in Fig. 75 and Fig. 76) and are strictly reproducible (at least three tests in the same conditions were performed) and do not exist in the Vickers indenter test. Note that the scratching sequence on the linear sclerometer is governed by imposing the load and not controlled by displacement. Unfortunately, this situation is obviously favorable to instability occurrences.

First of all, let’s discuss the accidents that were previously found on the scratches performed with the conical indenters. The photos of singular points reported in Fig. 75 and Fig. 76 were magnified for better analysis of the phenomena corresponding to these accidents.

Let’s study the scratch obtained with the 136° conical indenter illustrated on Fig. 75. The first magnified detail, corresponding to the first accident on the friction coefficient curve, illustrates the transition from the chipping regime to the micro-abrasive regime. The origin of the second accident may only remain as a hypothesis: the damage seems important and may show that it has reached a critical point. It could be caused by a glass defect at this point, a dynamical effect or a control failure due to the loading-unloading transition, or a removing of debris under the indenter. Lastly, the third accident is clearer: it corresponds actually to the reverse regime transition observed and analyzed in the first accident: from the micro-abrasive regime to the micro-chipping regime. Moreover, a chip precedes this singularity, witness of the instability behavior of the material at this load. Then, sub-surface lateral cracks start to appear just after this transition.

Let's study now the scratch obtained with the 90° conical indenter reported in Fig. 76. The first and last singular events, pointed out by the magnified frames, are similar to the equivalent events found on the scratch previously studied. The singularity of these points can also be pointed out on the friction curve (see Graph 25) by considering the change in the slope of the curve occurring on these two points. The huge accident that occurred around 3 N is certainly due to the load that reached a critical value. Moreover, data collected during tests showed that the normal load doesn't follow its expected straight slope. It might come from a local break down of the material under the indenter.

These kinds of events don't appear in the curve obtained during a scratch test performed with a Vickers indenter (see Graph 25). Then the geometry difference between a Vickers and a conical indenter influences strongly the material response. Actually, the Vickers indenter has a *ploughing* shape whereas the conical indenter has a revolution shape. Then, the deformation process of the material due to the contact between the indenter and the sample is obviously different depending of the penetrator shape and the material behavior to penetration.

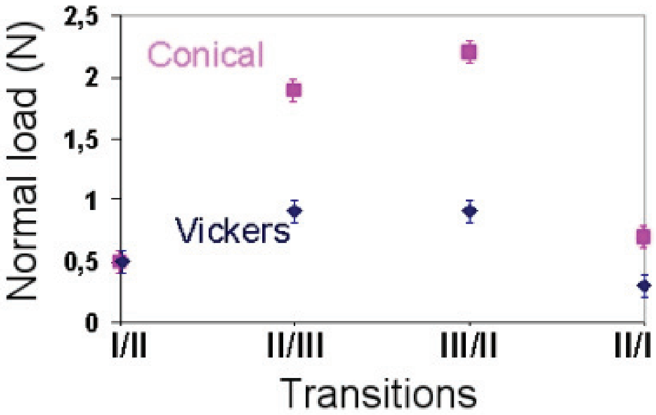

Graph 26: Damage transition loads measured in the case of scratches performed with a Vickers indenter and a conical indenter (136° of apex angle).

The second remark deals with the *severity* of the surface damage. This qualitative criterion is used in this work following the rule: the more severe the face looks, the lower the transition loads between the different damage regimes are. Concerning the three scratches, the tendency is clear: the severity of the surface damage goes from the scratch performed with: i) 136° conical indenter to the one with ii) 90° conical indenter to iii) Vickers indenter.

The evolution of the severity of the damage patterns can be quantified by determining the transition loads that are plotted in Graph 26 only for the case of the 136° conical and Vickers indenters for reading convenience. The transition loads were determined by average on five similar scratches. Similarly with the study of the dependence on the residual stresses, these evolutions can be explained by the three-axial repartition of the stresses with regard to the indenter. It is obvious that important stress concentrations appear in the surrounding of the front edge of a Vickers indenter compared to a conical indenter on which the stresses will be regularly spread on the half surface of revolution. The stresses are also more important in the case of a 90° conical indenter than in the 136° one. The shift of the different transition loads of damage regimes is then directly explained by these simple geometric considerations.

The damage regimes will appear more early (in a load sense) with rising local stresses. Actually, the damage behavior of the material is essentially dictated by the local stresses. Then, the micro-plastic regime of a 136° conical scratch will be "longer" than with a Vickers indenter. It is the same for the cracking regime. These considerations lead to the observed shift of the transition loads depending on the indenter geometry that are reported in Graph 26 for the 136° conical and the Vickers indenters.

4.2.3.5 Dependence on humidity (% r.h.) and other environmental effects

Fig. 78 shows the scratches together with the normal load recorded during the experiments at different humidity levels on an annealed standard float glass. The only parameter that varies during these experiments is the humidity level in the enclosure.

0 % humidity

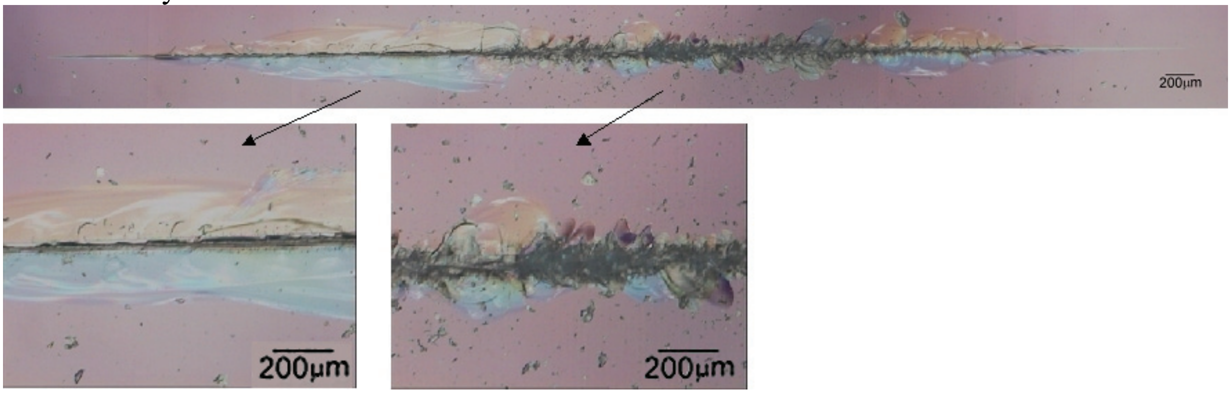

30 % humidity

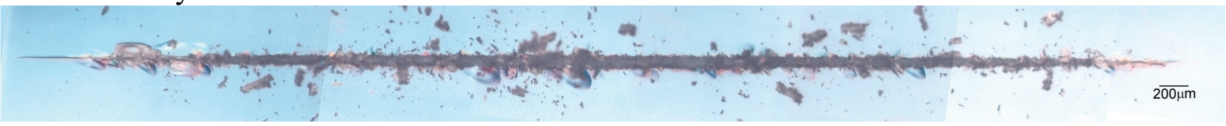

65 % humidity

100 % humidity

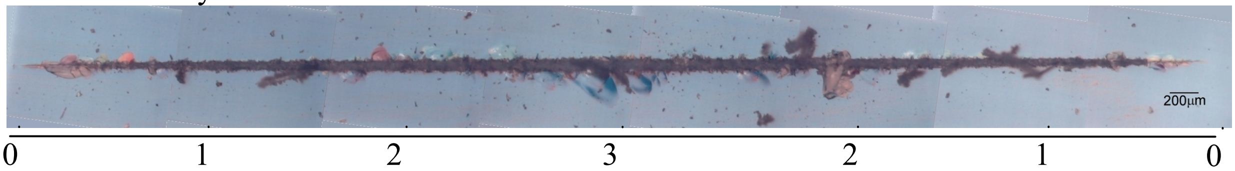

Fig. 78: Pictures of scratches conducted under different humidity levels with a Vickers penetrator following a slope load-unload process (3 N of maximum normal load).

As expected from the background studies on the effect of humidity on the fracture behavior of soda-lime silica glasses [42, 61], the scratch patterns significantly depend on the humidity level: the more important the humidity level is, the earlier (with regard to the normal load) the different damage processes appear. Then, the transition loads between the different damage regimes obviously evolve with the humidity level: the plastic, cracking and abrasive regimes tend to develop at higher loads when the moisture decreases as reported in Graph 27.

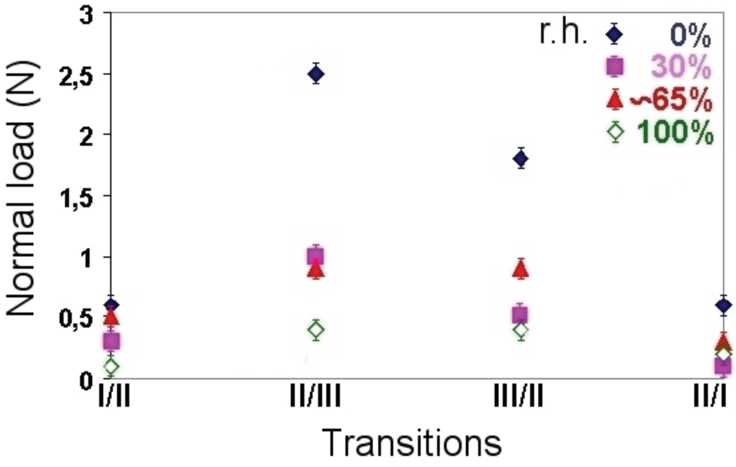

Graph 27: Transition loads with regard to the humidity level.

Another observation concerns the scratch obtained with 0 % of humidity. Note that the particular level of 0 % of humidity corresponds to a real humidity less than 50 ppm of water vapor in the atmosphere of the glove box. In this case, damage is characterized by a large lateral crack which remains under the surface of the sample. A similar but shorter crack occurs during the unload process. This phenomenon fades rapidly as the humidity level is raised. The particular morphology of the scratch made at 0 % of humidity is interesting. From a morphological point of view, it is difficult to determine if the micro-abrasive regime is established between 2.5 and 3 N because of the numerous chips on both sides of the track. A test up to 4 N was then justified. The result is a non-evolution of the scratch pattern between 3 and 4 N. Briefly, the micro-abrasive regime is established after 2.5 N. One can notice that there is almost a total lack of radial cracks while the lateral crack extends over a large distance under the surface (Fig. 78) without reaching out before 2.5 N of normal load. Sub-surface lateral cracks, which propagate after the experiment, were found to be insensitive to the humidity level and remain under the surface of the material. Chipping process usually occurs when radial cracks intersect a lateral crack. This mechanism of chips creation will be analyzed in detail and discussed in part § 4.2.4. In the case of 0 % of humidity, this phenomenon does not occur because of the lack of radial crack. Then the chipping occurs at higher load. The radial cracks, located on the surface of the glass are directly exposed to ambient air and then to static creep phenomenon as described in § 2.1.7. On the contrary, the sub-surface lateral crack does not undergo any interaction with the moisture of the ambient air. It explains why lateral cracks occur whatever the humidity level is in the enclosure during the tests.

The explanation of the lack of radial crack remains still a hypothesis: it may be due to the nature of the interface between the indenter and the material because of the humidity level that certainly dictates the critical loads for cracking. A second hypothesis could be that the humidity level in the case of an ambient atmosphere makes possible the sub-critical crack growth of the radial cracks (and median cracks when enough developed) like defined in § 2.1.7.

In conclusion, the particularity of this scratch is not more a large sub-surface lateral crack than the lack of radial crack because of the low humidity level. This explains the impressive size of the lateral crack.

It is also interesting to compare the indentation behavior of the glasses to their scratching behavior. This comparison expresses the influence of the sliding movement of the indenter, i.e. the potential dynamical effect of this test. Then, indentation tests were performed in order to complete the study of the influence of the humidity level on the standard annealed float glass. The scratch tester was used as a micro-indentation machine, especially developed (see details in appendix 2) for a $\frac{\dot{h}}{h} = constant$ control with h the penetrating depth as it will be discussed further in this study (§ 5.7.3.1). Even if this micro-indentation machine is controlled and instrumented, Load-Displacement curves that were recorded during these tests will not discussed. The direct advantage of using the same machine for scratching and micro-indentation on glass is to ensure the same machine compliance during the two different tests. The comparison between the results is not subject to doubts like it may be if two different machines were used. The applied normal loads during the indentation tests were: 0.2, 0.4, 0.6, 0.8, 1, 1.2, 1.4, 1.6, 1.8, 2, 2.5 and 3 N. Fig. 79 presents the two series of indentations: the 0 % humidity level and the ambient (~65 %) humidity level respectively.

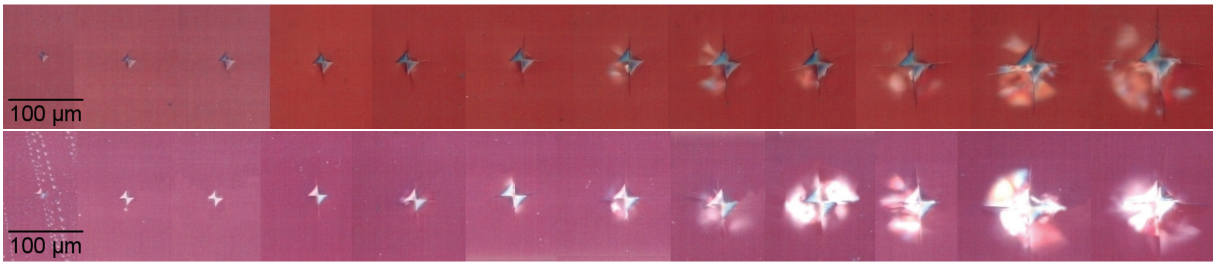

Fig. 79: Series of indentations with 0 % humidity level and ambient (~65 %) humidity level respectively.

The conclusion of these tests is that the critical load for radial/median and lateral cracks occurrence slightly shifts in higher loads for the 0 % humidity level tests. These results were expected in the light of the scratch tests which show the same tendency. However, the shift in indentation results is not so important that it could have been expected: no significant differences (in apparition loads, length of cracks,...) were pointed out by these indentation tests, so it is not possible to clearly conclude. Then, the clear behavior exhibited by the glass during scratching in humidity-controlled atmosphere seems to depend on the influence of the humidity level but combined with the dynamical effect of the sliding move that probably enhances the observed differences in indentation tests.

A remark can be drawn on the video shots which will be presented further in Fig. 83 about the role of humidity level on the scratching behavior. Actually, the video was directed in situ in a SEM, in which a high vacuum is maintained, providing this way a dry atmosphere for the tests. Moreover, the indenter was a cube corner that is a very sharp indenter compared to a Vickers one as mentioned in Table 17. Nevertheless, the normal load that was required to generate a radial crack was no less than 500 mN which is a very high value! This confirms and illustrates that radial cracks are inhibited by a low humidity level.

4.2.4 Phenomenology: identification and understanding of scratching damage

4.2.4.1 The micro-ductile regime

The micro-ductile regime in SLS glasses consists on a permanent scratch track without damage on each side and visible debris. This definition does not exclude damage inside and under the track, as long as they stay localized this way and they do not modify dramatically the scratch track appearance. To get insight into the comprehension of this regime, a lot of accurate *post mortem* observations were performed in SEM. Among these numerous observations, two were selected and reported in Fig. 80 and Fig. 81. The Fig. 80 represents a “classical” scratch track on the SLS glass. Few slight cracks inside the track are visible. Their occurrence doesn’t match with the frequency due to the relative compliance of the machine (potential “stick-slip” effect of the indenter on the surface). The Fig. 81 is far less classical. It shows a detail of a scratch track created at 0.4 N, close to the transition load of the micro-ductile/cracking regimes. The particularity of this picture is that the considered sample exhibits a side of its track pulled up while the other remains intact. There is even a part of the scratch that is left attached by a ligament located in the middle of the track. This suggests that the removal process inside the track goes from the border toward the middle of the plastic imprint. This picture illustrates from an unusual point of view the damage that takes place under a plastic track, composed of a rough surface with perpendicular fracture orientation that disappears as it approaches the middle of the track.

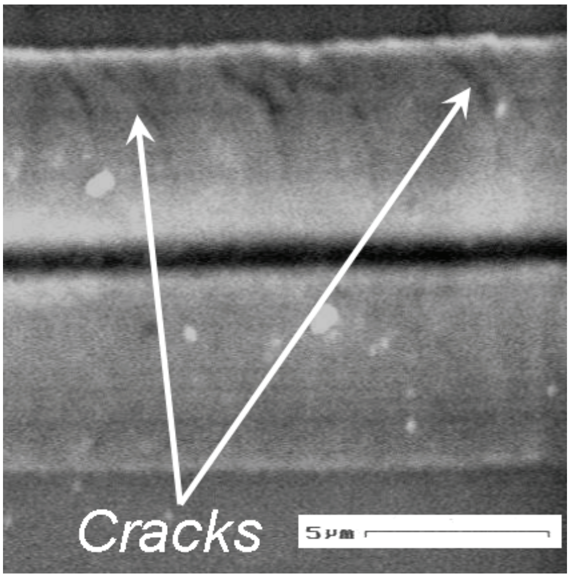

Fig. 80: Detail of the micro-ductile regime on the surface of a standard float glass. (SEM)

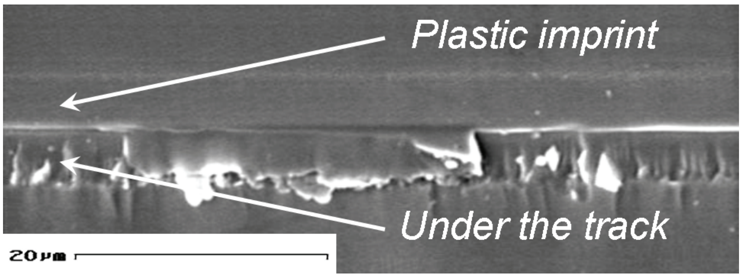

Fig. 81: Detail of a standard float glass scratched by a Vickers indenter in the micro-ductile regime. The plastic imprint and the damage under the scratch track are visible. (SEM)

4.2.4.2 The cracking regime

4.2.4.2.1 General

According to Rice et al. [19], the cracking regime is composed of different damage phenomena: i) median cracks that propagate deeply in the material, ii) lateral cracks that take place under the indenter in the depth of the sample corresponding to the limit of the so-called plastic zone as introduced by Cook et al. [8], iii) radial also known as chevron cracks that occur on the surface and iv) chipping. This part consists in the description of the three last quoted damage mechanisms (radials, laterals and chipping) during the scratching of a glass with added fractographic considerations.

4.2.4.2.2 Radial (chevron) crack events

At high magnification, the radial cracks resulting from the scratch process don't look exactly as those described by Ahn [20]. These cracks are significantly inclined toward the sliding direction, and propagate in a curved shape usually ending perpendicular to the scratch track as illustrated in Fig. 69, if there is no combination with another damage phenomenon (i.e. lateral cracks as will be discussed further). Thanks to the SEM, the Fig. 82 shows the initiation and the beginning of the propagation of a radial crack. It clearly initiates at the leading edge of the Vickers indenter and soon propagates from a direction parallel to the scratch track to a curved shape that tends to get perpendicular to the track. The, it would be better qualified as median/radial crack. The crack reaches out from the track with an angle noted θ on Fig. 82 that probably depends on the friction coefficient and the environmental parameters. Actually, it usually looks as if the crack initiates on the border of the track with the angle θ from the scratch because the crack initiation and propagation at the earliest steps is usually not visible in the track as it is probably *erased* by the moving indenter. Then, the chevron crack remains really close to the indenter tip at the contact. Note that the non-uniformity of the coating around the damage on the sample surface makes the SEM observations underline the different cracks as they are charged of electrons. Thus, damage is more visible but the drawback using a SEM is that the potential magnification with a good resolution is restricted.

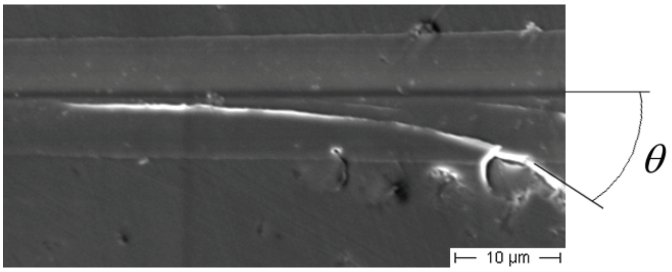

Fig. 82: Initiation and propagation of a radial (chevron) crack on the surface of a standard float glass. (SEM)

Fig. 83 shows a sequence of shots taken from a video. It deals with a scratch performed *in situ* in a SEM and was performed in EMPA. The indenter penetrates the glass and then move forward (transition in frame n°8). It enables to illustrate the crack advance during a scratch test. The major result is that the crack advance follows a stable propagation. In fact, the speed of the crack front advance is slow as the loading indenter moves.

This propagation can be qualified as semi-stable: i) after the initiation, it rapidly curves either on the right or on the left of the track; this choice is purely statistic and constitutes the unstable part of the crack propagation, and ii) the advance speed of the crack suggests a stable propagation; actually, the crack advances with a speed that is about the moving tip one (about 0.1 µm/s). Then, the semi-stable character gives account for both the stable propagation of the crack and the instability in the very first direction of the crack propagation.

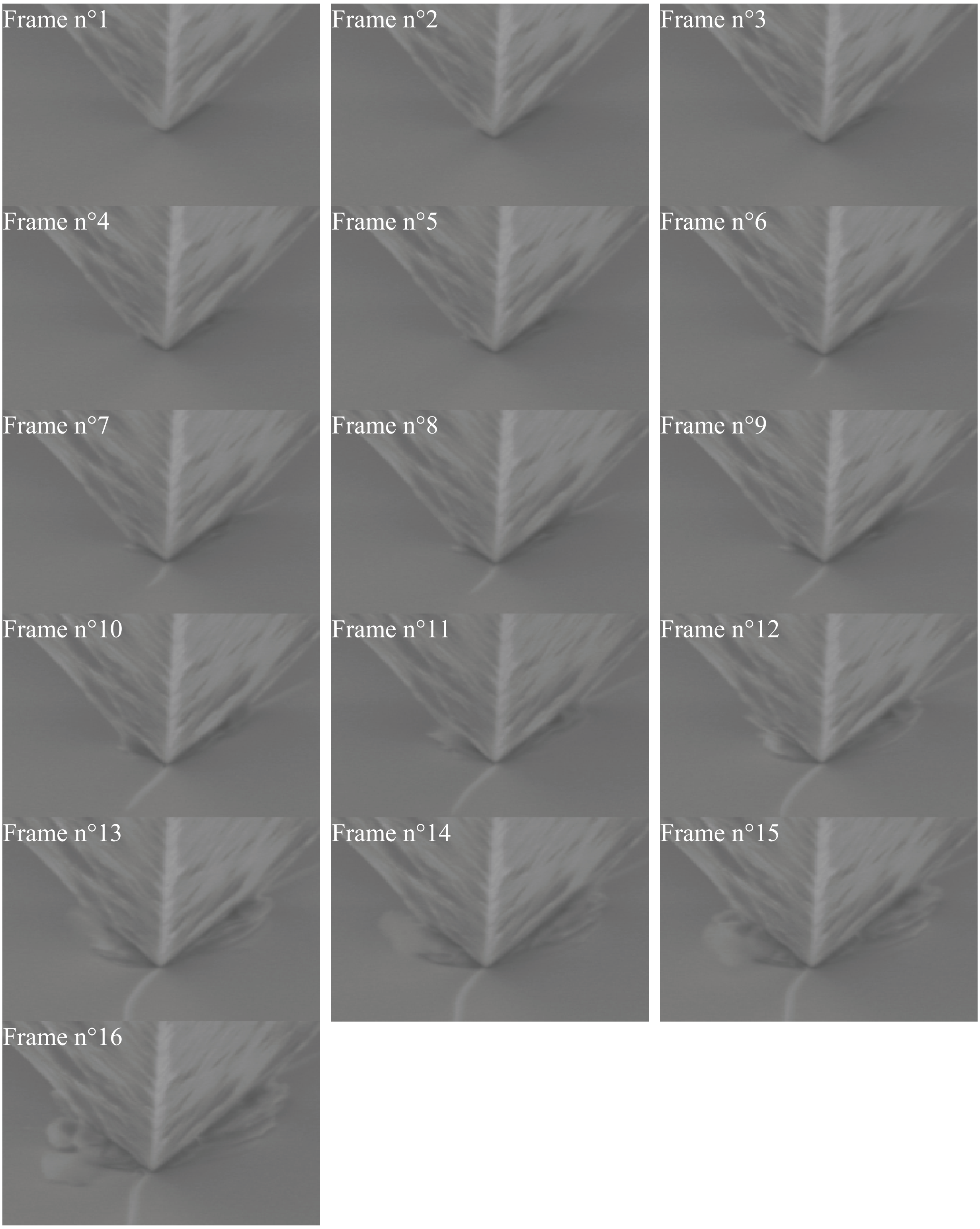

Fig. 83: Picture sequence from a video taken *in situ* in a SEM. The cube-corner indenter scratches the glass surface, generates and makes a radial crack propagate. The full scale is equal to 28 μm.

4.2.4.2.3 Understanding of the creation and the development of chips

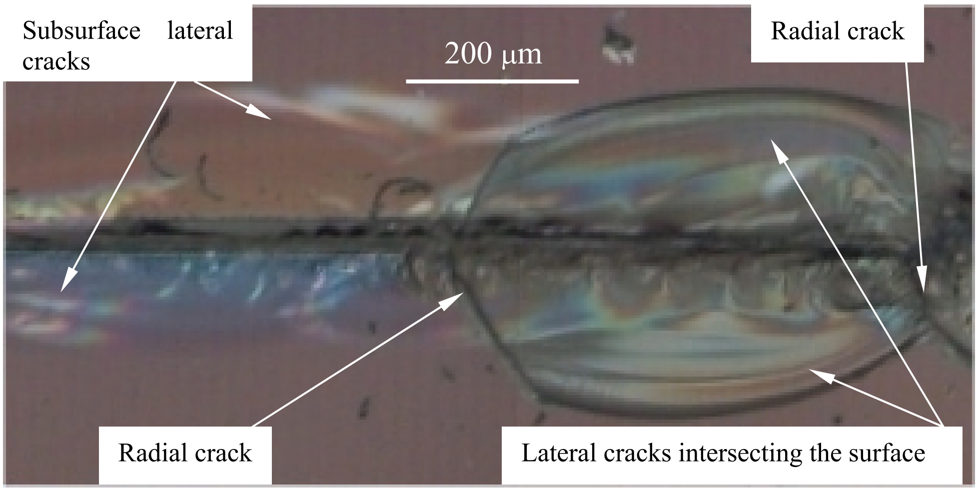

Fig. 84: Chip formation with the different involved damage.

Fig. 84 shows a chip. Its observation puts light onto the mechanism of the chipping process occurring during scratching: a chip is the combination of two radial cracks and a lateral one which then intersects the specimen surface. Two consecutive radial cracks located on the same side of the scratch track may intersect each other as a result of a deviation process resulting from the attractive forces between the two close cracks. The coupling with a lateral crack leads to a chip and thus to matter removal. When only one radial crack frames the lateral one, this latter crack may remain under the surface.

Then, the mechanism is clear: a chip is created when two radials (on the same side of the scratch track) intersect a sub-surface lateral crack, and emerges then to the surface of the specimen.

Fig. 71 (a) and (b) confirm this mechanism showing straight vertical borders of chips as they reach the surface suddenly due to the influence of the radial cracks (the borders may be smoother in the case of the absence of radial crack as suggested by Whittle et al. [107]).

To summarize, the interaction of radial and lateral crack events gives rise to chipping when the load is high enough. Complementary SEM investigations confirm this description. The Fig. 85 illustrates clearly this mechanism that is underlined by the two black arrows: the radial cracks interact with the lateral crack that starts to reach out to the surface with an inflexion of the shape on the surface at the intersection. Under the hypothesis that sufficient energy is involved, the last step of the chip formation should be, for the couple radial/lateral on the left of Fig. 85 for instance, that the lateral propagates to the surface when it reaches the second radial.

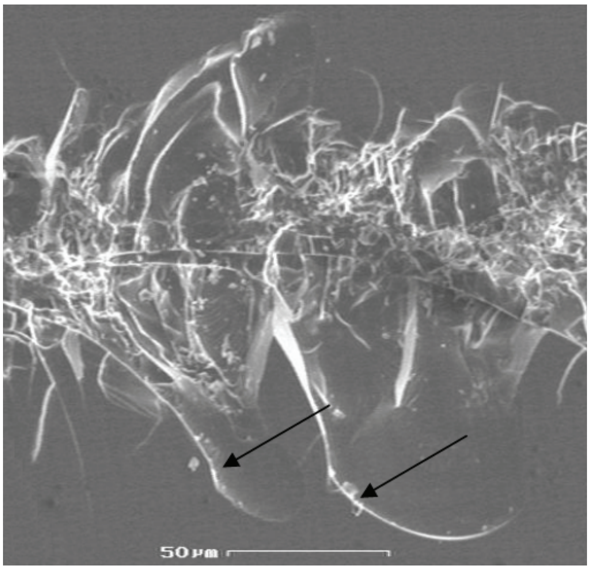

Fig. 85: Interaction between radial and lateral cracks without complete chip creation (SLS 1). (SEM)

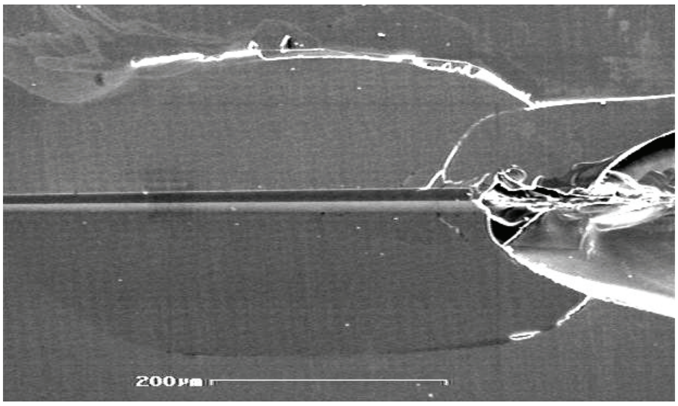

Fig. 86: Chipping by propagation of a lateral crack – absence of radial crack (SLS 4). (SEM)

In the case of non-existent radial cracks (case in low humidity level for example as discussed in § 4.2.3.5), chipping can also occur if there is enough spent energy to make the lateral crack reach out toward the surface. Fig. 86 shows a lateral crack that begins to create a chip as it almost reaches the surface.

Fig. 87 shows the surface below a chip in details. Note that the chip was removed by a cleaning process before been coated for SEM observation. Twist hackle [22-24] is clearly visible on the fracture surface. It suggests that the fracture is driven mainly in mode I combined with a weak mode III component. The river lines pattern indicates the direction of propagation of the crack that initiates without surprise under the track and propagates far from the track, usually perpendicular to the scratching direction. The river lines are approximately equally spaced well below 1 µm that is in good agreement with results reported in the literature [25].

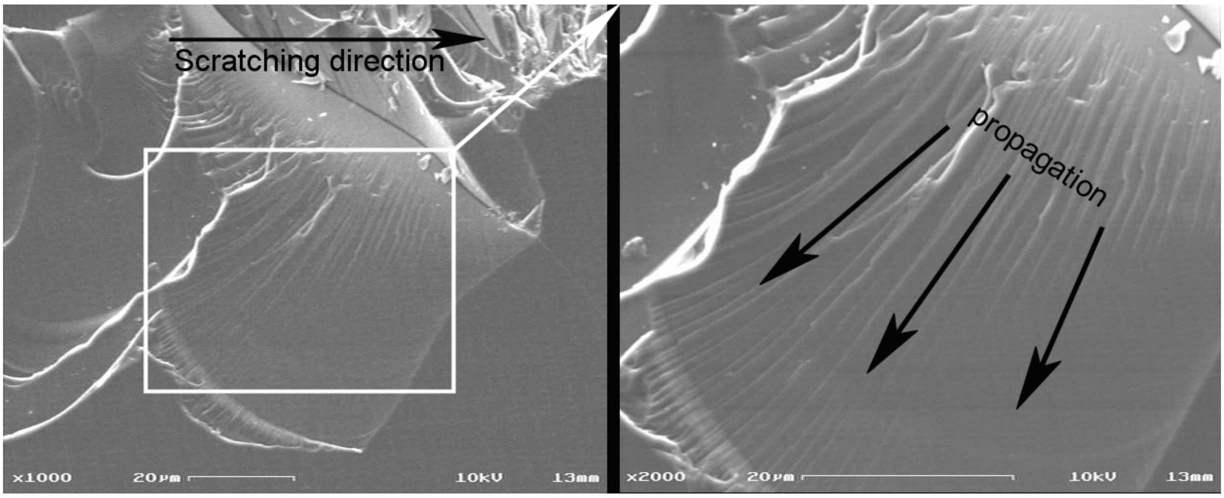

Fig. 87: Chip and its details. River lines give the direction of the propagation of the lateral crack (SLS 4). (SEM)

4.2.5 Dependence on the glass chemical composition

SLS glasses generally fall in a narrow range of compositions along the boundary between devitrite (Na_2O–3CaO–$6SiO_2$) and tridymite (SiO_2) in the Na_2O–CaO–SiO_2 phase diagram (see Graph 21). Shifting away from this narrow range affects various important characteristics, such as the glass melting behavior, crystallization tendency, glass workability, chemical durability and static behavior like developed in § 4.1.

As noted earlier, the scratchability is greatly affected by the chemical composition [10, 11] as shown in Fig. 88 with a representative scratch groove of each of the six studied glasses obtained for the present study with a monotonically increasing normal load up to 4 N. The scratches are quite different. The aim of this part is to interpret the results in the light of structural considerations linked to the amount of modifiers in their vitreous network.

Standard float glass:

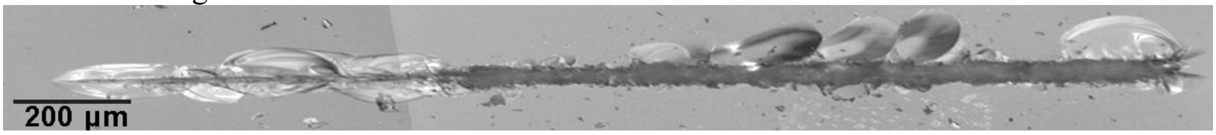

SLS 1:

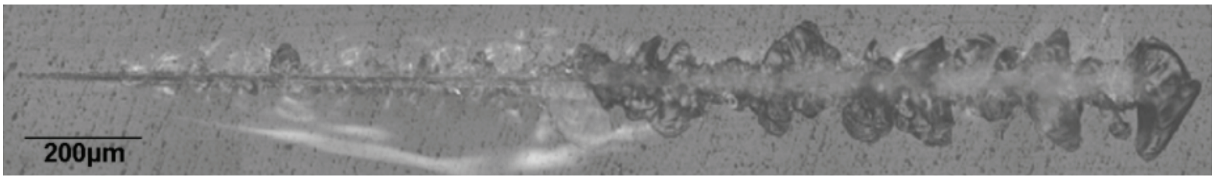

SLS 2:

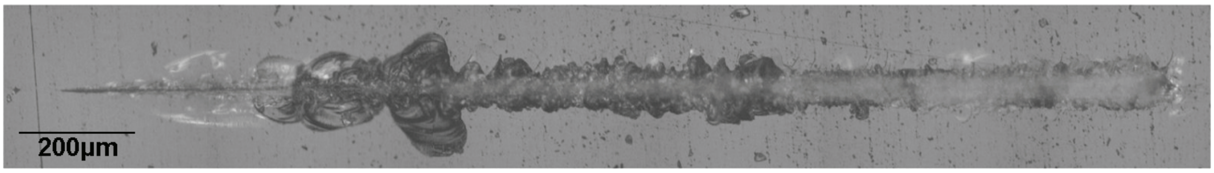

SLS 3:

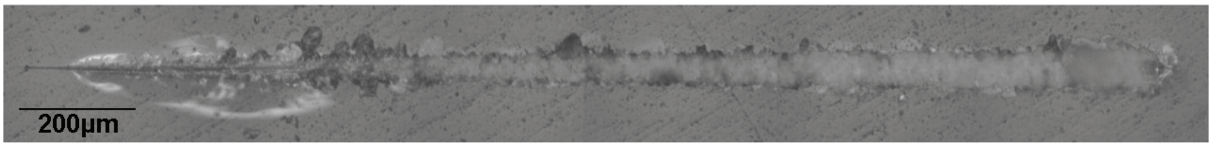

SLS 4:

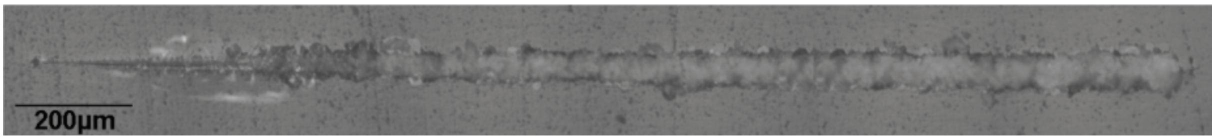

Fused silica:

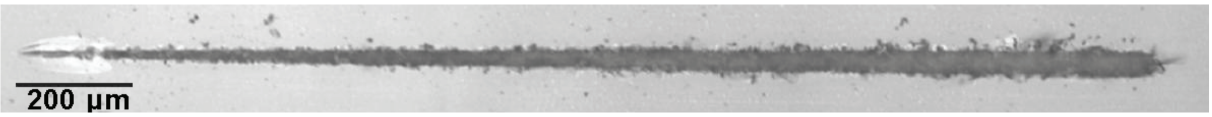

Fig. 88: Evolution of scratch resistance for the six considered glasses

The transition loads between the different damage regimes for the six glasses are summarized in Table 21. The lecture of this table in parallel to the following interpretations all along this part can be helpful. Note that the values reported in Table 21 are statistical values obtained on numerous scratches (typically about 10). These measurements were obtained on recomposed micrographs of scratches as those reported in Fig. 88: a scale permits to determine the transition loads with accuracy about 0.1 N.

Damage regimes / Glasses	Micro-ductile	Micro-cracking		Micro-abrasive
		Sub-surface laterals	Chips	
Standard float glass	0 – 0.4 N	0.4 – 0.8 N	0.8 – 1.2 N	1.2 – 4 N
SLS 1	0 – 0.35 N	0.35 – 2 N	2 – 4 N →	2 – 4 N
SLS 2	0 – 0.4 N	0.4 – 0.9 N	0.9 – 1.6 N	1.6 – 4 N
SLS 3	0 – 0.35 N	0.35 – 1 N	1 – 1.1 N	1.1 – 4 N
SLS 4	0 – 0.3 N	0.3 – 0.9 N	–	0.9 – 4 N
Fused silica	0 – 0.2 N	0.2 – 0.5 N	–	0.5 – 4 N

Table 21: Transition loads associated with changes in the scratch regimes. The arrow indicates the difficulty to dissociate the two considered regimes.

As a first glimpse, standard float glass, SLS 1 and 2 reported in Fig. 88 appear sensitive to chipping as a direct consequence of their normal character that mainly allows cracks to form by local shearing [11] due to percolation paths [26] that are lines of weakness in the vitreous network. SLS 3, 4 and fused silica with silica-like networks appear to be more resistant to both crack propagation and chipping during scratch experiments as a consequence of their anomalous character [11] that accommodates the deformation by network rearrangement (densification) without breaking bond [9].

As a result of these reminders, in the scratch pictures shown in Fig. 88, a micro-abrasive regime appears in the low-load domain for the fused silica, SLS 3 and SLS 4, with high-silica contents, whereas lateral chipping occurs for the standard float glass, SLS 1 and SLS 2 compositions. The SLS 2 glass is the weakest against lateral and radial crack propagation, while an increase in silica leads to the disappearance of chipping. The maximum compactness of the SLS 2 glass is consistent with this observation: the rearrangement of matter at the atomic or molecular scale is difficult and the glass responds to the high contact stress by allowing cracks to form and propagate. To summarize, glasses from devitrite phase field are sensitive to chipping and glasses with silica-like networks appear to be much more resistant to both crack propagation and chipping during scratch experiments. Note that a similar conclusion was drawn in a study devoted to the indentation-scratching behavior of silicon-oxycarbide glasses [12], where the covalently bonded carbon in 4-fold coordination was found to induce a more normal behavior.

This kind of behavior considerations linked to the chemical composition can also be applied to fractographic analysis in a lowest scale. For instance, Fig. 89 shows parts of the micro-cracking regime with its details on the standard float glass and the SLS 4 glass. Even if the global shape of the damage remains the same between the two materials in form of large chips (note that the cracking regime does not occur at the same load), the detail of the scratching track is totally different. In the case of the standard float glass, the scratch track exhibits small damage. The potential slipping sites in the structure of the glass are randomly located. Then, the shear bands can potentially make the rupture bifurcate and leads to a “fine” tortuous fracture pattern like shown on the detail of Fig. 89. In the case of the anomalous SLS 4 glass, the scratch track is composed of fractures that can be qualified as *quasi-cleavage* pattern as described by Hull [25]. The homogeneity of the structure permits cleavage on relatively large surface due to the equal strength of bonds that are met by the tips of propagating cracks.

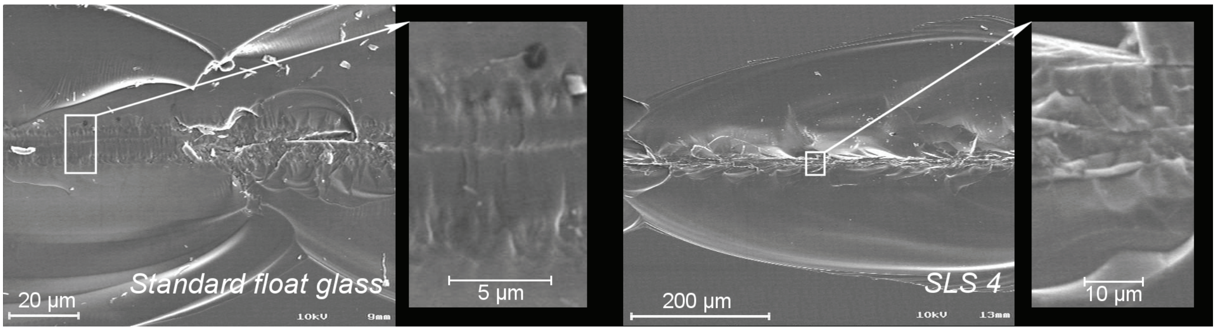

Fig. 89: Micro-cracking regime of a standard float glass and the SLS 4 glass and details of their scratch tracks. (SEM)

Lastly, the observation of the damage in the abrasive regime in function of the glass composition leads also to consistent conclusions with respect to sensitivity of the glasses to normal/anomalous behavior. The Fig. 90 shows details of abrasive regimes in the cases of the fused silica, the SLS 3 and the standard float glass. The fused silica exhibits the less tortuous track as expected in the light of previous conclusions; the SLS 3 shows large chipping process all along the track with quasi-cleavage patterns due to a higher trend to potential shearing in comparison to fused silica; under the sliding indenter the standard float glass produces long cracks and very fine and tortuous damage inside the track, comparable to the ones visible in the cracking regime.

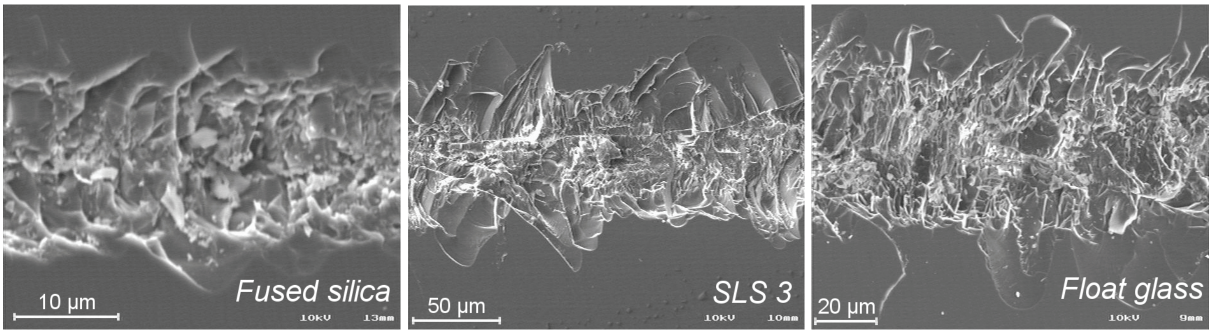

Fig. 90: Details of the micro-abrasive regime of a fused silica glass, the SLS 3 glass and a standard float glass. (SEM)

CHAPTER 5:
MECHANICAL MODELING

SUMMARY OF CHAPTER 5

5.1 Introduction: extension of Ahn's model

The nucleation of cracks and then the appearance of the associated damage can't be studied without considering the local stress distribution. This is a first clue in order to answer the following question: why is there some differences between the damage regimes with different indenter geometries? This is also true when changing the apex angle of a conical indenter as pointed out by Hagan et al. [53], or when testing different normal/anomalous glasses.

Moreover, most of studies (see [8, 20, 27] among others) consider that the singularities of an indenter like the Vickers one for example stay limited within the plastic zone and then does not influence the elastic stress field outside. This hypothesis can be considered as valid in most of the cases of indentation tests, but the proximity of the plastic zone boundary with a sliding indenter in the scratching direction suggests that this hypothesis may be too far from reality.

The first extension of Ahn's model that this work will deal with is to adapt Ahn's model to the singularity of a Vickers indenter. The part § 5.4 deals with this extension.

The second main extension concerns the materials. The chemical composition of the glasses influences dramatically their response to deformation and their damage behavior. The challenge in this study is to integrate these material particularities in the considered model. The part § 5.3 deals with this extension.

This chapter is dedicated to these two extensions of the existing model introduced by Ahn [20] derived from the work of Yoffe [27].

5.2 Description and new computation of Ahn's Model

Before adapting the model of Ahn to the Vickers indenter geometry and to the normal/anomalous behavior of glasses, the details of the existent method and a new calculation are needed. It could have been sufficient to quote the author's results, but the mismatch of the different sources about the formulation of the stress fields [20, 71, 72] calls for caution.

The model of Ahn is based on the axi-symmetric indentation model proposed by Yoffe [27]. As quoted earlier (§ 2.2.3.3.4), the complete stress field of Ahn is the superposition of the Boussinesq field (due to the point loading) and the *Blister* field for sliding (residual) as follows:

$$\sigma = \sigma^{n}_{Bous.} + \sigma^{t}_{Bous.} + \sigma^{r}_{Blister} \qquad \textbf{Eq. 119}$$

The coordinate system is a Cartesian one with the *x-y* plane corresponding to the surface of the indented material and the *z* axis oriented toward the depth of the solid.

The normal Boussinesq field corresponding to $\sigma^{n}_{Bous.}$ is given by Johnson [68]:

$$\sigma^{n}_{x} = \frac{P}{2\pi}\left[\frac{1-2\nu}{r^2}\left\{\left(1-\frac{z}{\rho}\right)\frac{x^2-y^2}{r^2}+\frac{zy^2}{\rho^3}\right\}-\frac{3zx^2}{\rho^5}\right] \qquad \textbf{Eq. 120}$$

$$\sigma^{n}_{y} = \frac{P}{2\pi}\left[\frac{1-2\nu}{r^2}\left\{\left(1-\frac{z}{\rho}\right)\frac{y^2-x^2}{r^2}+\frac{zx^2}{\rho^3}\right\}-\frac{3zy^2}{\rho^5}\right] \qquad \textbf{Eq. 121}$$

$$\sigma^{n}_{z} = -\frac{3P}{2\pi}\frac{z^3}{\rho^5} \qquad \textbf{Eq. 122}$$

$$\tau_{xy}^{n}=\frac{P}{2\pi}\left[\frac{1-2\nu}{r^{2}}\left\{\left(1-\frac{z}{\rho}\right)\frac{xy}{r^{2}}-\frac{xyz}{\rho^{3}}\right\}-\frac{3xyz}{\rho^{5}}\right] \qquad \textbf{Eq. 123}$$

$$\tau_{yz}^{n}=-\frac{3P}{2\pi}\frac{yz^{2}}{\rho^{5}} \qquad \textbf{Eq. 124}$$

$$\tau_{zx}^{n}=-\frac{3P}{2\pi}\frac{xz^{2}}{\rho^{5}} \qquad \textbf{Eq. 125}$$

already reported in § 2.2.3.3.2 as Eq. 37 to Eq. 42. r and ρ are defined in Eq. 43 and Eq. 44 respectively.

The tangential Boussinesq field corresponding to $\sigma_{Bous.}^{t}$ is given by Johnson [68]:

$$\sigma_{x}^{t}=-\frac{Q}{2\pi}\left[\frac{3x^{3}}{\rho^{5}}-(1-2\nu)\left\{\frac{x}{\rho^{3}}-\frac{3x}{\rho(\rho+z)^{2}}+\frac{x^{3}}{\rho^{3}(\rho+z)^{2}}+\frac{2x^{3}}{\rho^{2}(\rho+z)^{3}}\right\}\right] \qquad \textbf{Eq. 126}$$

$$\sigma_{y}^{t}=-\frac{Q}{2\pi}\left[\frac{3xy^{2}}{\rho^{5}}-(1-2\nu)\left\{\frac{x}{\rho^{3}}-\frac{x}{\rho(\rho+z)^{2}}+\frac{xy^{2}}{\rho^{3}(\rho+z)^{2}}+\frac{2xy^{2}}{\rho^{2}(\rho+z)^{3}}\right\}\right] \qquad \textbf{Eq. 127}$$

$$\sigma_{z}^{t}=-\frac{Q}{2\pi}\frac{3xz^{2}}{\rho^{5}} \qquad \textbf{Eq. 128}$$

$$\tau_{yz}^{t}=-\frac{Q}{2\pi}\frac{3xyz}{\rho^{5}} \qquad \textbf{Eq. 129}$$

$$\tau_{yz}^{t}=-\frac{Q}{2\pi}\frac{3x^{2}z}{\rho^{5}} \qquad \textbf{Eq. 130}$$

$$\tau_{xy}^{t}=-\frac{Q}{2\pi}\left[\frac{3xy^{2}}{\rho^{5}}+(1-2\nu)\left\{\frac{y}{\rho(\rho+z)^{2}}-\frac{x^{2}y}{\rho^{3}(\rho+z)^{2}}-\frac{2x^{2}y}{\rho^{2}(\rho+z)^{3}}\right\}\right] \qquad \textbf{Eq. 131}$$

already reported in § 2.3.1 as Eq. 95 to Eq. 100.

Q is the concentrated tangential load (see Fig. 52) that can be replaced by μP with μ the friction coefficient of the considered contact and P the normal load, r and ρ are defined in Eq. 43 and Eq. 44 respectively.

It remains to find the sliding *Blister* field for the Eq. 119 which is calculated from the expression of Yoffe's indentation model.

The stresses of the *Blister* field are formulated as follow in a spherical coordinate system by Yoffe [27]:

$$\sigma_{r}=\frac{A}{r^{3}}4\left[(5-\nu)\cos^{2}\theta-(2-\nu)\right] \qquad \textbf{Eq. 132}$$

$$\sigma_{\theta}=-\frac{A}{r^{3}}2(1-2\nu)\cos^{2}\theta \qquad \textbf{Eq. 133}$$

$$\sigma_{\phi}=\frac{A}{r^{3}}2(1-2\nu)\left(2-3\cos^{2}\theta\right) \qquad \textbf{Eq. 134}$$

$$\tau_{r\theta}=\frac{A}{r^{3}}4(1+\nu)\sin\theta\cos\theta \qquad \textbf{Eq. 135}$$

already reported in § 2.2.3.3.6.3 as Eq. 67 to Eq. 70 with r defined in Eq. 43. Note that to avoid ambiguities in the following development, the notation of the *Blister* field strength have been changed to A (instead of B).

The spherical form of Yoffe's equations gives in Cartesian coordinates:

$$\sigma_x^r = 2A\left[\frac{(1-2\nu)(x^2+2y^2)}{r^2\rho^3} + \frac{(-5+4\nu)x^2}{\rho^5} - \frac{(1-2\nu)(2x^2+3y^2)z^2}{r^2\rho^5} + \frac{15x^2z^2}{\rho^7}\right] \quad \textbf{Eq. 136}$$

$$\sigma_y^r = 2A\left[\frac{(1-2\nu)(2x^2+y^2)}{r^2\rho^3} + \frac{(-5+4\nu)y^2}{\rho^5} - \frac{(1-2\nu)(3x^2+2y^2)z^2}{r^2\rho^5} + \frac{15y^2z^2}{\rho^7}\right] \quad \textbf{Eq. 137}$$

$$\sigma_z^r = -2A\left[\frac{1-2\nu}{\rho^3} + \frac{2(4+\nu)z^2-(1-2\nu)r^2}{\rho^5} - \frac{15z^4}{\rho^7}\right] \quad \textbf{Eq. 138}$$

$$\tau_{xy}^r = -2A\left[\frac{(1-2\nu)xy}{r^2\rho^3} + \frac{(5-4\nu)xy}{\rho^5} - \frac{(1-2\nu)xyz^2}{r^2\rho^5} - \frac{15xyz^2}{\rho^7}\right] \quad \textbf{Eq. 139}$$

$$\tau_{yz}^r = -2A\left[\frac{6yz}{\rho^5} - \frac{15yz^3}{\rho^7}\right] \quad \textbf{Eq. 140}$$

$$\tau_{xz}^r = -2A\left[\frac{6xz}{\rho^5} - \frac{15xz^3}{\rho^7}\right] \quad \textbf{Eq. 141}$$

The superscript r denotes the residual character of the stresses in this field. r and ρ are defined in Eq. 43 and Eq. 44 respectively.

The scratching model of Ahn takes the Eq. 119 and the detail of the fields expressions as a basis. The scratch process is assumed to be successive quasi-static indentation steps, so that the superposition of the stress field can be considered. Practically, it corresponds to the plastic deformation accumulation along the scratch behind the indenter. The residual stress field due to the plastic zone in the indentation problem is Yoffe's *Blister* field. Then, this field has been integrated by Ahn to constitute the *sliding Blister* field (i.e. adapted to scratching), as a superposition of the quasi-static indentation *Blister* field all along the scratch. Then, the static *Blister* field is integrated from –infinity (the scratch beginning is considered as infinitely far) to 0 (the actual indenter position) to take into account the accumulation effect of the residual stresses. To do so, let A be the strength of the static *Blister* field and B the strength of the *Blister* field per length unit as:

$$A = B(\xi)\,d\xi \quad \textbf{Eq. 142}$$

Let's take the following notation:

$$\sigma_x^r = Af_\sigma(x,y,z) \quad \textbf{Eq. 143}$$

Then, the accumulation of the residual stress field gives:

$$\sigma_x^r = \int_{x_0}^{x_1} B(\xi)f_\sigma(x-\xi,y,z)\,d\xi \quad \textbf{Eq. 144}$$

for an indenter which scratches from x_0 to x_1.

Let's consider that the scratch starts infinitely far. The integration goes from $x_0 = -\infty$ to $x_1 = 0$:

$$\sigma_x^r = \int_{-\infty}^{0} B(\xi) f_\sigma(x-\xi, y, z) d\xi \qquad \textbf{Eq. 145}$$

Then, this sliding *Blister* field represents the residual stress field due to the accumulated plastic zone all along the scratch. The *Point Loading* stress field does not need modification for scratching because it represents the stress field due to the loading indenter on the sample, which continuously moves and does not accumulate along the scratch. Then, the Boussinesq field is kept like in the quasi-static indentation model. The complete stress field of Ahn, compared to Yoffe's expression for indentation Eq. 85, can be summarized as follows:

$$\sigma = \sigma_{Bous.}^{n} + \sigma_{Bous.}^{t} + \sigma_{Blister\ for\ scratching}^{r} \qquad \textbf{Eq. 146}$$

After the integration of Eq. 136 to Eq. 141, the final result of the scratching *Blister* field gives:

$$\sigma_x^r = 2B\left[\frac{-2\nu\left(y^2-z^2\right)}{\left(y^2+z^2\right)^2} + \frac{x}{\left(y^2+z^2\right)^2\rho^5}\left(2\nu x^4y^2 - 2x^2y^4 + 6\nu x^2y^4 - 2y^6 + 4\nu y^6 - 2\nu x^4z^2 \right.\right.$$
$$\left.\left. -4x^2y^2z^2 + 2\nu x^2y^2z^2 - 3y^4z^2 + 6\nu y^4z^2 - 2x^2z^4 - 4\nu x^2z^4 + z^6 - 2\nu z^6\right)\right] \qquad \textbf{Eq. 147}$$

$$\sigma_y^r = 2B\left[\frac{-2y^2\left(y^2-3z^2\right)}{\left(y^2+z^2\right)^3} + \frac{x}{\left(y^2+z^2\right)^3\rho^5}\left(2x^4y^4 + 6x^2y^6 - 2\nu x^2y^6 + 4y^8 - 2\nu y^8 - 6x^4y^2z^2 \right.\right.$$
$$-7x^2y^4z^2 - 6\nu x^2y^4z^2 - 2y^6z^2 - 8\nu y^6z^2 - 12x^2y^2z^4 - 6\nu x^2y^2z^4 - 15y^4z^4$$
$$\left.\left. -12\nu y^4z^4 + x^2z^6 - 2\nu x^2z^6 - 8y^2z^6 - 8\nu y^2z^6 + z^8 - 2\nu z^8\right)\right] \qquad \textbf{Eq. 148}$$

$$\sigma_z^r = 2B\left[\frac{2z^2\left(-3y^2+z^2\right)}{\left(y^2+z^2\right)^3} + \frac{xz^2}{\left(y^2+z^2\right)^3\rho^5}\left(6x^4y^2 + 15x^2y^4 + 9y^6 - 2x^4z^2 + 10x^2y^2z^2 \right.\right.$$
$$\left.\left. +12y^4z^2 - 5x^2z^4 - 3y^2z^4 - 6z^6\right)\right] \qquad \textbf{Eq. 149}$$

$$\tau_{xy}^r = 2B\left[\frac{-y\left(2x^2 - 2\nu x^2 + 2y^2 - 2\nu y^2 - z^2 - 2\nu z^2\right)}{\rho^5}\right] \qquad \textbf{Eq. 150}$$

$$\tau_{yz}^r = 2B\left[\frac{-4yz\left(y^2-x^2\right)}{\left(y^2+z^2\right)^3} + \frac{xyz}{\left(y^2+z^2\right)^3\rho^5}\left(4x^4y^2 + 10x^2y^4 + 6y^6 - 4x^4z^2 + 3y^4z^2 - 10x^2z^4 \right.\right.$$
$$\left.\left. -12y^2z^4 - 9z^6\right)\right] \qquad \textbf{Eq. 151}$$

$$\tau_{zx}^{r} = 2B\left[\frac{-z\left(2x^2+2y^2-z^2\right)}{\rho^5}\right] \qquad \textbf{Eq. 152}$$

B represents the strength of the sliding *Blister* field, ρ is defined in Eq. 44.

The mismatch of the different literature sources about the formulation of the sliding *Blister* stress field can now be clarified: Eq. 136 to Eq. 141 have been correctly written in the references [20, 71] and Eq. 147 to Eq. 152 in the references [71, 72].

5.3 Extension of Ahn's model to the normal/anomalous glasses - Principle

Everything tends to prove that the key in understanding the mechanisms of deformation and damage in glasses is the competition between densification and shear. In fact, while their chemical compositions are relatively close, the difference between regimes apparition during scratching of the six different considered glasses is effective.

It is the view point of the author that the intermediate behavior (normal/anomalous) is not expected to be linear (densification occurs until maximum compaction and then shear appears for example). Then the problem of the deformation under load of this glass series can be formulated as follows: the deformation behavior is due to both i) the deformation by densification and ii) the deformation by local shearing. The tendency to densification depends greatly from the chemical composition of the considered glass. Then, the subject of this study is to analyze the proportion of densification and the shearing process contribution in the deformation: the *competition Densification/Shearing* which is completely unknown *a priori*. To the knowledge of the author, no analytical model exists yet and even the understanding of the competition and its consequences on the glass behavior is an almost pristine field of research. Then the contribution of densification or shearing process will essentially be determined from experimental considerations. The identification of the densification/shearing competition in order to integrate it into the semi-analytical model will be discussed in § 5.7.

Adapting the previously given stress field (Eq. 135) to normal/anomalous glasses will lead to the form:

$$\sigma_{normal/anomalous\ glasses} = \sigma_{Bous.}^{n} + \sigma_{Bous.}^{t} + \sigma^{r}_{\substack{Blister\ for\ scratching \\ normal/anomalous\ glasses}} \qquad \textbf{Eq. 153}$$

5.4 Extension of Ahn's model to the Vickers indenter - Principle

Because of its geometric singularities, the stress field derived from the contact of a Vickers indenter had never been modeled analytically and its integration in an analytical model is obviously issued from a numerical way and then leads to a *semi-analytical model*.

Contrary to the extension of the model to normal/anomalous glasses, both stress *Blister* and *Point Loading* fields are concerned by the extension to Vickers geometry. The *Point Loading* model needs to be replaced by a model closer to the experimental reality of a scratch by a Vickers indenter. This extension will be developed in § 5.6 through a Finite Elements study performed with the help of the Abaqus code (version 6.2) and dealing with the difference between a conical and a Vickers indentation. Lastly, the *Blister* field will be extended to the Vickers geometry at the same time as it will be extended to the normal/anomalous glasses. In fact, the experimental development detailed in § 5.7 will take into account both the normal/anomalous characters and Vickers singularities at the same time. These considerations will be integrated in the expected final model and the Eq. 153 previously adapted to normal/anomalous glasses will become:

$$\sigma_{\substack{normal/anomalous \\ Vickers}} = \sigma^{n}_{Vickers} + \sigma^{t}_{Vickers} + \sigma^{r}_{\substack{Blister\ for\ scratching \\ normal/anomalous\ glasses \\ Vickers}} \qquad \textbf{Eq. 154}$$

The terms $\sigma^{n}_{Vickers} + \sigma^{t}_{Vickers}$ correspond to the indenter loading.

The term $\sigma^{r}_{\substack{Blister\ for\ scratching \\ normal/anomalous\ glasses \\ Vickers}}$ corresponds to the residual stresses.

The way chosen in this work to treat the Vickers integration is to use the F.E. method in order to give some analytical trends of the stress fields.

5.5 Summary of the method / expected final stress field form

It is useful to keep in mind the following organization chart which summarizes the method used to extend the Yoffe and Ahn's models to the normal/anomalous character and Vickers indenter geometry in scratching.

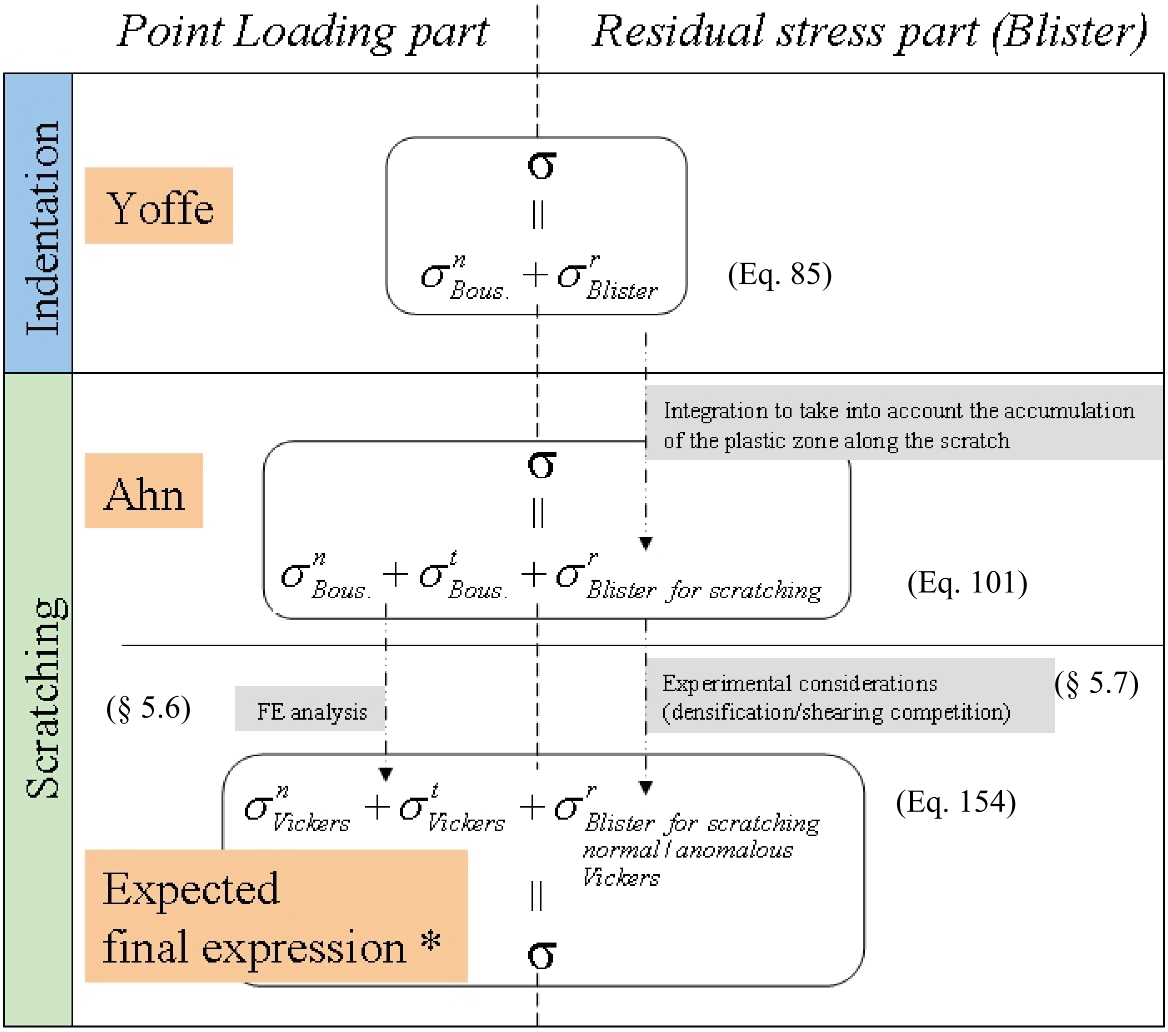

* The approximated final expression will be discussed in § 5.8.

Fig. 91: Organization chart to extend the model to normal/anomalous glasses and Vickers indenter.

5.6 Extension of Ahn's model to the Vickers indenter: the F.E. study

5.6.1 Introduction

The Finite Element Method (F.E.M.) approach is not the final goal of this study. Actually, it will take place in the extension of the analytical model of scratching to the Vickers geometry. However, the role of this numerical approach is very important: it deals with the analysis of the stress field in a material that is penetrated by a Vickers indenter in comparison with the stress field imposed by a conical indentation. The final goal is to integrate relevant parameters in the semi-analytical model that will take into account the geometric singularities of the Vickers indenter. This semi-analytical model is based on formulae derived from indentation models. So, the study will take place in the indentation context. Finally, the analytical formulae, that will be obtained, will be integrated to lead to the expected model of scratching adapted to the Vickers geometry of the indenter. Thus the topic of this study is: *Designing Finite Elements tools for the analysis of stress field due to Vickers indentation in comparison to the conical indentation.* This study prompts for a 4-months collaboration at EMPA in Thun (Switzerland) in summer 2004 in the Micromechanics and Micropatterning Group directed by J. Michler.

Lastly, note that the stress field in the analytical model as defined by Ahn and Yoffe are *elastic* fields that are added. As a consequence, the numerical simulations need only to be carried out with a perfectly elastic material.

5.6.2 General aim of the study

This study is divided in three main parts. The first part (§ 5.6.3) will be about the simulation in two dimensions of a conical indentation on a perfectly elastic body. It will be also the opportunity to improve the mesh and simulation parameters in the aim to tackle the second part more easily. This second part (§ 5.6.4) is far more critical. It deals with the three dimensional simulation of a Vickers indentation on a perfectly elastic body. The third part deals with the comparison between the indentation performed with a conical indenter and the one performed with a Vickers indenter.

5.6.3 2-D problem

5.6.3.1 Involved geometries

The geometries involved in this problem consist in two parts: i) the conical indenter defined as rigid and, ii) the indented body defined as a deformable and perfectly elastic solid. Its mechanical characteristics will be the ones of a soda-lime silica glass: E=70 GPa and ν=0.21.

5.6.3.2 Mesh

The mesh was built for the half space of the problem. Several meshes were designed before reaching an *optimized* one for the problem. The detail of this choice and the different tries are reported in Appendix 2. The optimized mesh is depicted in Fig. 92.

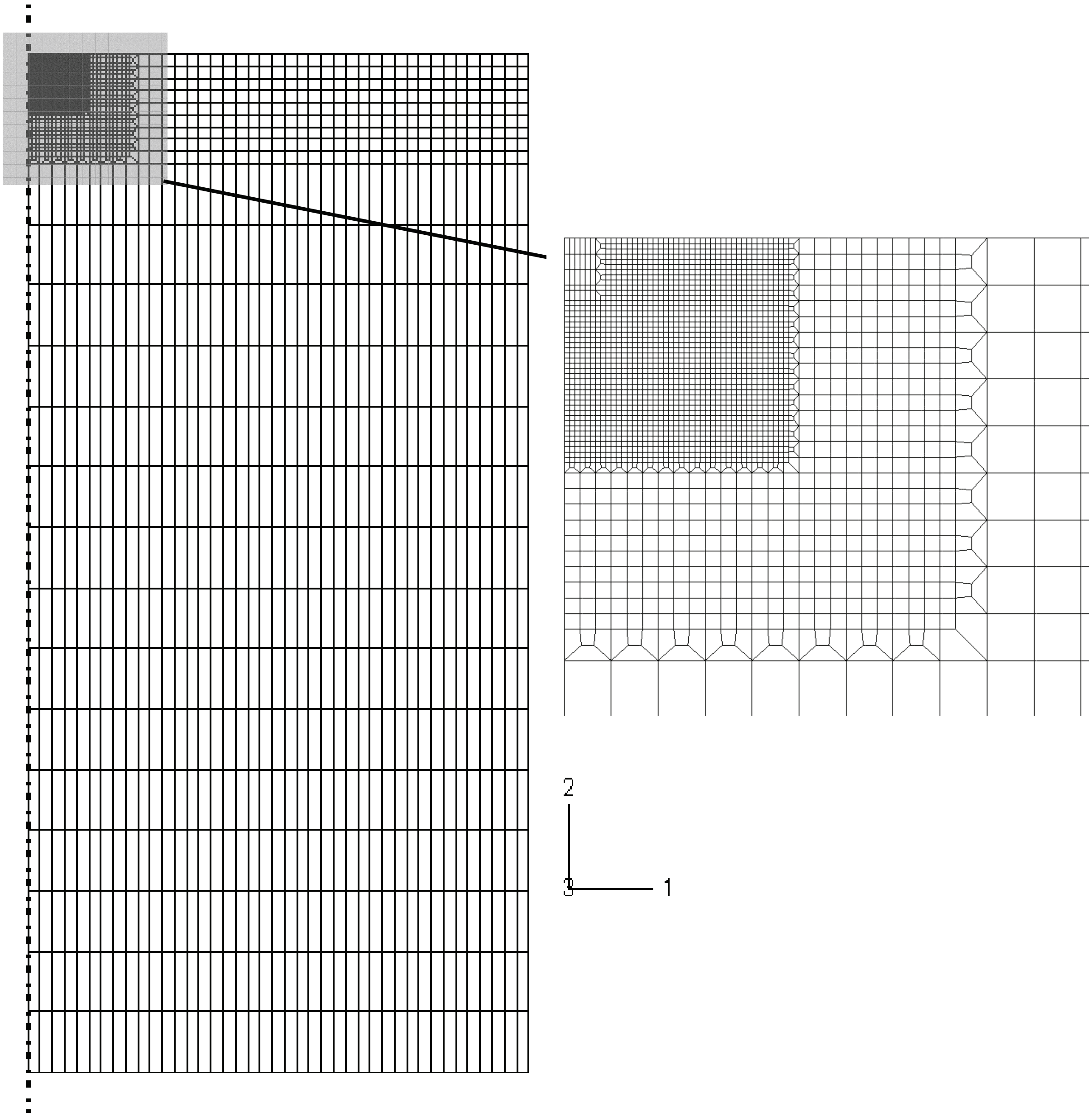

Fig. 92: Optimized mesh for the axi-symmetric 2-D problem of indentation.

The different characteristics of the mesh are summarized as follows:
Number of elements: 3282
Smallest size of element: 0.2 µm
Size of the indented body: 73.8x150.4 μm^2
Note that all the elements that compose the mesh are quadrilateral elements of linear type (CAX4 Abaqus code).

5.6.3.3 Boundary conditions

The boundary conditions are illustrated in Fig. 93. During the loading-unloading sequence, the bottom of the sample is constrained to 0 on the axis 2. The left boundary of the mesh (axis of symmetry) is constrained to evolve only on the axis 2. This is also the case for the indenter.

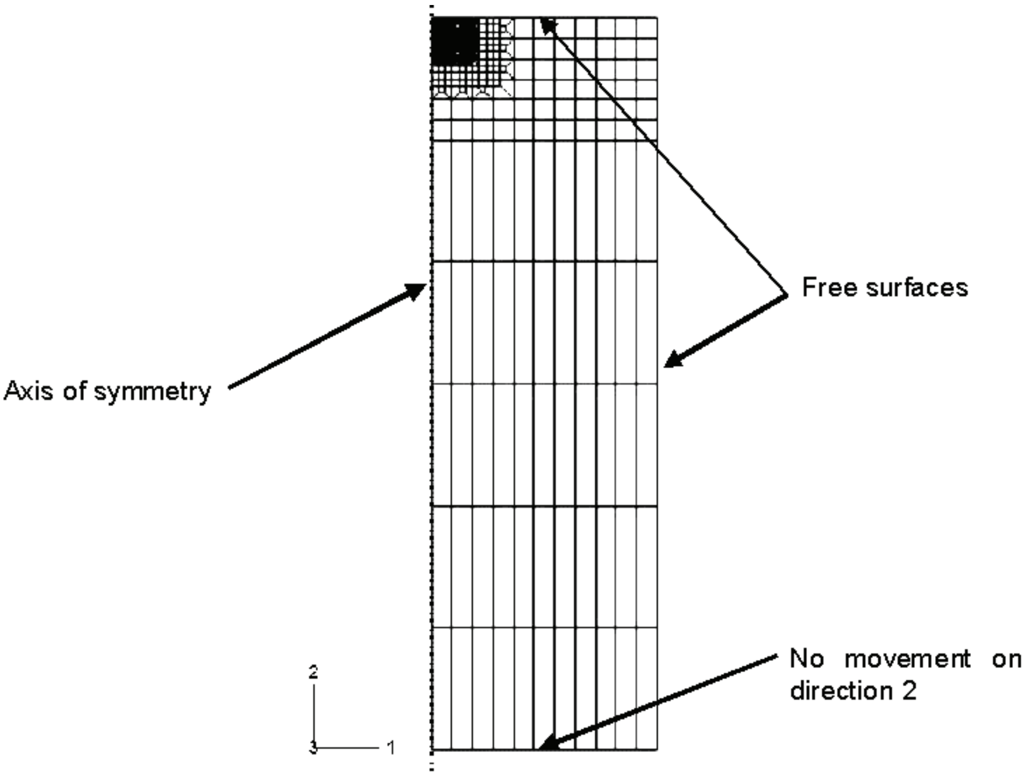

Fig. 93: Scheme of boundary conditions applied on the indented body.

5.6.3.4 Loading sequence

The loading sequence had been designed as follows:

1. Initial: initial step of the simulation.
2. Contact: initiation of the contact between the indenter and the elastic body.
3. Load: loading part of the sequence; the load reaches a value of 3 N at the end of this step.
4. Unloading: unloading part of the sequence; the load goes back to 0 N.
5. Indenter_Escape: the indenter leaves the surface.

5.6.3.5 Validation

5.6.3.5.1 Criteria to discriminate the meshes

The 2-D model was designed in order to make it evolve to the 3-D Vickers model. Nevertheless, the direct validation of the 3-D model leads to several difficulties: problems in comparison with experimental data, no theoretical expressions available for comparison,... Then, it will consist in validating only the 2-D model by comparison to some theoretical parameters. Afterwards, the validation of the 3-D model will be assumed by the simple validation of the 2-D one.

In order to validate the 2-D elastic simulation, some criteria inspired from literature have been designed:

1. An interesting parameter is the ratio between the maximum depth of indentation h on the depth between the last point in contact and the deepest point of indentation h_p as illustrated on Fig. 94.

Fig. 94: Definition of the depths *h* and h_p used to determine the γ coefficient.

This ratio is named γ [82]:

$$\gamma = \frac{h}{h_p} \quad \textbf{Eq. 155}$$

The comparison between a theoretical value of the γ coefficient and a simulated one is needed.

Theoretically, $\gamma = \frac{\pi}{2}$ [77] in the elastic case (conical indenter) and does not vary with the material parameters *E* and *v*. A simple test is to make these parameters vary and validate the hypothesis.

2. The theoretical deformed shape of the surface is given by Sneddon [76]. The comparison with the simulated one is a third good criterion to validate the elastic model.
3. Sneddon [82] gives the pressure distribution on the indenter by Eq. 156 (also reported by Johnson [68]). It is possible to verify this distribution in the elastic F.E. model.

$$p(x) = \frac{E\cot\alpha}{2(1-\nu^2)}\cosh^{-1}\left(\frac{a}{x}\right) \quad \textbf{Eq. 156}$$

Note that it is assumed in this validation part that some of these criteria are based on the work of Sneddon. Nevertheless, it has to be noted that Sneddon's model is open to criticism. Actually, the radial displacement of the matter during the conical indentation has been largely ignored by Sneddon as pointed out by Hay et al. [108].

5.6.3.5.2 γ evolution criterion

The coefficient γ was determined for different loads up to 3 N during a simulation. The results are reported in the Graph 28.

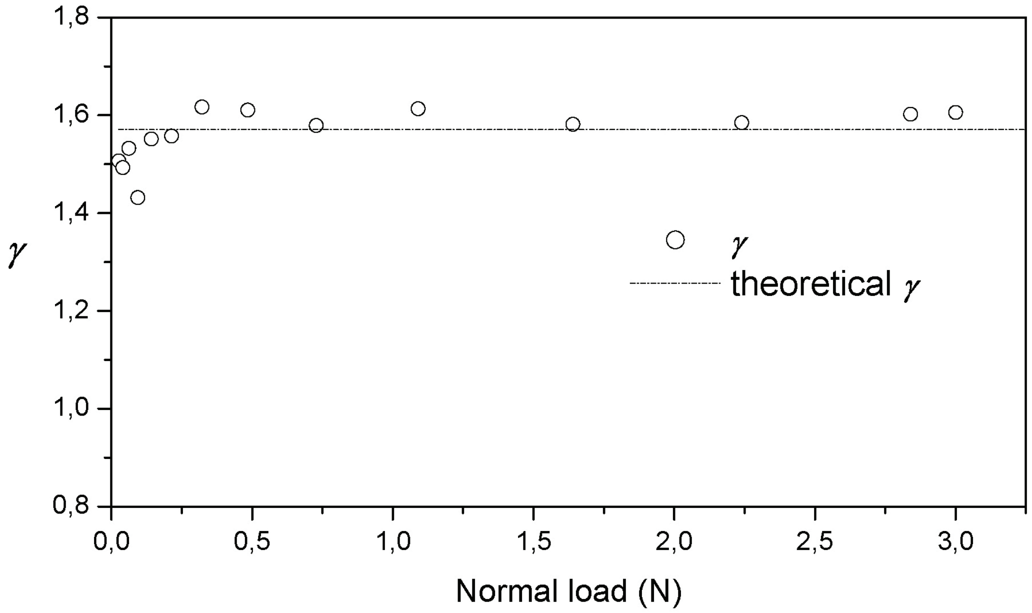

Graph 28: ***γ*** **evolution with respect to the normal load.**

Due to the mesh sampling, the first points lose accuracy compared to points at higher loads. At sufficient high loads to avoid this effect (i.e. > 0.3 N), the relative error between the theoretical γ value and the Finite Element γ coefficient is less than 3 %. This validates the model for this point.

Theoretically, the γ coefficient does not depend on the elastic properties, i.e. on the values of the Young's modulus E and the Poisson ratio ν [77]. Simulations with varying E from 10 GPa up to 300 GPa were performed with 3 N of normal load. The result on the evolution of γ is reported in the Graph 29.

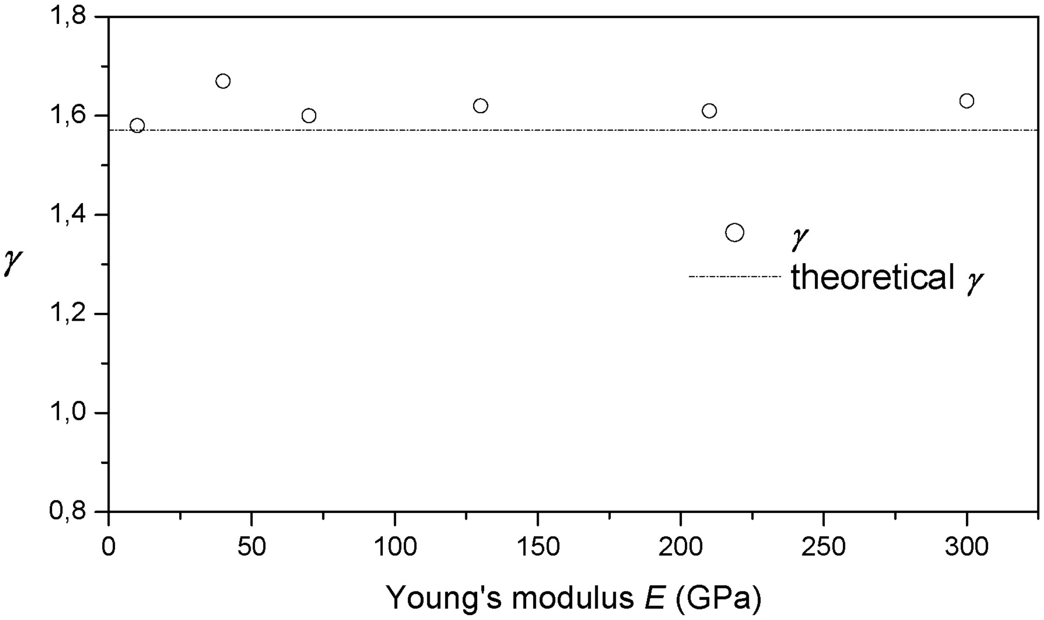

Graph 29: γ evolution with respect to the Young's modulus *E*.

The relative error between the theoretical γ value and the Finite Element γ coefficient, when E varies, is less than 6 %.

In the same way, ν was made to vary from 0.1 up to 0.5 and the evolution of γ was studied with 3 N of normal load. The results are shown in the Graph 30.

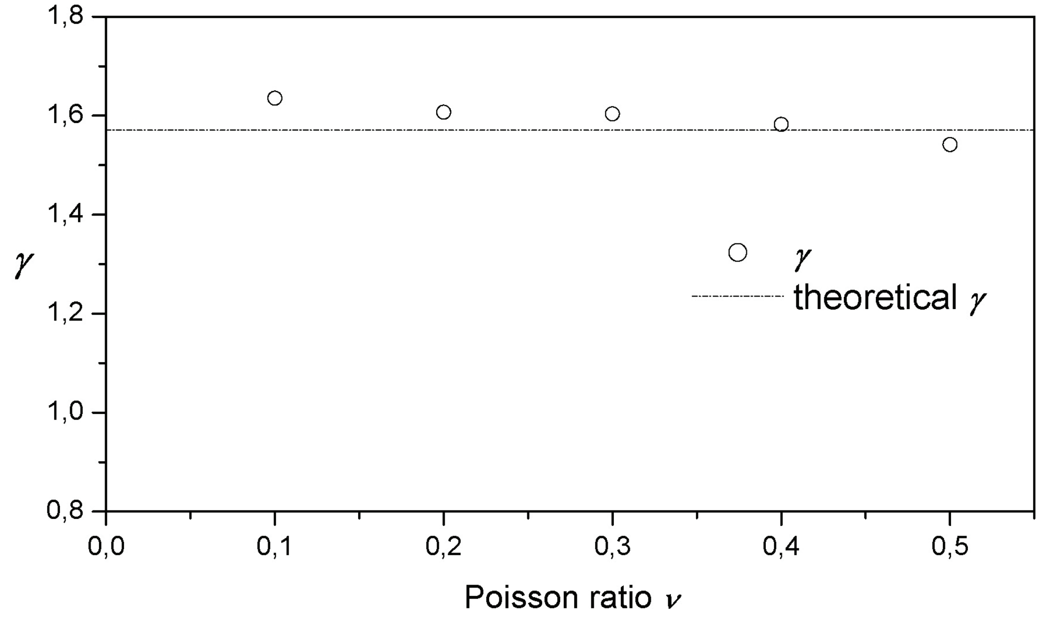

Graph 30: γ evolution with respect to the Poisson's ratio ν.

The relative error between the theoretical γ value and the Finite Elements γ coefficient, when ν varies, is less than 4.11 %.
These criteria validate the model from this point of view.

5.6.3.5.3 Profile of the surface under load

The theoretical profile of the surface is given by Sneddon [76]:

$$\left[u_z(r)\right]_{z=0} = \varepsilon\left(\frac{1}{2}\pi - \frac{r}{a}\right) \text{ when } r < a \qquad \textbf{Eq. 157}$$

$$\left[u_z\left(\frac{r}{a}\right)\right]_{z=0} = \varepsilon\left\{\sin^{-1}\left(\frac{a}{r}\right) + \sqrt{\left(\frac{r}{a}\right)^2 - 1} - \frac{r}{a}\right\} \text{ when } r > a \qquad \textbf{Eq. 158}$$

with $\varepsilon = a\cot\alpha$ where a is the contact radius, α the semi-apex angle of the conical indenter and r defined in Eq. 43.
The Graph 31 shows the profiles obtained with Finite Elements Method for different loads from 0.322 N up to 3 N. The two thick lines represent the Sneddon's profiles for the extreme loads. The F.E.M. profiles are in good agreement with the theoretical ones.

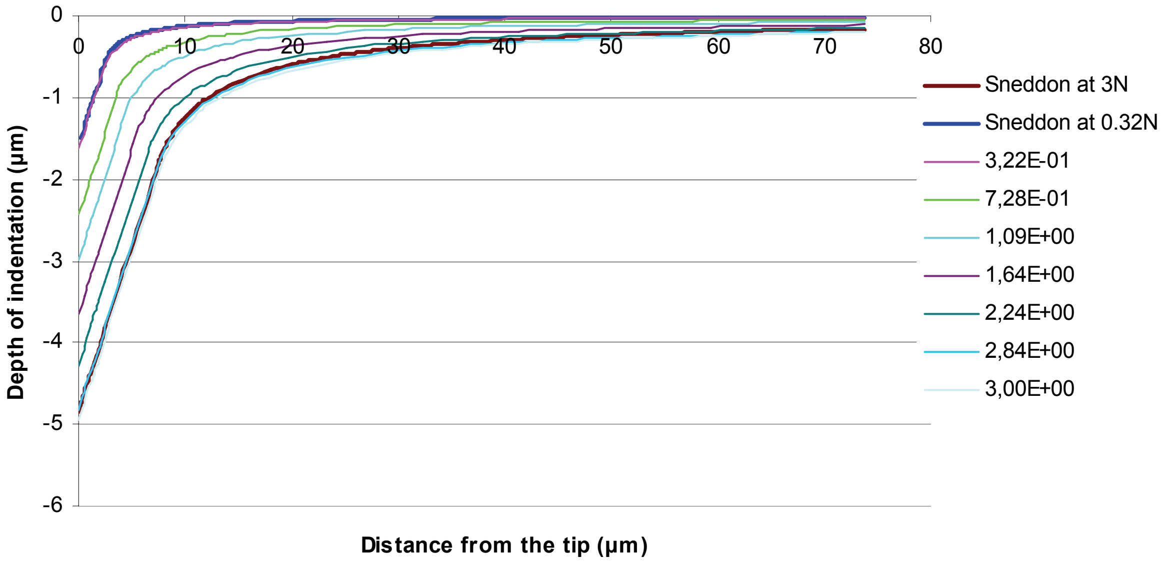

Graph 31: Profile of indentation with respect to the normal load.

5.6.3.5.4 The pressure distribution on the indenter

This last criterion considers the pressure distribution on the indenter under load. The Eq. 156 gives the theoretical pressure on the indenter. Graph 32 represents the pressure distribution on the indenter given by the F.E.M. for different normal loads and the Sneddon's solution for the two extreme loads (0.485 N up to 3 N), represented by the two thick lines.

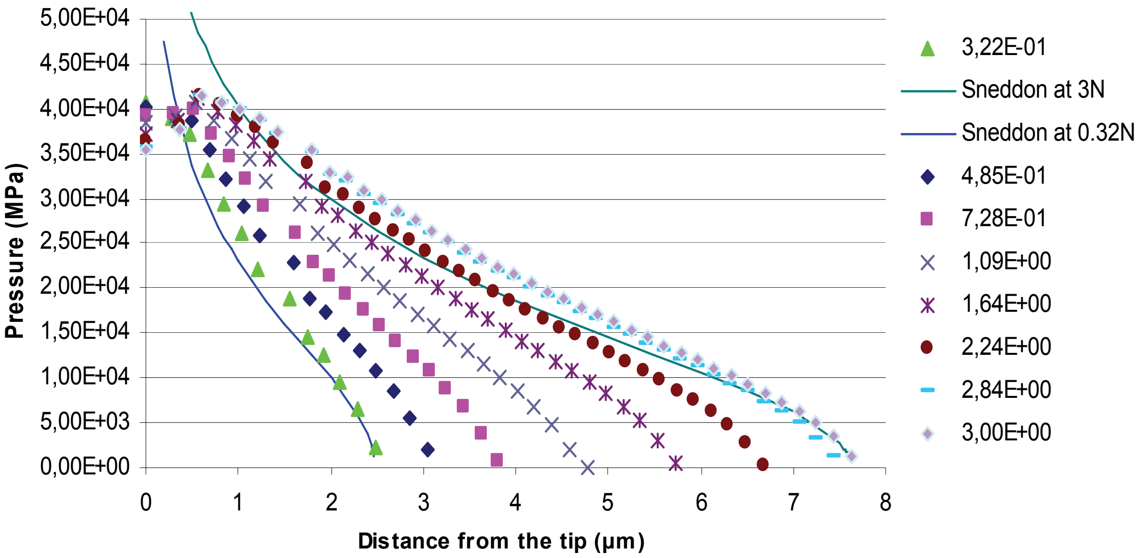

Graph 32: Repartition of the pressure on a conical indenter. Plotted on the half indenter.

The theoretical distribution of pressure exhibits an infinite value for x=0 because of the tip singularity at this abscissa. This value is of course not reported in the F.E.M. distribution because not realistic. This explains the deviation of the pressure values for points close to the tip. The global load is the same between the theoretical distribution of pressure and the F.E.M. one. The deviation of the pressure close to the tip has a direct repercussion on the whole distribution. This explains the slightly deviation of the global distribution of the pressure. Note the pressure decreases brutally on the closest points to the tip with the F.E.M. method. This corresponds to over-deformed elements that are "turned upside-down" and relaxed (in displacement sense) by Abaqus in order to finish the numerical calculation.

5.6.4 3-D Problem

5.6.4.1 Mesh: Strategy

The strategy adopted was to generate a mesh from the optimized 2-D mesh that was validated previously. The "symmetric model generation" command of Abaqus software was used. It allowed in our case to generate the 3-D mesh by revolution of the 2-D mesh along the axis common with the indenter on 45° because of symmetry considerations of the Vickers indentation problem as evoked in § 2.2.3.4.3.2.. Then 9 stages of elements were designed along the revolution of 45° of the original 2-D mesh for the Vickers model (see Fig. 95).

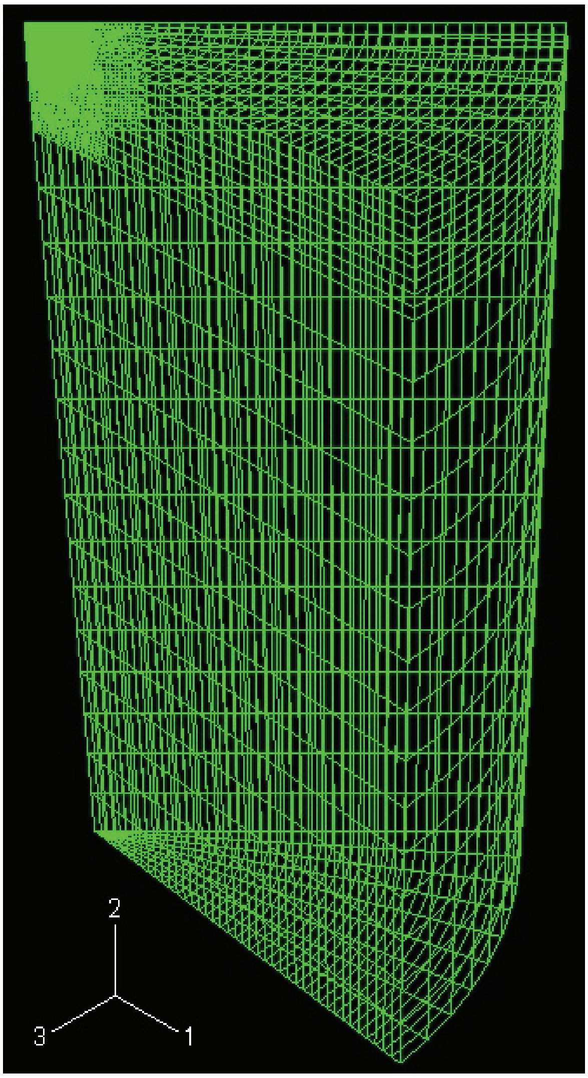

Fig. 95: 3-D mesh of the indented body adapted to Vickers indentation – perspective view.

5.6.4.2 Boundary conditions and loading sequence

The boundary conditions are somewhat similar to those of the 2-D model. During the loading-unloading sequence, the bottom of the sample is constrained to 0 on the axis 2. The two extreme faces (at 0° and 45°) have a symmetry condition to their respective normal vectors. The top and the "behind" parts are free surfaces. The indenter is constrained to evolve only on the axis 2. The boundary conditions are summarized in Fig. 96.

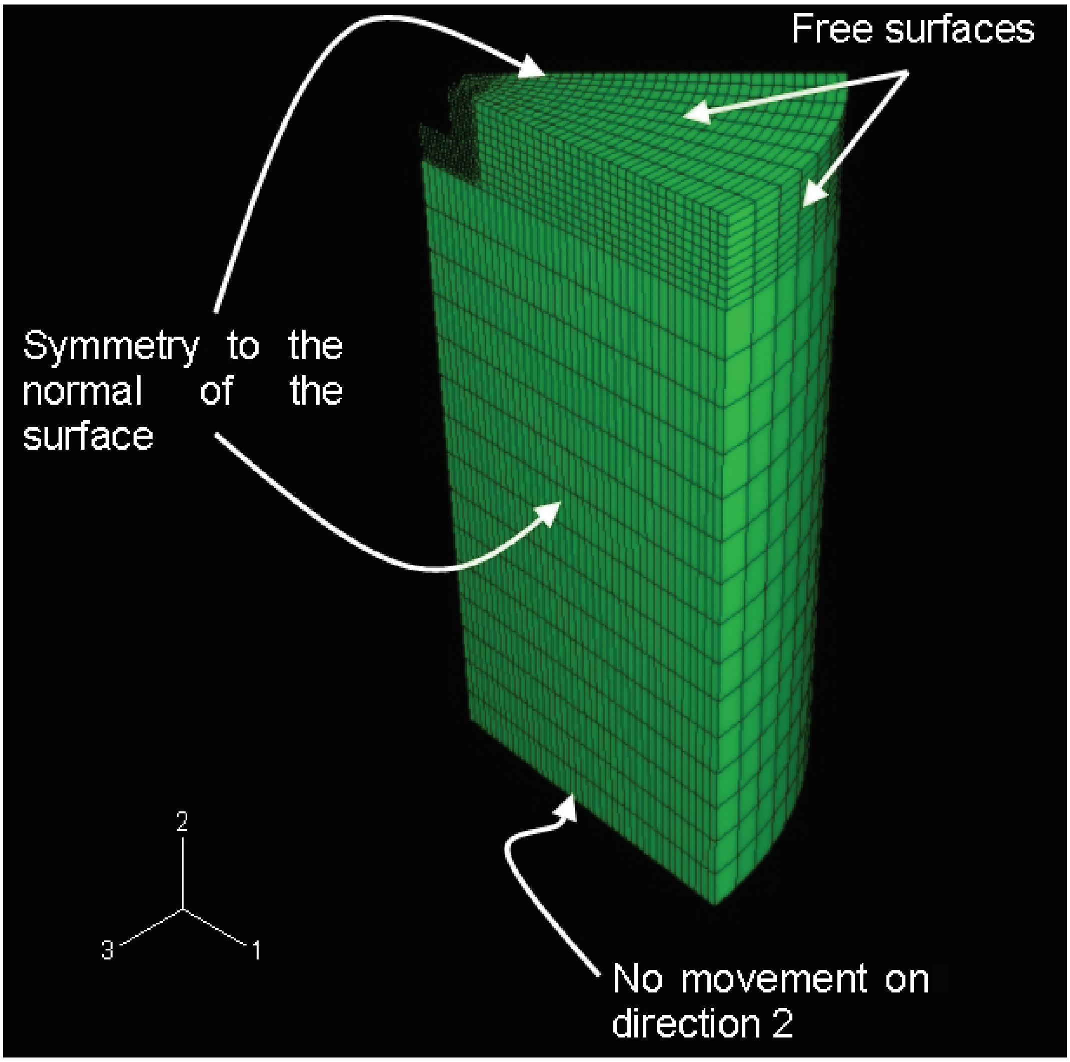

Fig. 96: Boundary conditions on the 3D mesh adapted for the Vickers problem.

5.6.4.3 Loading sequence

The loading sequence is exactly the same as for the 2-D axi-symmetric case and is designed as follows:

1. Initial: initial step of the simulation.
2. Contact: initiation of the contact between the indenter and the elastic body.
3. Load: loading part of the sequence; the load reaches a value of 3 N at the end of this step.
4. Unloading: unloading part of the sequence; the load goes back to 0 N.
5. Indenter_Escape: the indenter leaves the surface.

5.6.4.4 Insertion of the Vickers indenter in the 3-D model

As for Giannakopoulos et al. [84], only 1/8 of the Vickers indenter will be modeled because of its symmetry order of 8. The indenter is defined as discrete rigid and only the surface that may enter in contact with the indented material is modeled. The elements used for the mesh are only 2-D elements. The advantages of these choices are i) the drastic reduction of the number of elements (because the volume of the indenter is not meshed) and, ii) the calculation on 2-D rigid elements is greatly simplified. Its insertion on the F.E.M. model is represented on Fig. 97 and Fig. 98.

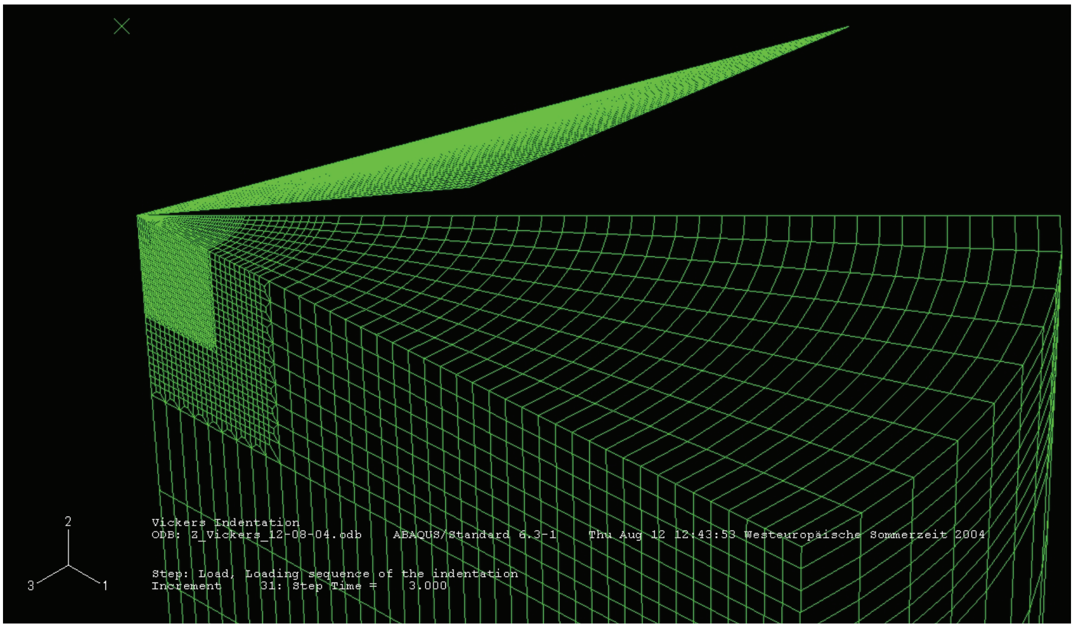

Fig. 97: The body and the indenter in the mesh module of Abaqus - Perspective view.

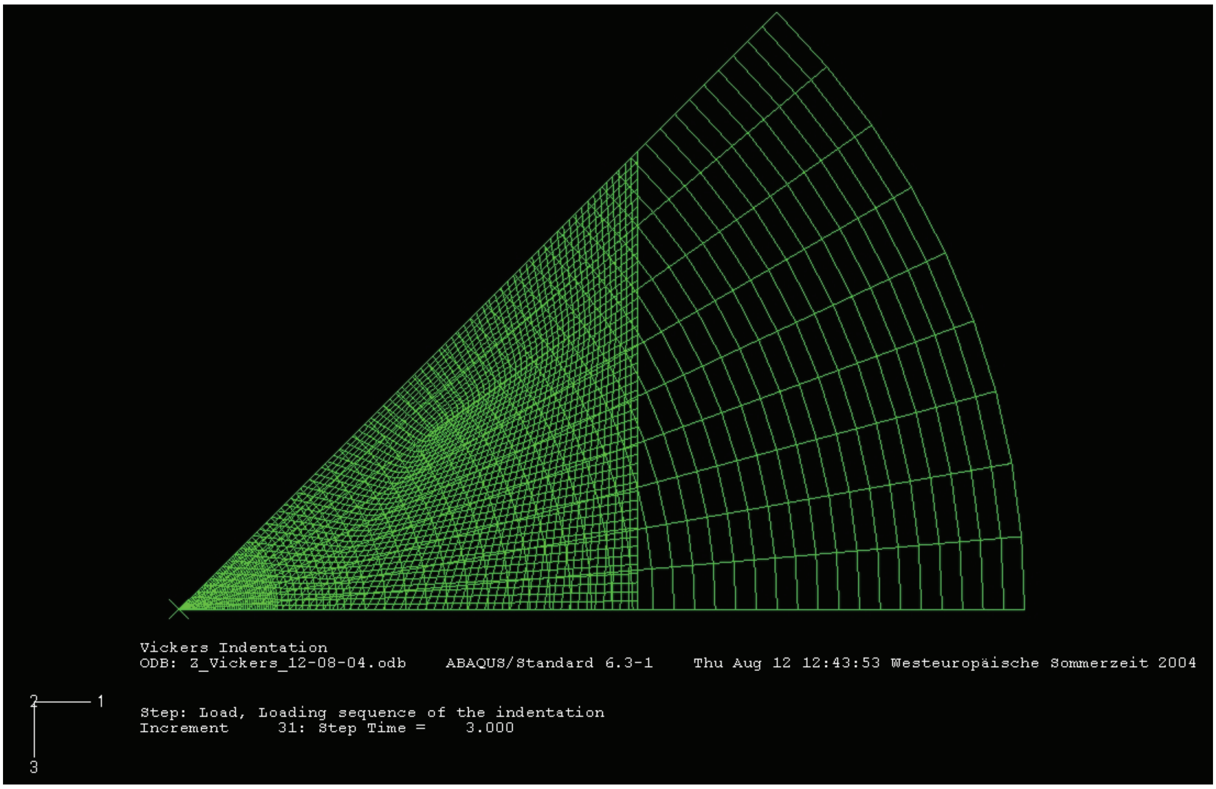

Fig. 98: The body and the indenter in the mesh module of Abaqus - View from the top.

5.6.5 Comparison Cone/Vickers – integration in the semi-analytical model

5.6.5.1 Method & first results

Fig. 99 represents the Von-Mises equivalent stress distribution in the elastic body with the F.E. method.

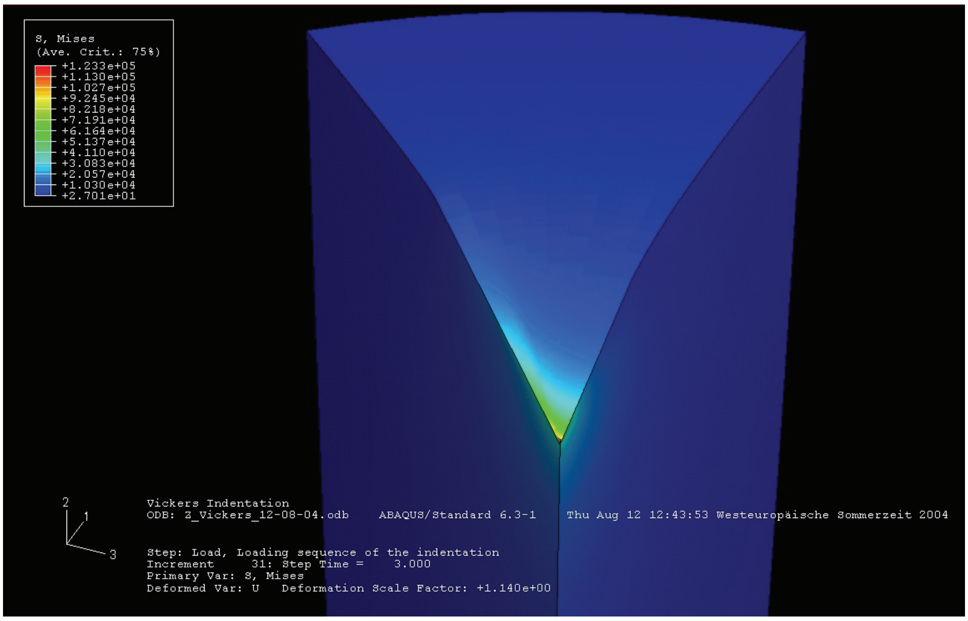

Fig. 99: Von-Mises distribution in the elastic body with the F.E. method.

The stress field appears to be complicated and not obviously analytically treatable. Graph 33 and Graph 34 represent the detail of the Von-Mises distribution in the conical 2D model (equivalent cone: 140.6° of apex angle), in the plane of the Vickers' face (i.e. ABC plane in Fig. 100) and in the plane of the Vickers' edge (i.e. ABD plane in Fig. 100).

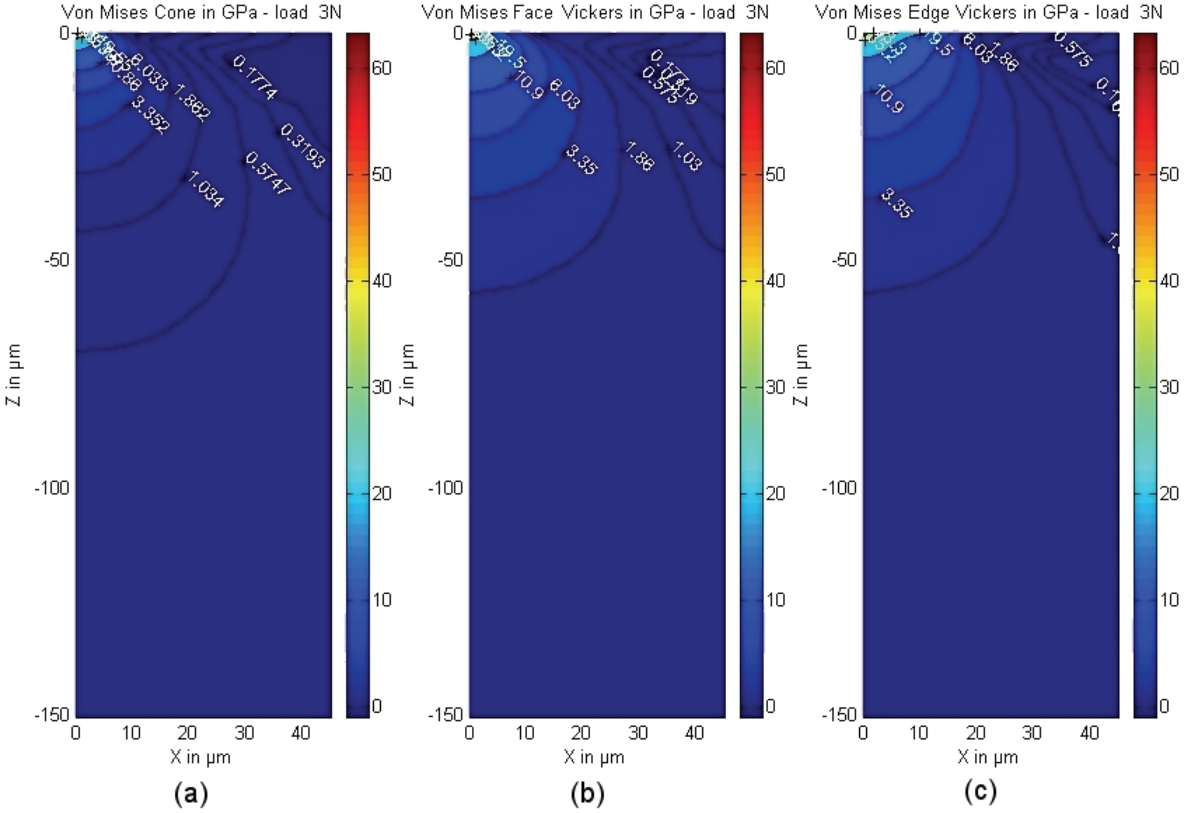

Graph 33: F.E. comparison of Von-Mises distribution between (a) the conical case (equivalent cone), (b) the Vickers' face case and (c) the Vickers' edge case.

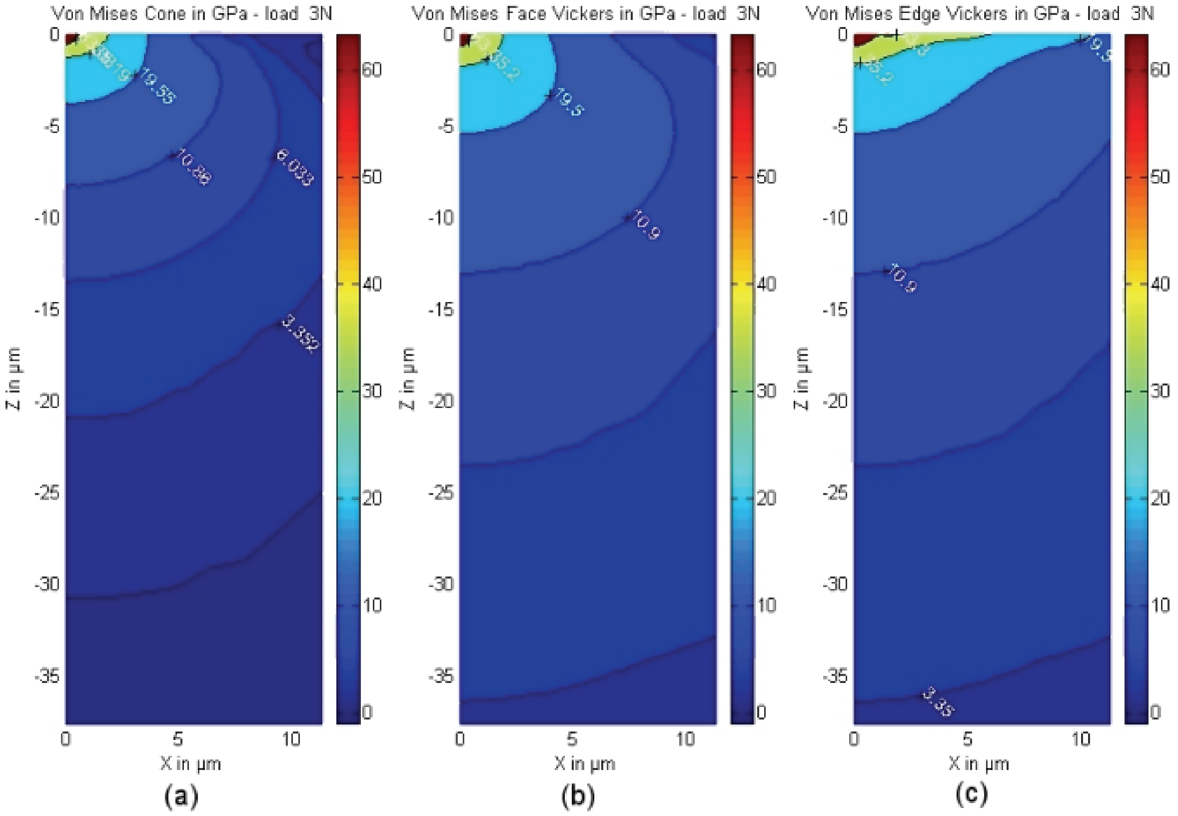

Graph 34: Details of the F.E. comparison of Von-Mises distribution between (a) the conical case (equivalent cone), (b) the Vickers' face case and (c) the Vickers' edge case.

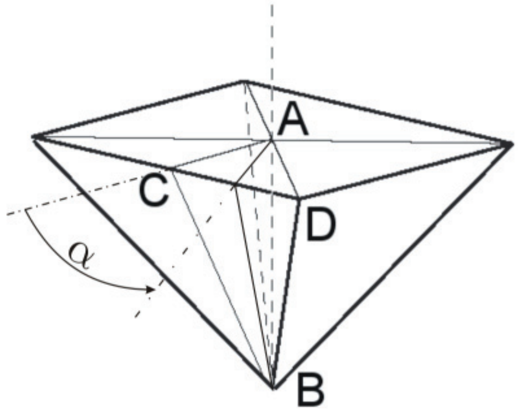

Fig. 100: Vickers representation with definition of ABC and ABD planes.

But let's investigate further these stress representations.

5.6.5.2 Results in the Vickers' face plane

The field in the Vickers face plane *looks like* the one produced by the conical indentation of the elastic body. This result was expected. Actually, in a first approximation one can assume a state close to plane strain in the plane that goes through the tip, the centre of the base of the indenter and the middle of the face border (ABC in Fig. 100). The investigation of the different stress components (σ_{xx}, σ_{yy},…) shows a similarity for the distribution that can be simply linked to the one of the conical indentation by introducing proportional correction coefficients, determined between about 0.73 and 1.21 depending on the considered stress component. This stress field in the Vickers' face plane (the reference face: 0° of angle – ABC in Fig. 100) can then be modeled by the analytical stress field of Sneddon for a conical indentation [76], or by the one of Hanson [28, 29] presented in § 2.2.3.3.4, which is however easier to compute. This latter stress field will be used.

5.6.5.3 Results in the Vickers' edge plane

Graph 33 and Graph 34 represent the Von-Mises distribution in the plane of the Vickers' edge (face at 45° - ABD in Fig. 100). The geometry of the indenter appears as a problem that could be designed as follows: a line loading on an infinite elastic half body, applying a non-uniform pressure along its axis as idealized in Fig. 101 (the problem symmetry is not represented i.e. the p_0 pressure is located on a point very-close to the tip). This loading process may be visualized as that produced by a non-uniformly pressed like-knife contact on the half-space.

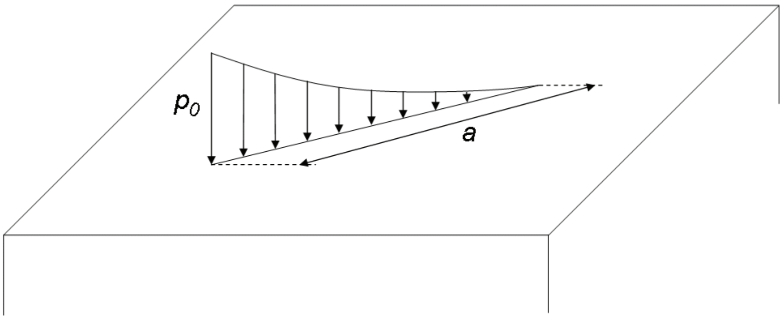

Fig. 101: Representation of a line loading on an infinite elastic half body, applying a non-uniform pressure.

This distribution of the normal pressure on the line loading is easily available by the F.E. developed model, and is given in Graph 35 for the normal load of 3 N.

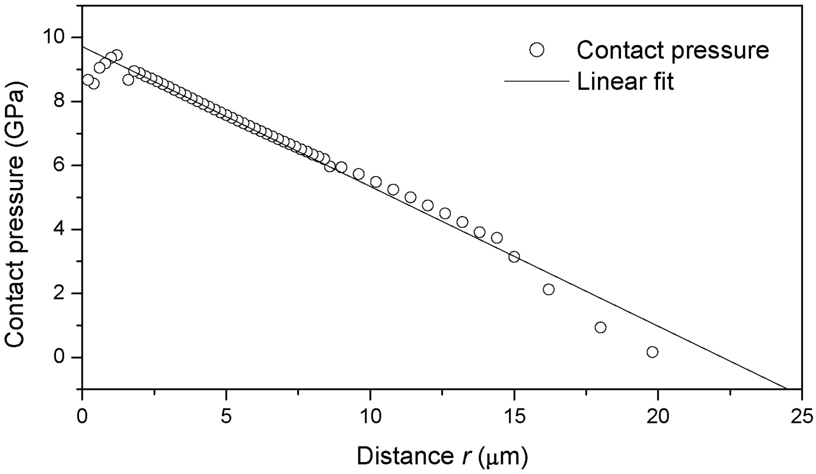

Graph 35: Contact pressure on the distance from the centre point of indentation in the edge plane of the Vickers indenter for a normal load of 3 N.

Note that similar proportional evolutions can be drawn for different loads during the indentation. It is also interesting to notice that the closest points to r=0 exhibit abnormal low values due to the over-distortion of the elements close to the tip. The slope of the curve slightly changes from the linear fit in r~8 µm and r~15 µm: this phenomenon is explained by the changes of mesh element size in these two places. The linear fit is given by Eq. 159 (determined for the normal load of 3 N).

$$p(r) = -4.37\text{x}10^{8} r + 9.7\text{x}10^{9} \quad \textbf{Eq. 159}$$

where p is the contact pressure and r the distance to the centre of the indentation.
Thus the idealized case of the line loading on an elastic body is reduced to the distribution of pressure as illustrated in Fig. 102.

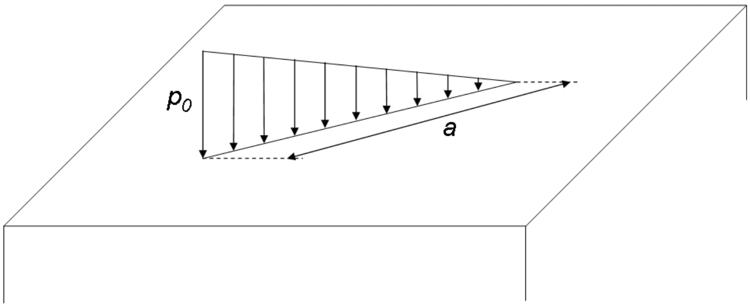

Fig. 102: Representation of a line loading on an infinite elastic half body, applying a uniform pressure.

5.6.5.4 Summary of the stress field caused by a Vickers indentation

To summarize, the stress field in the face plane of the Vickers indenter can easily be modeled in analytical form by the field described by Hanson for conical indentation. The stress field in the edge plane of the Vickers indenter should be modeled by the field corresponding to a progressively line-loading on an elastic half body.

It remains to find the stress field for any intermediate plane, i.e. for a plane with an angle α between 0° and 45° from the reference plane (see Fig. 100). The solution that was adopted is to design a transformation function that is equal to 0 for α=0°, 1 for α=45° and that represents the transformation in the stress field shown by the Finite Elements method. As the work of Galanov [109] lets expect, this function depends on α but also on r.

5.6.5.5 Theoretical limitations

The main problem in this analysis is to model the second stress field. To the knowledge of the author, no analytical model was developed for this line loading problem. One solution could have been to integrate a Boussinesq point loading field on the contact line with a decreasing normal load as suggested in Fig. 102. Such integrations give analytical results actually when computed with Mathematica^{TM} for example… After performing this integration, it was found that a formula for one stress field component is at least 1 page long. A classical linearization helped a bit but was far from being effective enough. Obviously, these results are not acceptable for the present model.

Because it is not directly possible to rigorously model the stress field as described previously, the model will be developed and analyzed as a conical indentation. Nevertheless, the comparison with the experimental Vickers scratches is possible. As it has been shown in § 4.2.3.4, using a conical indenter instead of a Vickers one leads to a shift in the transition load values as a consequence. The expected evolutions may be respected. However, further quantitative analysis is not reasonable in this case.

An alternative solution was tried to have an idea on the stress field evolution for a Vickers indentation: stress correction coefficients were determined between the Vickers edge field and a conical field obtained with an equivalent cone, both given by the F.E. model. The method used was to compare the highest tensile stress of each component to the one corresponding to the conical indentation F.E. model. See Graph 36 to Graph 39 for a representation of the stresses distribution for each component of the stress field. With the help of these latter figures, the comparison of the location of these highest stresses was the first criterion of validation. That means that the location of the highest tensile stress was checked first, before comparing these stresses and introducing stress correction coefficients. The highest tensile stresses were determined by taking the average of the 10 highest tensile stresses that are in a 1 % standard deviation range. This may suppress the singular high values that should come from over-stretched elements which don't represent pertinent values. These coefficients are determined this way, component of stress by component through direct comparison. The results are given in Table 22.

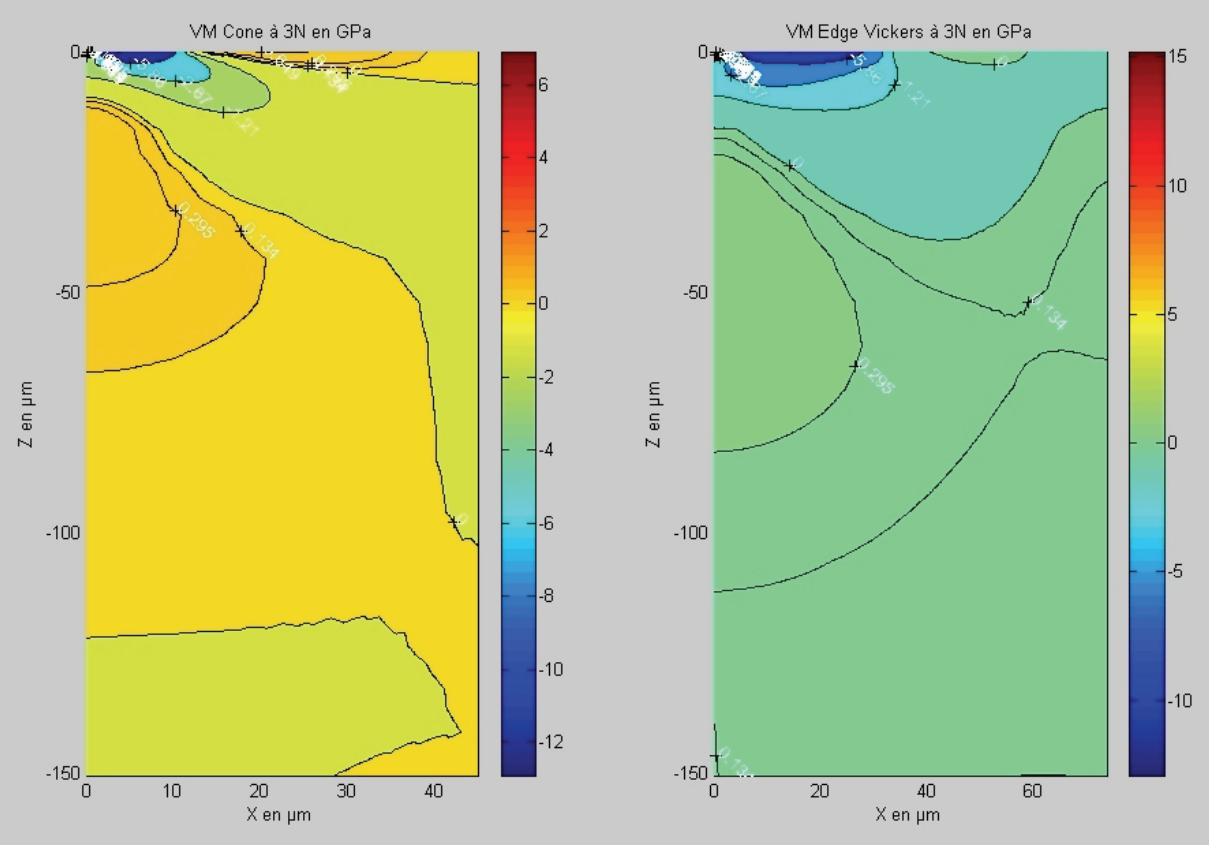

Graph 36: Comparison between the distribution of σ_{xx} in the F.E. conical case and in the Vickers edge plane case with regard to the depth of the indented body.

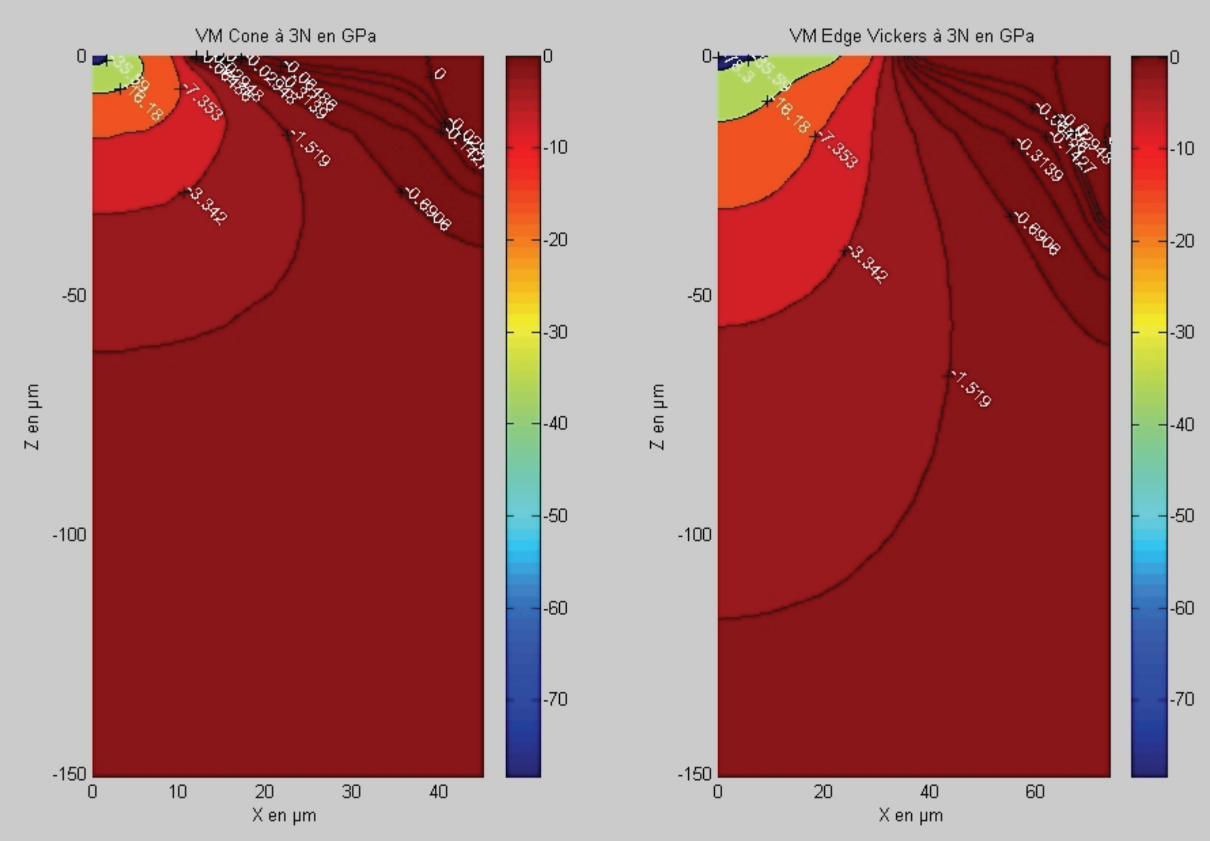

Graph 37: Comparison between the distribution of σ_{yy} in the F.E. conical case and in the Vickers edge plane case with regard to the depth of the indented body.

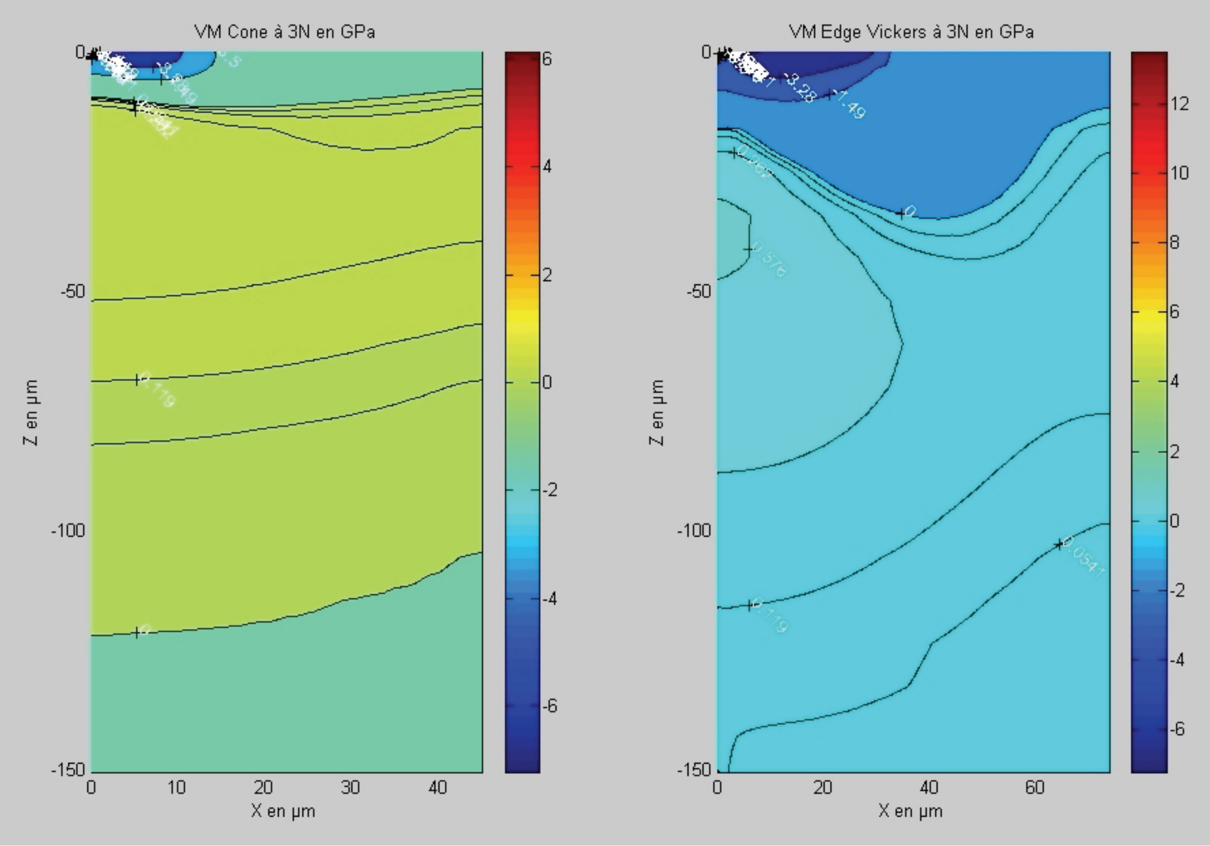

Graph 38: Comparison between the distribution of σ_{zz} in the F.E. conical case and in the Vickers edge plane case with regard to the depth of the indented body.

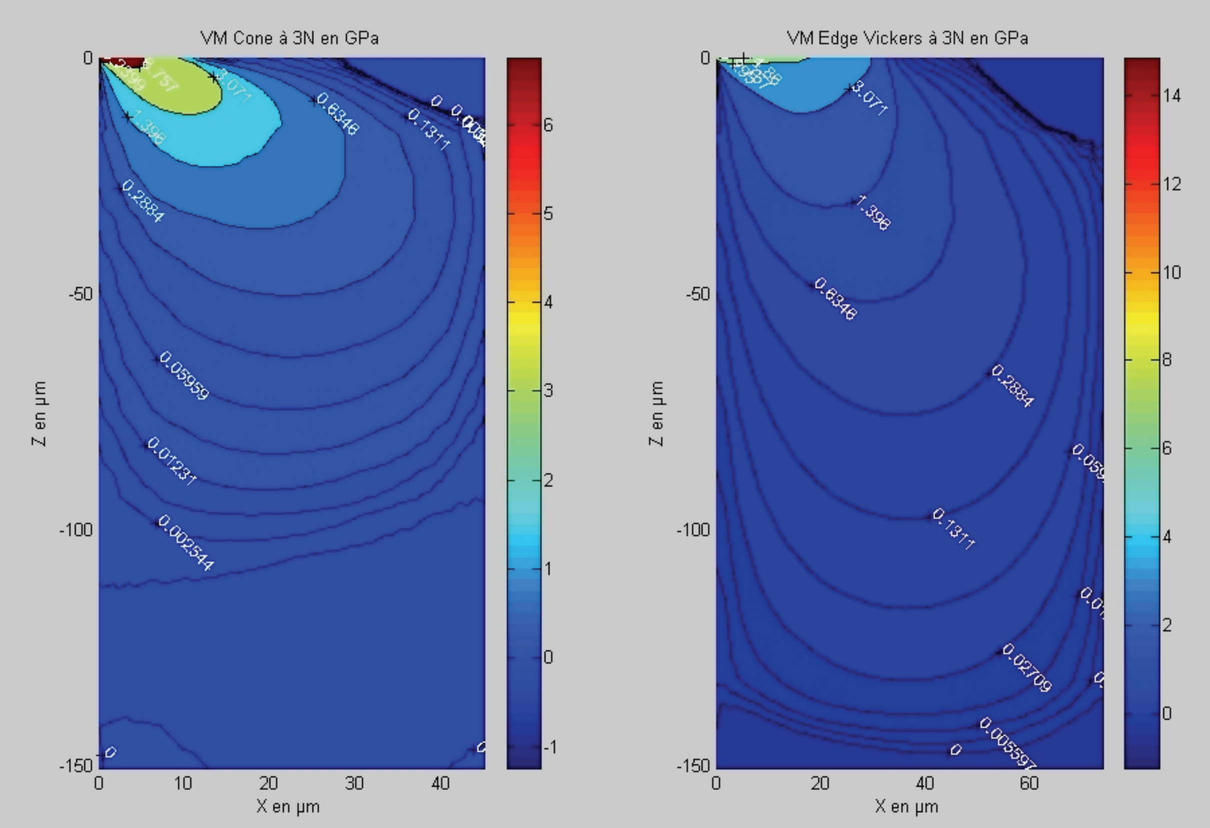

Graph 39: Comparison between the distribution of τ_{xy} in the F.E. conical case and in the Vickers edge plane case with regard to the depth of the indented body.

Stress component	σ_{xx}	σ_{yy}	σ_{zz}	τ_{xy}
Ratio $\frac{\sigma^{\max}_{Vickers}}{\sigma^{\max}_{Cone}}$	0.867	1.228	1.122	0.920

Table 22: Stress correction coefficients: Vickers-conical indentation comparison.

Interpreting these coefficients is of great interest and tends to prove that the difference between a Vickers and a cone penetrator in an indentation experiment is that the values of the components σ_{yy} and σ_{zz} will be higher with the Vickers than with the cone, while the components σ_{xx} and τ_{xy} will be lower. This remark is also valid in the case of the scratch test. Then, the occurrence of the median and lateral cracks may be at lower load when using the Vickers penetrator. This is verified experimentally as reported in part § 4.2.3.4.
Note that the τ_{xz} and τ_{yz} components and their influence have been largely ignored.

5.6.5.6 Contribution of this study in the global work

The results presented in this study are essentially focused on the model of a perfectly elastic indented material. One can wonder what is the goal of such a study that is apparently far from the material behavior in reality. As previously reported in the introduction § 5.6.1, the ultimate goal of this study is to understand the influence of a singular indenter like the Vickers one on the stress and strain fields in order to integrate the singular character of the problem in the analytical model. Then this F.E.M. work can seem to be a bit fundamental and out of experimental considerations, but its aim stands in its participation to the semi-analytical model for the scratching of different glasses.

5.6.5.7 Conclusion about the semi-analytical model

To integrate the Vickers geometry in the equations of the semi-analytical model rigorously as tried in § 5.6.5.1 is not possible yet. The coefficients of stress concentration determined in § 5.6.5.5 give clues to make analogies between the Vickers stress fields and the well-known conical stress fields.
The decision was taken to integrate in the semi-analytical model only a new Hanson stress field to replace the Boussinesq normal stress field in order to approach the reality of the indentation test as demonstrated in this part. Thus, the expression of the stresses of our semi-analytical model after integration of the geometry of the indenter gives:

$$\sigma = \sigma^{n}_{Hanson} + \sigma^{t}_{Bous.} + \sigma^{r}_{Blister} \qquad \textbf{Eq. 160}$$

It still remains to adapt the new model to the deformation behavior depending on the chemical composition of the six different glasses. This will be developed in the following part.

5.7 Extension of Ahn's model to the normal/anomalous glasses: identification of the densification/shear competition

5.7.1 Introduction

As evoked in § 2.1.9.2, the initiations of cracks in the glass during a scratch test occur at the boundary or out from the plastic zone. It is first needed to identify the deformation mechanism(s) of the material under a high stress field caused by a sharp indentation.
The notions of deformation by densification and by shear developed respectively in § 2.1.9.2.2 and § 2.1.9.2.3 and the linked aspect of normal/anomalous character introduced in § 2.1.9.2.4 gives the clues needed for the study of the SLS glasses. Actually, the six considered glasses (standard float glass, SLS series and fused silica) exhibit a deformation behavior

under stress that is more or less intermediate between an "ideally-pure" densifying and shearing glass, depending on each glass composition.

Thus, the study of the competition between densification and shearing in the deformation of glass is of primary interest in this exploratory work. Because of the complexity of quantifying rigorously the densification contribution in the case of an indentation test (not linked to the global densification in a bulk material yet), approaches like studying the hydrostatic stress as shortly illustrated in § 2.2.3.3.5 between the Boussinesq, Hertz and Sneddon's models are rule out from the present study. Actually, these approaches seem to anticipate too much the densification mechanism in glass: several studies [3, 4, 48] shown that the densification in glass is enhanced when shearing contribution in the solicitation increases (this corresponds to some limitations previously quoted in the concerned paragraph). Then, the competition between densification and shearing will be studied in this work through the identification of the parameter B (called strength of the *Blister* field) previously introduced (see § 2.3). This parameter will only represent an index of the studied competition and does not have the pretension to quantify the densification part of the deformation nor the shearing contribution.

5.7.2 Method

The opportunity is given by the chosen model to inaugurate a new technique especially developed for this work in order to identify the competition densification/shearing by quantifying the parameter B in the six glasses. Existing works deal with this problem and solve it in different manners as reported in § 2.2.3.3.6.3: i) stress compatibility condition [27], ii) created plastic volume [8, 80], iii) conservation of energy [48], iv) experimental considerations [20, 71, 72]. Only the methods reported in ii) et iv) are adapted to take into account a normal/anomalous behavior. Unfortunately, some details remain blurred in these methods, and some parameters are difficult to assess in our case.

A first possibility to assess the parameter B should have been to develop a second new technique based on the energy dissipated during instrumented indentation tests performed on the different glasses. A short remark will be given on this technique in § 5.7.3, even if it has been given up in this study due to the time cost of the post-treatment.

Then, the choice in this work had been to investigate a new technique inspired from the iv) point to assess the parameter of the *Blister* field B. The method is to consider the volume of the Vickers imprints for different loads for each glass. Actually, as seen earlier, the normal/anomalous character of the deformation of the considered glasses leads to a deformation with more or less (respectively) volume conservation. The measurement of the volume of Vickers imprints can then give some precious information. This method will be developed in § 5.7.4.

5.7.3 Energy approach

5.7.3.1 Remark

An interesting hypothesis on the way to pilot an instrumented indentation test is given by Lucas et al. [110] and can be somewhat summarized by:

$$\frac{\dot{P}}{P} = const. \quad \textbf{Eq. 161} \quad \text{is equivalent to} \quad \dot{\varepsilon} = \frac{\dot{h}}{h} = const. \qquad \textbf{Eq. 162}$$

This hypothesis leads to:

$$\frac{\dot{P}}{P} \propto \frac{\dot{h}}{h} \qquad \textbf{Eq. 163}$$

This equation constitutes no less than a constitutive law of the tested material.
In the present study, the goal of the instrumented indentation tests is to discriminate the glasses with regard to their deformation behavior. Then, they obey to different constitutive laws that can't be discriminated by the previous technique due to the quoted hypothesis.
Thus, the choice had been done to pilot the experimental setup of instrumented indentation with *real* $\dot{\varepsilon} = \frac{\dot{h}}{h} = Cste$. A displacement measurement (capacitive gauges) and a Labview program including various corrective coefficients were developed on the scratching machine to achieve this aim (see Appendix 1 § App.1-3). The $\frac{\dot{h}}{h}$ ratio is measured indirectly. Note that the "indirect" character of the measurement of this ratio does not warranty a "real" measurement of the ratio. No more result of the difference between $\frac{\dot{P}}{P} = Cste$ and $\dot{\varepsilon} = \frac{\dot{h}}{h} = Cste$ piloting will be discussed here even if a direct comparison between two indentations made by these two techniques suggests some interests.

5.7.3.2 Method

The exploratory work of Bobji et al. [48] gives an interesting basis. With combining this work with the one of Yoffe, it is possible to express *B* from the different energies given by an instrumented indentation. The scratch tester was then adapted in order to provide a quantitative instrumented indentation machine (as reported in Appendix 1 § App.1-3) with a program that enables to control the loading-unloading sequence so that $\dot{\varepsilon} = \frac{\dot{h}}{h} = Cste$.
As written earlier, this technique is time consuming with regard to the post-treatment of instrumented indentation results and has not shown clear results for the present study, so complementary tests and analysis had been given up. Nevertheless, this method seems to be hopeful as Suzuki et al. [111] studied with certain achievement the densification of the fused silica by considering the involved energies in an indentation test.

5.7.4 Volume measurements approach

5.7.4.1 Normal/anomalous behavior facts in indentation tests

Normal/anomalous considerations in structure and behavior of the studied glasses need to be quantified at low scale. During an indentation test, the normal glasses are more prone to pile-up due to the tendency to deform at constant volume (i.e. *plastically*) while the anomalous glasses are prone to sink-in as they densify. These two tendencies in behavior of the normal/anomalous glasses under load are illustrated in Fig. 103, which shows AFM pictures of a detail of Vickers indentations performed on both SLS 1 and SLS 4. Pile-up can be seen on the left of the SLS 1 imprint (the cutting section is around the middle of the face of the indenter) with several small cracks in the imprint while a sink in is visible on the SLS 4 imprint. Then, AFM measurement technique seems to be a good candidate for the concerned method of volume measurements of the indentation imprints.

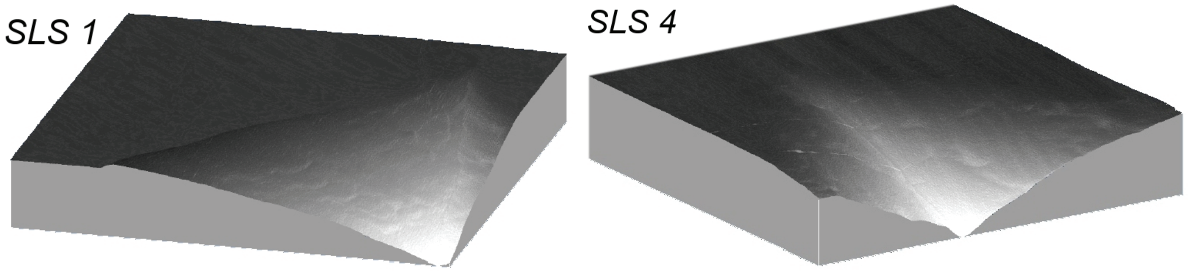

Fig. 103: Details of AFM pictures of indentations on SLS 1 & 4 (scan area: 5x5 µm^2 - load: 0.6 N - maximum depth: 700 nm for SLS 1 and 625 nm for SLS 4).

5.7.4.2 Theoretical developments

For static indentation with a sharp indenter, the increase in volume (ΔV) of any hemisphere of radius ρ ($\rho > a$, a = plastic zone radius) is constant and given by Yoffe [27]:

$$\Delta V = \frac{2\pi A(1-2\nu)}{3G} \qquad \textbf{Eq. 164}$$

where A is the strength of the static indentation *Blister* field, G is the shear modulus and ν the Poisson ratio of the material. The strength of the sliding *Blister* field, B, is defined in Eq. 142. By analogy with the work of Ahn on the sliding indentation *Blister* field for a conical indenter derived from the static indentation *Blister* field of Yoffe, the increase in volume around an infinitely long scratch due to the sliding indentation *Blister* field for a Vickers indenter can be estimated as:

$$\lim_{l\to\infty}\int_{-l}^{l} B\Delta V(x-\xi,y,z)d\xi = \lim_{l\to\infty}\left[\left(\frac{2a^2l}{\tan\theta}+\frac{2a^3}{3\tan\theta}\right)-\left(\pi a^2 l+\frac{4a^3}{3\tan\theta}\right)\frac{\delta Vc}{V}\right]Fpv \qquad \textbf{Eq. 165}$$

where $\frac{\delta Vc}{V}$ is the compaction ratio for glass and *Fpv* is the upward plastic flow factor adapted to the Vickers indenter. The terms in the first parenthesis on the right hand side of the previous equation represent the impression volume of the sliding indentation and the terms in the second parenthesis represent the original volume of the plastic deformation zone. $\frac{\delta Vc}{V}$ corrects this value by taking into account the glass compaction which occurs under the sliding indenter and that is accommodated within the plastic zone. *Fpv* replaces the original *Fp* factor as introduced by Ahn [20], that represents the upward flow that occurs due to the deformation undergone by the material adapted to the Vickers geometry (*post test* measurement).

Combining Eq. 164 and Eq. 165 leads to:

$$B = \frac{3Ga^2}{2\pi(1-2\nu)}\left(\frac{1}{\tan\theta}-\frac{\pi}{2}\frac{\delta Vc}{V}\right)Fpv \qquad \textbf{Eq. 166}$$

Note that the expression of B is the same as the one given by Ahn [20] (see § 2.3.2) for a conical indenter (with *Fpv* replacing *Fp*), because the sliding tracks have the same shape and on a infinitely scratch, the shape of the end of track is negligible and disappears in the limit operation.

Because $\frac{\delta Vc}{V}$ is difficult to assess for all our glasses, it is assumed that the same expression is used for each glass, given by Cheng et al. [89] that represents the compaction under hydrostatic pressure for the standard float glass and reported by Ahn [20]:

$$\frac{\delta Vc}{V}(\%)=\frac{\left(0.95128-0.72872p+1.9336p^2+0.25953p^3\right)}{\left(1-p\right)^2}\qquad\textbf{Eq. 167}$$

Because the glasses have actually different densification tendencies, this choice has to be justified. In the light of the normal/anomalous considerations given in § 2.1.9.2.4, when the anomalous tendency assert itself, $\frac{\delta Vc}{V}$ decreases, as well as *Fpv*. The Eq. 166 will show an evolution in the same way. This evolution will be considered only as a tendency. This tendency will be less visible because the compaction ratio will be the same for each glass. So, it leads to diminish the difference between the different *B* values. Nevertheless, the evolution will be clearly established as it will be reported further (see § 5.7.4.4).

Note also that the standard float glass is the glass that exhibits the fewer tendencies to compaction, hence that should have the highest $\frac{\delta Vc}{V}$ coefficient.

The expression of *a* can be found from experiments, like for example in the case of Ahn [20] with the help of a profilometry technique:

$$a=0.679P^{0.57}\qquad\textbf{Eq. 168}$$

It should be required in this case to know the *real* depth of indentation during scratching and not the *post test* depth of the scratch. Because the evolution of the difference between the "real" *a* during the test and the *a* value measured after the test with regard to the different glass behaviors is not known *a priori*, it is clear that this method could give any results, without the possibility to determine their veracities. A second problem is inherent to this method: what is the more consistent measure of *a* when pile-up or sink-in occurs?

On the other hand, an estimation of this expression is given analytically by Hanson [28] and will be use for implementing his equations in the semi-analytical model of this study. Then, it is consistent to use the same expression for the whole model. This expression is:

$$a=\sqrt{2\frac{1-\nu^2}{\pi E}P\tan\alpha}\qquad\textbf{Eq. 169}$$

with α the semi-apex angle of the indenter, *P* the normal load, *E* and ν the elastic properties of the material.

5.7.4.3 Performed tests

The major difference between Ahn's expression and the one adapted to the Vickers geometry is the upward flow factor. 2-D considerations are sufficient to determine *Fp* which constitutes an experimental measurement on the imprint. As reported in § 2.2.3.3.6.3, 3-D measurements are required in the case of the Vickers geometry to take into account the singularity of the indenter as well. A global measurement of the volume within the imprint as well as the volume of the upward flow has to be assessed to determine the *Fpv* factor. By analogy to Ahn [20], *Fpv* is given by:

$$Fpv=\frac{Vupward-Vimpr}{Vtotal}\qquad\textbf{Eq. 170}$$

with *Vupward* the volume of the upward flow, *Vimpr* the volume within the imprint (under the undeformed plane) and *Vtotal*, the total imprint volume (from the upper point – the top of pile-up if it occurs – to the deepest point of the indentation). The measurements are performed after the indentation tests.

To do so, indentation experiments were performed on each glass at different loads: 0.2, 0.4, 0.6, 0.8, 1, 1.5, 2 and 3 N. AFM investigations and 3-D image analysis of these imprints give the expected results on the volume measurements. The Fig. 104 shows typical results provided by the treatment of an imprint.

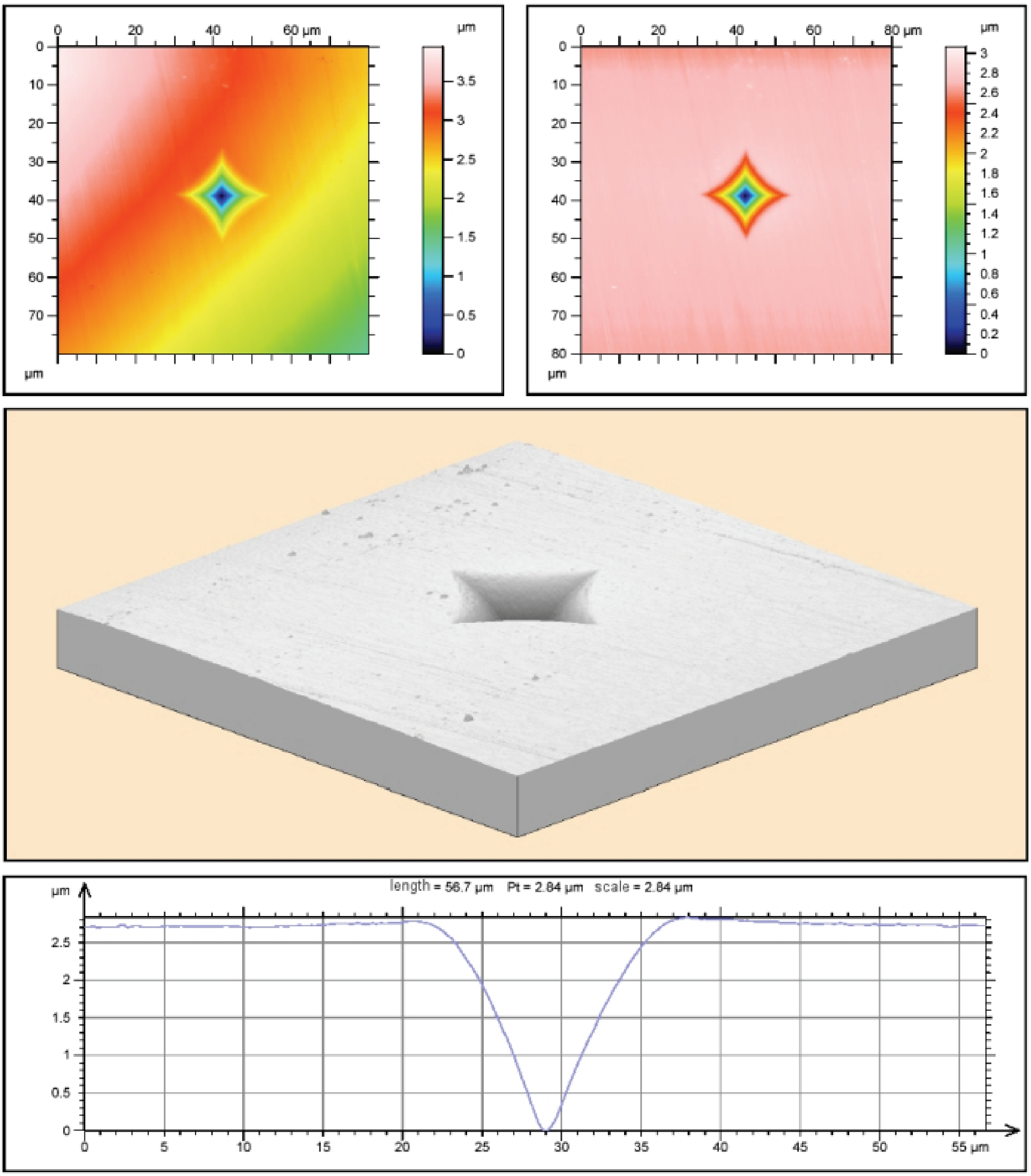

Fig. 104: Typical results of the 3D image treatment of a Vickers imprint.

On the top left, the measured data. On its right, the corrected data (planar fit on the non-deformed plane). Below, the 3-D reconstruction and finally, one extracted profile (face to face section) that illustrates the presence of a slight pile-up that is elusive on the 3-D reconstruction. But, the 3-D reconstruction shows a precise phenomenon of prior interest: the roughness can be an important parasite to the volume measurements. The solution adopted to avoid this drawback was to subtract the volume of the roughness from our results by

measuring a pristine surface close to the considered zone. A particular attention was taken to use representative size of surface in each case.
Measurements were done systematically on three imprints for each load, on each glass to ensure a good reproducibility (that means a maximum error around 7 % for these first steps of the new born method).

5.7.4.4 Results

The volume measurements had been carried out with the three different methods available with the image analysis software described in § 3.3.6. The ratio *Fpv* is the volume of the peak (corresponding to the upward flow) minus the volume of the hole (corresponding to the volume of the imprint) to the total volume of the imprint. A representative graph of the similar ratio volume of upward flow (Vol. peak) on volume of imprint (Vol. hole) as a function of the measurement method is given as an example for the standard float glass in Graph 40. The important difference in the results between the three methods of measurement (that mainly depend on the resolution of the pictures) need to be solved. It is, to the knowledge of the author, not more justified to use one rather than the other. Then, it is assumed that the ratio *Fpv* will be computed from the arithmetic average of these three measurements. Even if only the ratio of volume will be reported here, one can give an order of magnitude for the volumes involved (taking into account the correction due to the roughness). The volumes of holes are about few μm^3 for low loads (typically around 5±2 μm^3 for 0.2 N), few ten μm^3 for medium loads (typically 35±10 μm^3 for 1 N) and a hundred or more μm^3 for higher loads (typically 120±30 μm^3 for 2 N). The high range given for each order of magnitude does not represent the precision of the method but the range of the volumes measured for the six glasses of the study.

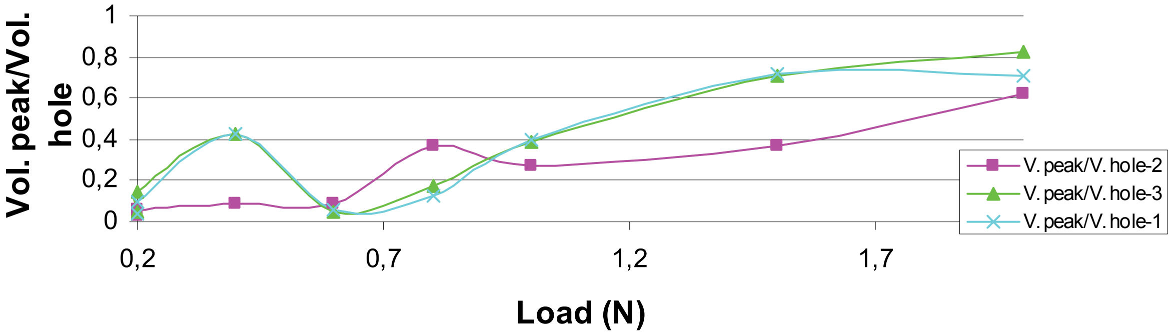

Graph 40: Example of Vol. peak/Vol. hole corrected by the roughness – the three methods of measurements.

The parameter *B* (depending on the load, the densification/shear behavior of the material, the geometry of the indenter and other experimental parameters – environmental effect,…) is then assessed for each glass by the method described previously. The results are summarized in Graph 41 to Graph 46. The evolution of the *B* parameter for each glass seems to be well fitted by a power-law equation as defined in Eq. 171. Table 23 summarizes the coefficients *C* and *n* invoked in the Eq. 171 for each glass.

$$B = CP^n \qquad \textbf{Eq. 171}$$

with *C* and *n* constants.

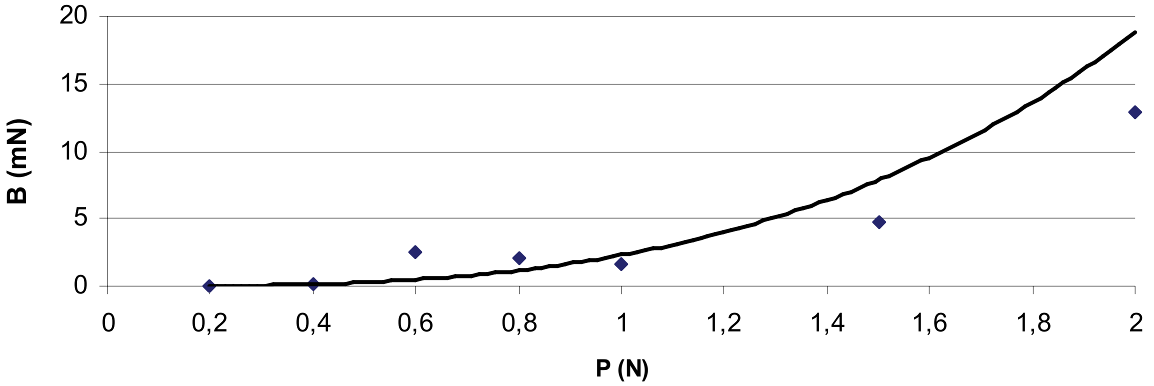

Graph 41: The evolution of the sliding indentation Blister field constant *B* with the indentation load *P* for the standard float glass.

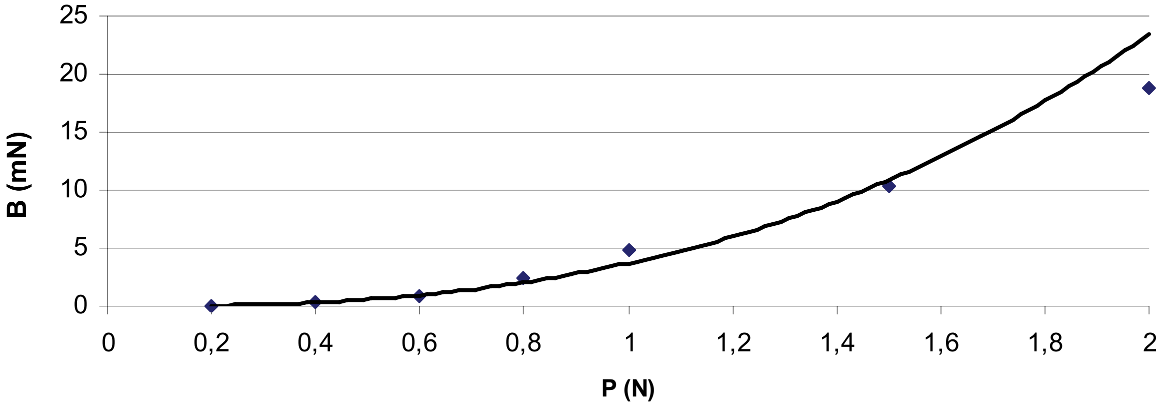

Graph 42: The evolution of the sliding indentation Blister field constant *B* with the indentation load *P* for the SLS 1 glass.

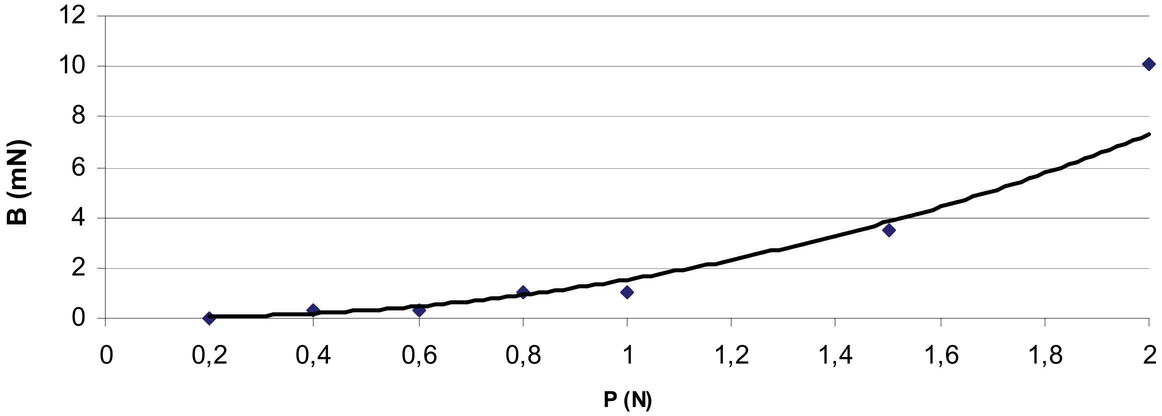

Graph 43: The evolution of the sliding indentation Blister field constant *B* with the indentation load *P* for the SLS 2 glass.

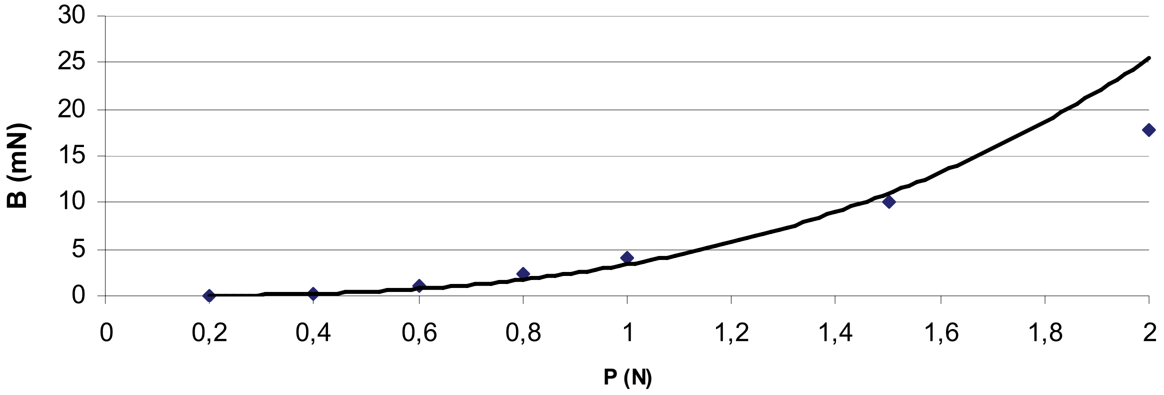

Graph 44: The evolution of the sliding indentation Blister field constant *B* with the indentation load *P* for the SLS 3 glass.

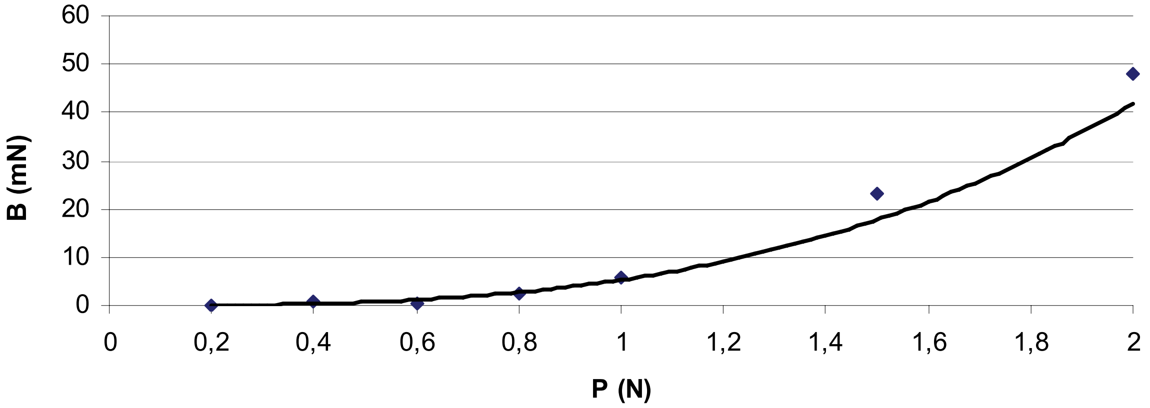

Graph 45: The evolution of the sliding indentation Blister field constant *B* with the indentation load *P* for the SLS 4 glass.

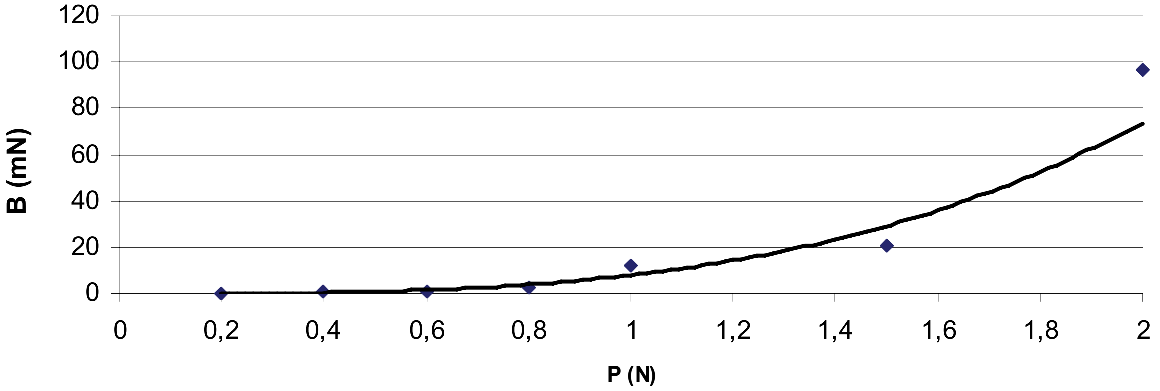

Graph 46: The evolution of the sliding indentation Blister field constant *B* with the indentation load *P* for the fused silica glass.

Glasses Constants	Standard float glass	SLS 1	SLS 2	SLS 3	SLS 4	Fused silica
C	2.2974	3.6848	1.5360	3.3563	5.3146	7.9615
n	3.0293	2.6687	2.2508	2.9223	2.9734	3.2116
Regression coefficient R^2	0.87	0.95	0.84	0.95	0.87	0.75

Table 23: Summary of *C* and *n* values (see Eq. 171) for each glass.

Note that the evolutions of *B* make sense compared to Ahn's one (see Graph 18).
As expected in this load range, the more the densifying tendency is, the highest *B* appears. The exception must be noted for the SLS 2 glass which exhibits the lowest *B* in this load range. All these evolutions and results will be discussed further in § 5.9 as the stress fields will be interpreted with regard to cracking considerations.

5.8 Complete expression of the model

As for Yoffe [27] and Ahn [20], The complete stress field is obtained by direct superposition of the three different stress fields:

$$\sigma = \sigma^{n}_{Hanson} + \sigma^{t}_{Bous.} + \sigma^{r}_{\substack{Blister \\ normal/anomalous \\ Vickers}} \qquad \textbf{Eq. 172}$$

and

$$\tau = \tau^{n}_{Hanson} + \tau^{t}_{Bous.} + \tau^{r}_{\substack{Blister \\ normal/anomalous \\ Vickers}} \qquad \textbf{Eq. 173}$$

The superscript *n* denotes the stress field due to the normal loading and uses the Hanson's equations; The superscript *t* denotes the stress field due to the tangential loading and uses the Boussinesq's equations; The superscript *r* denotes the residual stress field due to the plastic zone and corresponds to the sliding *Blister* field adapted to normal/anomalous glasses and to the Vickers indenter geometry.
Note that a Coulomb friction coefficient of 0.4 (consistent with Graph 25) has been used to give the relative proportion of the tangential stress field with regard to the normal stress field.
Finally, note that because of the chosen coordinate system linked to the model (see Fig. 52), the indenter is considered to scratch the material along the *x*-axis, from - $x=-\infty$ to its current position at $x=0$.

5.9 Semi-analytical model results

5.9.1 Preliminary remark

The fundamental crack patterns that occur during scratching on the six glasses are median/radial and lateral cracks as described in § 4.2. No purely radial cracks (i.e. that initiate perpendicular to the scratch track) were observed. Ahn [20] shortly discussed the difficulty to anticipate radial cracking. The accurate experimental observations of the radial crack initiation and propagation (§ 4.2.4.2) show that no radial crack occurs, validating the absence of significant tensile stress σ_{xx}. Then, only the stresses σ_{yy} and σ_{zz} will be investigated and analyzed because of their prior role in the crack initiation during scratching, respectively median/radial cracks as described in § 4.2.4.2 and lateral cracks.
Note that checking the stresses (like done in the next parts) in order to predict crack occurrence has sense only under the assumption that the cracks grow perpendicular to the maximum principal stress if it is tensile. This assumption is commonly accepted in the materials considered in this study (see [8, 14, 15, 20, 27] among others). Actually, it has been checked before each interpretation reported in the next parts, that the considered component (σ_{yy} or σ_{zz}) dominates the solution and that the other components, like shear components for example, are of minor contribution.
Finally, cracking occurrences obviously perturb the stress field. This fact was largely ignored in this analysis and then calls for caution in further quantitative investigations.

All the following results are visualized in the form of stress distribution in the indented body. A great improvement compared to the work of Ahn [20, 71] is that the stresses are drawn as contour domains that help for visualization and interpretation. The plotted stresses correspond to the indenter having moved from x=-∞ to x=0, its present location. All these drawings were computed with 300 points of sampling on each axis.

5.9.2 Phenomenology

5.9.2.1 Prediction of the median/radial crack occurrence

The component corresponding to the cone loading (i.e. $\sigma^n_{yy-Hanson} + \sigma^t_{yy-Bous.}$) largely dominates the complete stress σ_{yy} for low values of P (typically < 0.6 N). The initiation of the median/radial cracks is driven by the tensile part of this component. The highest tensile stress is located close to the surface as shown in Graph 46, just under and a bit in front of the indenter on the x axis.

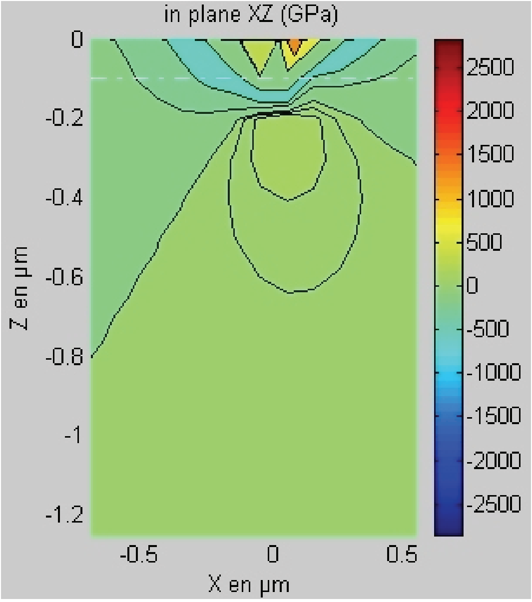

Graph 47: Representation of the considered part of the stress σ_{yy} in the XZ plane (case of P=0.5 N).

Then, the opening of the median/radial crack occurs in front of the moving penetrator. These conclusions are consistent with experimental observations. Nevertheless, pure median cracks occur right below the scratch and usually propagates accompanying the load but "step by step" i.e. the crack first propagates then stops when the stocked energy relaxes, until the indenter is close enough to make it propagate again, etc. This phenomenon leads to a characteristic fractographic pattern, illustrated in Fig. 105 and also reported in a drawing in the *Literature review* part § 2 (see Fig. 39).

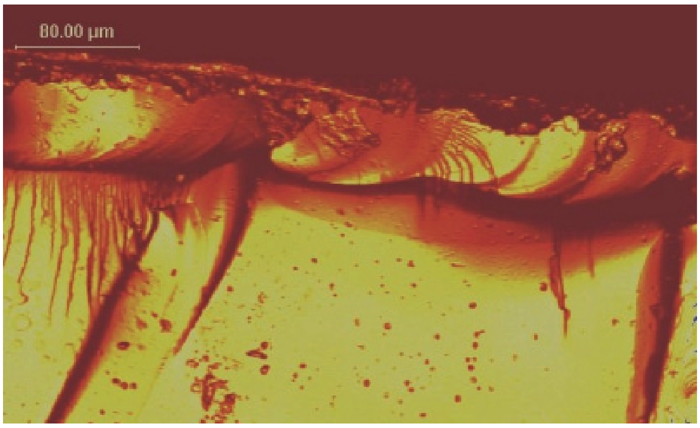

Fig. 105: Section of a scratched sample broken along the scratch track. (confocal microscope)

The Graph 48 shows the component $\sigma^{n}_{yy-Hanson} + \sigma^{t}_{yy-Bous.}$ in the plane XY (section at z=-0.1 µm).

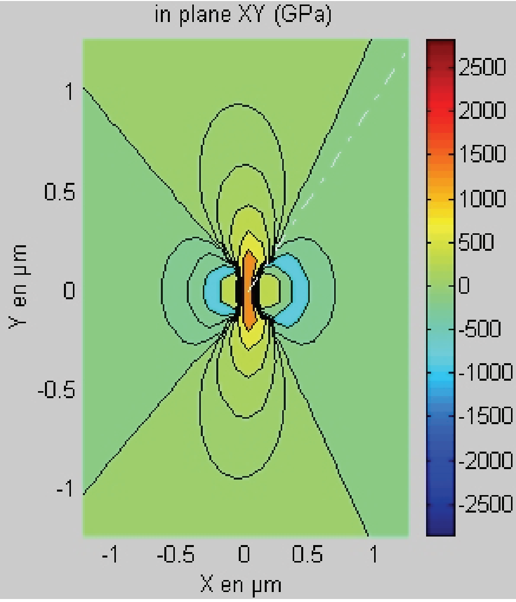

Graph 48: Representation of the considered stress σ_{yy} in the XY plane (case of P=0.5 N).

The median/radial crack that just initiates under the indenter does not propagate straight due to a compressive component in the x direction. Then, as the indenter moves, the crack tends to propagate by inclining either on the left or the right. As reported in § 4.2.4.2, these conclusions are consistent with the experiments.

5.9.2.2 Prediction of the lateral crack occurrence

The residual component (i.e. the *Blister* component) largely dominates the complete stress σ_{zz} when P is high enough (> 0.6 N). Then, the initiation of the lateral cracks is expected to be driven by tensile part of this component. The highest tensile stress is located (see Graph 49 and Graph 50 – case of 0.8 N of normal load) in the depth of the body close to the boundary between the plastic zone and the elastic body. Its precise location is a bit behind the indenter on the x axis. This is consistent with the experimental observations that show the creation and the propagation of the lateral cracks behind the moving tip and the static behavior (i.e. indentation behavior) that reports lateral cracking occurrence on the unloading sequence [8].

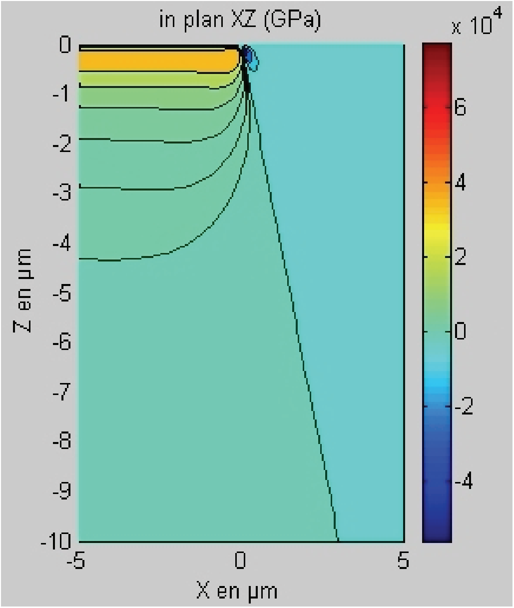

Graph 49: Representation of the considered stress σ_{zz} in the XZ plane.

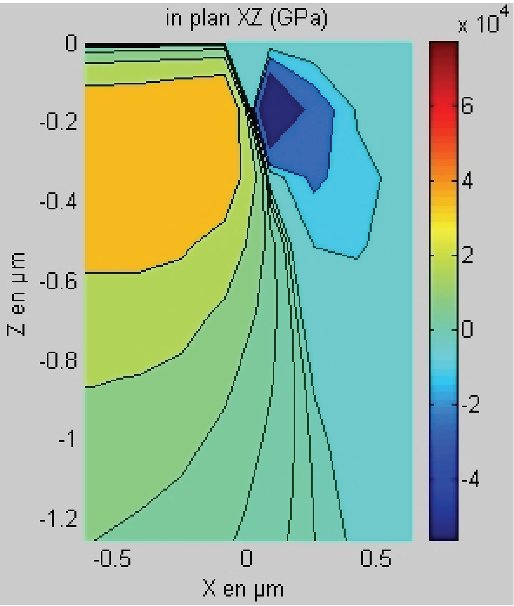

Graph 50: Detail of the representation of the considered stress σ_{zz} in the XZ plane.

High values of this component stay all along the scratch, even if the indenter passes far away: then, the residual stress field equals the complete stress field (case of large negative values of x).

The compressive component in the $x > 0$ prevents the propagation of the lateral crack in front of the indenter.

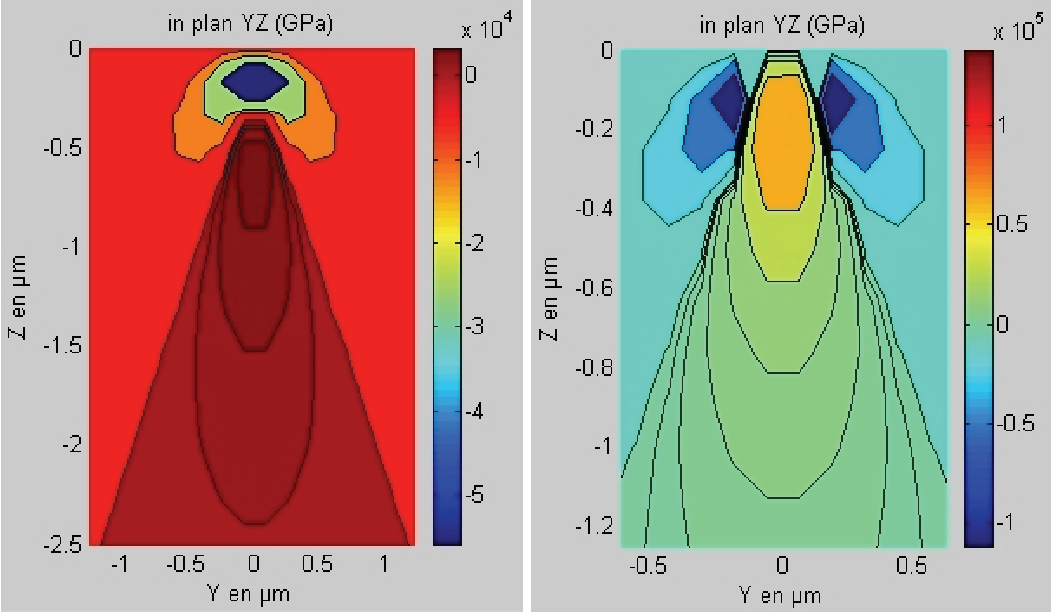

(a) x=0.1 µm (b) x=-0.1 µm

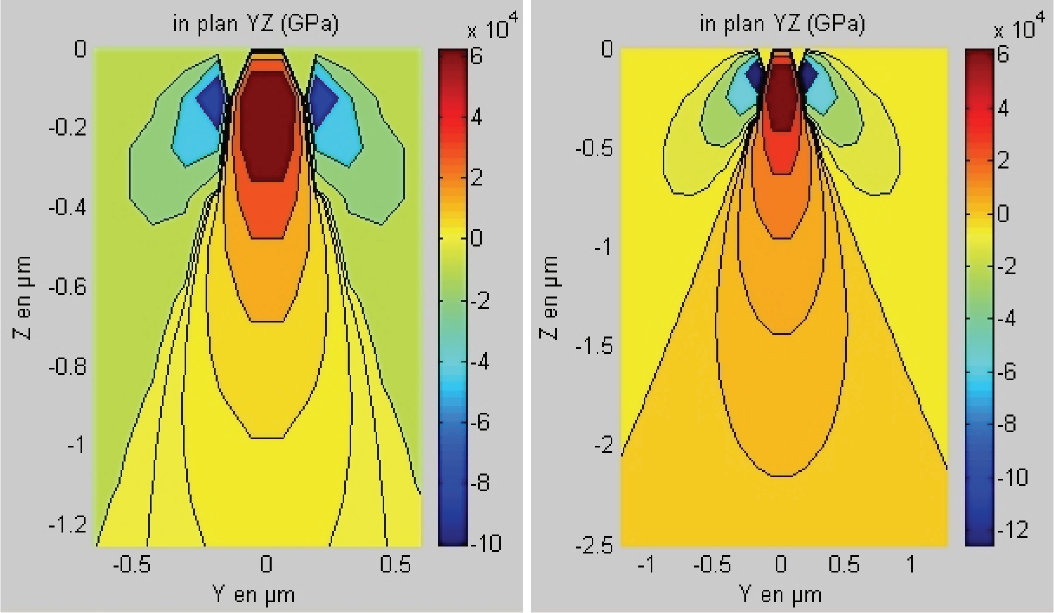

(c) x=-1 µm (d) x=-3 µm

Graph 51: Distribution of the considered stress σ_{zz} in the YZ plane along the x axis.

Graph 51 informs on the shape of the stress distribution along the *x* axis. The *x* value is written under each picture. The compressive zone in front of the indenter can be seen on the Graph 51 (a). It separates as the indenter moves on, in the form of two compressive zones on each side of the scratch. As also shown in the Graph 51, the singularity of the stress remains really close to the contact loading and faded quickly after the indenter has gone, as illustrated by the Graph 51 (b), (c) and (d). This strongly suggests that the initiation of the lateral cracks happen immediately after the indenter passes. Bulsara [21] reported that with a Vickers indenter in a standard float glass, the lateral crack does not appear until the indenter is lifted from the surface. This has also been observed in this study during the experimental tests. Once the load is removed, the lateral crack forms beneath the end of the scratch and propagates rapidly along the entire length of the scratch until the beginning of the scratch track where it stops. Note that this phenomenon appears during constant load scratching. In the case of a monotonic slope of load, the lateral crack front moves with the loading indenter.

However, contrary to Bulsara's interpretation, it is the opinion of the author that the "backward propagation" of the lateral crack is just the apparition and the propagation of a thin air layer that shows the open crack. The lateral cracks would have already been created, but are not visible until the indenter is lifted from the surface and there is enough free unloading energy to make the strip air goes as the analysis of the Graph 49 to Graph 51 suggests.
Finally, the presence of the two surrounding compressive zones all along the track as shown by the pictures of Graph 51 suggests that the lateral cracking initiates but propagates only with a width comparable to the plastic zone width. This result is obviously wrong from the experimental point of view as shown several times in scratching photos in the previous parts and illustrates the limit of this model that does not include fracture mechanic analysis.

5.9.3 Dependence on the chemical composition

5.9.3.1 Preliminary remark

Before analyzing the stress field, a remark must be done on *what* is necessary to analyze. According to Ahn [20], it has been reported in the previous phenomenology part (§ 5.9.2) that the median/radial cracking is dominated by the "point" loading and that lateral cracking is mainly due to residual stresses. However, to study the influence of the chemical composition on the stress system, the difference between the complete expression has to be analyzed. In fact, the chemical changes appear only in the residual stress field of the model. Thus, the study of the median/radial cracking in the light of chemical composition needs the analysis of $\sigma_{yy} = \sigma^{n}_{yy-Hanson} + \sigma^{t}_{yy-Bous.} + \sigma^{r}_{yy-Blister}$ and not only $\sigma^{n}_{yy-Hanson} + \sigma^{t}_{yy-Bous.}$.

5.9.3.2 Prediction of the median/radial crack occurrence

Graph 52 represents the complete $\sigma_{yy} = \sigma^{n}_{yy-Hanson} + \sigma^{t}_{yy-Bous.} + \sigma^{r}_{yy-Blister}$ stresses in the planes XY and XZ for the six different glasses with the maximum tensile stress value determined with the method previously reported in § 5.6.5.5. The load used during the computation is 0.5 N. At this load, both the residual field and the "point" field are important for the six glasses. The difference in the experimental parameters *B* influences directly the residual stress field that is superposed with $\sigma^{n}_{yy-Hanson} + \sigma^{t}_{yy-Bous.}$ on these graphs.

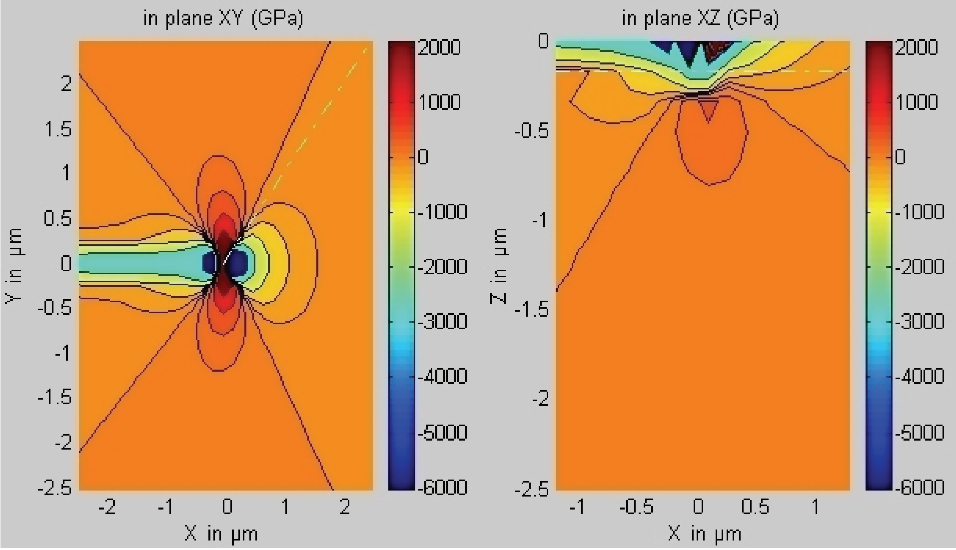

(a) Standard float glass – σ_{yy}^{max} = 2152 GPa

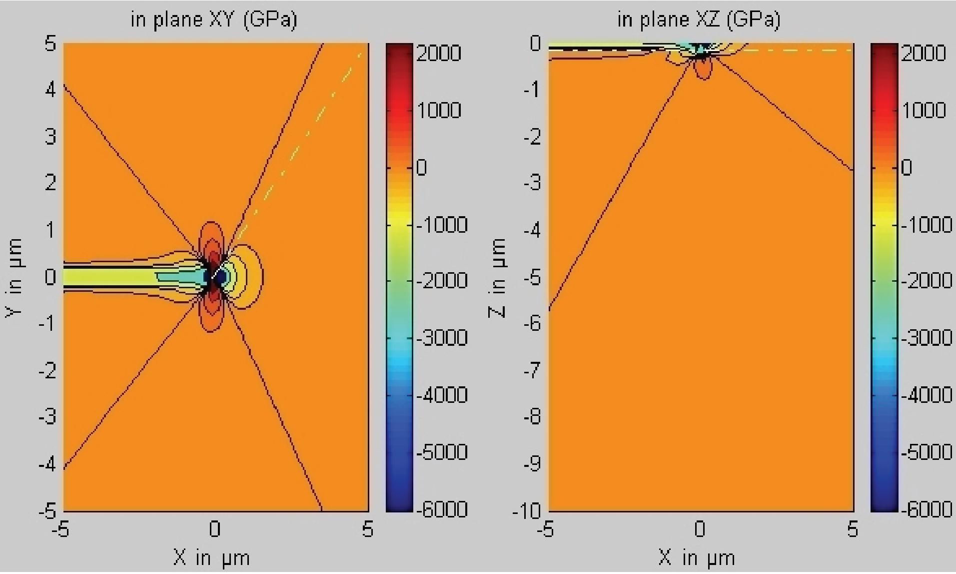

(b) SLS 1 – σ_{yy}^{max} = 2198 GPa

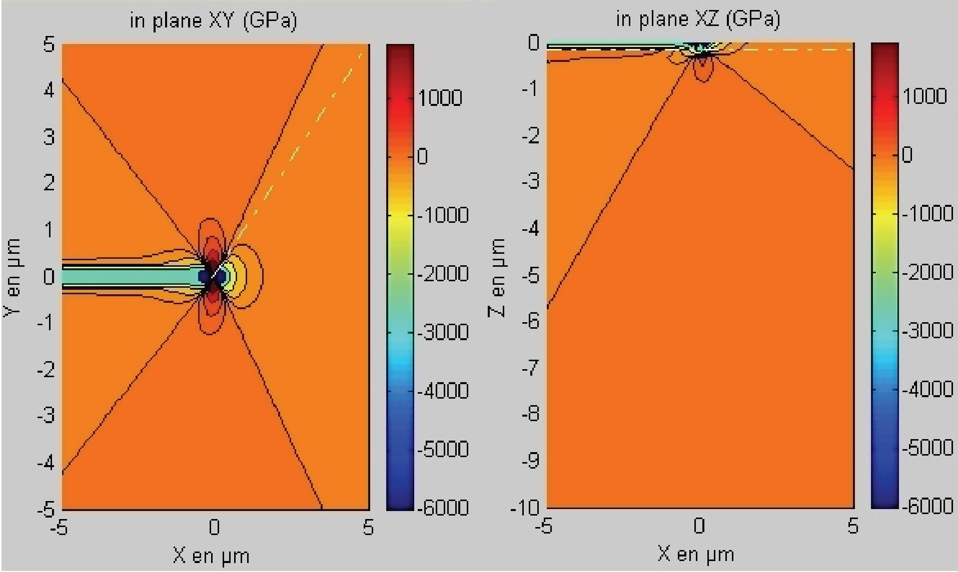

(c) SLS 2 – σ_{yy}^{max} = 1842 GPa

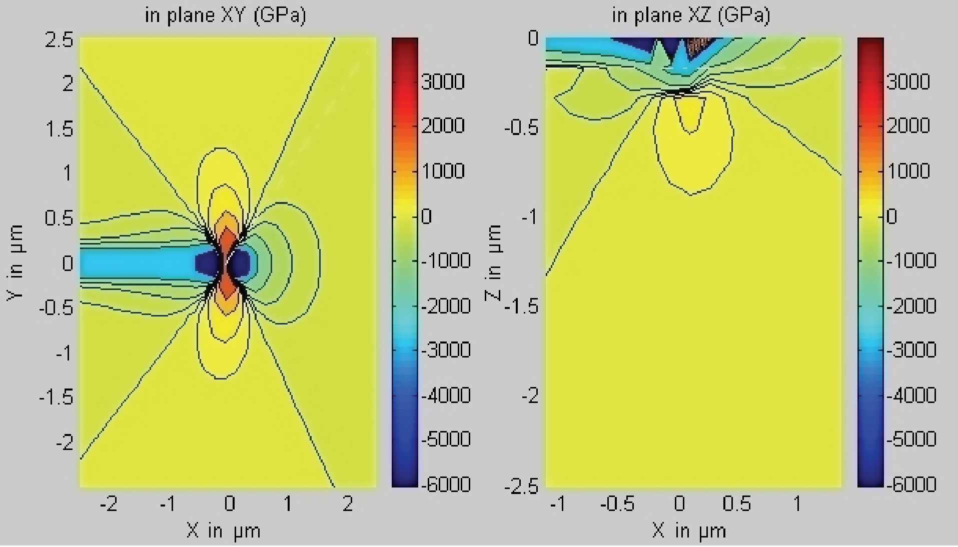

(d) SLS 3 – σ_{yy}^{max} = 3666 GPa

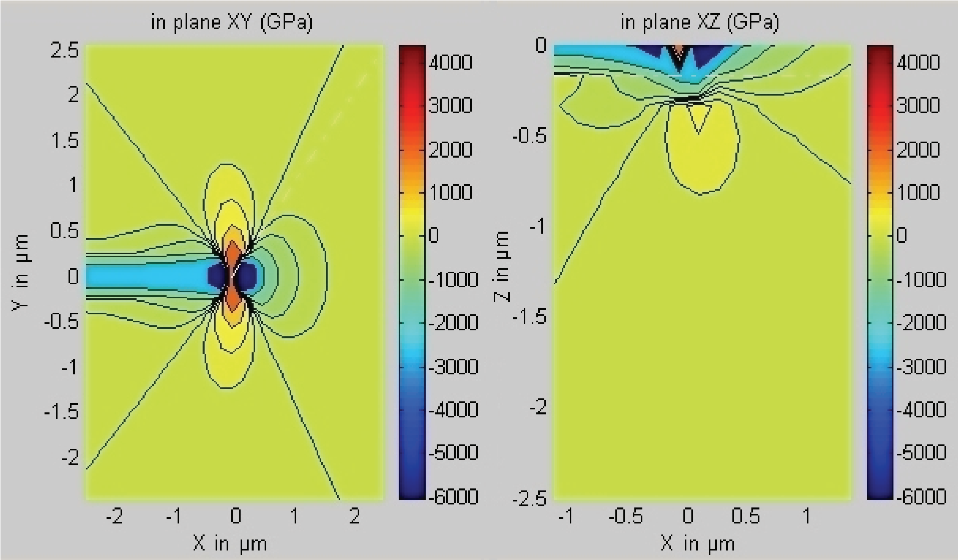

(e) SLS 4 – σ_{yy}^{max} = 4213 GPa

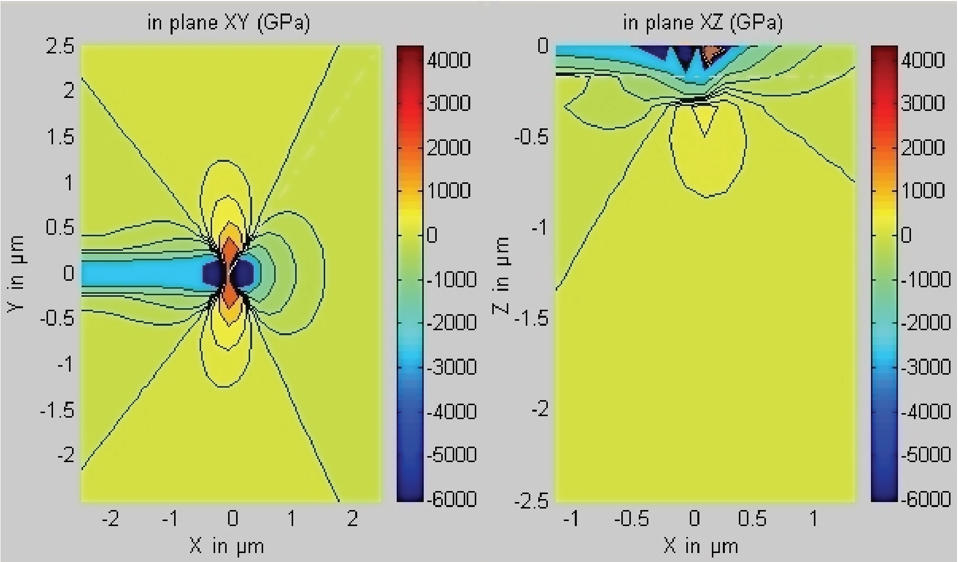

(f) Fused silica – σ_{yy}^{max} = 4350 GPa

Graph 52: Representation of the considered stress σ_{yy} in the XY and XZ planes for each glass composition.

To comment the plotted stress for each glass is not of great interest. However, the evolution of the plots from the standard float glass to the fused silica shows a results that have to be compared to the scratching pattern obtained in § 4.2.5. The Fig. 106 is a copy of the Fig. 88 (page 130) placed here for reading convenience. The comparison with Table 21 can also be useful.

The highest tensile stresses recorded for each glass differ even for the same load. This is a consequence of the difference shown between their parameters *B* as reported in § 5.7.4.4.

The highest the stresses are, the earlier (with regard to the normal load) the crack initiates. The evolution is clearly established in these graphs: from the standard float glass to the fused silica following the increase of silica content, the highest stress increases. Then, the median/radial cracking appears "earlier" as the silica content increase. The exception of the SLS 2 completes this analysis: it exhibits the lowest "highest" stress. The direct comparison with the scratch pattern in Fig. 106 and the Table 21 is consistent with the results given by the model.

Standard float glass:

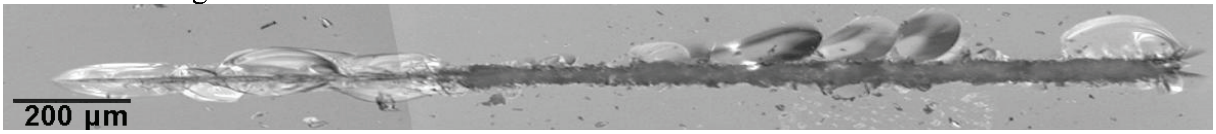

SLS 1:

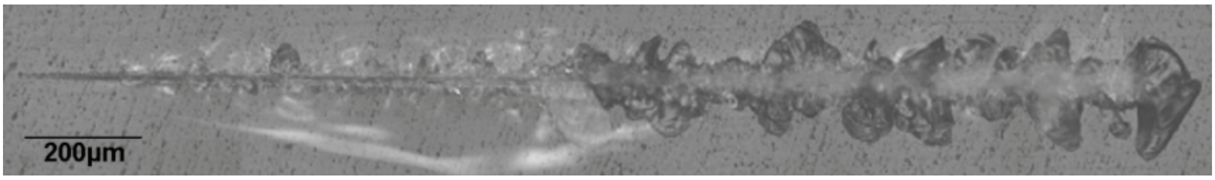

SLS 2:

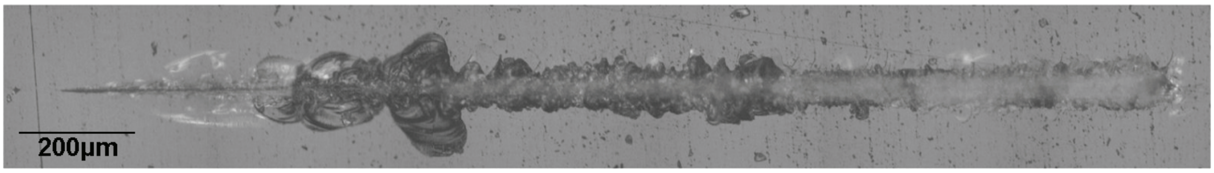

SLS 3:

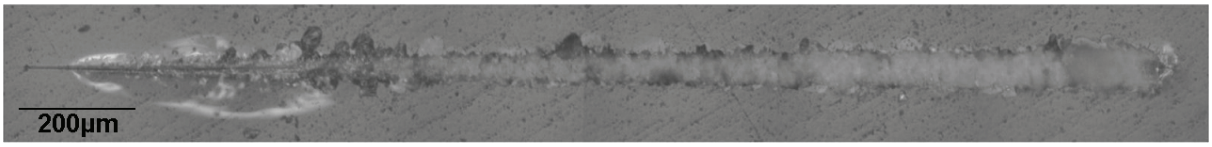

SLS 4:

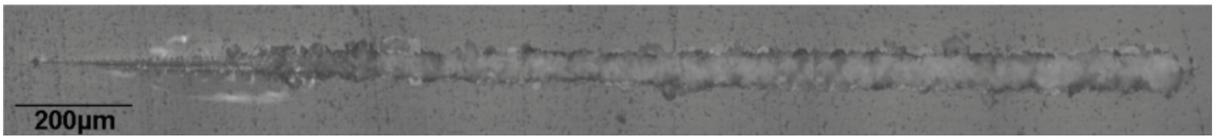

Fused silica:

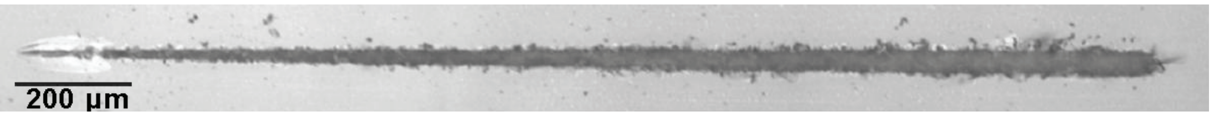

Fig. 106: Evolution of scratch resistance for the six considered glasses

5.9.3.3 Prediction of the lateral crack occurrence

Along these lines, Graph 53 represents the complete $\sigma_{zz} = \sigma^{n}_{zz-Hanson} + \sigma^{t}_{zz-Bous.} + \sigma^{r}_{zz-Blister}$ stress in the plane XY and XZ for the six different glasses. The load used during the computation is 0.8 N. The morphology of the stress field does not change dramatically through the glasses nuances. The influence of the material parameter *B* only appears in the values of the residual stress field that is superposed on these graphs with $\sigma^{n}_{zz-Hanson} + \sigma^{t}_{zz-Bous.}$ with the maximum tensile stress value determined with the method previously reported in § 5.6.5.5.

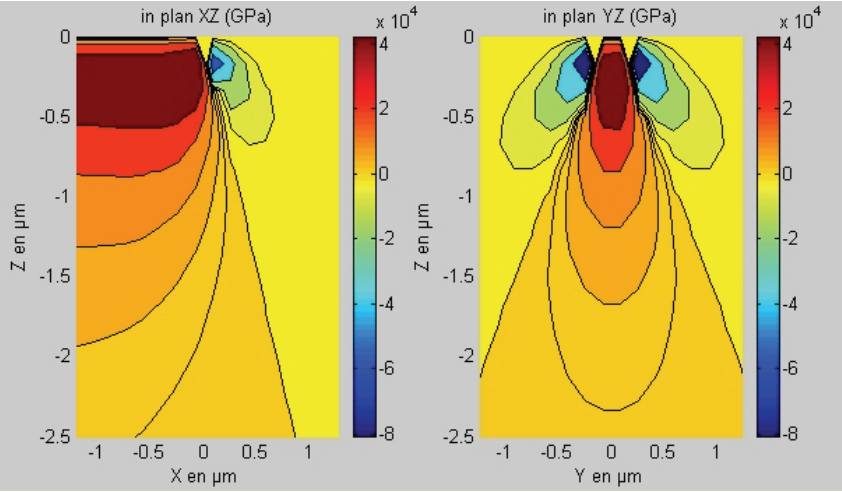

(a) Standard float glass – σ_{zz}^{max} = 4320 GPa

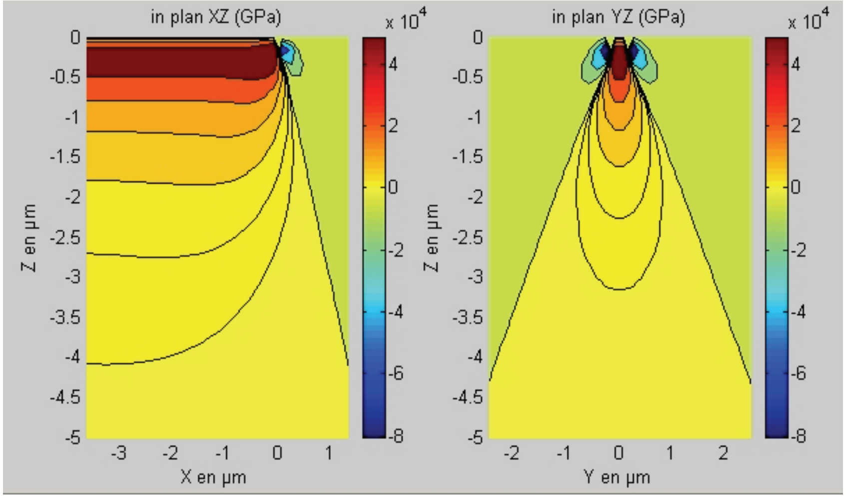

(b) SLS 1 – σ_{zz}^{max} = 4765 GPa

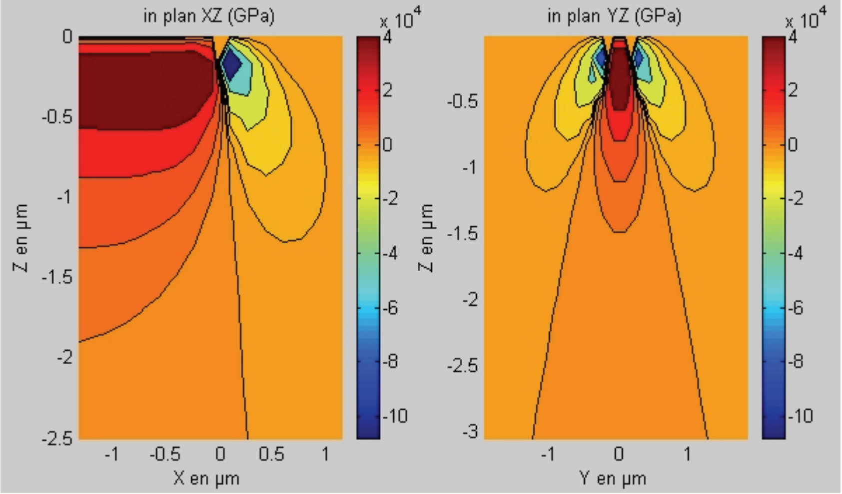

(c) SLS 2 – σ_{zz}^{max} = 4132 GPa

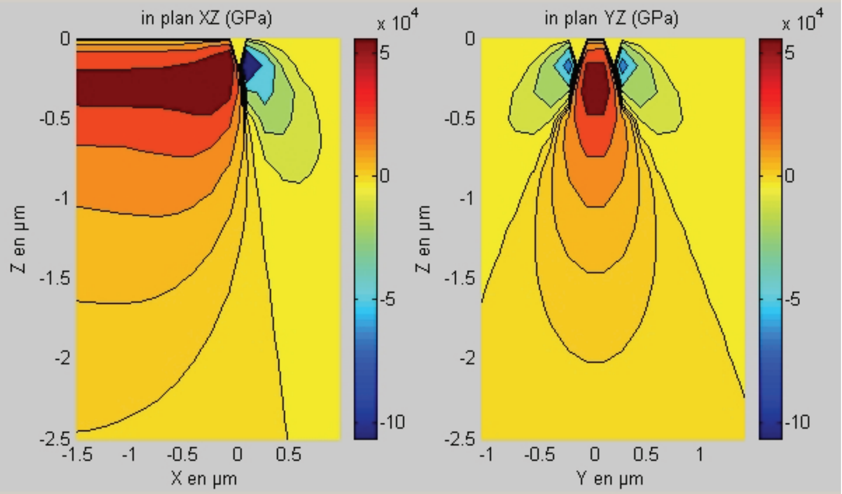

(d) SLS 3 – σ_{zz}^{max} = 5535 GPa

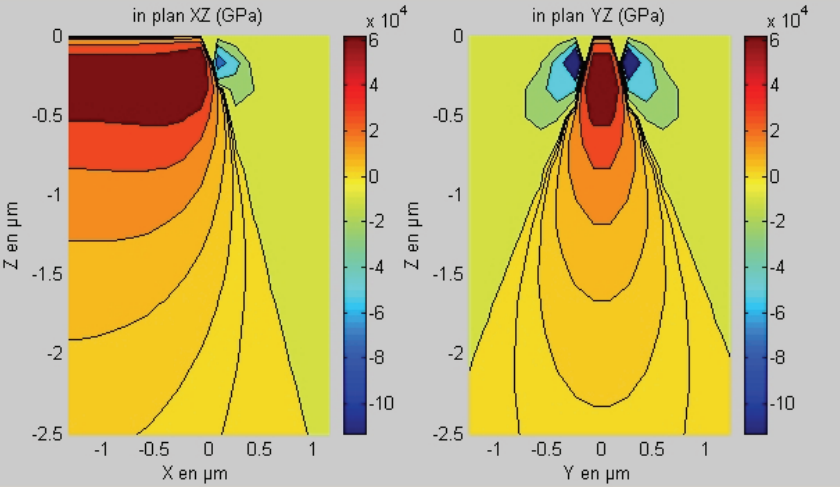

(e) SLS 4 – σ_{zz}^{max} = 6105 GPa

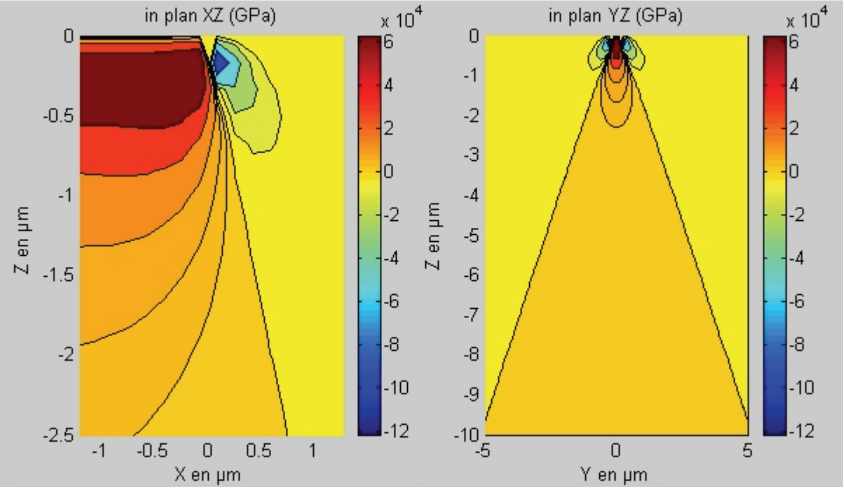

(f) Fused silica – σ_{zz}^{max} = 6562 GPa

Graph 53: Representation of the considered stress σ_{zz} in the XZ and YZ planes for each glass composition.

The evolution of the plots from the standard float glass to the fused silica shows similar results than the previous analysis about the median/radial crack initiation. The comparison between each stress distribution gives also different highest tensile stresses for each glass for the same load. This also illustrates the difference between their parameters *B*.

From the standard float glass to the fused silica following the increase of silica content, the highest stress increases in the stress distribution in Graph 53. The graphs clearly establish conclusions that are consistent with the experimental results: the lateral cracking appears at a lower load in the fused silica than in the standard float glass, following the same order in the intermediate glasses. The SLS 2 is again the exception: it exhibits the lowest "highest" stress. The direct comparison with the scratch pattern in Fig. 106 and Table 21 is consistent with the results given by the model.

5.9.3.4 Final remark and attempt for the micro-abrasive regime prediction

As already evoked earlier, no quantitative analysis is today reasonable with this model and there are still some parameters and hypothesis that are pointed out in this work that are too restrictive to lead to a quantitative model in the case of this study.

But finally, one can try to predict the evolution of the occurrence of the micro-abrasive regime: the micro-abrasive regime is still of great interest for understanding the damage mechanisms that occur. However, all the scratch tests seem to reveal that the micro-abrasive regimes follow the same evolution than the rest of the scratch, i.e. if the micro-cracking regime appears early (i.e. at low normal load), the micro-abrasive regime appears early as well. It seems that the local stresses involved in the scratching just reach critical values for the micro-abrasive regime to occur that is consistent with the critical local stresses needed for the other damage events (i.e. micro-cracking regime appearance). Then it seems that this conclusion is consistent but calls for caution for further interpretation. It needs first a better understanding of the damage that occurs during micro-abrasive regime to show the veracity or the weakness of this conclusion.

CHAPTER 6:
CONCLUSIONS

<u>SUMMARY OF CHAPTER 6</u>

6.1 Conclusions

6.1.1 General

The scratchability of six glasses (commercial float glass, SLS 1 to 4 and fused silica) belonging to the soda-lime silica glass system has been studied. An apparatus, named *scratch tester*, allowing for a variable loading cycle during a single experiment, was designed for the present work. This device was placed into a glove box in order to study the effect of the humidity.

6.1.2 Experimental results

Monotonic trends of density, Young's modulus and Poisson ratio were found out for the studied glasses (fused silica excluded) with regard to the increasing silica content in their composition. These evolutions were discussed with regard to structural considerations. Both hardness and toughness show minima for the SLS 2 composition and are attributed to the particular structure of this glass that is supposed to be interpenetration of two networks.

The scratch behaviors of the considered glasses were found very sensitive to the loading history and three major scratch-damage regimes were observed, namely the micro-ductile, the micro-cracking and the micro-abrasive regimes.

Some preliminary results were pointed out: i) a dynamical effect due to the load history was noticed; ii) no dependence of the face of the float glass (tin or air) was shown in the load range of this study; iii) the residual stresses were found to greatly influence the severity of the scratch pattern; iv) the indenter geometry plays a great role in the scratch process since the more severe the indenter shape is the more early (in a load sense) the damage regimes appear.

A detailed study of the damage phenomenology leaded to several conclusions: i) the "plastic" track obtained when scratching at low loads hides sub-surface damage; ii) the so-called chevron cracks were found to be median/radial cracks that propagate in a semi-stable way: they initiate straight in front of the indenter and that reach out from the track by deviating but propagate with a stable speed; iii) the chip creation is most of the time due to the intersection between lateral and radial cracks.

The studied glasses were also found to be very sensitive to the relative humidity since it mainly affects the median-radial crack propagation and has therefore a direct incidence on the chip formation and on the micro-cracking regime. A significant shift of the regime transition loads was noticed with regard to the humidity level.

Finally, the influence of the chemical composition on the scratching behavior of the considered materials was investigated. On one hand, the higher the silica content is and the more significant the flow-densification process becomes, and as a result the lower the critical loads for radial and lateral crack formation are. On the other hand, the glass compositions with the highest network compacity (SLS 1/2) can hardly accommodate sharp contact loading and are thus the most sensitive glasses to micro-cracking. These results are consistent in the light of both indentation and scratching behaviors.

6.1.3 Extension of Ahn's model

A semi-analytical model for prediction of crack occurrence during scratching process was established. It is based on the extension of Ahn's sliding analytical model of stress field [20, 71, 72] to i) Vickers indenter geometry and ii) the normal/anomalous behaviors of the studied glasses.

The first point was treated by a comparison between a Vickers and a conical indentation performed with a 3D Finite Elements approach. A 3D Finite Elements model was designed (Abaqus FE code) and validated.

The stress field in the face plane of the Vickers indenter can easily be modeled in an analytical form by the field designed by Hanson for conical indentation. The stress field in the edge plane of the Vickers indenter should be modeled by the field corresponding of a progressively line-loading on an elastic half body. Unfortunately, no expression to model the edge plane's stress field is available yet, so some corrections were made to the final model.

The second point of the model extension was solved by considering closely the deformation of the considered materials: the competition between the flow deformation process by local shearing (conservative volume deformation) and the deformation by densification (accommodation with loss of volume) was studied. To do so, a new experimental method was developed based on the AFM measurements of the volume of Vickers imprints. Trends to densification or shearing of the six glasses were consistently established. Finally, clues for a second new method to quantify the densification/shearing competition considering the energies involved in instrumented indentation tests were given.

6.1.4 Results of the model / Accordance with the experimental results

After integrating these two extensions of the analytical model (which is then qualified as semi-analytical model), phenomenology about experimental cracking occurrences was regained:

i. The median/radial crack that just initiates under the indenter does not propagate straight due to a compressive stress component in this direction. It inclines either on the left or the right as observed in experiments.
ii. The initiation of the lateral crack is expected to occur in the depth of the body behind the indenter due to high tensile residual stresses at this location. A compressive component prevents the propagation of the lateral crack in front of the indenter.

The evolutions of the crack occurrences with regard to the chemical composition of glass confirmed the experimental results:

i. The median/radial cracking appears "earlier" as the silica content increases.
ii. It is also clearly established that the lateral cracking appears at lowest normal load in the fused silica than in the standard float glass case, following again the same order in the intermediate glasses.

In these evolutions, the SLS 2 is the exception: for both median/radial and lateral crackings, it exhibits the less resistance.

Finally, it can be considered that the micro-abrasive regimes follow the same evolution than the micro-cracking regimes occurrence that was just described. This conclusion is consistent with experimental results but calls for caution for further interpretation.

6.2 Remarks & perspectives

In form of some remarks, here are summarized the limits of this study and other restrictions, perspectives and author's personal thoughts about this work.

It could be useful to get insight the micro-abrasive regime from a fractographic point of view, while it does not seem to be useful to go further to the experimental phenomenology for other damage events during scratching from a fractographic point of view.

The assumptions of the mechanical model developed in this work are open enough to take into account a lot of experimental parameters (friction coefficient, indenter geometry,...) so that it is expected that it can directly work on most of the brittle materials and also on semi-brittle materials such as semi-conductors for example. Only the identification of the strength of the sliding *Blister* field from experimental data is required.

The experimental technique of measurements of the morphologies of indentation (measurements of volume imprints by AFM) is a very promising technique that can find an accurate goal in different problems of the contact mechanic: true Hardness, elastic recovery,...

In the case of the present study, the assessment of the constitutive law of concerned materials can be determined with more accuracy to lead to a quantitative model that still remains in this work only qualitative for previously quoted reasons.

The analytical model have limits that are underlined in this study but can sometimes be helped by experimental procedures or Finite Elements models in order to build a *mixed* model.

An obvious complementary work to this study may be to introduce a rupture mechanic approach in the treatment of the indentation and scratching problem.

An energy approach could be considered to treat specific mechanisms like crack propagations or periodic phenomena (periodicity for energy stocking before a next crack occurs as the indenter moves).

REFERENCES

[1] K.W. Peter, *Densification and flow phenomena of glass in indentation experiments,* J. Non-Cryst. Solids, **5**, (1970), p. 103-115.

[2] D.M. Marsh, *Plastic flow in glass,* Proc. Roy. Soc. A, **279**, (1964), p. 420-435.

[3] P.W. Bridgman and I. Simon, *Effects of very high pressures on glass,* Journal of Applied Physics, **24** (4), (1953), p. 405-413.

[4] S. Sakka and J.D. Mackenzie, *High pressure effects on glass,* J. Non-Cryst. Solids, **1**, (1969), p. 107-142.

[5] J.D. Mackenzie and R.P. Laforge, *High-pressure densification of glass and the effects of shear,* Nature, **197**, (1963), p. 480-481.

[6] J.T. Hagan, *Shear deformation under pyramidal indentations in soda-lime glass,* Journal of Materials Science, **15**, (1980), p. 1417-1424.

[7] A.E. Giannakopoulos and S. Suresh, *Determination of elastoplastic properties by instrumented sharp indentation,* Scripta Materialia, **40** (10), (1999), p. 1191-1198.

[8] R.F. Cook and G.M. Pharr, *Direct observation and analysis of indentation cracking in glasses and ceramics,* J. Am. Ceram. Soc., **73** (4), (1990), p. 787-817.

[9] A. Arora, D.B. Marshall, B.R. Lawn, and M.V. Swain, *Indentation deformation/fracture of normal and anomalous glasses,* J. Non-Cryst. Solids, **31**, (1979), p. 415-428.

[10] S. Dériano, *Conception chimique de verres silicatés à hautes performances mécaniques*, University of Rennes 1, (France), (2002).

[11] V. Le Houérou, J.-C. Sangleboeuf, S. Dériano, T. Rouxel, and G. Duisit, *Surface damage of soda-lime-silica glasses: Indentation scratch behavior,* J. Non-Cryst. Solids, **316**, (2003), p. 54-63.

[12] T. Rouxel, J.-C. Sanglebeouf, J.-P. Guin, V. Keryvin, and G-D. Sorarù, *Surface damage resistance of gel-derived oxycarbide glasses : hardness, toughness, and scratchability,* J. Am. Ceram. Soc., **84** (10), (2001), p. 2220-2224.

[13] M. Yamane and J.D. Mackenzie, *Vicker's hardness of glass,* J. Non-Cryst. Solids, **15**, (1974), p. 153-164.

[14] B.R. Lawn, A.G. Evans, and D.B. Marshall, *Elastic/plastic indentation damage in ceramics : the median/radial crack system,* J. Am. Ceram. Soc., **63** (9-10), (1980), p. 574-581.

[15] D.B. Marshall, B.R. Lawn, and A.G. Evans, *Elastic/plastic indentation damage in ceramics : the lateral crack system,* J. Am. Ceram. Soc., **65** (11), (1982), p. 561-566.

[16] J.T. Hagan, *Micromechanics of crack nucleation during indentations,* J. Mater. Sci., **14**, (1979), p. 2975-2980.

[17] J. Sehgal and S. Ito, *A new low-brittleness glass in the soda-lime-silica glass family,* J. Am. Ceram. Soc., **81** (9), (1998), p. 2485-2488.

[18] K. Niihara, R. Morena, and D.P.H. Hasselman, J. Am. Ceram. Soc., **65**, (1982), p. C116.

[19] R.W. Rice and J.J. Mecholsky, *Special publication 562*, in *National Bureau of Standards*, (1965), p. 351.

[20] Y. Ahn, *Deformation about sliding indentation in ceramics and its application to lapping*, Purdue University, (USA), (1992).

[21] V.H. Bulsara, *Scratch formation in brittle solids and its application to polishing*, Purdue University, (USA), (1997).

[22] *Fractography of glasses and ceramics*, Advanced in ceramics, ed. J.R. Varner and V.D. Frechette, Vol. 22, Westerville, American Ceramic Society, (1988).

[23] *Ceramics and Glasses*, in *Engineered materials handbook volume 4*, ASM International, (1991), p. 636.

[24] *Standard practice for interpreting glass fracture surface features*, in *C 1256 - 93 (reapproved 2003)*, ASTM International, (1993).

[25] D. Hull, *Fractography: observing, measuring and interpreting fracture surface topography*, Cambridge University Press, (1999).

[26] G.N. Greaves, *EXAFS and the structure of glass,* J. Non-Cryst. Solids, **71**, (1985), p. 203-217.

[27] E.H. Yoffe, *Elastic stress field caused by indenting brittle materials,* Philosophical Magazine A, **46** (4), (1982), p. 617-628.

[28] M.T. Hanson, *The elastic field for conical indentation including sliding friction for transverse isotropy,* J. of Applied Mech., **59**, (1992), p. S123.

[29] M.T. Hanson, *The elastic field for a sliding conical punch on an isotropic half-space,* J. of Applied Mech., **60**, (1993), p. 557.

[30] H. Doweidar, *Density-structure correlations in* Na_2O-Al_2O_3-SiO_2 *glasses,* J. Non-Cryst. Solids, **240**, (1998), p. 55-65.

[31] H. Doweidar, *Density-structure correlations in silicate glasses,* J. Non-Cryst. Solids, **249**, (1999), p. 194.

[32] G. Geiger, *Introduction to ceramics*, in *American Ceramic Society*.

[33] A. Pilkinton, *The Float-Glass Process,* Proc. R. Soc. London A, **314**, (1969), p. 1-25.

[34] J.D. Mackenzie, *State of art and prospects of glass science,* J. Non-Cryst. Solids, **52**, (1982), p. 1-8.

[35] J. Zarzycki, *Les verres et l'état vitreux*, Paris, Masson, (1982).

[36] J. Zarzycki, *Verres*, in *techniques de l'ingénieur*, (1990), p. 1-23.

[37] H. Scholze, *Le verre nature structure et propriétés*, Second ed., Paris, Institut du Verre, (1974).

[38] Z.W. Zachariasen, J. Am. Ceram. Soc., **54**, (1932), p. 3841.

[39] W.D. Kingery, H.K. Bowen, and D.R. Uhlmann, *Introduction to ceramics*, Wiley Interscience, (1979).

[40] J.J. Mecholsky, *Fracture analysis of glass surfaces*, in *Strength of Inorganic Glass*, C.R. Kurkjian, Editor, Plenum Press, New York, (1985), p. 569-590.

[41] K. Hirao and M. Tomozawa, *Microhardness of* SiO_2 *glass in various environments,* J. Am. Ceram. Soc., **70** (7), (1987), p. 497-502.

[42] T. Michalse and B. Bunker, *La fracture du verre,* Pour la Science, (February 1988).

[43] V.M. Sglavo and D.J. Green, *Subcritical growth of indentation median cracks in soda-lime-silica glass,* J. Am. Ceram. Soc., **78** (3), (1995), p. 650-656.

[44] C.J. Simmons and S.W. Freiman, *Effect of corrosion processes on subcritical crack growth in glass,* J. Am. Ceram. Soc., **64** (11), (1982), p. 683-686.

[45] A.A. Griffith, *The theory of rupture*, in *International Congress for Appl. Mech.*, Delft, (1924).

[46] R. Roy and H.M. Cohen, Nature, **190**, (1961), p. 768.

[47] E.B. Christiansen, S.S. Kistler, and W.B. Gogarty, J. Am. Ceram. Soc., **45**, (1962), p. 172.

[48] D.R. Uhlmann, *Densification of alkali silicate glasses at high pressure,* J. Non-Cryst. Solids, **13**, (1973/74), p. 89-99.

[49] B.R. Lawn and M.V. Swain, *Microfracture beneath point indentations in brittle solids,* Journal of Materials Science, **10**, (1975), p. 113-122.

[50] D. Tabor, *The Hardness of Metals*, Oxford at the Clarendon Press, (1951).

[51] J. Lubliner, *Plasticity theory*, New York, Macmillan Publishing Company etc., (1990).

[52] F.M. Ersnberger, *Role of densification in deformation of glassers under point loading,* J. Am. Ceram. Soc., **51**, (1968), p. 545-547.

[53] J.T. Hagan and S. Van Der Zwaag, *Plastic processes in a range of soda-lime-silica glasses,* Journal of Non-Crystalline Solids, **64**, (1984), p. 249-268.

[54] E.C. Ziemath and P.S.P. Herrmann, *Densification and residual stresses induced in glass surfaces by Vickers indentations,* Journal of Non-Crystalline Solids, **273**, (2000), p. 19-24.

[55] C.R. Kurkjian and G.W. Kammlott, *Indentation behavior of soda-lime silica glass, fused silica, and single-crystal quartz at liquid nitrogen temperature,* J. Am. Ceram. Soc., **78** (3), (1995), p. 737-744.

[56] B.R. Lawn and E.R. Fuller, *Equilibrium penny-like cracks in indentation fracture,* Journal of Materials Science, **10**, (1975), p. 2016-2024.

[57] M.V. Swain, *Microfracture about scratches in brittle solids,* Proc. R. Soc. Lond. A, **366**, (1979), p. 575-597.

[58] V.H. Bulsara, *Direct observation of contact damage around scratches in brittle solids*, in *SPIE*, (1997), p. 76-88.

[59] A.G. Evans and D.B. Marshall, *Wear mechanisms in ceramics*, in *Fundamentals of Friction and Wear of Materials*, American Society of Metals, Metals Park, Ohio (USA), (1980), p. 439-452.

[60] D.B. Marshall, A.G. Evans, B.T. Khuri Yakub, J.W. Tien, and G.S. Kino, *The nature of machining damage in brittle materials,* Proc. R. Soc. Lond. A, **385**, (1983), p. 461-475.

[61] K. Li, Y. Shapiro, and J.C.M. Li, *Scratch test of soda-lime glass,* Acta Mater., **46** (15), (1998), p. 5569-5578.

[62] I.N. Sneddon, *Fourier transforms*, McGraw-Hill book company, INC., (1951).

[63] N.A. Stilwell and D. Tabor, *Elastic recovery of conical indentations,* Proc. Phys. Soc., **78**, (1961), p. 169-179.

[64] R. Hill, *The mathematical theory of plasticity*, Oxford, Clarendon, (1950).

[65] R.F. Bishop, R. Hill, and N.F. Mott, *The theory of indentation and hardness tests,* Proceedings, Physics Society, **57**, (1945), p. 147.

[66] D. Tabor, *The hardness of solids,* Review of Physics in Technology, **1**, (1970), p. 145-179.

[67] K.L. Johnson, *The correlation of indentation experiments,* J. Mech. Phys. Solids, **18**, (1970), p. 115-126.

[68] K.L. Johnson, *Contact Mechanics*, Cambridge University Press, (1985).

[69] G.M.L. Gladwell, *Contact problems in the classical theory of elasticity*, Sijthoff & Noordhoff, (1980).

[70] D. Maugis, *Contact, Adhesion and Rupture of Elastic Solids*, Vol. 130, Springer Series in Solid-State Sciences, (2000).

[71] Y. Ahn, T.N. Farris, and S. Chandrasekar, *Elastic stress fields caused by sliding microindentation of brittle materials*, in *Machining of advanced materials, NIST SP 847, S. Jahanmir*, (1993), p. 71-81.

[72] Y. Ahn, T.N. Farris, and S. Chandrasekar, *Sliding microindentation fracture of brittle materials : role of elastic stress fields,* Mechanics of Materials, **29**, (1998), p. 143-152.

[73] M.T. Hüber, Ann. Phys., **14**, (1904), p. 153.

[74] A.E.H. Love, *The stress produced in a semi-infinite solid by pressure on part of the boundary,* Phil. Trans. R. Soc. A, **228**, (1929), p. 377-420.

[75] V.I. Fabrikant, *Applications of potential theory in mechanics : a selection of new results*, The Netherlands, Kluwer Academic Publishers, (1989).

[76] I.N. Sneddon, *Boussinesq's problem for a rigid cone,* Proceedings of the Cambridge Philosophical Society, **44**, (1948), p. 492-507.

[77] A.E.H. Love, *The mathematical theory of elasticity*, Vol. 4th edition, Dover Publications, (1927).

[78] S.S. Chiang, D.B. Marshall, and A.G. Evans, *The response of solids to elastic/plastic indentation. I. Stresses and residual stresses,* J. Appl. Phys., **53** (1), (1982), p. 298-311.

[79] S.S. Chiang, D.B. Marshall, and A.G. Evans, *The response of solids to elastic/plastic indentation. II. Fracture initiation,* J. Appl. Phys., **53** (1), (1982), p. 312-317.

[80] C.J. Wagner, *Influence of composition on crack initiation behavior of glasses*, Alfred University (New York), (France), (1997).

[81] J.L. Loubet, J.M. Georges, and G. Meille, *Vickers indentation curves of elastoplastic materials*, in *Microindentation Techniques in Materials Science and Engineering, ASTM STP 889, P.J. Blau and B.R. Lawn*, American Society for Testing and Materials, Philadelphia, (1986), p. 72-89.

[82] I.N. Sneddon, *The relation between load and penetration in the axisymmetric Boussinesq problem for a punch of arbitrary profile,* Int. J. Engng Sci., **3**, (1965), p. 47-57.

[83] J.L. Bucaille, S. Stauss, E. Felder, and J. Michler, *Determination of plastic properties of metals by instrumented indentation using different sharp indenters,* Acta Materialia, **51**, (2003), p. 1663-1678.

[84] A.E. Giannakopoulos and P.-L. Larsson, *Analysis of pyramid indentation of pressure-sensitive hard metals and ceramics,* Mechanics of Materials, **25**, (1997), p. 1-35.

[85] A.E. Giannakopoulos and S. Suresh, *Indentation of solids with gradients in elastic properties : part II. Axysymmetric indentors,* Int. J. Solids Structures, **34** (19), (1997), p. 2428-2428.

[86] S. Carlsson and P.-L. Larsson, *On the determination of residual stress and strain fields by sharp indentation testing. Part I : theoretical and numerical analysis,* Acta Mater., **49**, (2001), p. 2179-2191.

[87] J.L. Bucaille, *Simulation numérique de l'indentation et de la rayure des verres organiques*, Ecole Nationale Supérieure des Mines de Paris, (France), (2001).

[88] A.E. Giannakopoulos, P.-L. Larsson, and R. Vestergaard, *Analysis of Vickers indentation,* Int. J. Solids Structures, **31** (19), (1994), p. 2679-2708.

[89] W. Cheng, E. Ling, and I. Finnie, *Median cracking of brittle solids due to scribing with sharp indenters,* J. Am. Ceram. Soc., **73**, (1990), p. 580-586.

[90] H. Rawson, *Inorganic Glass-Forming Systems*, Academic Press, London, (1967), p. 88.

[91] G.M. Pharr and R.F. Cook, *Instrumentation of a conventional hardness tester for load-displacement measurement during indentation,* J. Mater. Res., **5** (4), (1990), p. 847-851.

[92] J. Malzbender, J.M.J. den Toonder, A.R. Balkenende, and G. de With, *Measuring mechanical properties of coatings : a methodology applied to nano-particle-filled sol-gel coatings on glass,* Materials Science and Engineering, **R 36**, (2002), p. 47-103.

[93] A.C. Fischer-Cripps, *Nanoindentation*, Mechanical Engineering Series, Springer-Verlag New York Inc, (2004).

[94] J. Malzbender, *Comment on hardness definitions,* Journal of the European Ceramic Society, **23**, (2003), p. 1355-1359.

[95] J.A. Williams, *Analytical models of scratch hardness,* Tribology international, **29** (8), (1996), p. 675-694.

[96] J.M. Challen and P.L.B. Oxley, *An explanation of the different regimes of friction and wear using asperity deformation models,* Wear, **53**, (1979), p. 229-243.

[97] J.M. Challen, L.J. McLean, and P.L.B. Oxley, *Plastic deformation of a metal surface in sliding contact with a hard wedge : its relation to friction and wear,* Proc. R. Soc. Lond. A, **394**, (1984), p. 161-181.

[98] S. Lafaye, C. Gauthier, and R. Schirrer, *A surface flow line model of a scratching tip: apparent and true local friction coefficients,* Tribology international, **38**, (2005), p. 113-127.

[99] V. Jardret, H. Zahouani, J.L. Loubet, and T.G. Mathia, *Understanding and quantification of elastic and plastic deformation during a scratch test,* Wear, **218**, (1998), p. 8-14.

[100] C.A. Brookes, P. Green, P.H. Harrison, and B. Moxley, *Some observations on scratch and indentation hardness measurements,* J. Phys. D. : Appl. Phys., **5**, (1972), p. 1284-1293.

[101] J.-P. Baïlon and J.-M. Dorlot, *Des matériaux*, Third ed., Montréal, Presses internationales polytechniques, (2000).

[102] C.J.R. Sheppard and D. Shotton, *Confocal laser scanning microscopy*, Oxford, Bios, (1997).

[103] K.H. Sun, J. Am. Ceram. Soc., **30** (9), (1947), p. 277.

[104] C.L. Babcock, J. Am. Ceram. Soc., **52** (3), (1969), p. 143.

[105] B.R. Lawn and D.B. Marshall, J. Am. Ceram. Soc., **62** (7-8), (1979), p. 574.

[106] B.R. Lawn, *Fracture of Brittle Solids*, Cambridge University Press, (1993), p. 339-340.

[107] B.R. Whittle and R.J. Hand, *Morphology of Vickers indent flaws in soda-lime-silica glass,* J. Am. Ceram. Soc., **84** (10), (2001), p. 2361-2365.

[108] J.C. Hay, A. Bolshakov, and G.M. Pharr, *A critical examination of the fundamental relations used in the analysis of nanoindentation data,* J. Mater. Res., **14** (6), (1999), p. 2296-2305.

[109] B.A. Galanov, *An approximate method for the solution of some two-body contact problems with creep in the case of an unknown contact area,* Soviet Applied Mechanics, **18**, (1982), p. 711.

[110] B.N. Lucas, W.C. Oliver, G.M. Pharr, and J.-L. Loubet, *Time dependent deformation during indentation testing,* Mat. Res. Soc. Symp. Proc., **436**, (1997).

[111] K. Suzuki, Y. Benino, T. Fujiwara, and T. Komatsu, *Densification energy during nanoindentation of silica glass,* J. Am. Ceram. Soc., **85** (12), (2002), p. 3102-3104.

LIST OF TABLES

LIST OF GRAPHS

LIST OF FIGURES

APPENDIX 1:
SCRATCH TESTER - BUILDING, INSTRUMENTATION & TESTING

SUMMARY OF APPENDIX 1

App.1-1 Building the scratch tester

App.1-1.1 Requirement specifications

The scratch test could be summarized as dragging a well-defined hard tip called indenter on the sample surface while applying a particular normal load P. A *scratch tester* also known as *linear sclerometer* is a device that allows performing scratch test.
A scratch tester was built for this work. It was first needed to define the requirements specification of the machine. It lies into several main functions that can be listed as follows:

- quasi-static scratch process,
- high stiffness-machine due to the relative high stiffness of the tested samples,
- variable loading patterns,
- moisture controlled tests,
- ability to change easily the indenter with a good reproducible orientation,
- ability to hold a lot of geometries of samples,
- in-situ visualization of the indenter/sample contact,
- accurate indenter/sample approach,
- full video acquisition,
- full data collecting.

According to these requirement specifications, the principle of the main machine was drawn and is reported in Fig. 107.

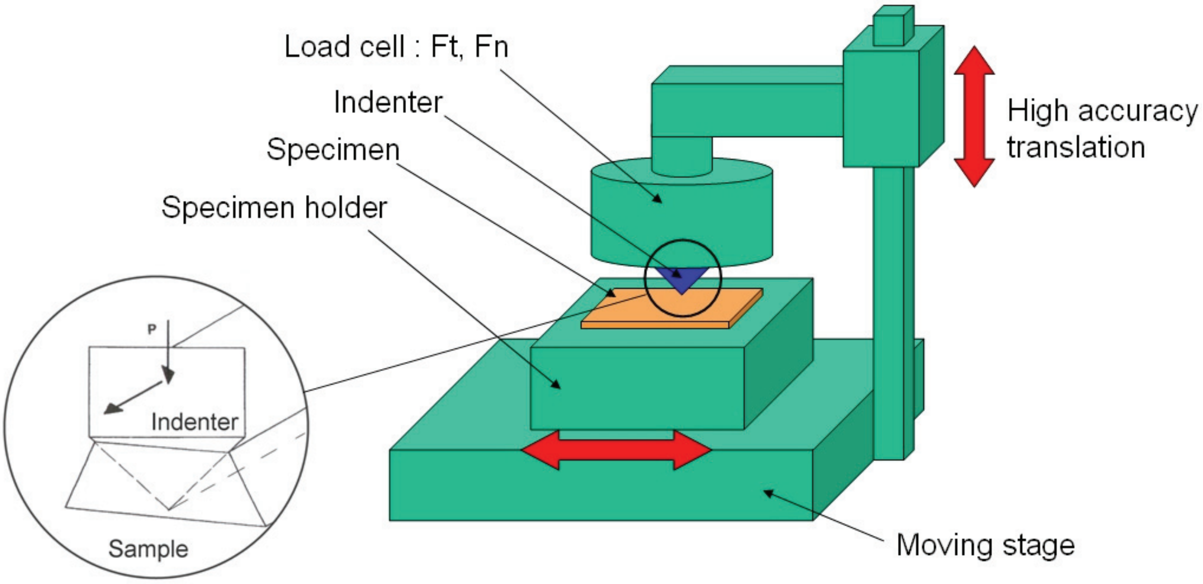

Fig. 107: Principle diagram of the scratch tester – main functions.

App.1-1.2 Machine details

Fig. 108 shows the details of the whole apparatus. The linear sclerometer lies on the right of the figure. A long-distance microscope equipped of a CCD camera is set right under the machine (in vertical position) in order to visualize the scratching phenomenon. A video camera (and its monitor on the left of the figure) completes the video setup and is used essentially for accurate indenter/sample approach. The machine is computer controlled through an electronic interface (see Fig. 108) and Labview programs. Loads (T and N) and vertical and scratching displacements are continuously monitored and acquired (double acquisition: on the computer and on the electronic data plotter). A second computer is devoted to the video acquisition (from the long-distance microscope) and a third one (the notebook on the photo) for data treatment.

Fig. 109 shows the linear sclerometer in details. An elastic double-cantilever with a double left-and-right screw was designed to ensure a controlled coarse translation for indenter/sample approach (approximately 10 mm of displacement). A piezo-electric actuator provides the fine vertical translation for loading the indenter on the surface. This piezo-electric ceramic (100 μm of displacement range) is computer controlled through the X-Y load cell (5 N maximum of normal load – accuracy of 0.02 N) data collecting in order to follow the loading process pattern selected for the test. A bearing slide provides the scratching displacement and is computer controlled (1 μm/s up to 5 mm/s of speed – 1 μm of displacement accuracy).

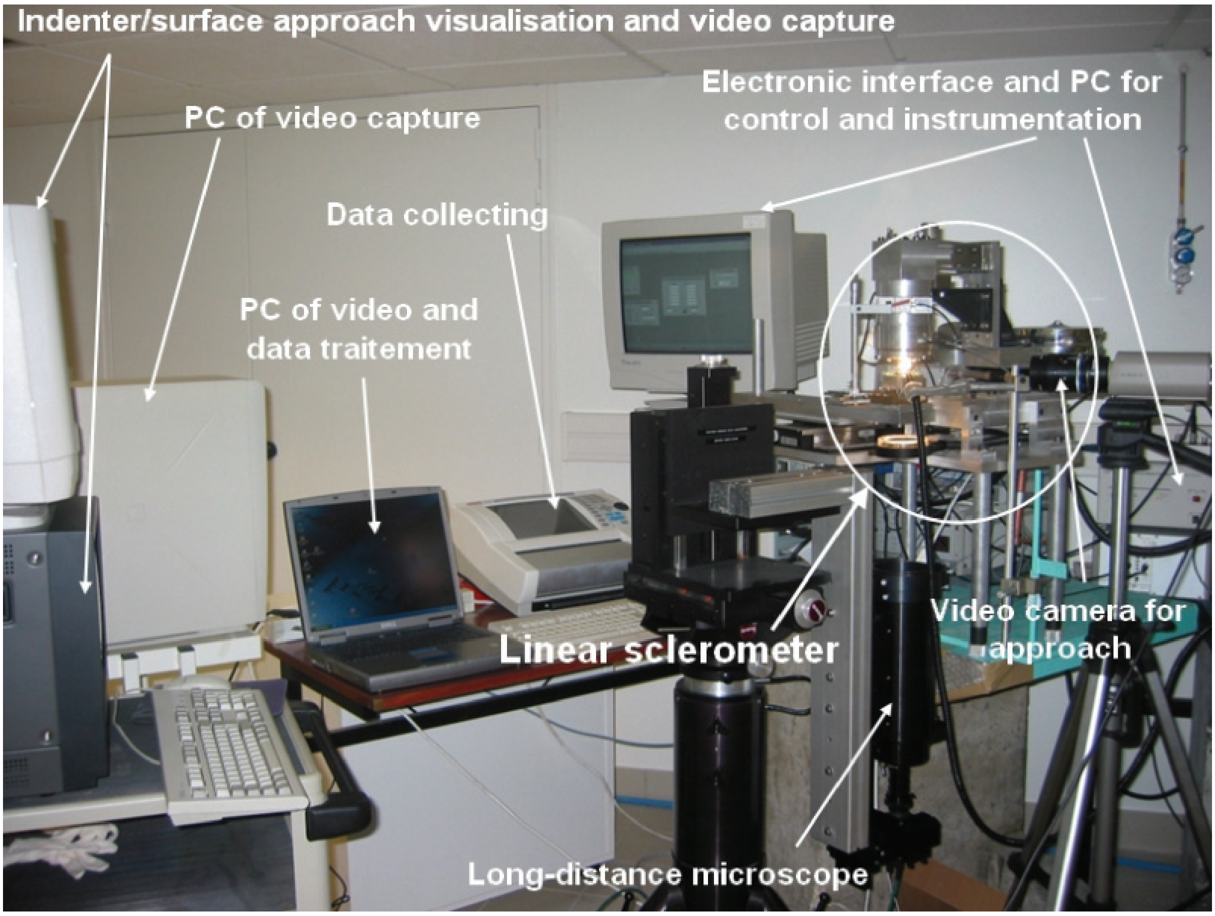

Fig. 108: The complete linear sclerometer experimental setup.

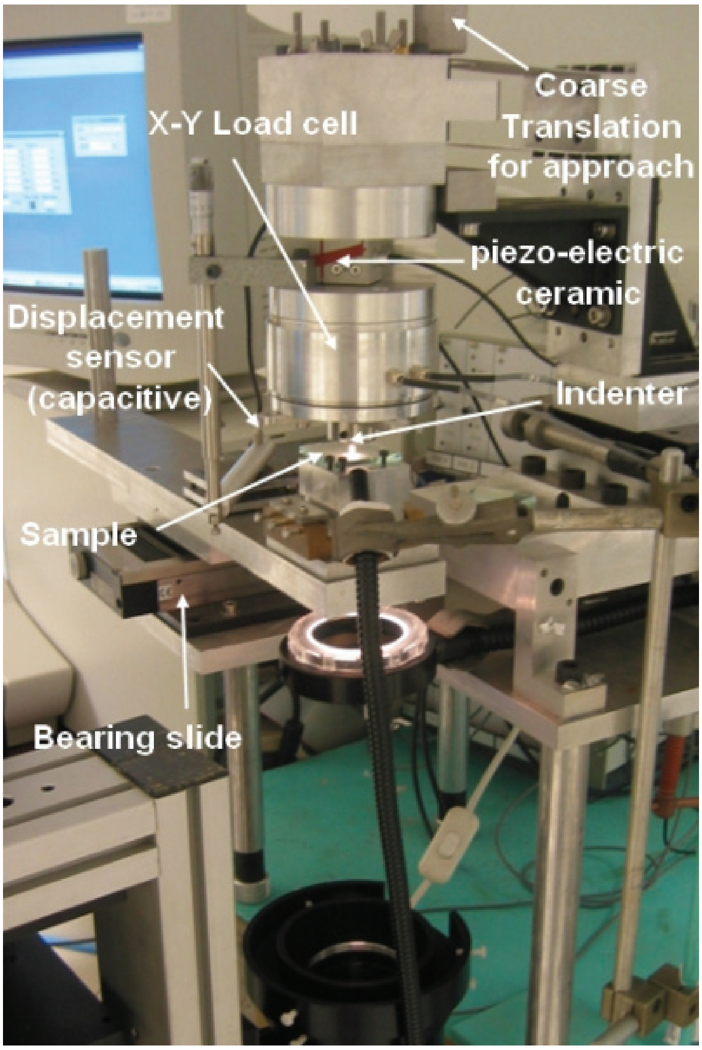

Fig. 109: Details of the linear sclerometer.

Two specimen holders were designed. The first one (see Fig. 110 (a)) is equipped of a large hole (not visible on the photo) which allows the visualization of the contact indenter/glass during the scratching process. The sample is whether held by screws or glued. This specimen holder was dimensionally rectified to ensure the good parallelism condition evoked in next lines. The second specimen holder is illustrated in Fig. 110 (b) and was designed in order to automatically rectify the non-parallelism between the tested surface and its opposite face of relatively small samples by pressing an iron ball toward the sample with the help of a screw (not visible on Fig. 110 (b)). Then, the top surface of the sample is in contact and parallel to the reference surface of the specimen holder. This function was of prior interest because of the limit of 100 μm of vertical displacement range during scratching, especially when the test is performed on a long scratching distance.

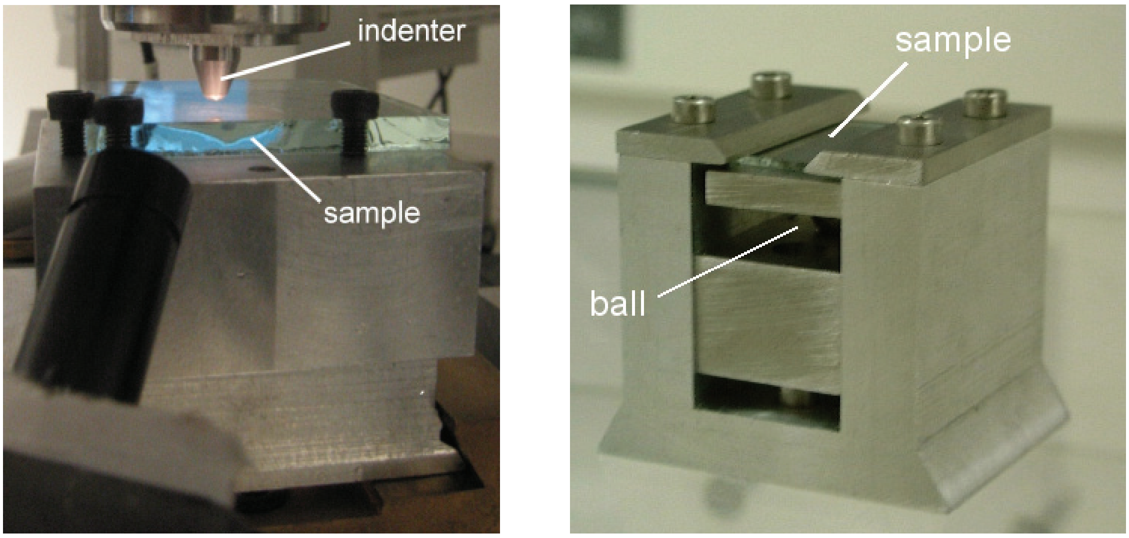

(a) (b)

Fig. 110: Sample holders: (a) the *generic* sample holder, and (b) the *parallelism corrector* sample holder.

App.1-1.3 The environmental enclosure

Fig. 111 represents the machine inside the enclosure. This glove box (the rubber gloves were removed for the photo) is moisture controlled with the help of a pumping/drying system and a humidity/temperature sensor (visible on the left of the figure). Note that no in-situ video acquisition is available when the setup is installed in the glove box (i.e. during scratch tests in moisture-controlled atmosphere).

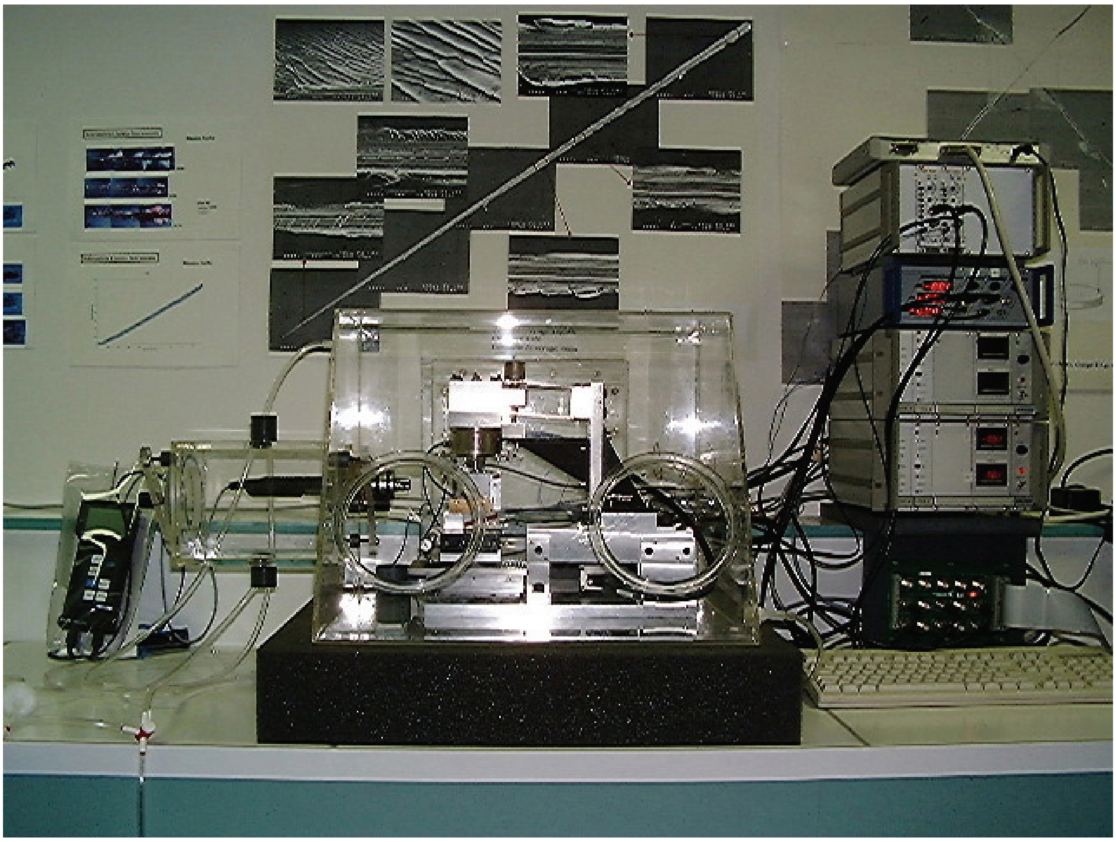

Fig. 111: The scratch tester inside the moisture controlled enclosure (the rubber gloves were removed for the photo).

App.1-1.4 Available loading procedures

Different loading procedures were designed to control the loading process:

- constant normal load all along the scratch,
- monotonic increasing normal load from 0 N up to a maximum load,
- monotonic load-unload process from 0 N up to a maximum load reached at the half-length of the scratch and back to 0 N at the scratch end.

These patterns are performed on the scratch tester as real-time controlled patterns: the load is real-time measured through the load cell and the displacement imposed by the piezo-electric actuator is almost instantly corrected with the help of the Labview software (the control loop lasts 50 ms) to impose the required normal load.

App.1-2 Detailed scratch test procedure

The test steps of the procedure can be listed as follows:

1. cleaning the sample of glass and the indenter with alcohol and drying with air,
2. placing and clamping the sample in the adapted sample holder,
3. placing and clamping the sample holder in the machine,
4. initializing the chosen loading program,
5. calibrating the load cell by adjusting the balance screws,
6. approaching the indenter close to the sample surface with the coarse translation and with the help of the video monitoring (see Fig. 112),
7. approaching the capacitive gauge to the dedicated reference surface for the vertical displacement measurement and adjusting for full range measurement,
8. launching the data collecting, the video acquisition (long-distance microscope) and the Labview program to perform the test,
9. test performing with monitoring of the normal load, the tangential load, the scratching distance and the vertical displacement,
10. saving the video and the collected data,
11. lift off the indenter far from the sample.

Fig. 112: Monitoring of the indenter/sample for accurate approach with the elastic double-cantilever driven by the coarse translation screw.

App.1-3 The micro-instrumented indentation case

App.1-3.1 Strategy/Improvement of the scratching machine

App.1-3.1.1 Introduction

To understand the scratching behavior of glass, the static (i.e. indentation) behavior has to be studied too. Then, the need of well-controlled indentation tests involves building a micro-indentation tester. The choice to build a machine that is instrumented (i.e. micro-instrumented indentation tester) was driven by the energy considerations evoked in this work, even if no results dealing with this approach have been reported in the study.

An *instrumented* indentation experiment consists in recording a load-displacement curve (*P*-*h* curve – *P* is the load and *h* is the penetration depth) as a function of the time during a loading-unloading indentation cycle.

App.1-3.1.2 Strategy

It has been decided to improve the scratch tester in order to perform the indentation tests on the same device. The direct benefit of this choice is to get rid of lots of parameters that could have changed if using a second machine like: different stiffness of the machine, different accuracy of displacement and/or load measurements, geometry similarity of indenters, accuracy of the control-loop, loading patterns... As many parameters that could have been sources of uncertainties.

App.1-3.1.3 Improvement of the scratching machine

The improvement of the scratching machine to perform micro-instrumented indentation tests consisted in installing a displacement measurement sensor. The choice was to use a capacitive gauge (10 nm of accuracy). The relatively small measurement range of this gauge (200 μm) compared to the long scratch distance leaded to consider the parallelism of the reference surface as a prior problem. The solution was to provide an orientation adjustable table as reference surface to the machine. This setup is shown in Fig. 113.

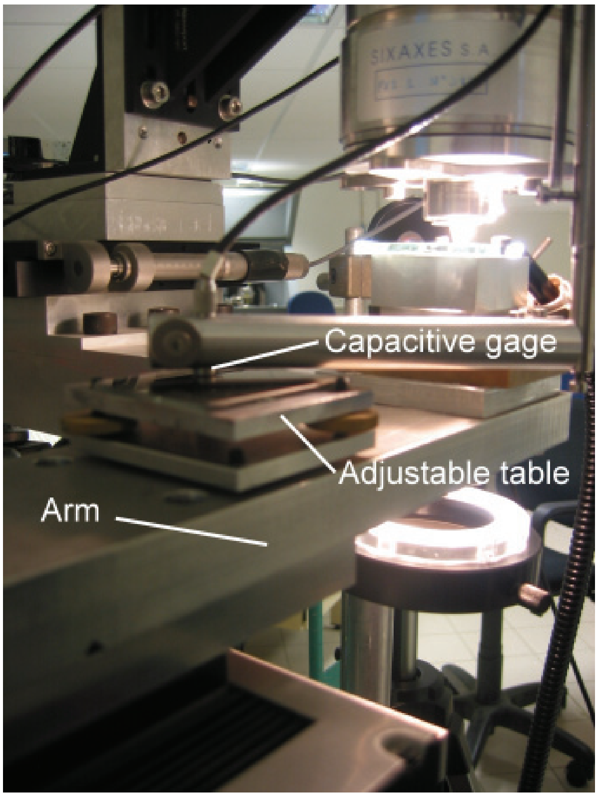

Fig. 113: Capacitive gauge used for highly accurate displacement measurement with its planar reference surface.

App.1-3.2 Program details

Labview program were designed to ensure a loading-unloading process. As previously detailed in this work, it is crucial to perform a constant strain rate test (i.e. $\frac{\dot{h}}{h} = Cste$). Three main corrections have to be ensured to validate this condition:

- the load cell stiffness correction,
- the arm flexure correction,
- the non-linear Volt-displacement law of the piezo-electric actuator correction.

Lastly, initialization condition of the loading process was a problem to solve. Actually, ensuring the constant strain rate condition imposes to start the program with an arbitrary constant that depends on the stiffness of the machine, the control loop time, the several corrections,... It has been reasonably set for this machine to 0.001.

Fig. 114 presents the main step of the Labview program performing the constant strain rate indentation test. The several corrections to ensure this indentation process are highlighted.

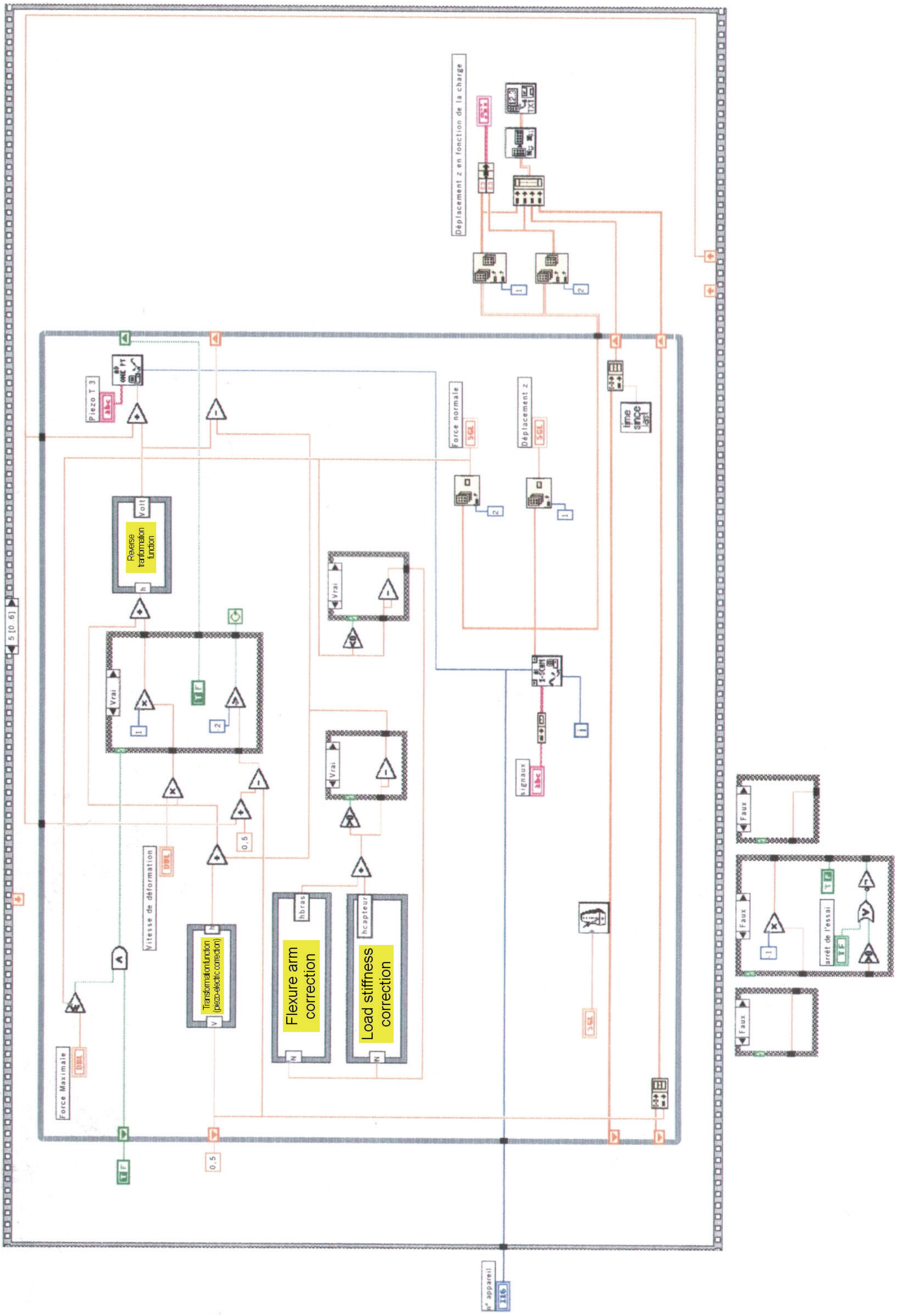

Fig. 114: Labview program performing the constant strain rate indentation test with the several corrections.

Fig. 115 represents the measured strain rate during a micro-instrumented indentation test on a glass. The fitted data shows that the constant strain rate condition is reasonably validated.

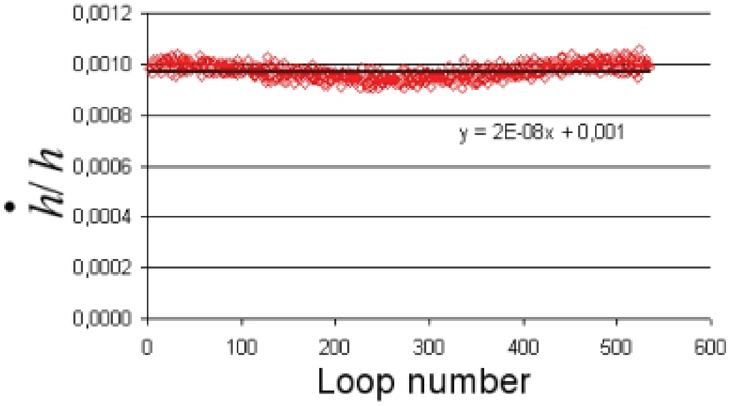

Fig. 115: Measured and fitted strain rates during a micro-instrumented indentation test on a glass.

App.1-3.3 Typical results & treatment techniques

Due to signal noise, the best method for smoothing the *P-h* indentation curve is the 15 points average method (tested methods: 5, 7, 15, 25 points average methods, 7 and 15 points Savitzky-Golay methods). The Graph 54 shows the case of a typical *P-h* indentation curve performed on a glass with a maximum normal load of 0.2 N. Then, it is the worse case due to the maximum relative noise signal compared to the normal measured load. The corresponding smoothed data is also reported in Graph 54.

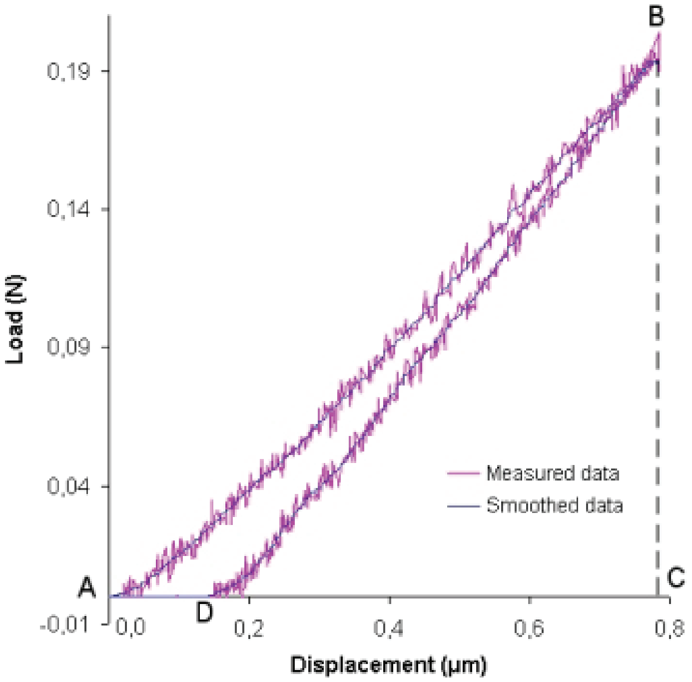

Graph 54: Typical indentation load-displacement curve – Measured and smoothed data.

From an energy point of view, the *P-h* curve can be investigated as follows:

- the surface defined by ABCA on Graph 54 represents the necessary work for the creation of the indentation, W_T,
- the DBCD surface corresponds to the work released by the specimen, W_E,
- the ABDA corresponds to the retained work, W_R.

Then it comes:

$$W_T = W_E + W_R$$

APPENDIX 2:
DETAILS OF THE 3D FINITE ELEMENTS MODEL OF VICKERS INDENTATION

SUMMARY OF APPENDIX 2

App.2-1 Short introduction to the Finite Elements Method (F.E.M.)

App.2-1.1 Principle of the Finite Elements Method

A Finite Elements model is a discrete representation of physical objects in a mechanical (or thermal,…) problem treated by software. Thus this is a numerical method that imposes the models to be validated. The objects that are modeled are divided (meshed) in elements.
These elements are constrained to follow:

- physical laws (local equilibrium)
- constitutive laws (material properties)
- displacement and load constrains

The simulation leads to the calculation of stresses and strains. They are:

- calculated for each element & for each step of the calculation
- continuous from one element to its neighbors

App.2-1.2 Chronology of a F.E. model

A F.E. model usually follows the descending chronological scheme reported in Fig. 116 that is more or less common to all Finite Elements softwares.

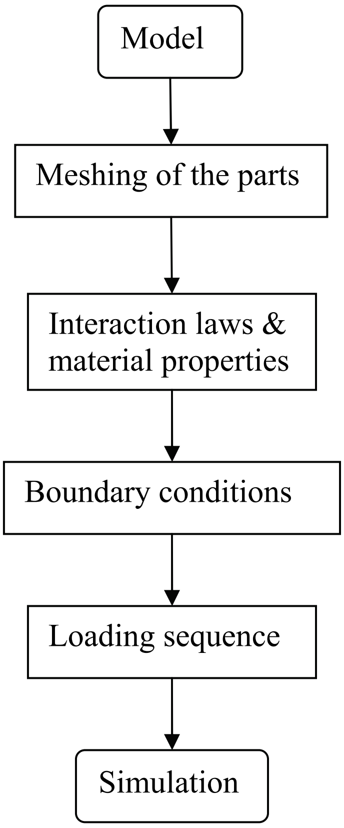

Fig. 116: F.E.M descending chronological scheme.

App.2-2 2D-problem

App.2-2.1 General

The indentation process deals with a contact problem between a semi-infinite half-space and an indenter. In the present study due to the axi-symmetric reason of the conical indentation, the system will be meshed in two dimensions. Furthermore, the indenter will be modeled as perfectly rigid, the friction coefficient will be the Coulomb's coefficient at the local scale (i.e.

true friction) and particular attention will be paid to build and validate carefully the mesh of the indented body. The indentation depth was estimated to be about 5 µm when a load of 3 N is applied on the considered indenters (conical indenters with large apex angles, Vickers, Berkovich). The mesh of the indented body will have to be coherent with this value.

App.2-2.2 Meshes inspired by pre-existing meshes

It was decided to start with already-existing meshes. The first one was a mesh inspired by the one of Giannakopoulos [84], simplified in a number of elements sense. The Fig. 117 illustrates the non-deformed mesh.

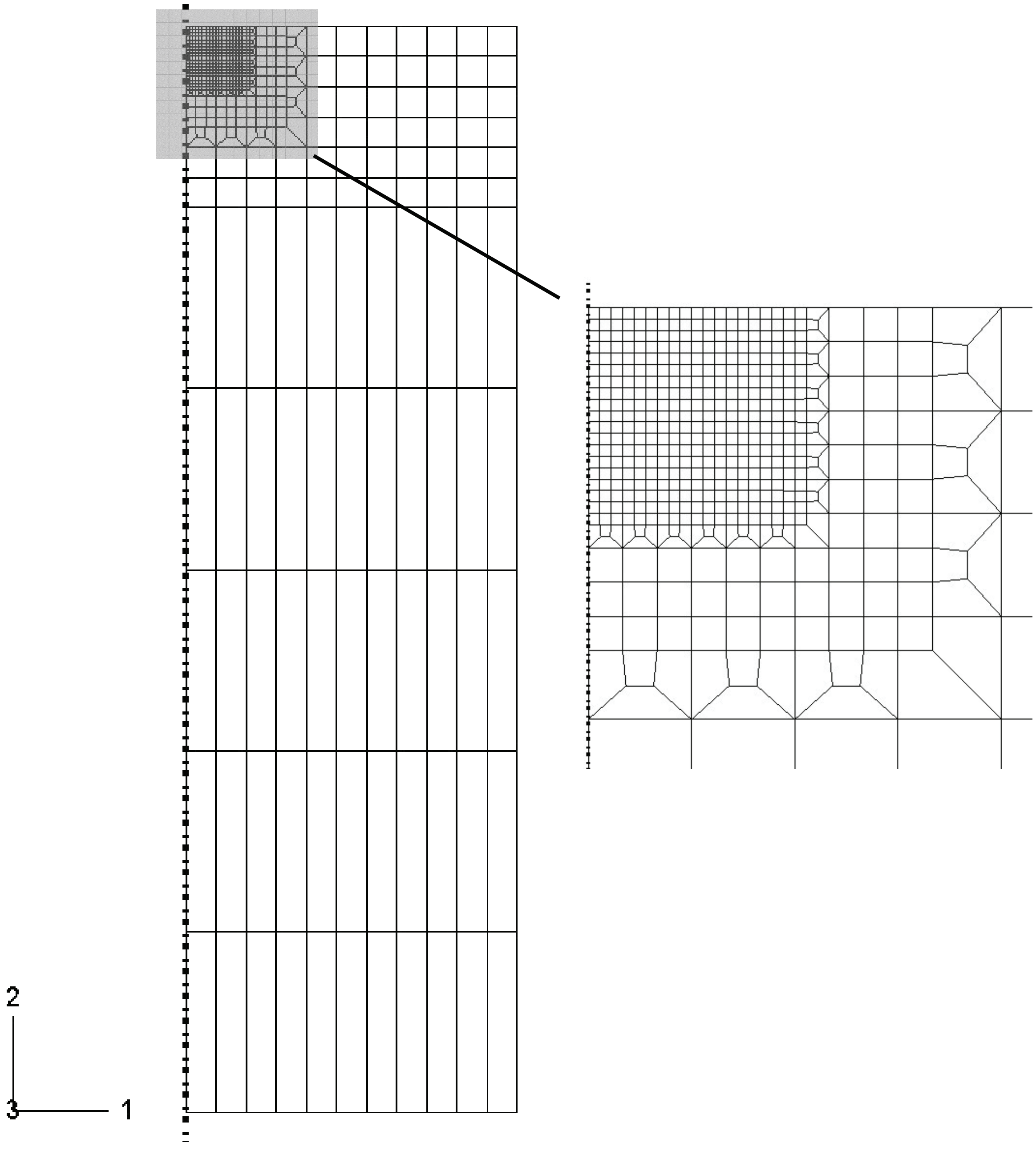

Fig. 117: Simplified Giannakopoulos-like mesh.

The different characteristics of the mesh are summarized as follows:

- Number of elements: 593
- Smallest size of element: 1 µm
- Size of the indented body: 99x324 µm^2

Technically, this mesh is built to be more fine around the indenter. One can note that its height is particularly big and more than 3 times the size in width. This is to validate the boundary condition that is imposed on the bottom of the specimen (see [88] for more details). To avoid increasing the number of elements, some high ones were designed (5 times higher than large). The boundary condition on the right side of the sample is assumed as free surface. Actually, at maximum load, the stresses in the most far places are at least 1000 times less than the highest ones. Then, the size of this mesh seems to be adapted. However, the convergence is not systematic. For example, the use of an indenter with a rounded tip of 3 µm of curvature makes the simulation fails (because of the finest elements that are only 1 µm^2). Then, it also fails for 1 µm and 2 µm of tip curvature.

Thus, a second pre-existing mesh was drawn and is represented in Fig. 118. It is this time inspired by the one used by Carlson et al. [86].

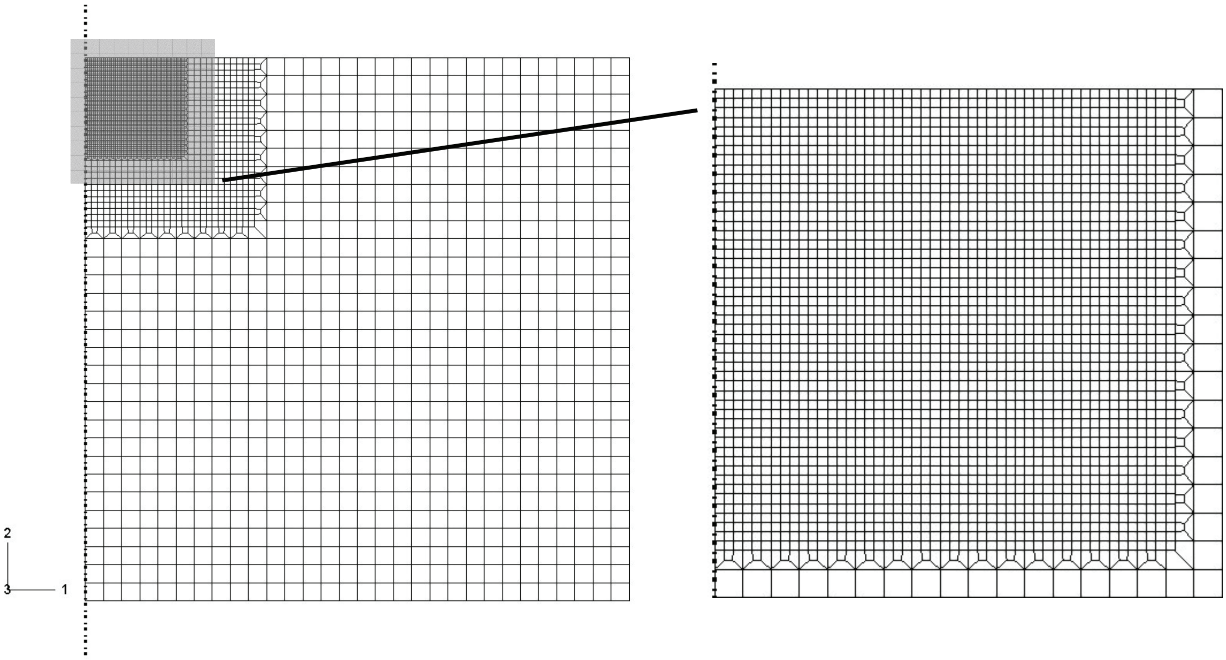

Fig. 118: Simplified Carlsson-like mesh.

The different characteristics of the mesh are summarized as follows:

- Number of elements: 3900
- Smallest size of element: 0.2 µm
- Size of the indented body: 54x54 µm^2

More fine and more precise are the advantages of this mesh. It is also really easy to draw, and has a 0.2 µm precise mesh close to the indenter. But, some drawbacks exist: first the size (3900 elements), second the height that doesn’t match with the bottom boundary condition as good as the previous mesh.

To find a compromise between the two first meshes without having their drawbacks, the third mesh reported in Fig. 119 was designed.

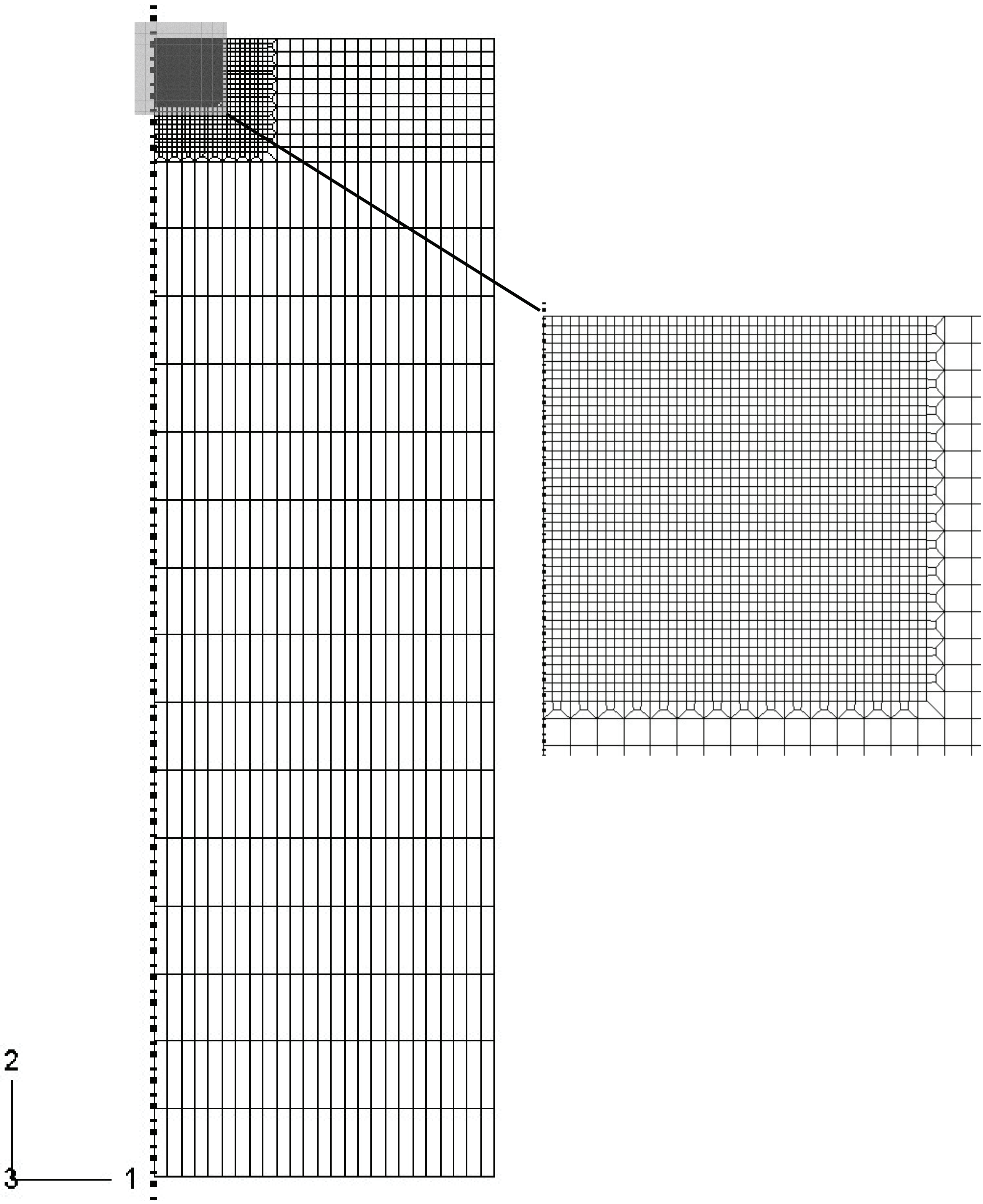

Fig. 119: Third designed mesh combining the two previous ones.

The different characteristics of the mesh are summarized as follows:

- Number of elements: 2948
- Smallest size of element: 0.2 µm
- Size of the indented body: 45x150.4 μm^2

Unfortunately, when the radius of the indenter is changed, the simulation sometimes fails. It can be explained by considering the Fig. 120 (load of 3 N, radius of the tip: 1 µm, Von Mises stresses distribution): the elements just below the tip are almost completely flattened.

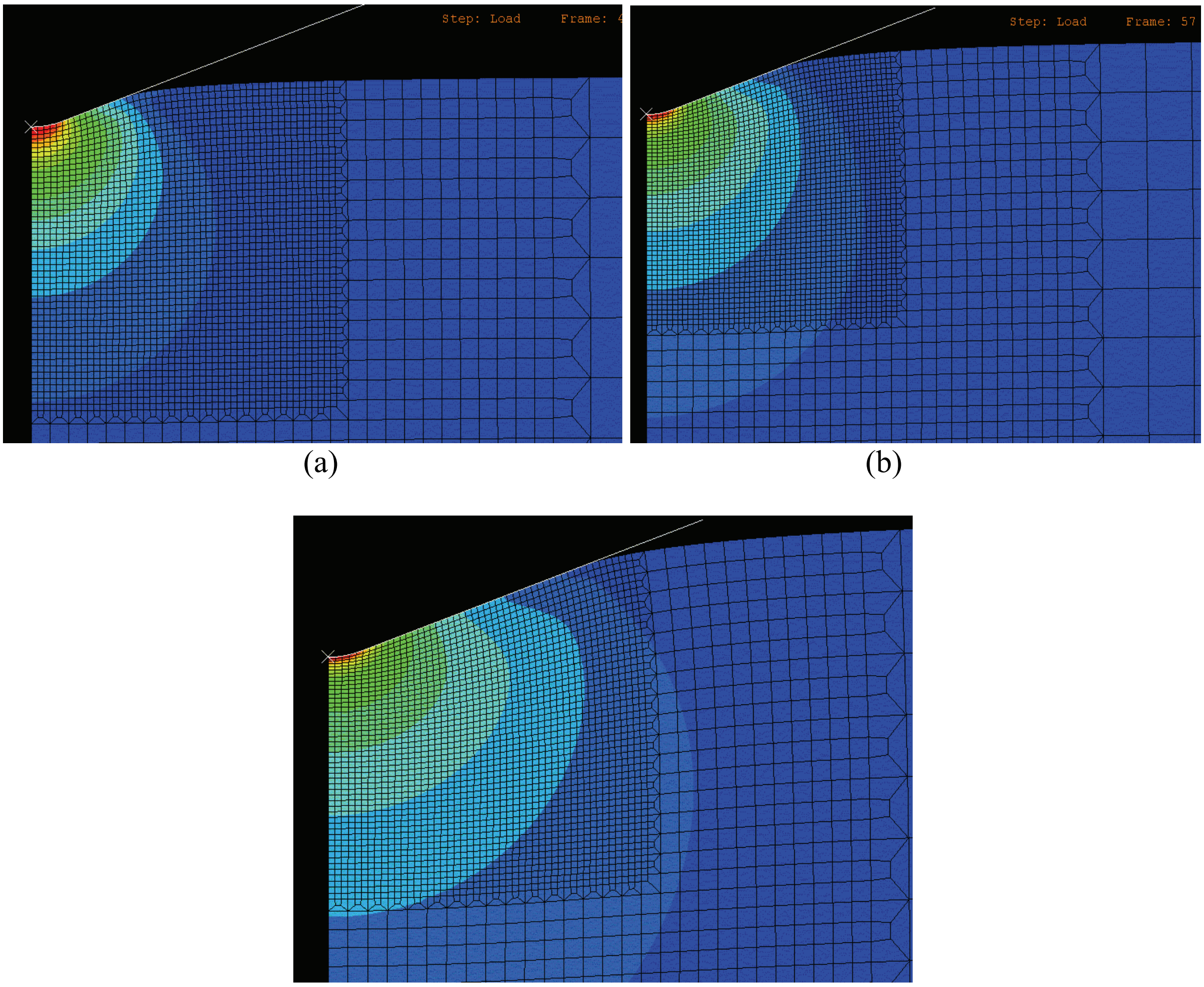

(a) (b)

(c)

Fig. 120: Results (Von Mises stresses distribution) of the simulation of a conical indentation with a 1 µm tip radius on the third designed mesh and with a maximum load of 3 N (c); (b) intermediate results at 2 N of load; (a) intermediate results at 1 N.

App.2-2.3 Improvements

Then, it was decided to make a Giannakopoulos-like mesh, with a number of elements around 3000 if possible, fine (0.2 µm) close to the indenter, and with high elements in contact with the tip of the indenter to avoid high flattening effect at this strategic place. The interest of these elements is also that under load, the element reaches a shape that is more and more close to the "ideal" one (i.e. a square) for the calculations at the Gaussian point and then enhance the precision. It has to be noticed that at the beginning of the simulation the precision is less good as a consequence of the original shape of the element. Then, the interest is more to avoid that the convergence fails in the middle of the simulation than to enhance the precision on the whole model calculations. As a result, the model will fail at the beginning or there is only little chance that it fails before the end. The Fig. 121 (a-d) are respectively: the undeformed mesh, a deformed one (Von-Mises stresses distribution) at the beginning, a second one in the middle and the last one at the maximum load. Note the quasi-ideal shape of these high elements beneath the indenter at maximum load.

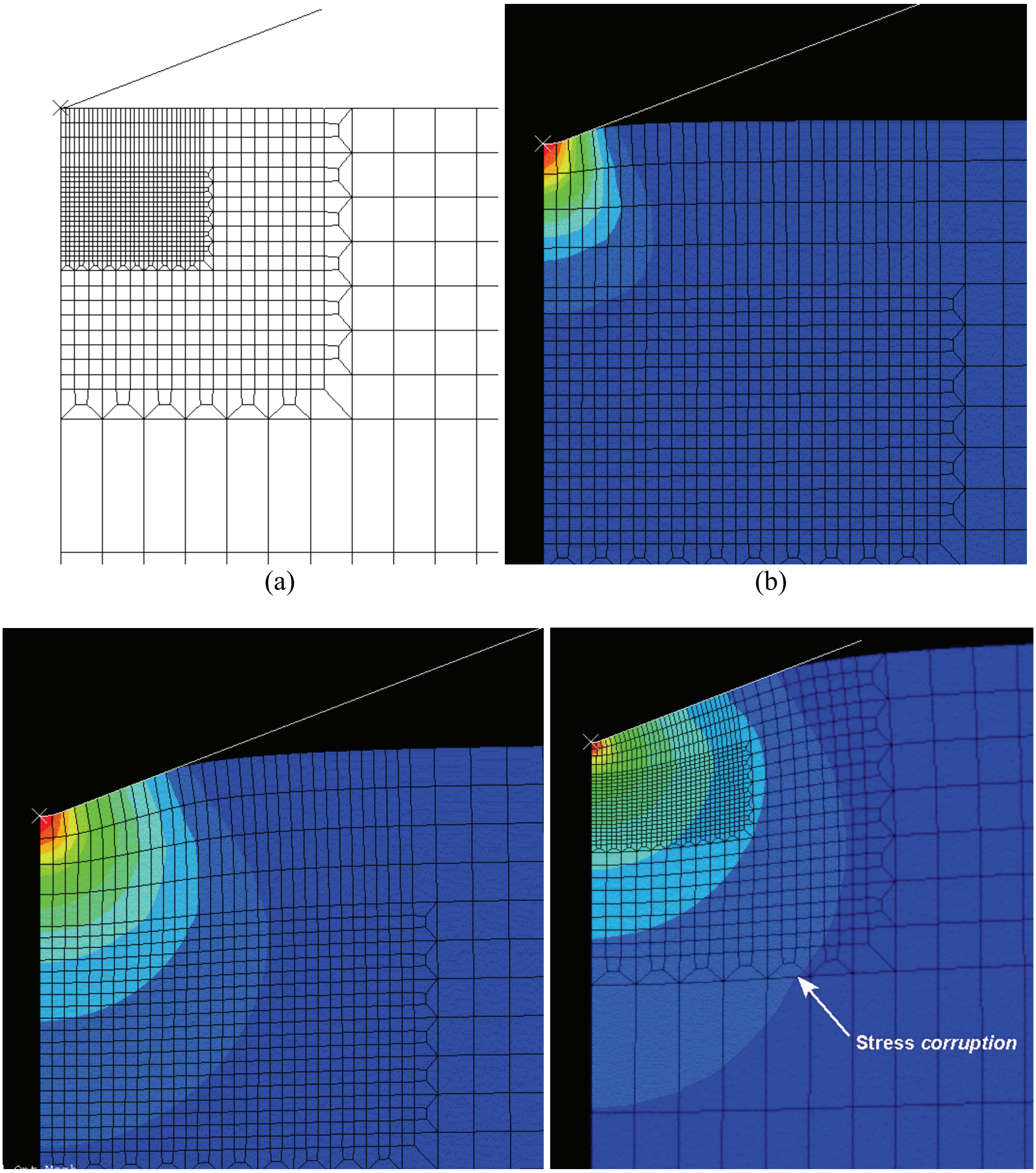
(a) (b)

(c) (d)

Fig. 121: Results (Von Mises stresses distribution) of the simulation of a conical indentation with a 1 µm tip radius on the improved mesh and with a maximum load of 3 N (d); (b) intermediate results at about 0.3 N of load; (c) intermediate results at 1 N; (a) undeformed mesh.

The different characteristics of the mesh are summarized as follows:

- Number of elements: around 2700
- Smallest size of element: 0.2 µm
- Size of the indented body: 45x150.4 µm^2

The comparison between the conical indentation and the test performed with a Vickers (or Berkovich) will need an accurate precision in the stress field occurring in the elastic body. Then, the final mesh should not influence too much these fields. Unfortunately, one's can see on the three deformed bodies that the stresses distribution seems to be "corrupted" (see the arrow on Fig. 121 (d)) by the high elements that were added.

Then, a direct improvement is to limit their number to the strict minimum to avoid this drawback and still have the advantages of high deformable elements just beneath the indenter. The details of this new mesh, qualified as optimized mesh, is pictured in Fig. 122.

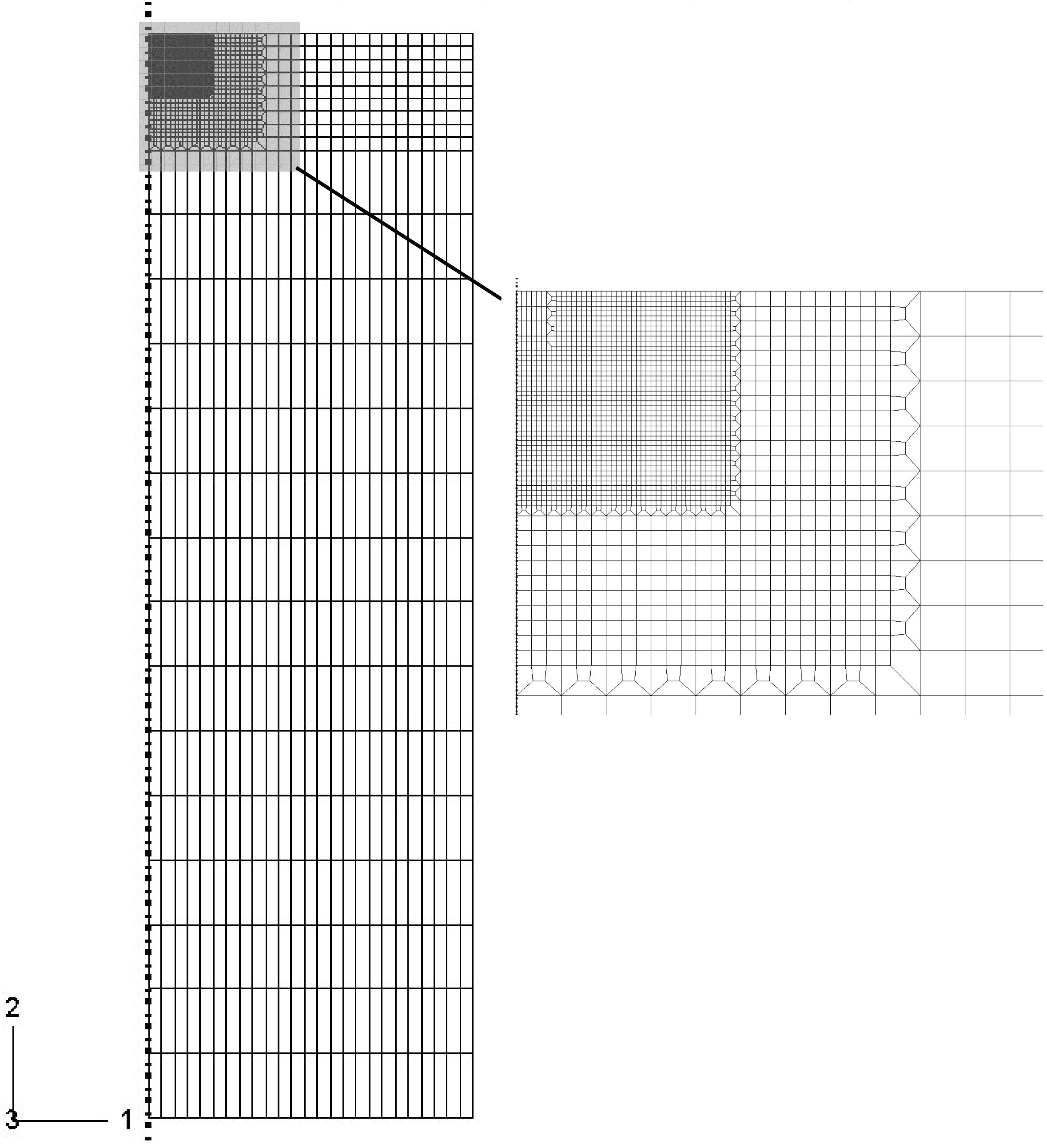

Fig. 122: Optimized mesh and detail.

The different characteristics of the mesh are summarized as follows:

- Number of elements: 2898
- Smallest size of element: 0.2 µm
- Size of the indented body: 45x150.4 µm^2

The Von Mises stresses distribution is plotted on the Fig. 123 at the beginning and at the end of the loading process, respectively.

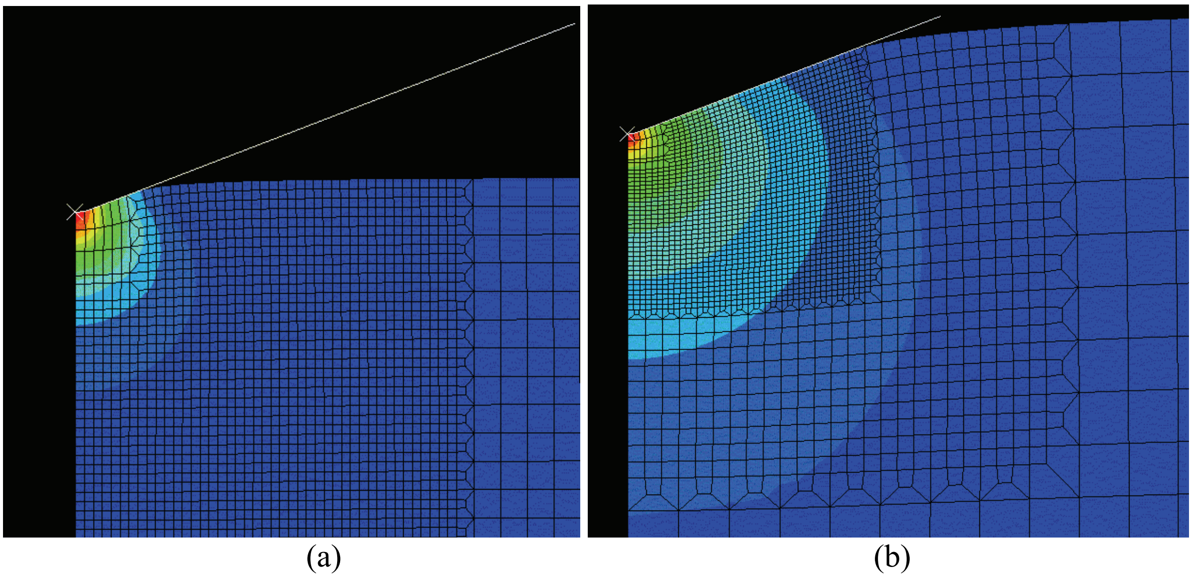
(a) (b)

Fig. 123: Results (Von Mises stresses distribution) of the simulation of a conical indentation with a 1 µm tip radius on the optimized mesh and with a maximum load of 3 N (b); (a) intermediate results at 0.5 N of load.

The closest elements to the indenter still behave like expected, and the stress fields appear not to be influence too much by the mesh structure. To obtain this meshing, a block meshing procedure is needed by Abaqus. The detail of the block meshing is reported in Fig. 124.

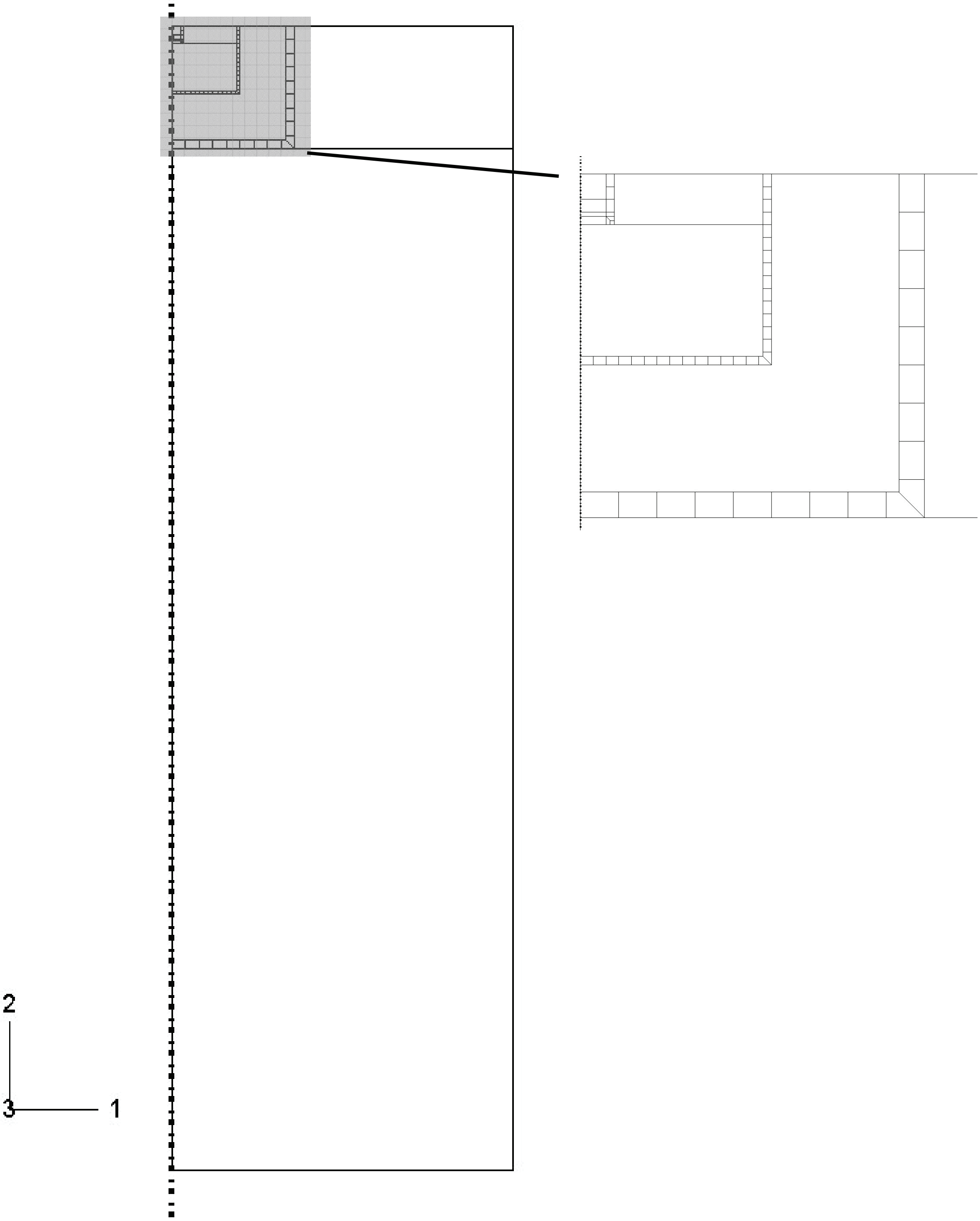

Fig. 124: Block meshing procedure used to obtain the optimized mesh.

As already treated in this work, an interesting parameter to validate the elastic simulation is to follow the evolution of the geometric coefficient γ as defined by Sneddon [82] (see § 5.6.3.5.1 p 145). It needs a fine meshing of the surface to neglect the discrete nature of the curve. The previous mesh was then modified a bit as shown in Fig. 125.

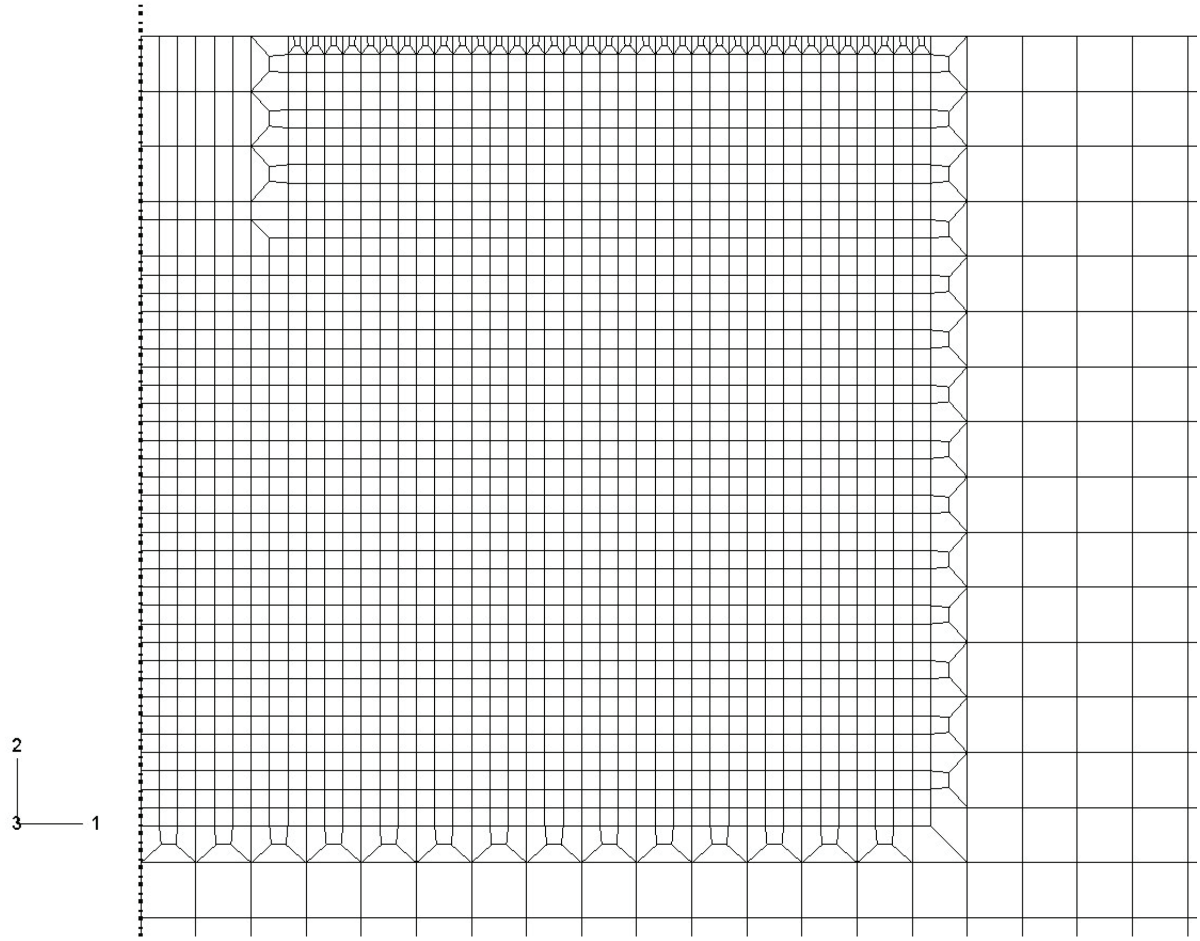

Fig. 125: Optimized mesh that was modified with fine elements on the surface in order to follow the evolution of the geometric coefficient γ for validation considerations.

The different characteristics of the mesh are summarized as follows:

- Number of elements: 3003
- Smallest size of element: 0.066 µm
- Size of the indented body: 45x150.4 µm^2

Even if it seems to be a good mesh to study the evolution of γ, the convergence is far more long and the simulation is less stable, i.e. the increments of the steps during loading part vary a lot. The convergence fails sometimes for extreme values of parameters (minimum of increment, ν, friction coefficient,...). Because of its accurate stability, it has been decided that the optimized mesh should still be the one for the present study, even if it is less precise to follow the evolution of γ.

App.2-2.4 Choice of the final 2-D Mesh

The validation of the previous meshes leads to do some critics for each. The mesh that seems to be validated in the best way by the criteria used is the "optimized mesh". Unfortunately, the profiles of indentation are really far from the one given by theoretical data as will be developed further. The reason is the width size of the body that is not big enough to satisfy the boundary condition of free surface on an infinite body for the top and the extreme vertical surfaces of the model. A final mesh, illustrated in Fig. 126, was designed to fix this problem. The width has been changed from 45 µm to 73.8 µm.

Note that all the elements that compose the mesh are quadrilateral elements of linear type (CAX4 Abaqus code).

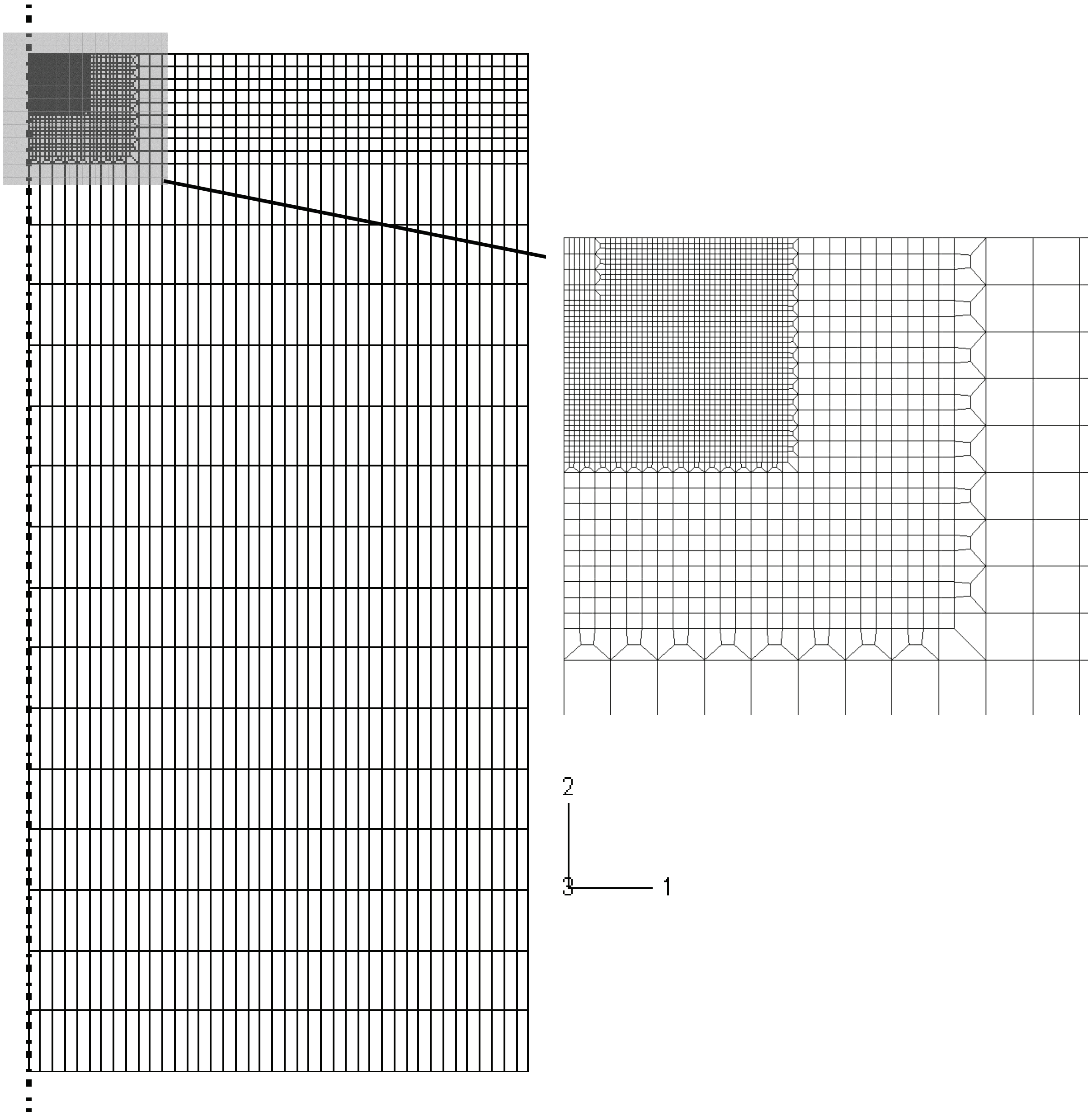

Fig. 126: Final mesh for 2-D simulations.

The different characteristics of the mesh are summarized as follows:

- Number of elements: 3282
- Smallest size of element: 0.2 μm
- Size of the indented body: 73.8x150.4 μm^2

App.2-2.5 Simulation parameters

Here are summarized the main parameters of the simulation, in the aim to reproduce this model easily by everyone:

- **Material** module:
    - Glass: Elastic → E=70 GPa, ν =0.21
    - Copper: Elastic → E=125 GPa, ν =0.25; Plastic → Yield stress: 30 MPa, Plastic strain: 0 (means perfectly plastic)

- **Step** module:

Steps / parameters	Time (s)	Number of increments	Initial increment	Minimum increment	Maximum increment
Initial	1	NA	NA	NA	NA
Contact	1	100	0.1	10^{-5}	1
Load	1	1000	0.01	10^{-6}	0.2
Unloading	1	1000	0.1	10^{-6}	0.1
Indenter_Escape	1	100	0.3	10^{-5}	0.3

- **Interaction** module: interaction law between the two materials
  - Tangential behavior: *Penalty* of 0.5 (friction coefficient of 0.5)
    Note that the calculations used for the present study and the corresponding results reported in the thesis work were performed with a friction coefficient equal to zero.
  - Normal behavior: *Hard contact* with allowing the separation after contact
- Surfaces definition: 2 surfaces were designed
  - Indented_Body_Surface: top surface of the sample
  - Indenter_Surface: "bottom" surface of the indenter
- Sets definition: several sets were designed to make the change in simulation more easy (shape of indenter, 3-D evolution,...)
  - Bottom: set of the bottom of the sample
  - Top: set of the top of the sample
  - Axi: set of the border of the sample on the symmetry axis
  - Sample: set of the closest nodes to the indenter to have the complete stress and strain fields for each step of the simulation
  - Depth_Monitor: monitor point to follow the evolution of the tip point of the indenter during the simulation
- **Load** module:
  - Boundary conditions:

BC / steps	Initial	Contact	Load	Unload	Indenter_Escape
Axi	U1=U2=UR3=0	U1=0	U1=0	U1=0	U1=0
Bottom_Indented_Body	U1=U2=UR3=0	U2=0	U2=0	U2=0	U2=0
Indenter_BC	U1=U2=UR3=0	U1=UR3=0	U1=UR3=0	U1=UR3=0	U1=U2=UR3=0

  - Load definition:

Load / steps	Initial	Contact	Load	Unload	Indenter_Escape
Indentation_Load	-	CF2=-1	CF2=-3.10^{6} (3N)	CF2=0	CF2=0

Note about special calculation options in Abaqus:

- the choice of the method of calculation in each element is of fundamental interest. If the indented material is elastic, it is strongly recommended to use a complete integration calculation; if the material have a plastic behavior (or elasto-plastic,…), it is strongly recommended to use the reduced integration calculation method.
- the high deformation option is strongly recommended in this case of problem (indentation, rolling,…). However, it appear from this study that it is not recommended to use it in the present case if the material is perfectly elastic: this option usually makes the simulation fails or gives non negligible residual stresses after unloading (!).

App.2-2.6 Validation of the 2D-model

The validation of the 2-D model is fully treated in the associated thesis (see § 5.6).

App.2-3 3D-problem

App.2-3.1 Intermission: why also the modeling of the Berkovich indentation?

The Berkovich indentation was also modeled during this work. One's can wonder why. There are two main reasons that justify this choice:

- The Berkovich indentation exhibits an important similarity with the Vickers indentation: singularity materialized by the edges of both indenters, existence of symmetries,… To build a model for the Berkovich indentation leads then to solve the same problems than for the Vickers model.
- The Berkovich indenter is one of the more used tips for nano-indentation and nano-scratching. In fact, its three-sided pyramidal shape can be obtained with very small rounded tip because of crystallographic considerations compared to the Vickers indenter. This high geometric accuracy makes it the indenter the most adapted for ultra-low load application.

Note also that the 3-D mesh of the Berkovich model can be used to model the indentation by a cube-corner.

App.2-3.2 The mesh

The "symmetric model generation" command of Abaqus software was used to generate a 3D mesh from the optimized 2D mesh like previously evoked in the thesis. The choice of the size of the elements was oriented to have similar elements between the Vickers mesh and the Berkovich mesh. Then, 9 stages of elements were designed along the revolution of 45° of the original 2D mesh for the Vickers model. 12 stages of elements were designed along the revolution of 60° for the Berkovich model, which leads to exactly the same size of elements. Then, the Vickers mesh (of the indented body) can be considered as a part of the Berkovich mesh. Fig. 127 represents the Vickers mesh generated from the optimized 2D mesh.

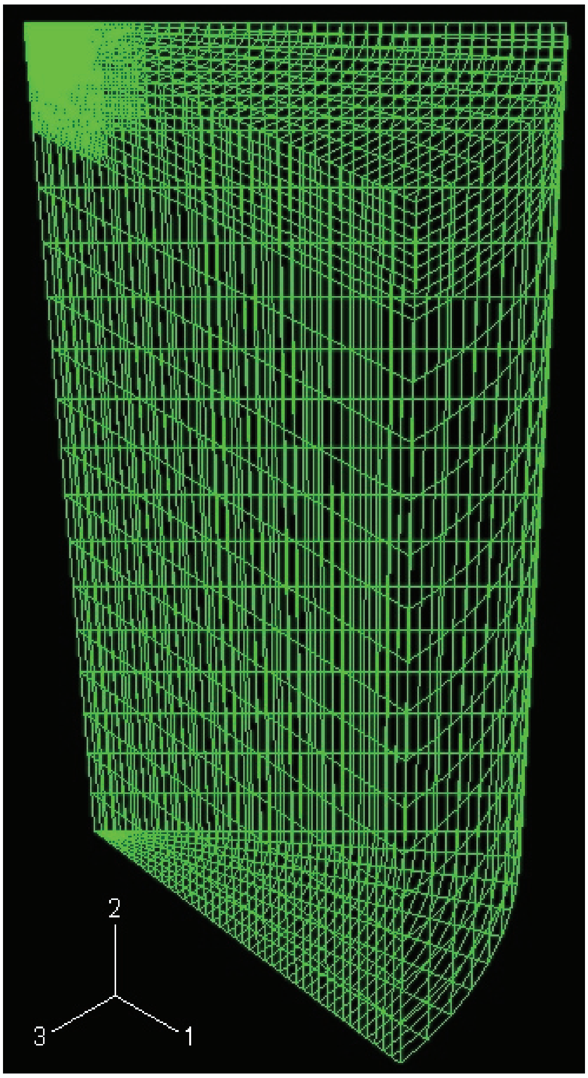

Fig. 127: 3D mesh generated from the optimized 2D mesh.

App.2-3.3 Boundary conditions and loading sequence

The boundary conditions are obvious and already treated. They are summarized for the indented body in Fig. 128.

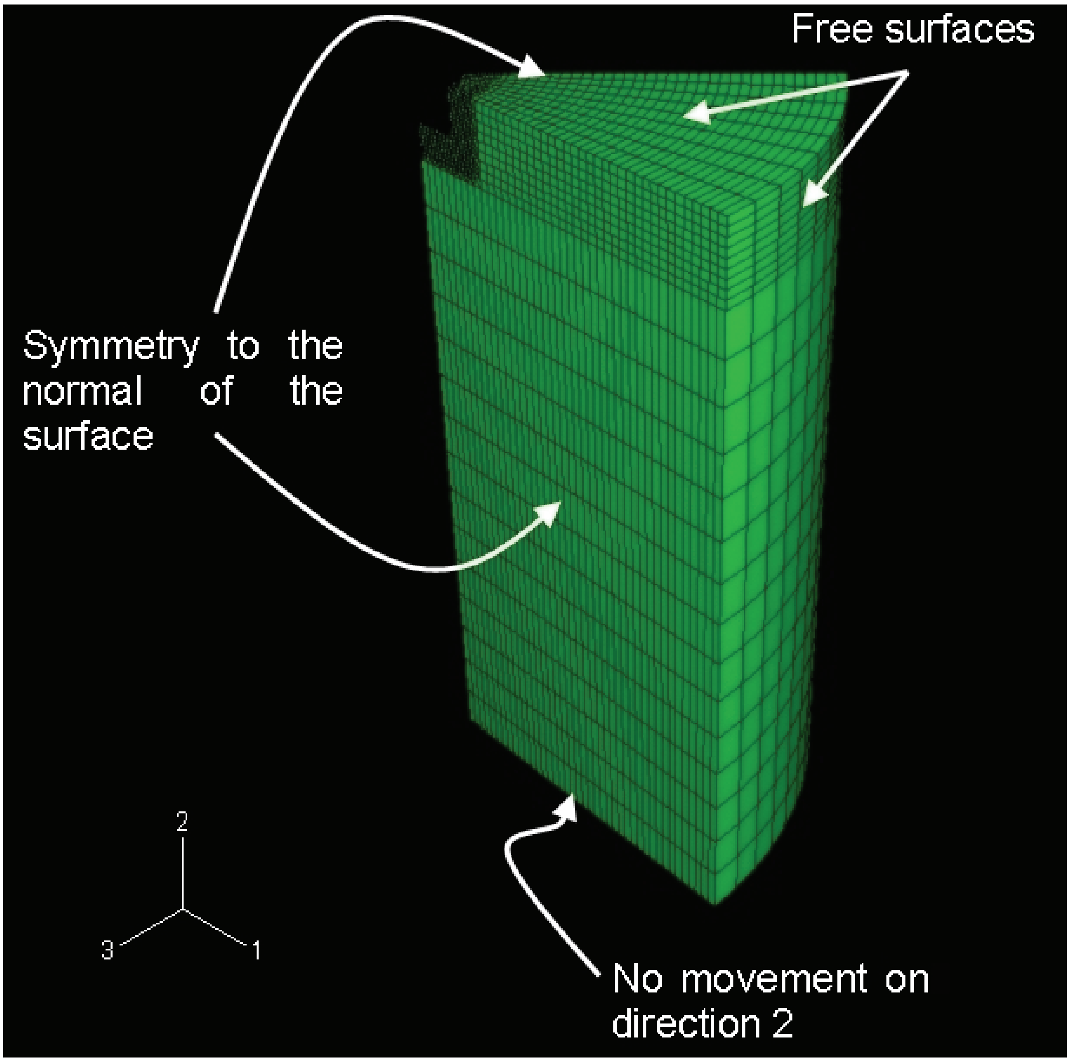

Fig. 128: Boundary conditions on the indented body for the 3D problem.

The loading sequence is the same than for the 2D axi-symmetric case.

App.2-3.4 Insertion of the Vickers indenter in the 3D model

All indenters are modeled as perfectly rigid like reported in § App.2-2.1 of this appendix. Only 1/8 (respectively 1/6) of the Vickers (resp. Berkovich) indenter was modeled because of its symmetry order of 8 (resp. 6) as already reported in the thesis work. The indenter presented in the thesis is a *sharp* indenter, i.e. with a sharp tip that doesn't exhibit any geometric defect. However, four other indenters were created in order to study the effect of a rounded tip in the case of a Vickers (or Berkovich) indenter. This specific characteristic is to exhibit a rounded tip of 1, 2, 3 et 5 µm, as illustrated in Fig. 129.

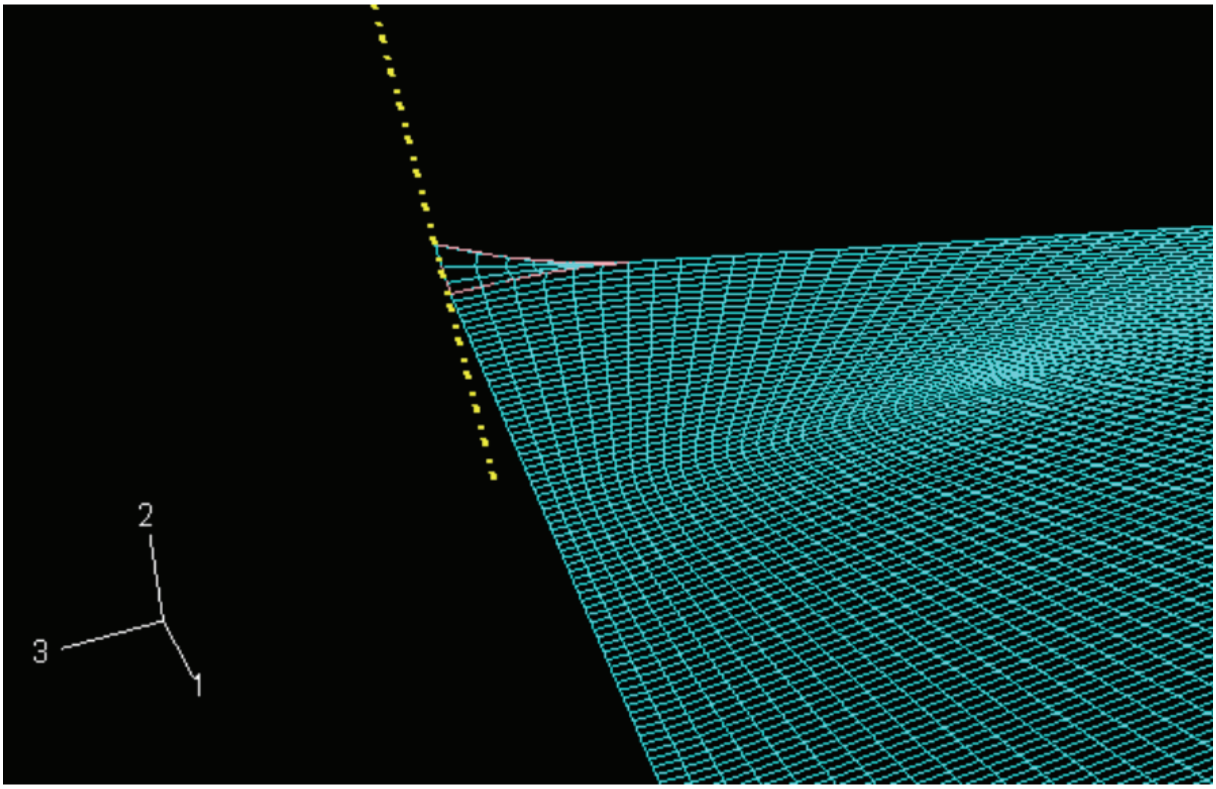

Fig. 129: Detail of the 3 µm rounded indenter - Perspective view.

App.2-3.5 Simulation parameters

Here are summarized the main parameters of the simulation, in the aim to reproduce this model easily by everyone:

- **Material** module:
    - Glass: Elastic → E=70 GPa, v =0.21
    - Copper: Elastic → E=125 GPa, v =0.25; Plastic → Yield stress: 30 MPa, Plastic strain: 0
- **Step** module:

Steps / parameters	Time (s)	Number of increments	Initial increment	Minimum increment	Maximum increment
Initial	1	NA	NA	NA	NA
Contact	1	100	0.1	10^{-5}	1
Load	1	1000	0.01	10^{-6}	0.2
Unloading	1	1000	0.1	10^{-6}	0.1
Indenter_Escape	1	100	0.3	10^{-5}	0.3

- **Interaction** module: interaction law between the two materials
    - Tangential behavior: *Frictionless*
    - Normal behavior: *Hard contact* with allowing the separation after contact
- Surfaces definition: 2 surfaces were designed
    - Indented_Body_Surface: top surface of the sample
    - Indenter_Surface: “bottom” surface of the indenter
- Sets definition: several sets were designed to make the change in simulation more easy (shape of indenter, locating the BC, ...)
    - Bottom: set of the bottom of the sample
    - Top: set of the top of the sample
    - Axi: set of the border of the sample on the axis of symmetry

  - Depth_Monitor: monitor point to follow the evolution of the tip point of the indenter during the simulation
- **Load** module:
  - Boundary conditions:

BC / steps	Initial	Contact	Load	Unload	Indenter_Escape
Axi	U1=U2=U3=0	U1=U3=0	U1=U3=0	U1=U3=0	U1=U3=0
Bottom_Indented_Body	U1=U2=U3=0	U2=0	U2=0	U2=0	U2=0
Indenter_BC	U1=U2=U3=0 UR1=UR2=0	U1=U3=0 UR1=UR2=UR3=0	U1=UR3=0 UR1=UR2=UR3=0	U1=UR3=0 UR1=UR2=UR3=0	U1=U2=U3=0 UR1=UR2=UR3=0
Sample_Edge	U1*=U2*=U3*=0	U3*=0	U3*=0	U3*=0	U3*=0
Sample_Face	U1=U2=U3=0	U3=0	U3=0	U3=0	U3=0

The degrees of freedom with a * concern a local cylindrical axis system linked with the “Edge” face of the sample.

  - Load definition:

Load / steps	Initial	Contact	Load	Unload	Indenter_Escape
Indentation_Load	-	CF2=-1	CF2=-3.10^6 (3N)	CF2=0	CF2=0

Note about special calculation options in Abaqus: same recommendations than in the 2D-problem (see App.2-2.5).

App.2-3.6 Data collecting

The data are directly collected as ASCII files from Abaqus, depending on the output functions selected. All the components of stress, strain, pressure, Von-Mises or Tresca distribution, invariants, (…) are available.

App.2-3.7 Capabilities of the model and first results

App.2-3.7.1 Load-Displacement curve

One of the easiest results to extract is the load-displacement curve during a loading-unloading sequence of indentation. The interest is less important when the simulation deals only with a perfectly elastic indented material but is a complementary criterion in order to validate the model. Graph 55 was extracted from a simulation of an elastic indented body (corresponding to an imaginary elastic glass: *E*=70 GPa ; *ν*=0.21). The loading and unloading curves are merged as expected.

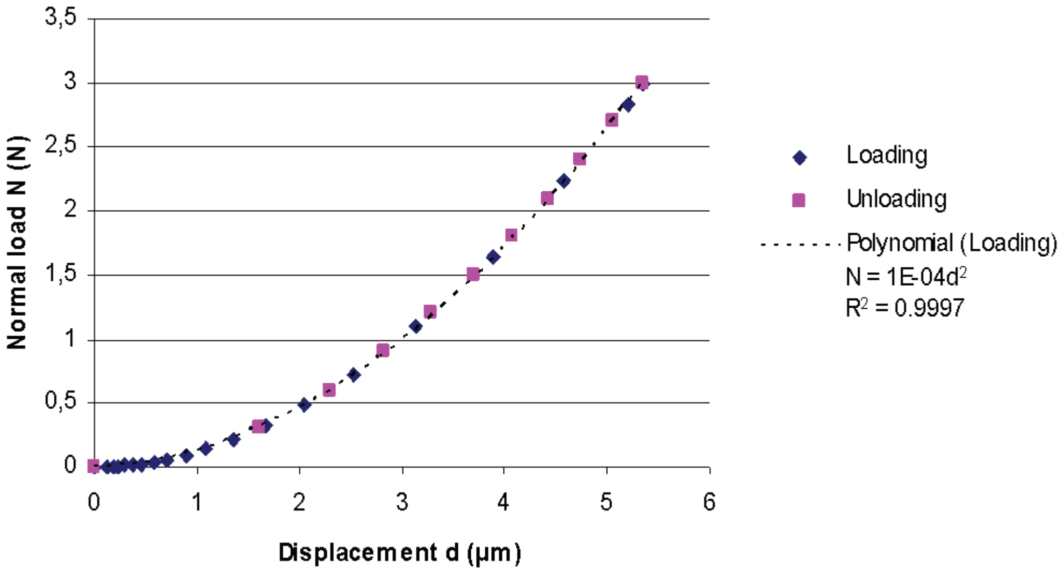

Graph 55: Loading-unloading displacement curve in the perfectly elastic case.

App.2-3.7.2 Stress and strain visualization

The extraction of the stress and strain fields is usually useful. Actually, Abaqus allows to plot all these data directly on the model or to extract them in an ASCII file for post-treatment. The analysis of a particular stress, for instance σ_{zz}, can give good clues on the initiation place of lateral cracks in the material as well as the corresponding critical load. Fig. 130 is the distribution of Von-Mises stresses on an elastically deformed body (same material properties than previously quoted) in perspective.

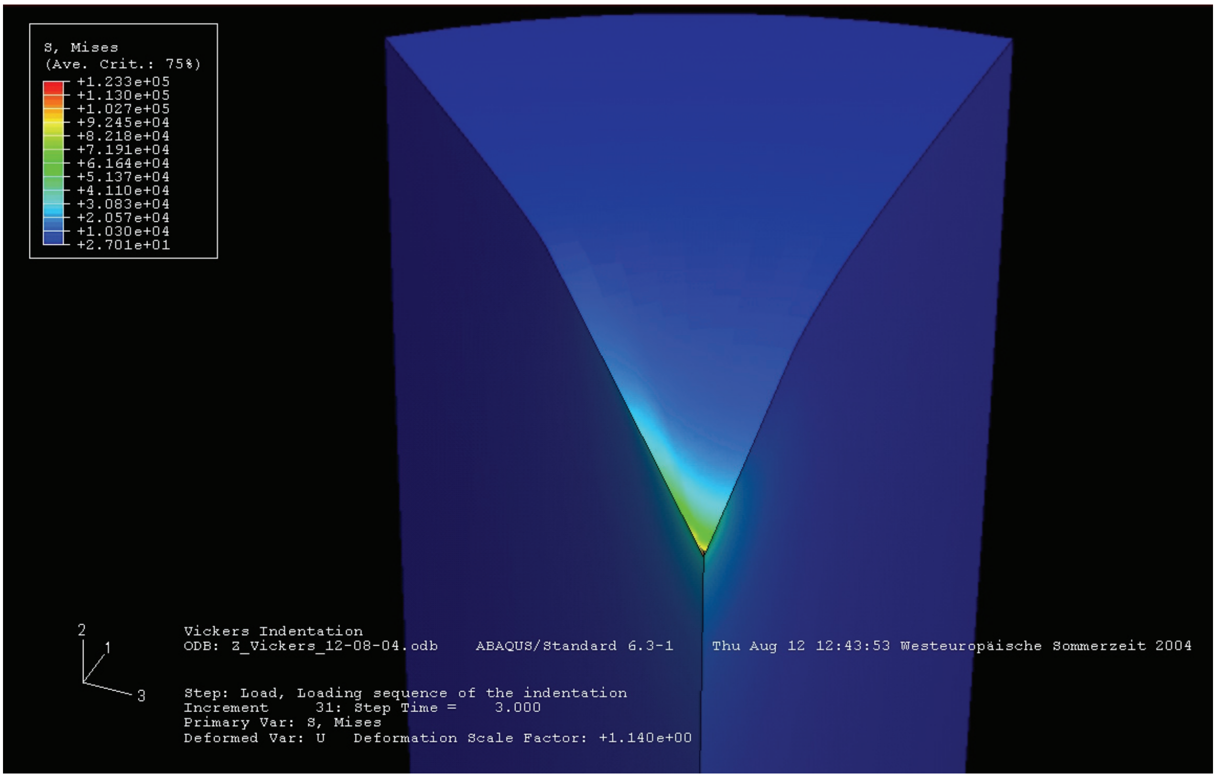

Fig. 130: Von-Mises stresses distribution of an elastically deformed body – perspective view.

App.2-3.7.3 Contact pressure

The contact pressure between the indenter and the body can be an interesting variable to plot (see Fig. 131). Actually, it can give interesting parameters like:

- The pressure distribution on the indenter
- The real area of contact under load or after unloading (case of a plastic material).

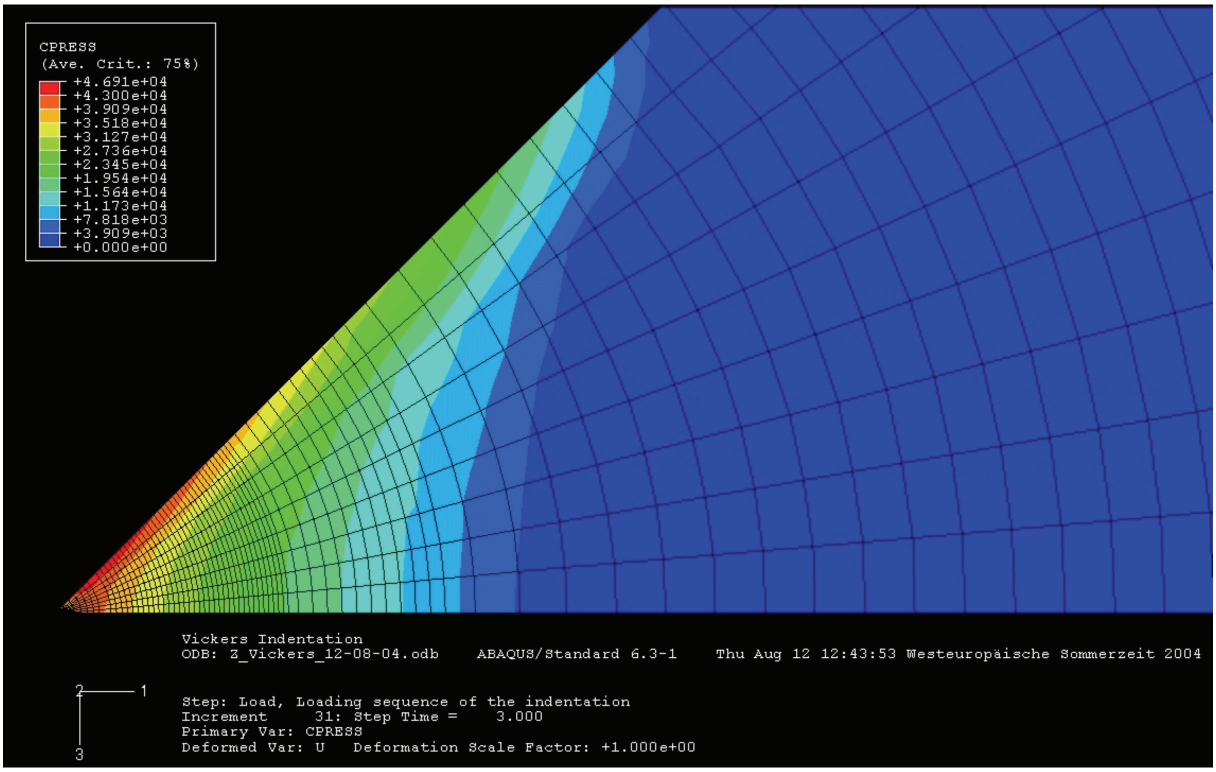

```
Vickers Indentation
ODB: Z_Vickers_12-08-04.odb    ABAQUS/Standard 6.3-1    Thu Aug 12 12:43:53 Westeuropäische Sommerzeit 2004

Step: Load, Loading sequence of the indentation
Increment     31: Step Time =    3.000
Primary Var: CPRESS
Deformed Var: U   Deformation Scale Factor: +1.000e+00
```

Fig. 131: Pressure distribution due to the contact indenter/material. The indenter is not represented for obvious reasons of reading convenience.

App.2-3.7.4 Influence of friction

As it can be seen in Graph 56, there is no significant influence of the friction law on the depth of penetration during indentation (also reported in literature – these results were obtained for the 2-D model). Actually, all the curves are merged, even if the local coefficient *mu* (i.e. true friction coefficient) is not equal to zero. Nevertheless, this justifies that the 3-D model is designed as frictionless.

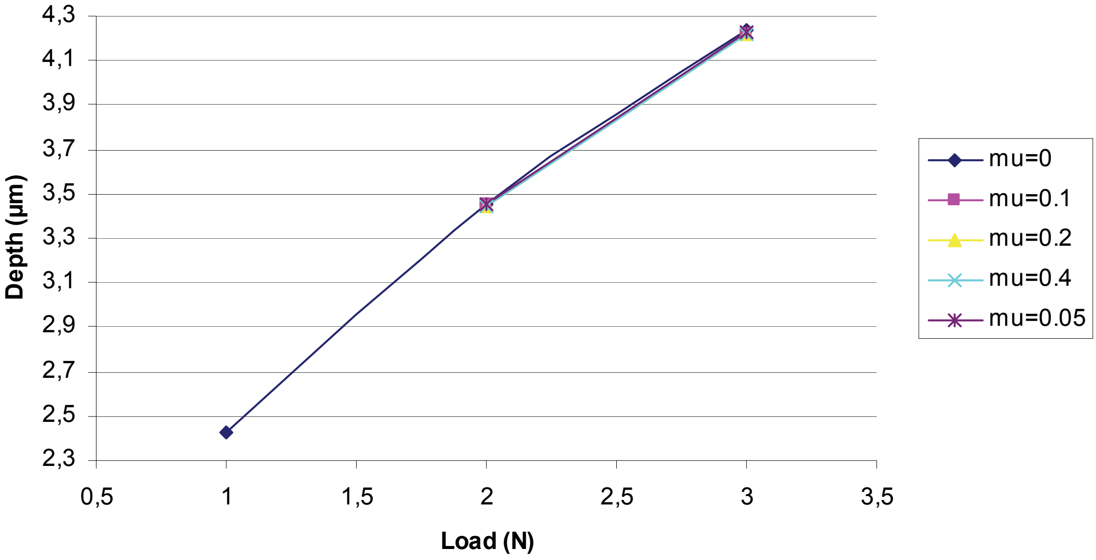

Graph 56: Depth of penetration during the indentation process depending on the true friction coefficient.

App.2-3.7.5 Influence of the tip radius of the indenter on the load

The evolution of the depth of indentation was studied as a function of the load and the size of the rounded defect at the tip of the indenter (only 2-D model case reported in Graph 57). The

result that a sharper indenter will enter more in the matter than a blunter indenter was a bit obvious, but the complete evolution drawn in Graph 57 was not *a priori* known. This difference of penetration depth is partly due to the direct geometrical difference between the tip radius of the considered indenters.
Note that one can draw a similar evolution for the 3-D model for Vickers indentation.

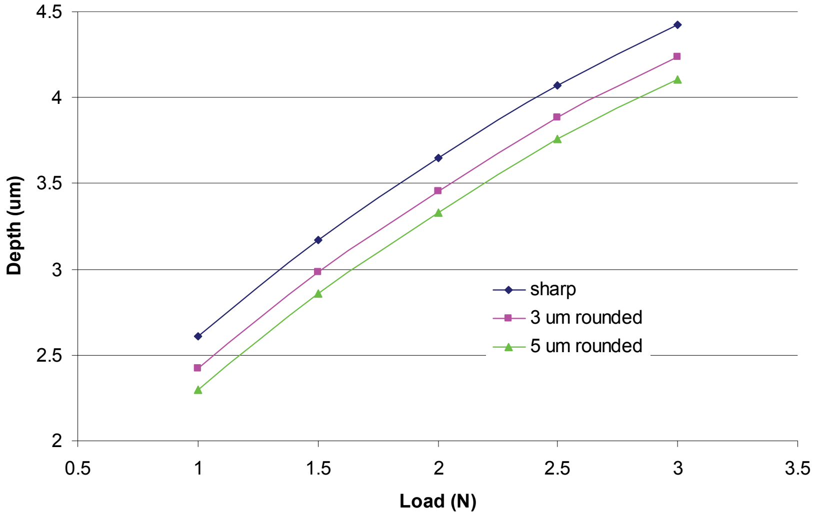

Graph 57: Depth of penetration during the indentation process depending on the tip radius (2D model).

App.2-3.7.6 Influence of the angle of the indenter on the load

The evolution of the depth of indentation was studied as a function of the load and the angle of the indenter (sharp indenter - only 2-D model case reported in Graph 58). The result that a more wide-opened indenter will enter less in the matter was a bit obvious, but the complete evolution drawn in Graph 58 was not *a priori* known.
Note that one can draw a similar evolution for the 3-D model for Vickers indentation.

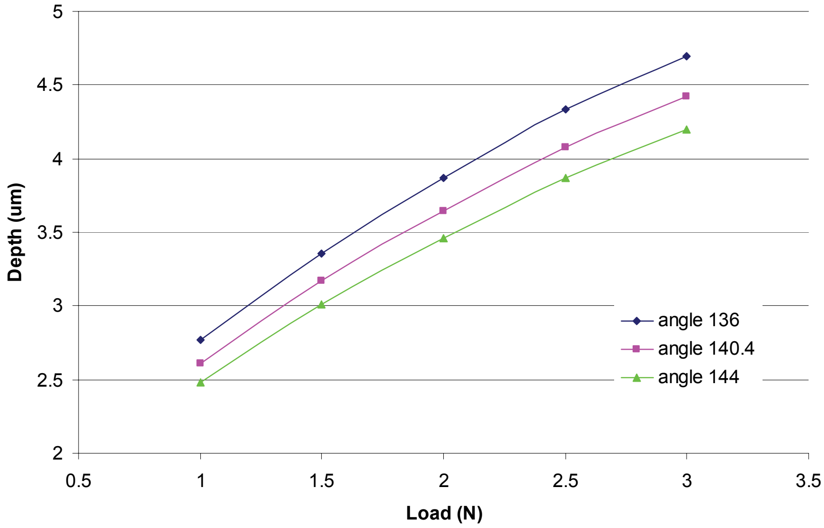

Graph 58: Depth of penetration during the indentation process depending on the true friction coefficient.

App.2-3.7.7 Stresses extraction by face

The great advantage of Finite Elements models is that they make a lot of information easily available. For example, all the components of stress and strain can be plotted on the whole model or only on one part of interest. Fig. 132 and Fig. 133 represent the Von-Mises stresses distribution respectively on the "face" plane of the Vickers (plane at 0° in the model) and on the "edge" plane (at 45°). One can appreciate the difference of stress field produced by the presence of an edge, the singularity of this indenter. One can also plot easily all that is available in the Abaqus post-processor, as σ_{zz} only on one "slice" of the model for instance.

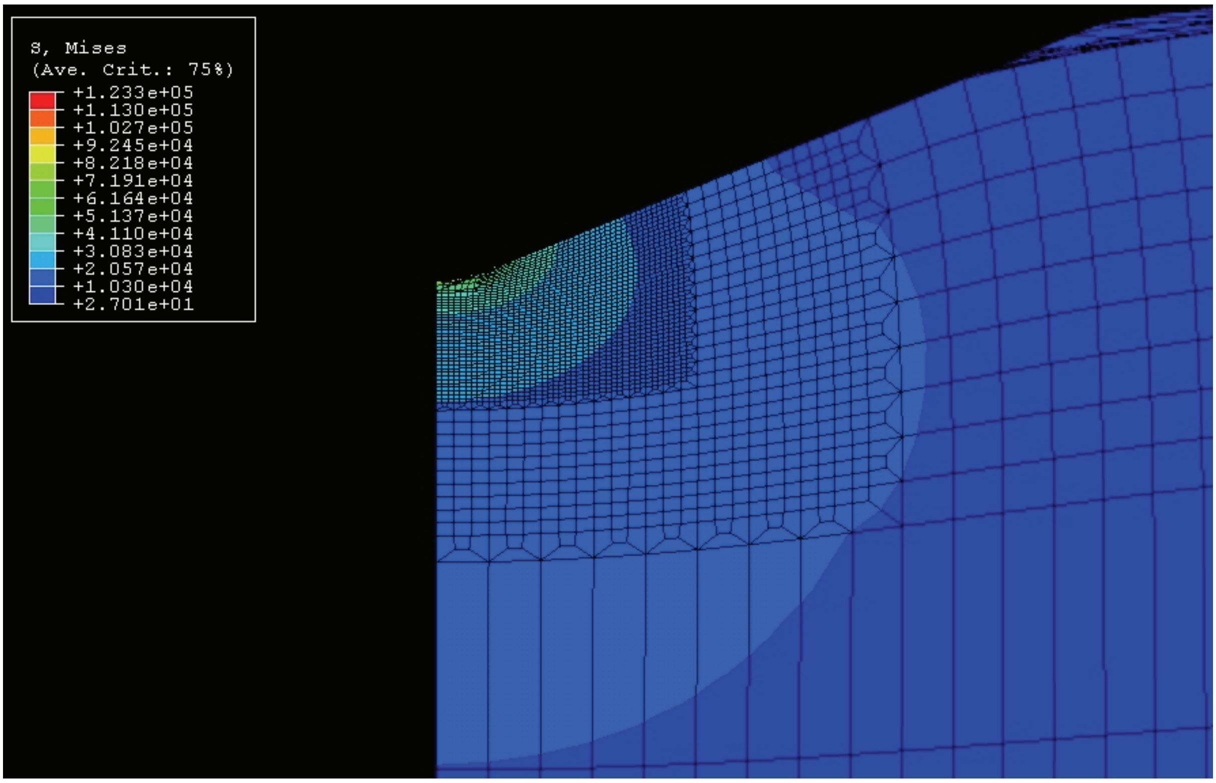

Fig. 132: Von-Mises stresses distribution on the "face" plane of the Vickers (plane at 0° in the model) – Perspective view.

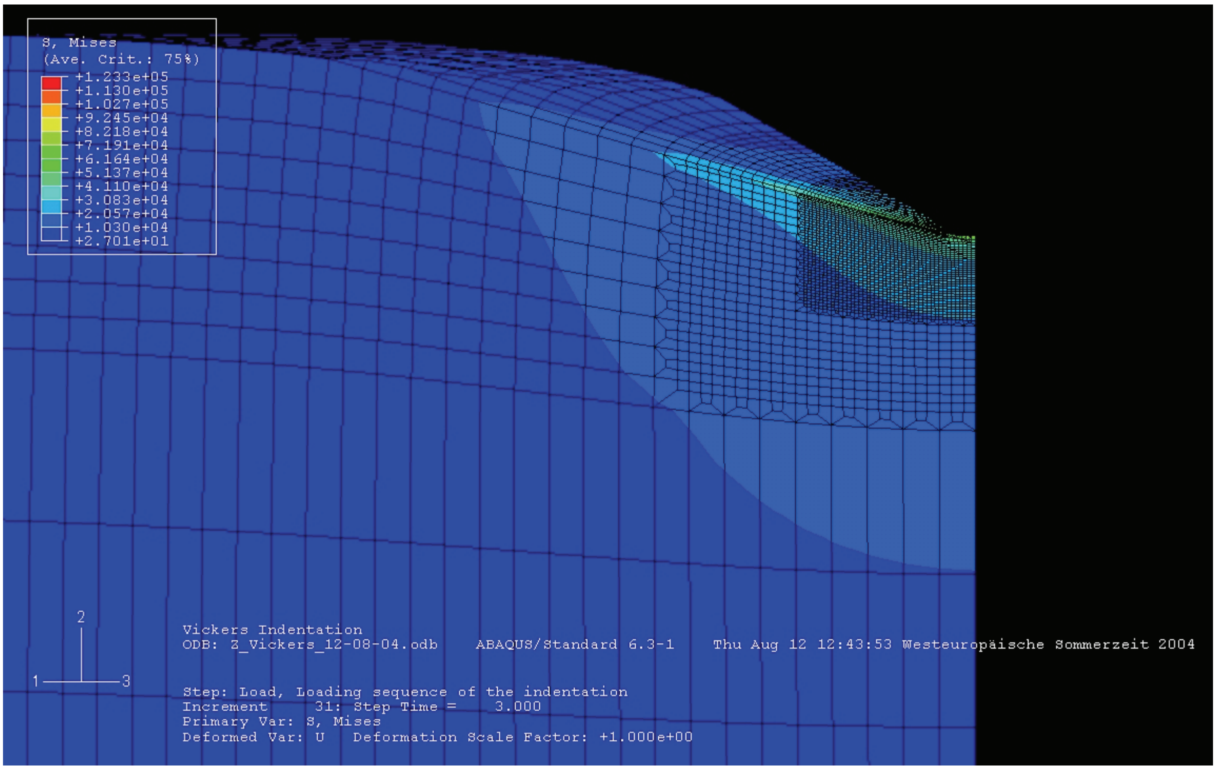

```
Vickers Indentation
ODB: Z_Vickers_12-08-04.odb    ABAQUS/Standard 6.3-1    Thu Aug 12 12:43:53 Westeuropäische Sommerzeit 2004

Step: Load, Loading sequence of the indentation
Increment     31: Step Time =    3.000
Primary Var: S, Mises
Deformed Var: U   Deformation Scale Factor: +1.000e+00
```

Fig. 133: Von-Mises stresses distribution on the "edge" plane of the Vickers (plane at 45° in the model) – Perspective view.

APPENDIX 3:
ARTICLES ASSOCIATED TO THIS WORK

SUMMARY OF APPENDIX 3

App.3-1 : V. Le Houérou, J.-C. Sangleboeuf, S. Dériano, T. Rouxel and G. Duisit, Surface damage of soda-lime-silica glasses: indentation scratch behavior, *Journal of Non-Crystalline Solids, 316 (1), (2003), pp. 54-63.*

ELSEVIER
Available online at www.sciencedirect.com
SCIENCE DIRECT®
Journal of Non-Crystalline Solids 316 (2003) 54–63
JOURNAL OF NON-CRYSTALLINE SOLIDS
www.elsevier.com/locate/jnoncrysol

Surface damage of soda–lime–silica glasses: indentation scratch behavior

V. Le Houérou [a,*], J.-C. Sangleboeuf [a], S. Dériano [a], T. Rouxel [a], G. Duisit [b]

[a] *LARMAUR, UPRES-JE 2310, Bât. 10B, Université de Rennes 1, Campus de Beaulieu, 35042 Rennes cedex, France*
[b] *Saint-Gobain Recherche, 39 quai Lucien Lefranc, B.P. 135F, 93303 Aubervilliers cedex, France*

Abstract

Contact mechanics problems are of fundamental interest both to understand the process of surface damage and matter removal in brittle materials, and to develop a method to evaluate their scratch resistance. In order to get insight into these problems in the case of soda–lime–silica glasses, a classical indentation apparatus was used, and an original scratch experimental setup was designed, allowing for a monotonic loading (or unloading) of the indenter combined with a controlled sliding of the specimen beneath the indenter. The influences of the normal load, the moisture level and the glass composition have been studied, and clear relationships were established between the glass compositions and the indentation-scratching behavior. The indentation and scratching characteristics such as the critical-crack-initiation loads and the transition loads between the different scratch regimes were correlated and interpreted in the light of the brittleness index and structural considerations.

PACS: 61.43.Fs; 62.20.–x; 62.20.Mk

1. Introduction

The study of the scratch resistance of soda–lime–silica (SLS) glasses is of great interest to better understand the causes for optical losses and for the fracture (assisted or not by humidity) of windows or lenses due to surface damage in service. Previous studies mostly investigated the relationships between the composition of oxide glasses and their physical and thermo-mechanical properties such as density, coefficient of thermal expansion, elastic moduli, Poisson's ratio, hardness [1] and toughness [2]. The present exploratory work mainly focuses on the influence of the glass composition on its resistance against surface damage. The roles of the loading history and of the humidity were also characterized.

The glass compositions were defined in such a way that with regard to their indentation behavior, the studied glasses cover the range from typical normal glasses to near so-called 'anomalous' glasses [3]. One recalls that normal glasses are characterized by the absence – or a minor contribution – of a densification process in the area beneath an applied contact stress. Indentation experiments showed that in this case irreversible

---

[*] Corresponding author. Tel.: +33-2 23 23 67 18; fax: +33-2 23 23 63 59.

E-mail address: vincent.le-houerou@univ-rennes1.fr (V. Le Houérou).

0022-3093/03/$ - see front matter © 2003 Elsevier Science B.V. All rights reserved.
PII: S0022-3093(02)01937-3

deformation occurs by 'plastic' rearrangement, or shear flow, as suggested by the presence of 'slip' lines in the elastic–plastic contact zone [4]. According to Peter [5], oxide glasses become normal when the modifier content exceeds 15–20 mol%. On the contrary, a flow-densification process shows up in anomalous glasses, and the ability of glasses with relatively high silica content to density under sharp contact loading has a great influence on the indentation and on the scratch damage features, and is thus of primary interest.

The correlations between the scratch damage resistance and the bulk properties of glasses [6,7], the composition of glasses [7] or the environmental parameters [6,8] are not clearly established yet and only a few papers were published so far to the knowledge of the authors. Some new experimental results concerning the scratch behavior and its dependence on the humidity rate, and the indentation versus scratch correlation were obtained in the present study, using an original experimental setup.

2. Materials and experimental techniques

2.1. Materials

A commercially available SLS float glass [1] was studied. $40 \times 15 \times 4$ mm^3 specimens were cut using diamond-type cutting tools from a pane annealed at 560 °C (i.e. at $T_g + 15$ °C) in air during 1 h and cooled at 2 °C min^{-1}. In addition, different glasses were synthesized in the Na_2O–CaO–SiO_2 phase diagram. These glasses are referred as SLS (1–4), and were obtained by substituting SiO_2 for ($Na_2O + CaO$) while keeping Na_2O/CaO ratio constant and equal to 1.52. The glass compositions and their properties are given in the Table 1. Glasses through the SLS series were synthesized starting from pure and dried SiO_2, $CaCO_3$, $NaHCO_3$ powders. Small quantities (in a total proportion of less than 0.5 mol%) of fluxing agents, such as ZnO, $BaCO_3$, $SrCO_3$ and As_2O_3 were added to ensure a good homogeneity of the glasses. Batches were then melted at 1600 °C in a platinum (Pt/Rh 10%) crucible in air during few hours and stirred with a platinum stirrer for 1 h to refine the melt. Approximately 200 g of glass melt were finally poured into a carbon mould, preheated at 550 °C, and slowly cooled to room temperature by cutting the furnace off. After determination of their T_g (located between 558 and 561 °C) by calorimetric measurement (DSC), glasses were annealed for half an hour at T_g and slowly cooled at a rate of 1 °C min^{-1}. Note that the same samples were used for all measurements. Glasses from the SLS series were cut and their surfaces were carefully polished up to 3 μm grid. Glass specimens were kept in a dried atmosphere to avoid moisture pollution before testing.

2.2. Experimental setup and procedure

The glass density (ρ) was measured on powdered samples by the pycnometry method; Young's modulus (E) and Poisson's ratio (ν) were measured by the pulse–echo technique on 4 mm thick rectangular specimen. Vickers indentations (load of 9.8 N applied during 15 s), were performed to estimate both Meyer's hardness (H) and the 'indentation' fracture toughness (K_c) [9] by means of the following equations:

$$H \quad P/2a^2 \tag{1}$$

and

$$K_c \quad 0.016(E/H)^{1/2}P/c^{3/2}, \tag{2}$$

where P is the load, a is half the mean size of the two diagonals, E is Young's modulus, H is Meyer's hardness, and c is half the mean length of the two radial cracks (tip to tip).

An apparatus allowing for a variable loading cycle during a single experiment was designed, and placed into a glove box in order to achieve a good moisture control in the range 0–100%, so as to study the effect of the environment (Fig. 1).

The horizontal displacement of the indenter (to produce a groove) is obtained by a bearing slide, while a piezoelectric actuator controls the vertical movement. Both the penetration and the tangential forces are continuously monitored. The main characteristics of the apparatus are a maximal

---

[1] Planilux™, Saint-Gobain.

Table 1
Composition and physical properties of glasses

Glasses	SiO_2 (mol%)	Na_2O (mol%)	CaO (mol%)	T_g (°C)	ρ ($g\,cm^{-3}$)	α (10^{-6} °C^{-1})	E (GPa)	ν	H (GPa)	K_c ($MPa\,m^{1/2}$)
Float glass	70.9	12.8	10.1	562	2.55	9.3	71.5	0.21	6.12	0.72
SLS 1	71	17.5	11.5	558	2.53	10.9	70.2	0.202	5.35	0.71
SLS 2	74	15.7	10.3	559	2.50	10.1	69.3	0.188	5.11	0.70
SLS 3	77	13.9	9.1	560	2.47	9.1	68.6	0.181	5.15	0.76
SLS 4	80	12.1	7.9	561	2.43	7.7	68.1	0.172	5.19	0.82
Experimental error				±2	±0.005	$\pm 0.2 \times 10^{-6}$	±1	±0.01	±0.01	±0.02

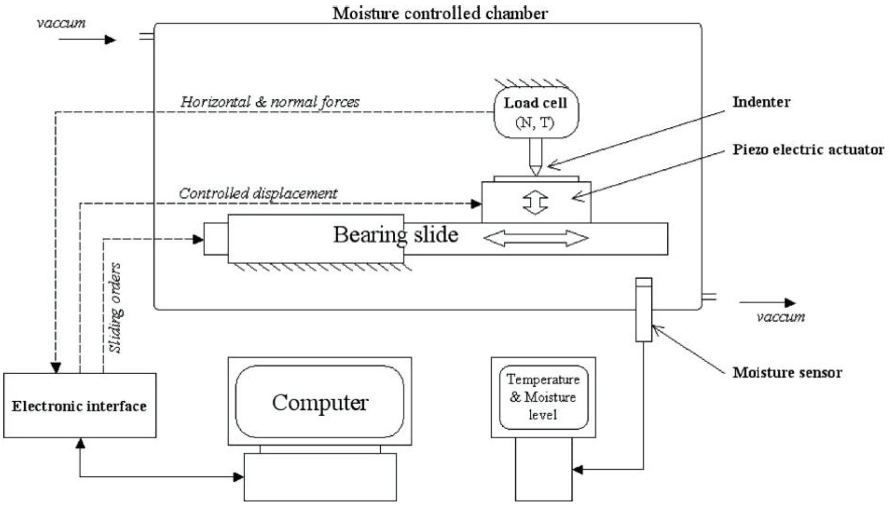

Fig. 1. Diagram of the experimental setup designed for variable loading scratch test in a moisture and temperature controlled atmosphere.

normal load of 50 N with an accuracy of 0.05 N, a vertical penetration displacement limited to 100 μm, and a bearing slider allowing for a displacement accuracy better than 1 μm and a maximum speed of 5 mm/s. The displacement of the bearing slider is computer controlled, and displacements and environmental parameters are continuously monitored.

The scratch resistance (tangential load) was followed through constant normal load and low rate loading–unloading experiments (from 0 N to the maximum load and reverse to 0 N at a sliding velocity (slow regime) of 0.01 mm/s). Such experiments allow first to study a wide load range within a single experiment and second, to reveal any possible dynamical effect, by studying the symmetry of the scratch pattern.

In order to characterize the influence of humidity on the scratch resistance of glasses, experiments were conducted under hygrometric levels of 0%, 30%, 65% and 100% humidity. The peculiar value of 100% of humidity was obtained by placing boiling water inside the enclosure.

Three different types of run were conducted: (i) scratching of the commercial annealed SLS glass with a Vickers penetrator at 65% of humidity under a predetermined constant load at an horizontal displacement rate of 0.01 mm/s; (ii) scratching of the commercial annealed SLS glass with a Vickers penetrator with different hygrometric levels: 0%, 30%, 65% and 100% of humidity (0–3 N load–unload slope on a 6 mm distance at 0.01 mm/s speed); and (iii) scratching of the SLS grades and the fused silica glass (0–4 N load slope on a 2 mm distance at 0.1 mm/s speed).

The Vickers penetrator (inverse pyramidal, 136° face to face angle) was used with a leading edge orientation. The samples and the indenters are cleaned with ethanol before each test. Four different grooves were made on each glass to ensure a good reproducibility of the results.

Scratch patterns were observed by means of an optical microscope under Nomarski contrast conditions. The observations were systematically made 2 min after the mechanical testing, so that the possible incidence of fatigue–corrosion phenomena is about the same for all the specimens.

3. Experimental results and discussion

3.1. Quasi-static behavior

The physical and mechanical properties measured on the studied glasses are summarized in Table 1. Most of the properties, such as ρ, E, ν and α, showed a monotonic trend with increasing SiO_2 content, while H and K_c exhibit maxima for the SLS2 composition (i.e. for glass containing 74 mol% of silica).

The density decreases with rising silica contents, from 2.55 to 2.43 $\mathrm{g\,cm^{-3}}$ for the float glass and the SLS4 grade respectively (note that pure vitreous silica has a density of about 2.2 $\mathrm{g\,cm^{-3}}$), as Si^{4+} former ions replace modifiers (Na^+ and Ca^{2+}). In fact, the silica network has an opened structure with a lot of vacancies, and is therefore able to accommodate interstitial cations in a large proportion. Our results are consistent with those of Doweidar [10] who showed that linear relations could be found in simple silicate systems. Young's modulus decreases slightly when the amount of modifiers decreases. Two concurrent effects are in competition: (i) the increase of the bond strength ($E_{\mathrm{Si\ O}} \gg E_{\mathrm{Ca\ O}} > E_{\mathrm{Na\ O}}$ [11]) and (ii) the decrease of the bond density when less and less modifiers fill the voids of the high silica content vitreous network. This latter effect leads to a more and more open and flexible network and predominates over the first effect, which is a short range one. Indeed, the more the amount of network modifying cations decreases, the more the network stiffness is controlled by the variations of the Si–O–Si intertetrahedral angles and by the mutual orientation of SiO_4 tetrahedra, whereas the other structural parameters do not appreciably change [12]. This effect governs macroscopic properties such as elasticity and thermal expansion. As a result, E, α and ν also decrease with rising silicon content (note that for pure vitreous silica, $\alpha \quad 5.5 \times 10^{-7}$ °C^{-1}).

Silica has a small Poisson's ratio of 0.16 and therefore shows a great tendency for an elastic (or reversible) volume change under stress. Yamane and Mackenzie [13] proposed a relationship between Poisson's ratio and a parameter (C) reflecting the glass network compacity where ν changes linearly with C ($\nu \quad 1.12C \quad 0.313$). In a detailed theoretical and experimental investigation of the hardness (H) and the elastic properties of glasses, these authors showed that the higher the glass compacity, the higher the hardness and the elastic moduli. These previous investigations together with the present results strongly suggest that a low Poisson's ratio also favors densification (irreversible volume decrease). The hardness measures the resistance of glass to a permanent deformation process. The maximum values obtained for the SLS1 grade and the float glass can be explained by a more filled three-dimensional network. In fact, interstitial cations, such as Na^+ and Ca^{2+}, enter into the empty sites of the network and so lead to a monotonic increase of E, ν and ρ in this range. It is anticipated however that when all these latter sites are filled, the silica network becomes disrupted and begins to weaken.

Noteworthy, hardness and indentation fracture toughness exhibit non-monotonic changes and, following the analysis of Babcock [14], the existence of minima for the SLS2 composition could stem from the presence of two imbricated networks. In order to explain these experimental observations, the lecture of the phase diagram of the ternary SiO_2–Na_2O–CaO is helpful [15]. In fact, we can see from the diagram (Fig. 2) that the SLS2 grade has an intermediate composition between two different primary phase fields, namely the tridymite (SiO_2)

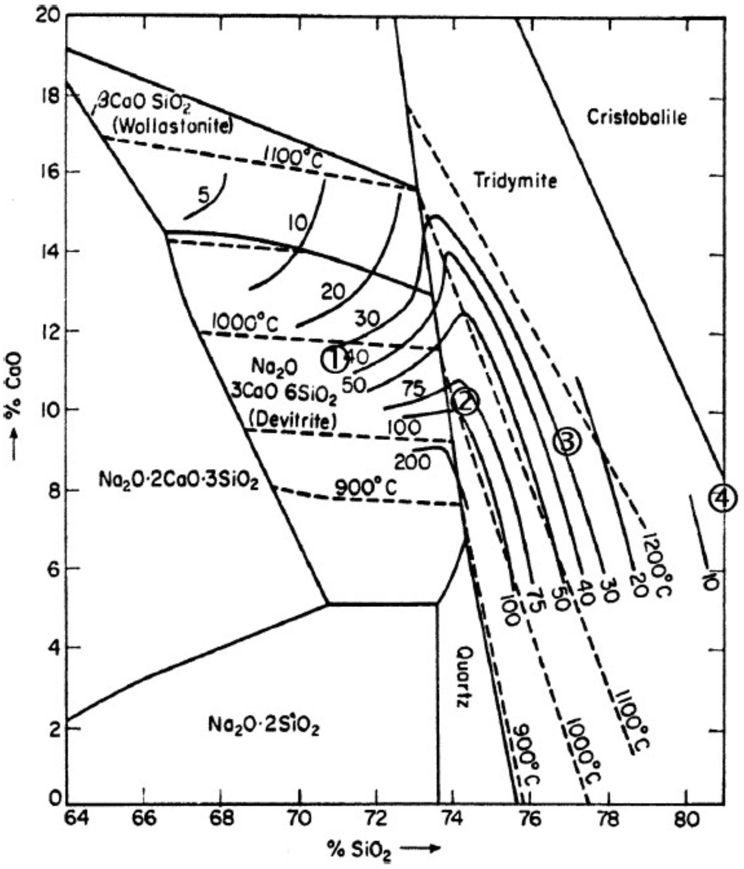

Fig. 2. Na_2O–CaO–SiO_2 phase diagram in mol% [15], with the four SLS glasses synthesized for this study.

phase field, containing SLS3 and SLS4 glasses, and the devitrite (Na_2O–3CaO–6SiO_2) phase field containing the SLS1 composition.

The indentation-derived fracture toughness K_c increases with the silica content for $SiO_2 \geqslant 74$ mol%. Again the shift toward a more and more anomalous indentation behavior has to be invoked. Indeed the energy dissipation due to the flow-densification process beneath the indenter results in a less important micro-cracking, and in shorter radial–median cracks. The progressive shift toward Hertzian cone cracks – which are typically observed in vitreous silica – also contribute to the shortening of the radial–median cracks. However, we must keep in mind that a quantitative comparison of K_c between glasses with significantly different silica content calls for caution, since the experimental method is based on a pure normal behavior. What seems clear though is that a high silica content in the starting powder mixture favors flow-densification and enhances the fracture toughness, as was previously noticed by Seghal and Ito [16]. (Note that a fracture toughness of 0.77 $MPa\,m^{1/2}$ was obtained on pure vitreous silica by means of a single edge notch beam method [17].)

3.2. Scratch behavior

3.2.1. Load dependence of the scratch behavior (standard glass)

During an indentation experiment performed with a Vickers indenter on a SLS glass, cracks are known to occur during loading or unloading, and depend strongly on the load level [18]. In a scratching experiment, the scratch pattern also strongly depends on the level of the normal load, and for low loads the different kinds of micro-cracks which form during, or with the scratch process; they are namely: (i) the median cracks, (ii) the radial cracks and (iii) the lateral cracks. This last kind of cracks induces chipping when crack propagation toward the specimen surface occurs.

At high magnification, the radial cracks (also called chevron cracks) resulting from the scratch process do not look exactly as those described by Ahn et al. [19]. These cracks are significantly inclined toward the sliding direction, and propagate in a curved shape usually ending perpendicular to the scratch direction (Fig. 3, top-view detail), when there is no combination with another damage phenomenon (i.e. lateral cracks as we will see further).

Monotonic loading/unloading cycles were conducted in order to screen all the possible damage events in a single scratch experiment. Indeed, following Ahn [20] and Bulsara [21], a schematic drawing illustrating the three different regimes appearing during a typical scratch experiment at a constant loading rate could be depicted (Fig. 3): (i) the first regime is associated with a permanent groove with eventually the formation of sub-surface lateral cracks under the plastic track, and corresponds to a micro-ductile regime, (ii) the second one, so-called micro-cracking regime, is characterized by an important damage by micro-cracking (lateral cracks intersecting the surface and radial cracks) and (iii) the third one is a micro-abrasive regime and gives birth to many debris, with sometimes small lateral cracks along the track.

The transition forces between the different regimes were recorded and are summarized in Table 2. Values for the critical loads are slightly lower than those found by Ahn or Bulsara, likely because of the differences between the glass compositions, as will be further discussed in Section 3.2.3. In addition, the transition loads obtained during loading sequence were found to be unaffected by the loading history, i.e. the application of a monotonic loading rate during scratching gives a transition load similar to that obtained by constant loading scratch experiments (Table 2). However, the transition loads on the unloading path are slightly lower, likely because crack initiation and propagation are unstable phenomena. The crush scratch track appears at high loads (typically $F_n > 0.8$ N), and many debris are present.

3.2.2. The role of humidity

Fig. 4 shows the scratches together with the normal load applied during the experiments at different humidity levels.

As expected from the background studies on the effect of humidity on the fracture behavior of

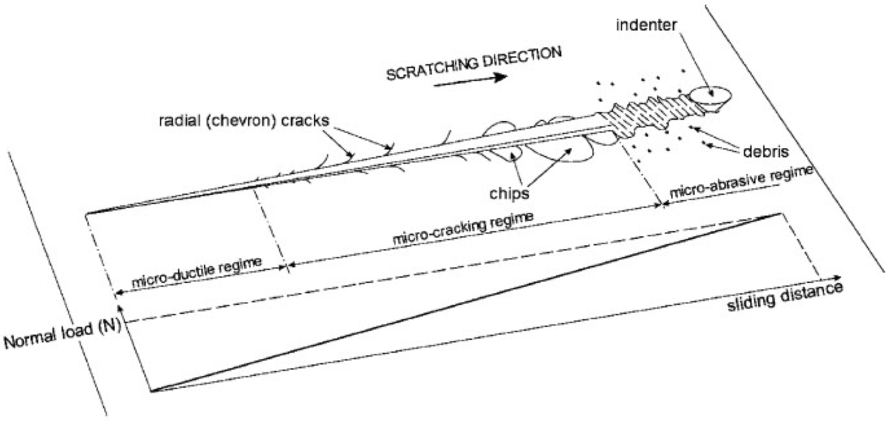

Fig. 3. Typical scratch pattern made on the surface of the SLS glass by a Vickers penetrator (leading edge) during a monotonic loading cycle (see load history below the schematic drawing).

Table 2
Transition loads associated with changes in the scratch regime

Fracture pattern	Normal load (N)			
	Constant loading experiments		Monotonic loading experiments	
	Ahn [19]	This study	Loading rate 0.01 N/s	Unloading rate 0.01 N/s
No crack	∼0 0.05	∼0 0.3	∼0 0.4	∼0.3 0
Median cracks	∼0.05 0.8			
Median cracks and lateral cracks under plastic scratch	∼0.8 1.5			
Median, radial cracks and lateral cracks intersecting the surface	∼1.5 3	∼0.3 0.8	∼0.4 0.9	∼0.9 0.3
Median cracks and crushed scratch groove	∼3 6	>0.8	>0.9	0.9>

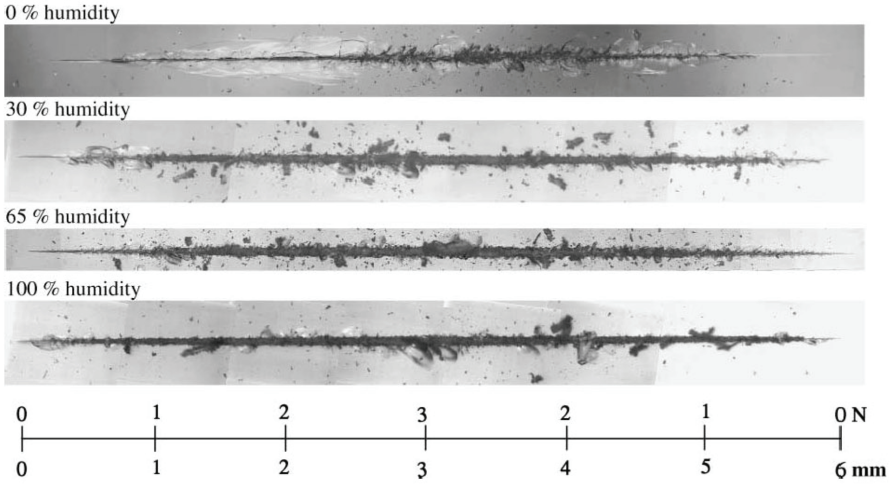

Fig. 4. Pictures of scratches conducted under different hygrometric levels with a Vickers penetrator following a slope load unload process.

SLS glasses [22,23], the scratch patterns significantly depend on the hygrometric level: the more important the hygrometric level is, the earlier (with regards to the normal load) the different damage processes appear. Another observation concerns the scratch obtained with 0% of humidity. Note that the peculiar level of 0% of humidity corresponds to a real hygrometry less than 50 ppm of water vapor in the atmosphere of the glove box. In the case of 0% of humidity, the damage is characterized by a large lateral crack remaining under the surface of the sample. A similar but shorter crack occurs during the unload process. This phenomenon fades rapidly as the humidity level is raised.

The peculiar morphology of the scratch made at 0% of humidity is interesting. We can notice that there is almost a total lack of radial cracks while lateral cracks, which never reach the surface, extend over a large distance (Fig. 4). This observation put in light the mechanism of the chipping process occurring during scratching: a chip is the combination of two radial cracks and a lateral one which then intersects the specimen surface (Fig. 5). Two consecutive radial cracks located on the same side of the scratch track may intersect each other as a result of a deviation process resulting from the attractive forces between two close cracks. The coupling with a lateral crack leads to a chip and thus to matter removal. When only one radial

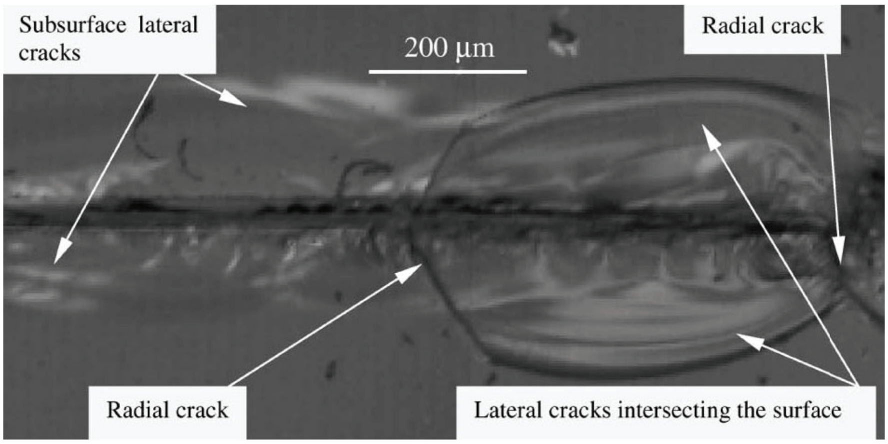

Fig. 5. Lateral cracking of the commercial SLS glass under a Vickers indenter resulting from a constant loading rate in dry atmosphere.

crack frames the lateral one, this latter crack may remain under the surface (Fig. 5, left side).

Sub-surface lateral cracks, formed just behind the indenter, were found to be insensitive to the hygrometric rate and to remain under the surface of the material.

3.2.3. *Role of the glass composition*

SLS glasses generally fall in a narrow range of compositions along the boundary between devitrite (Na_2O–$3CaO$–$6SiO_2$) and tridymite (SiO_2) in the Na_2O–CaO–SiO_2 phase diagram. Shifting away from this narrow range affect various important characteristics, such as the glass melting behavior, crystallization tendency, glass workability and chemical durability. The scratchability is also affected as depicted in Fig. 6 showing one of the four scratch grooves for each glass through the SLS 1–4 series. A micro-abrasive regime appears in the low-load domain for the SLS3 and SLS4, with high silica contents, whereas lateral chipping occurs for the SLS1 and SLS2 compositions. Glasses from the devitrite phase field are sensitive to chipping and glasses with silica-like networks appear to be much resistant to both crack propagation and chipping during scratch experiments. At the atomic or molecular scale, the resistance of the high silica content glasses to chipping or micro-cracking is due to the opened structure of the glass network, allowing both for the network flexibility and for the flow-densification process [24]. On the other hand, glasses with high modifying cation content (typically >25%), such as SLS1 and 2, contain more non-bridging oxygens which provide easy paths for fracture and slip. Note that a similar conclusion was drawn in a study devoted to the indentation-scratching behavior of silicon-oxycarbide glasses [17], where the covalently bonded carbon in fourfold coordination was found to induce a more normal behavior.

In the aim to correlate indentation and scratch behaviors, indexes or parameters combining both flow and fracture properties are useful. Among them, the brittleness parameter B introduced by Lawn and Marshall [25] accounts for two competitive processes: plastic deformation and crack propagation. The higher the value for B is, the more 'brittle' the glasses are considered (Table 3). B is given by

$$B = H/K_c, \tag{3}$$

where K_c is the fracture toughness and H is Meyer's hardness.

B values allow for a comparison of the brittleness of glasses belonging to the same family (e.g. SLS glasses). However, to interpret the scratch behavior, the appearance or the disappearance of the different crack systems is of paramount importance. In first attempt to characterize the sensitivity of glasses to micro-cracking indentation

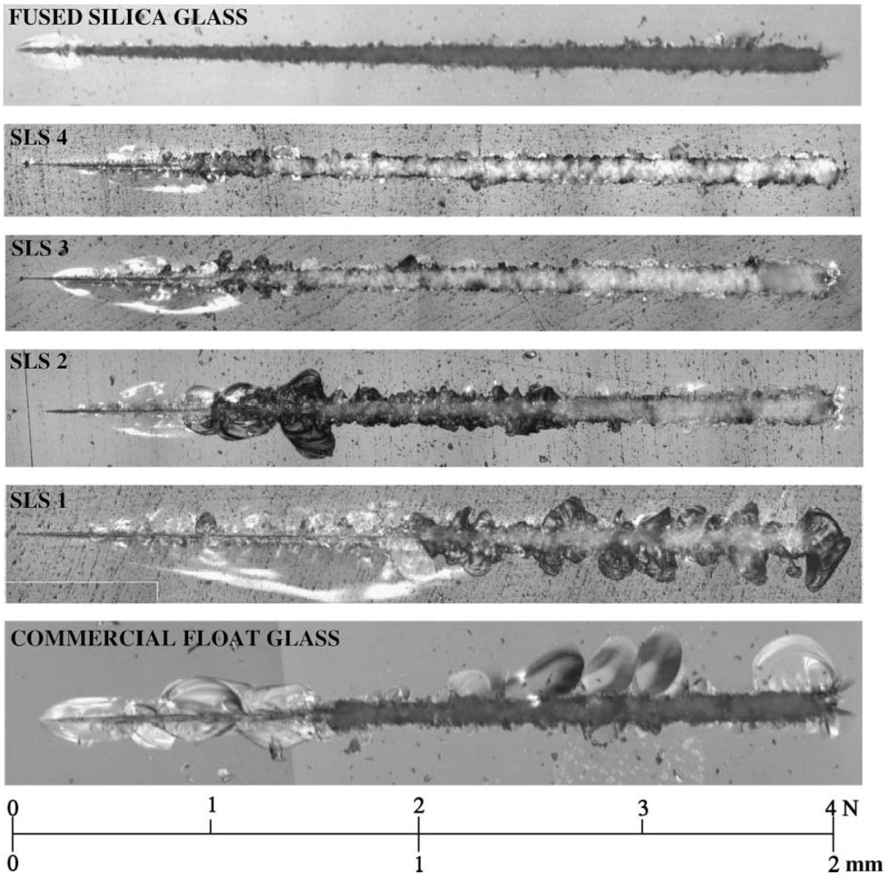

Fig. 6. Evolution of scratch resistance for the five SLS glasses and the fused silica glass.

Table 3
Brittleness (B), experimental and calculated radial-crack-initiation loads (P_C^R and $P_C^{R_*}$ respectively) and experimental and calculated lateral crack threshold loads (P_C^L and $P_C^{L_*}$ respectively) for the SLS glasses

Glasses	$B = H/Kc$ ($m^{-1/2}$)	P_C^R (N)	$P_C^{R_*}$ (N)	P_C^L (N)	$P_C^{L_*}$ (N)
Float glass	8500	0.25 0.50	0.30	1 2	
SLS1	7500	0.10 0.25	0.70	0.25 0.50	1.18
SLS2	7350	0.10 025	0.68	0.25 0.50	1.17
SLS3	6800	1 2	1.01	2 3	1.75
SLS4	6350	1 2	1.34	2 3	2.28

experiments were made at 0.1, 0.25, 0.50, 1, 2 and 3 N. The critical load P_C^R and P_C^L for crack initiation were measured for radial and lateral cracks respectively (Table 3). The experimental values were compared with the theoretical ones proposed by Lawn et al. [26] or Hagan [27] for radial critical load $P_C^{R_*}$ which is expressed as

$$P_C^{R_*} = \alpha K_c^4/H^3 \tag{4}$$

and for the lateral critical load $P_C^{L_*}$ given by Marshall et al. [28]:

$$P_C^{L_*} = \beta E K_c^4/H^4, \tag{5}$$

where E is Young's modulus. The values reported in Table 3 were obtained in the present study for α and β: $\alpha \quad 3.9 \times 10^5$, $\beta \quad 4.9 \times 10^4$ for the SLS series and $\alpha \quad 2.2 \times 10^4$ for the float glass.

The gap between the behaviors of SLS1/SLS2 and SLS3/SLS4 is predicted (Table 3). In the case of the commercial float glass, the addition of modifiers is responsible for significant changes in the glass network. More specifically, the void concentration and the flexibility of the (SiO_4) tetrahedral arrangement are assumed to be much lower than in a model glass (SLS series) of nominally identical silica content. Although the changes on the bulk properties are small, major consequences on theoretical parameters like B, $P_{\mathrm{C}}^{\mathrm{R}_{\dashv}}$ and $P_{\mathrm{C}}^{\mathrm{L}_{\dashv}}$ were noticed.

4. Conclusion

The scratch behavior of glasses belonging to the SLS glass system has been studied, and was found very sensitive to the loading history, the hygrometry level and the glass composition. Three major scratch–damage regimes were observed, namely a micro-ductile, a micro-cracking and a micro-abrasive regime. On one hand, the higher the silica content is and the more significant the flow-densification process becomes, and as a result the higher the critical loads for radial and lateral crack formation are. On the other hand, glass composition with relatively high contents (>25 mol%) of glass network modifying cations can hardly accommodate sharp contact loading and are thus more sensitive to micro-cracking. The hygrometry level mainly affects the median–radial crack propagation and has therefore a direct incidence on the chip formation and on the micro-abrasive regime.

Acknowledgements

The authors are very grateful to Mrs M.H. Chopinet from the Saint-Gobain Company for her technical assistance during the elaboration of the SLS glass series at Saint-Gobain Research (Aubervilliers, France) and to B. Truffin (LARMAUR, Rennes, France) for encouragements and technical support.

References

[1] H. Scholze, Le verre nature structure et propriétés, 2nd Ed., Institut du Verre, Paris, 1974.
[2] E. Vernaz, F. Larche, J. Zarzycki, J. Non-Cryst. Solids 37 (1980) 359.
[3] A. Arora, D.B. Marshall, B.R. Lawn, M.V. Swain, J. Non-Cryst. Solids 31 (1979) 415.
[4] J.T. Hagan, J. Mater. Sci. 15 (1980) 1417.
[5] K.W. Peter, J. Non-Cryst. Solids 5 (1970) 103.
[6] K. Li, Y. Shapiro, J.C.M. Li, Acta Mater. 46 (17) (1998) 5569.
[7] S. Yoshida, H. Tanaka, T. Hayashi, J. Matsuoka, N. Soga, J. Ceram. Soc. Jpn. 109 (6) (2001) 511.
[8] A.W. Ruff, H. Shin, C.J. Evans, Wear 181–183 (1995) 551.
[9] G.R. Anstis, P. Chantikul, B.R. Lawn, D.B. Marshall, J. Am. Ceram. Soc. 64 (9) (1981) 533.
[10] H. Doweidar, J. Non-Cryst. Solids 249 (1999) 194.
[11] K.H. Sun, J. Am. Ceram. Soc. 30 (9) (1947) 277.
[12] S. Sakka, J.D. Mackenzie, J. Non-Cryst. Solids 1 (1969) 107.
[13] M. Yamane, J.D. Mackenzie, J. Non-Cryst. Solids 15 (1974) 153.
[14] C.L. Babcock, J. Am. Ceram. Soc. 52 (3) (1969) 151.
[15] H. Rawson, Inorganic Glass-Forming Systems, Academic Press, London, 1967, p. 88.
[16] J. Seghal, S. Ito, J. Am. Ceram. Soc. 81 (9) (1998) 2485.
[17] T. Rouxel, J.-C. Sangleboeuf, J.-P. Guin, V. Keryvin, J. Am. Ceram Soc. 84 (10) (2001) 2220.
[18] K. Niihara, R. Morena, D.P.H. Hasselman, J. Am. Ceram. Soc. 65 (1982) C116.
[19] Y. Ahn, T.N. Farris, S. Chandrasekar, Mech. Mater. 29 (1998) 143.
[20] Y. Ahn, PhD thesis, Purdue University, USA, 1992.
[21] V.H. Bulsara, PhD thesis, Purdue University, USA, 1997.
[22] S.M. Wiederhorn, in: Fracture Mechanics, vol. 2, Plenum, New York, 1974, p. 613.
[23] M. Tomozawa, Phys. Chem. Glass 2 (39) (1998) 65.
[24] J.D. Mackenzie, J. Am. Ceram. Soc. 46 (10) (1963) 461.
[25] B.R. Lawn, D.B. Marshall, J. Am. Ceram Soc. 62 (7–8) (1979) 347.
[26] B.R. Lawn, A.G. Evans, D.B. Marshall, J. Am. Ceram. Soc. 63 (9–10) (1980) 574.
[27] J.T. Hagan, J. Mater. Sci. 14 (1979) 2975.
[28] D.B. Marshall, B.R. Lawn, A.G. Evans, J. Am. Ceram. Soc. 65 (11) (1982) 561.

App.3-2 : *J.-C. Sangleboeuf, T. Rouxel, J.-P. Guin, S. Dériano and V. Le Houérou,* Comportement à l'indentation et au rayage de verres spéciaux*, Verre, Vol. 9 (4), (August 2003), pp 29-33.*

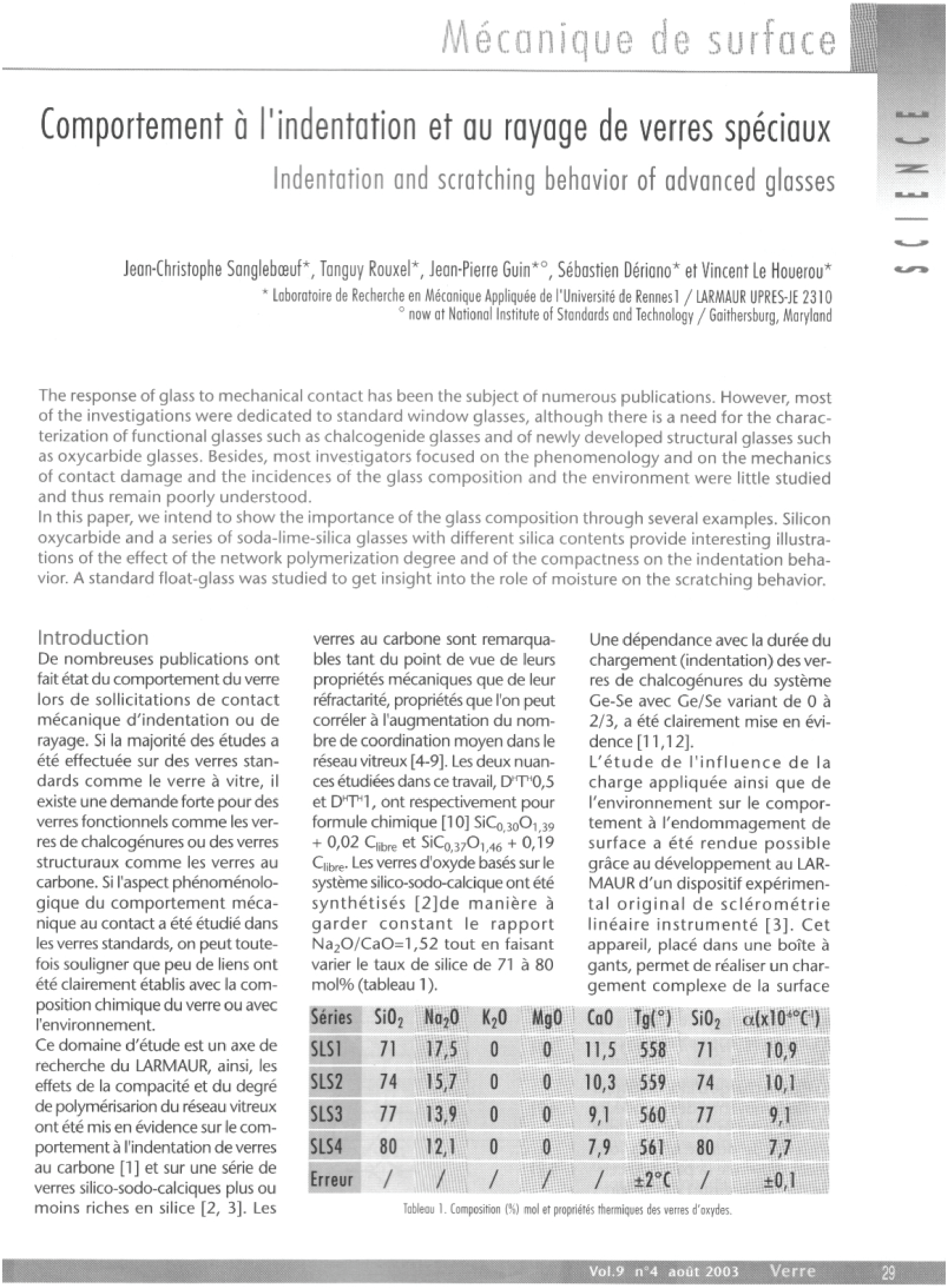

Comportement à l'indentation et au rayage de verres spéciaux

Indentation and scratching behavior of advanced glasses

Jean-Christophe Sanglebœuf*, Tanguy Rouxel*, Jean-Pierre Guin*°, Sébastien Dériano* et Vincent Le Houerou*
* Laboratoire de Recherche en Mécanique Appliquée de l'Université de Rennes1 / LARMAUR UPRES-JE 2310
° now at National Institute of Standards and Technology / Gaithersburg, Maryland

The response of glass to mechanical contact has been the subject of numerous publications. However, most of the investigations were dedicated to standard window glasses, although there is a need for the characterization of functional glasses such as chalcogenide glasses and of newly developed structural glasses such as oxycarbide glasses. Besides, most investigators focused on the phenomenology and on the mechanics of contact damage and the incidences of the glass composition and the environment were little studied and thus remain poorly understood.

In this paper, we intend to show the importance of the glass composition through several examples. Silicon oxycarbide and a series of soda-lime-silica glasses with different silica contents provide interesting illustrations of the effect of the network polymerization degree and of the compactness on the indentation behavior. A standard float-glass was studied to get insight into the role of moisture on the scratching behavior.

Introduction

De nombreuses publications ont fait état du comportement du verre lors de sollicitations de contact mécanique d'indentation ou de rayage. Si la majorité des études a été effectuée sur des verres standards comme le verre à vitre, il existe une demande forte pour des verres fonctionnels comme les verres de chalcogénures ou des verres structuraux comme les verres au carbone. Si l'aspect phénoménologique du comportement mécanique au contact a été étudié dans les verres standards, on peut toutefois souligner que peu de liens ont été clairement établis avec la composition chimique du verre ou avec l'environnement.

Ce domaine d'étude est un axe de recherche du LARMAUR, ainsi, les effets de la compacité et du degré de polymérisarion du réseau vitreux ont été mis en évidence sur le comportement à l'indentation de verres au carbone [1] et sur une série de verres silico-sodo-calciques plus ou moins riches en silice [2, 3]. Les verres au carbone sont remarquables tant du point de vue de leurs propriétés mécaniques que de leur réfractarité, propriétés que l'on peut corréler à l'augmentation du nombre de coordination moyen dans le réseau vitreux [4-9]. Les deux nuances étudiées dans ce travail, D^HT^H0,5 et D^HT^H1, ont respectivement pour formule chimique [10] $SiC_{0,30}O_{1,39} + 0,02\ C_{libre}$ et $SiC_{0,37}O_{1,46} + 0,19\ C_{libre}$. Les verres d'oxyde basés sur le système silico-sodo-calcique ont été synthétisés [2]de manière à garder constant le rapport $Na_2O/CaO=1,52$ tout en faisant varier le taux de silice de 71 à 80 mol% (tableau 1).

Une dépendance avec la durée du chargement (indentation) des verres de chalcogénures du système Ge-Se avec Ge/Se variant de 0 à 2/3, a été clairement mise en évidence [11,12].

L'étude de l'influence de la charge appliquée ainsi que de l'environnement sur le comportement à l'endommagement de surface a été rendue possible grâce au développement au LARMAUR d'un dispositif expérimental original de sclérométrie linéaire instrumenté [3]. Cet appareil, placé dans une boîte à gants, permet de réaliser un chargement complexe de la surface

Séries	SiO_2	Na_2O	K_2O	MgO	CaO	Tg(°)	SiO_2	α(x10^{-6}°C^{-1})
SLS1	71	17,5	0	0	11,5	558	71	10,9
SLS2	74	15,7	0	0	10,3	559	74	10,1
SLS3	77	13,9	0	0	9,1	560	77	9,1
SLS4	80	12,1	0	0	7,9	561	80	7,7
Erreur	/	/	/	/	/	±2°C	/	±0,1

Tableau 1. Composition (%) mol et propriétés thermiques des verres d'oxydes.

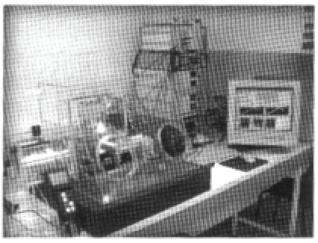

Figure 1. Dispositif expérimental de sclérométrie linéaire instrumenté sous atmosphère contrôlée (les gants ont été enlevés sur la photographie)

du matériau lors d'une opération de rayage par un indenteur Vickers (arête menante) tout en ayant le contrôle du taux d'humidité de l'environnement dans la gamme 0 % (< 50 ppm) - 100 % (figure 1).

Un ensemble de techniques expérimentales plus classiques [2, 11, 13] a été employé pour mesurer les différentes propriétés des verres étudiés: la calorimétrie différentielle à balayage (DSC) pour la température de transition vitreuse (T_g), la diatométrie pour le coefficient de dilatation thermique (α), la picnométrie à hélium pour la densité (d), l'échographie ultrasonore en mode pulse-écho pour les propriétés élastiques (module d'Young (E) et coefficient de Poisson(ν)), l'indentation Vickers pour la dureté Meyer (H) et la ténacité d'indentation [14] (K_c) au travers des équations suivantes:

$$H = P/2a^2 \qquad (1)$$

et

$$K_c = 0,016\,(E/H)^{1/2}\,P/c^{3/2} \qquad (2)$$

où P est la charge d'indentation, a la valeur moyenne des longueurs des diagonales de l'empreinte projetée de dureté et c la longueur moyenne (à partir du centre de l'empreinte) des fissures d'indentation.

Séries	d	E(GPa)	G(GPa)	ν	H(GPa)	K_c(MPa.√m)	Tg (°C)
SiO_2	2,2	73	31,8	0,148	7,2	0,73	1190
D"T"0,5	2,23	104	n.d.	n.d.	8,63	0,7	≈1350
D"T"1	2,2	110	n.d.	n.d.	10,6	0,57	>1350
SLS1	2,53	70,2	29,2	0,202	5,35	0,71	558
SLS2	2,50	69,3	29,2	0,188	5,11	0,70	559
SLS3	2,47	68,6	29,0	0,181	5,15	0,76	560
SLS4	2,43	68,1	29,1	0,172	5,19	0,82	561
Verre à vitre«	2,55	72,0	30,0	0,21	5,30	0,72	562
Se[1]	4,28	10,25	3,74	0,322	0,39	0,16	41
Ge_5Se_{95}	4,31	11,05	4,18	0,316	0,57	0,09	68
$Ge_{10}Se_{90}$	4,34	12,08	4,59	0,307	0,77	0,12	92
$Ge_{15}Se_{85}$	4,36	13,8	5,33	0,295	1,05	0,22	110
$Ge_{20}Se_{80}$	4,37	14,73	5,72	0,286	1,38	0,28	162
$Ge_{25}Se_{75}$	4,36	16,05	6,25	0,281	1,72	0,22	228
$Ge_{30}Se_{70}$	4,32	17,9	6,82	0,264	2,02	0,20	300
$Ge_{40}Se_{60}$	4,36	22,38	8,80	0,273	2,35	0,16	340
Erreur	±0,05	±1 GPa	±1 GPa	±0,01	±0,01GPa	±0,01MPa.√m	±2 (°C)

Tableau 2. Densité, modules élastiques, dureté et ténacité par indentation. n.d.: non determiné. [1]Partiellement dévitrifié. «Planilux, Saint-Gobain Co.

Comportement "normal" ou "anormal" du verre

La morphologie des empreintes d'indentation permet de distinguer les verres normaux, conduisant au développement de fissures médianes-radiales aux angles de l'empreinte, des verres anormaux comme la silice vitreuse, qui eux présentent un système de fissuration conique [15, 16]. L'anormalité du comportement est attribuée au processus de densification sous haute pression, processus trouvant son origine dans la faible raideur des liaisons angulaires Si-O-Si et dans l'existence du volume libre, permettant une redistribution des éléments (atomes, molécules...) constituant le verre. Différents types de morphologie des empreintes d'indentation ont été reportés dans le tableau 3, et ce pour trois niveaux de charge.

Charge Charge d'indentation (N)	Verre vitre	Silice vitreuse	D"T"0,5	D"T"1
2,94				
4,91				
9,81				

Tableau 3. Morphologie des empreintes d'indentation pour différentes charges.

Si le système de fissuration médiane-radiale se développe bien pour le verre à vitre standard, il en va de même pour la fissuration conique dans la silice, fissures dont l'intersection avec la surface produit des cercles qui possèdent pour certains un diamètre supérieur à la diagonale de l'empreinte d'indentation (figure 2). Pour le verre $D^HT^H0,5$, ce même comportement anormal est observé mais avec les fissures coniques qui intersectent la surface au droit des angles des empreintes. Pour des charges supérieures à 9,8 N, nombre de fissures coniques secondaires apparaissent sans toutefois laisser cours au système de fissuration médiane-radiale qui est présent dès 4,9 N pour le verre D^HT^H1. Autrement dit, plus le verre est riche en carbone, plus son comportement tend à être normal. L'augmentation de la teneur en carbone covalent réduit fortement la capacité d'adaptation par densification du réseau riche en silice et contraint celui-ci à une déformation par cisaillement localisé conduisant à l'apparition de fissures médianes-radiales.

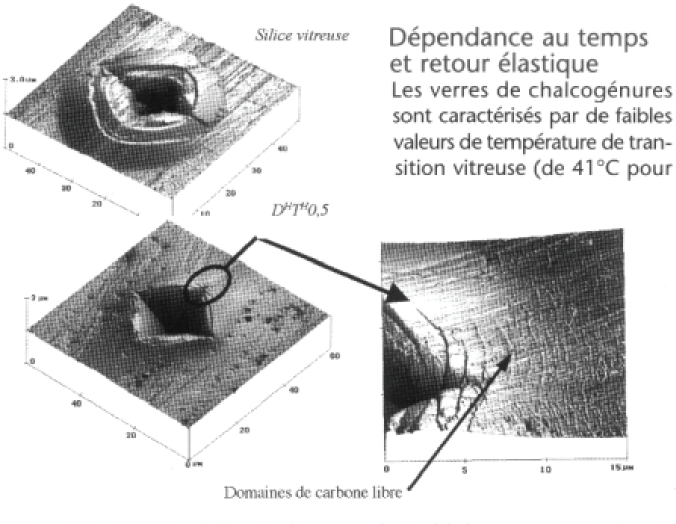

Figure 2. Image AFM (mode contact) d'indentations Vickers à 2,94 N réalisées sur de la silice vitreuse et sur un verre $D^HT^H0,5$.

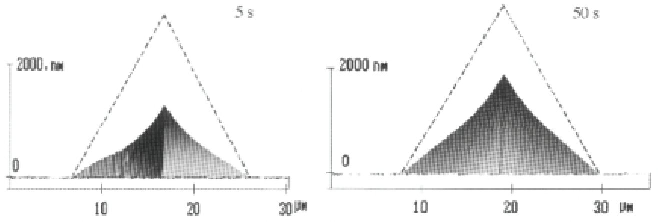

Figure 3. Image AFM (mode contact) d'indentations Vickers à 0.1 N pour 5 s (gauche) et 50 s (droite) réalisées sur du sélénium vitreux

Une observation attentive de l'empreinte en microscopie à force atomique (AFM) révèle la présence d'un réseau de microfissures au droit de l'angle, microfissures dont l'origine est le carbone libre turbostratique présent dans le verre. La coalescence de ces microfissures forme les fissures de Hertz qui intersectent majoritairement les quatre coins de l'empreinte. Ces nanodomaines graphitiques conduisent de par leur orientation à une anisotropie dans la fissuration (D^HT^H1, tableau 3), et se comportent surtout comme des sites d'initiation de microfissures facilitant par ailleurs leur coalescence en créant des chemins de faible énergie de rupture (prédécoupage de la structure du verre suivant un "pointillé" de nanodomaines graphitiques).

Dépendance au temps et retour élastique

Les verres de chalcogénures sont caractérisés par de faibles valeurs de température de transition vitreuse (de 41°C pour (Se) à 340°C pour ($Ge_{40}Se_{60}$)) [11,17] et par des enthalpies d'activation d'écoulement basses (de 285 à 592 kJ/mol) [18]. La conséquence majeure est une dépendance de la dureté au temps d'application de la charge, et ce, à température ambiante et spécialement pour les compositions riches en sélénium [12] (figure 3). Ces verres sont donc d'excellents candidats pour l'étude de la viscosité à température ambiante. Leur tenue en fluage lors de leur emploi dans des structures comme des lentilles ou des fibres reste cependant problématique.

L'étude du comportement visqueux de verres de chalcogénures peut donc être effectuée au travers de la géométrie d'une empreinte d'indentation, qui conduit à considérer que la profondeur résiduelle de l'empreinte correspond au déplacement de fluage du matériau u_{fl}, et que la différence entre la profondeur de pénétration à charge maximale u et la profondeur résiduelle correspond au retour élastique u_{el} du matériau lors du déchargement :

$$u=u_{el}+u_{fl} \qquad (3)$$

Le déplacement dû à l'écoulement est mesuré directement par AFM alors que le déplacement total est extrapolé à partir des angles de l'empreinte en prenant un angle de 74,05° correspondant au demi-angle entre arrêtes pour un indenteur Vickers. Sur la base d'un modèle d'écoulement d'un fluide visqueux autour d'un cône dont la surface de contact correspond à celle d'un indenteur Vickers, on établit que la viscosité apparente a pour expression :

$$\eta=\frac{\partial\, tan\acute{a}}{4}\, t\, H(t) \qquad (4)$$

où α est le demi-angle au sommet du cône équivalent ($\alpha \approx 70{,}29°$), ainsi l'équation (4) devient :

$$\eta=2{,}19\, t\, H(t) \qquad (5)$$

La dureté n'est pas simplement dépendante de 1/t et il a été montré que cette famille avait un comportement rhéofluidifiant très marqué impliquant une chute rapide de la viscosité apparente à mesure que la charge appliquée augmente [12]. Comme pour beaucoup de verres, ce comportement est particulièrement marqué pour des températures d'essais inférieures à la température de transition vitreuse et pour de fortes contraintes appliquées. Par ailleurs, pour les verres de chalcogénures étudiés, ce caractère rhéofluidifiant augmente avec la teneur en germanium. Une très bonne description de la dépendance au temps de la dureté peut être obtenue en couplant une description non-newtonienne des mécanismes d'écoulement à une approche standard de type Norton-Arrhenius pour l'écoulement ($d\varepsilon/dt=A\sigma^n$). Ainsi la dépendance au temps de la dureté peut s'exprimer de la façon suivante:

$$H(t)=\left[\frac{2}{\partial A(1+i)tan\acute{a}}\right]^{1/n} t^{-1/n} \exp\left(+\frac{\ddot{A}G_a}{nRT}\right) \qquad (6)$$

L'identification de l'exposant de contrainte n ($11 < n < 62$) montre que celui-ci augmente avec le taux de germanium contrairement au coefficient de Poisson (excepté pour $Ge_{40}Se_{60}$, tableau 2). Autrement dit, à déformation normale imposée, plus le taux de germanium augmente, plus il apparaît de changement de volume, phénomène qui peut favoriser l'alignement des unités structurales dans l'axe de traction même si l'on opère à une température éloignée de la T_g, domaine où le comportement est majoritairement élastique. Par ailleurs, plus la T_g est élevée, plus les évolutions de η et ν indiquent que l'écoulement du verre sera non-newtonien.

Dépendance au chargement

Le dispositif expérimental de la figure 1 permet d'asservir par ordinateur la force de pénétration ainsi que la vitesse et l'accélération de l'indenteur. Des rampes de chargement (de 0 à 4 N) ont été réalisées afin de balayer une large gamme de charge sur une seule rayure.

La morphologie de la rayure dépend fortement de la valeur de la charge normale appliquée [1, 3, 19, 20], ainsi trois régimes majeurs peuvent être identifiés : i) le régime micro-ductile avec ou sans fissuration latérale sub-surfacique, ii) le régime d'écaillage avec formation de fissures radiales et latérales conduisant à la formation d'endommagement surfacique important, et iii) le régime micro-abrasif qui donne lieu à la génération de nombreux microdébris. La rayabilité des verres SLS est fortement conditionnée par leur composition [2] (figure 4).

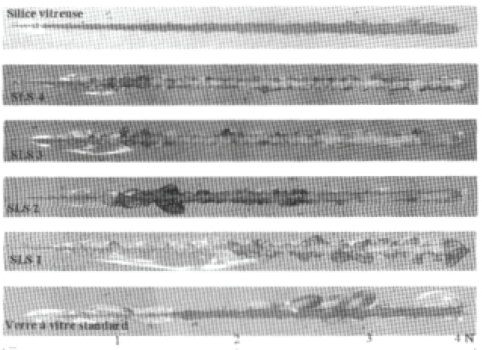

Figure 4. Comportement au rayage de verres SLS.

Plus le réseau du verre est proche de celui de la silice vitreuse, plus le régime micro-abrasif apparaît pour des charges normales faibles (SLS3-4) alors que les compositions plus riches en modificateurs de réseau présentent une tendance à l'écaillage très marquée (SLS1-2), ce que l'on retrouve sur le verre à vitre standard. Les verres SLS sont dans des compositions proches de la dévitrite (Na_2O–$3CaO$–$6SiO_2$) et de la tridymidite (SiO_2) au sein du diagramme de phase Na_2O–$3CaO$–$6SiO_2$. Ainsi les verres de composition proche de celle de la tridymite ont une tendance marquée à l'écaillage alors que ceux dont le réseau vitreux est proche de celui de la silice présentent une résistance particulière à ce phénomène. Comme pour les verres au carbone, on peut avancer que la structure ouverte, qui est celle de la silice vitreuse, présente l'intérêt manifeste de pouvoir se réorganiser par densification et ainsi pouvoir résister plus fortement à la fissuration. Ainsi la présence de cations modificateurs de réseau (typiquement > 25%) augmente la proportion d'oxygène non-pontant dans le réseau et engendre des chemins de moindre résistance pour le cisaillement et donc la fissuration [3]. Comme pour les verres au carbone, le "raidissement" de la flexibilité initiale du réseau de la silice vitreuse par introduction de modificateurs conduit les verres SLS à avoir un comportement normal, ce qui implique le développement d'un système de fissuration par cisaillement au détriment du processus de densification.

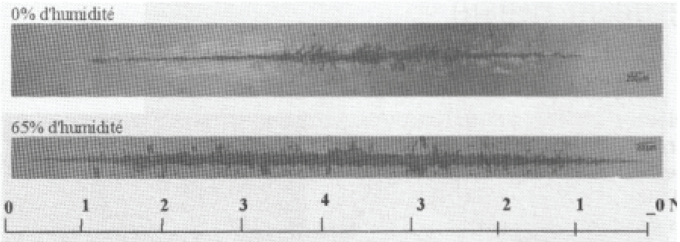

Figure 5. Rayures réalisées sous deux taux d'humidité différents lors d'un cycle de charge/décharge sur un verre à vitre standard recuit

Rôle de l'humidité

La figure 5 illustre parfaitement l'influence du degré d'humidité sur la résistance au rayage d'un verre à vitre standard recuit. Un cycle de chargement/déchargement (0 – 4 – 0 N) a été réalisé de façon à mettre en évidence l'ensemble des régimes attendus lors du rayage, et une possible disymétrie de la rayure [3].

Comme il a déjà été observé sur les verres silico-sodo-calcique, l'humidité joue un rôle important sur le comportement à rupture [21], ce qui se vérifie sur les rayures obtenues puisqu'un décalage important dans les charges de transition caractéristiques des différents régimes d'endommagement est observé. On remarquera en particulier la taille importante de la fissuration latérale sub-surfacique présente dans le régime micro-ductile de la rayure effectuée à 0% d'humidité. Le fait que cette fissure latérale n'ait pas débouché est lié à la non-apparition de la fissuration radiale qui ne s'est pas développée en même temps. Ainsi, aucune écaille n'a pu se former conformément à des observations déjà réalisées sur du verre à vitre qui tendent à montrer qu'une écaille résulte d'un couplage simultané de la fissuration latérale et radiale.

On pourra enfin indiquer que ces fissures sub-surfaciques ne débouchent pas à la surface, même après un long temps de séjour en atmosphère humide.

Conclusion

Le comportement à l'indentation et au rayage de verres spéciaux a été corrélé à leurs structures particulières et comparé à celui de compositions vitreuses standards comme la silice et le verre à vitre.

L'influence de certains paramètres comme l'humidité et la dépendance au temps de la dureté a permis de montrer que cette problématique reste très ouverte et que des études plus poussées doivent encore être menées ■

REMERCIEMENTS

Le LARMAUR tient à remercier les personnes extérieures qui ont fortement contribué à ces études, en particulier G.D. Soraru de l'Université de Trente en Italie pour les verres au carbone, I. Melscoët du Laboratoire Verres et Céramiques UMR CNRS 6512 Rennes pour les verres de chalcogénures et G. Duisit de la société Saint-Gobain Recherche.

BIBLIOGRAPHIE

[1] T. Rouxel, J-C. Sangleboeuf, J-P. Guin, V. Keryvin, Surface damage resistance of gel-derived oxycarbide glasses: hardness, toughness, and scratchability, J. Am. Ceram. Soc., 84 [10] 2220-24 (2001).

[2] S. Dériano, Conception chimique de verres silicatés à hautes performances mécaniques, thèse de doctorat, Université de Rennes, Décembre 2002.

[3] V. Le Houérou, J-C. Sangleboeuf, S. Dériano, T. Rouxel, G. Duisit, Surface damage of soda-lime-silica glasses: indentation and scratch behavior, J. Non-cryst. Sol., 316 54-63 (2003).

[4] J. Homeny, G.G. Nelson and S.H. Risbud, Oxycarbide glasses in the Mg-Al-Si-O-C system, J. Am. Ceram. Soc., 71 [5] 386-390 (1988).

[5] H. Zhang and C.G. Pantano, Synthesis and characterization of silicon oxycarbide glasses, J. Am. Ceram. Soc., 73 [4] 958-963 (1990).

[6] F. Babonneau, G.D Soraru, G. D'Andrea, S. Dire and L. Bois, Silicon oxycarbide glasses from sol-gel precursors, Mat. Res. Soc Symp. Proc., 271 789-94 (1992).

[7] G.D. Soraru, Silicon oxycarbide glasses from gels, J. Sol-Gel Science and Tech., 2 843-48 (1994).

[8] G.M. Renlund, S. Prochazka and R.H. Doremus, Silicon oxycarbide glasses: Part II. Structure and properties, J. Mater. Res., 6 [12] 2723-34 (1991).

[9] G.D. Soraru, E. Dallapicola and G. D'Andrea, Mechanical characterization of sol-gel-derived silicon oxycarbide glasses, J. Am. Ceram. Soc., 79 [8] 2074-80 (1996).

[10] G.D. Soraru, G. D'Andrea, R. Campostrini and F. Babonneau and G. Mariotto, Structural characterization and high temperature behaviour of silicon oxycarbide glasses prepared from Sol-Gel precursors containing Si-H bonds, J. Am. Ceram. Soc., 78 379-387 (1995).

[11] I. Melscoët, Synthèse, caractérisation et optimisation de verres optiques pour des applications infrarouges dans la fenêtre 8-12 µm, thèse de doctorat, Université de Rennes, Décembre 2000.

[12] J-P. Guin, T. Rouxel, V. Keryvin, J-C. Sangleboeuf, I. Serre, J. Lucas, Indentation creep of Ge-Se chalcogenide glasses below Tg: elastic recovery and non-Newtonian flow, J. Non-cryst. Sol., 298, 260-269 (2002).

[13] J-P. Guin, thèse de doctorat, Université de Rennes, Octobre 2001.

[14] G.R. Anstis, P. Chantikul, B.R. Lawn and D.B. Marshall, A critical evaluation of indentation techniques for measuring fracture toughness: I, direct crack measurements, J. Am. Ceram. Soc., 64 [9] 533-538 (1981).

[15] A. Arora, D.B. Marshall, B.R. Lawn and M.V. Swain, Indentation deformation/fracture of normal and anomalous glasses, J. Non-cryst. Sol., 31 415-428 (1979).

[16] C.R. Kurkjian, G.W. Kammlott, M.M. Chaudhri, Indentation behavior of soda-lime silica glass, fused silica, and single-crystal quartz at liquid nitrogen temperature, J. Am. Ceram. Soc., 78 3 737-744 (1995).

[17] V.F. Kokorina, Glasses for Infrared Optics, Clarendon Press (1996).

[18] See for example: U. Senapati and A. K. Varshneya, Viscosity of chalcogenide glass-forming liquids: an anomaly in the "strong" and "fragile" classification, J. Non-cryst. Sol. 197 (1996) 210-218.

[19] V. H. Bulsara, Scratch formation in brittle solids and its application to polishing, PhD Thesis, Perdue University, USA (1997).

[20] J-P. Guin, T. Rouxel, J-C. Sangleboeuf, Hardness, toughness, and scratchability of germanium-selenium chalcogenide glasses, J. Am. Ceram. Soc., 85 [6] 1545-52 (2002).

[21] S.M. Wiederhorn, in Fracture Mechanics vol 2 Plenum Press New York, (1974) 613.

App.3-3 : V. Le Houérou, J.-C. Sangleboeuf and T. Rouxel, Scratchability of Soda-Lime Silica (SLS) Glasses: Dynamic fracture analysis, *Key Engineering Materials, Vol. 290, (2005), pp 31-38.*

Scratchability of Soda-Lime Silica (SLS) Glasses: Dynamic Fracture Analysis

V. Le Houérou[1,a], J.-C. Sangleboeuf[1,b] and T. Rouxel[1,c]

[1] LARMAUR - FRE CNRS 2717, Campus de Beaulieu - Bat. 10B, University of Rennes 1, 35042 Rennes cedex, France.

[a] vlehouerou@hotmail.com,

[b] jean-christophe.sangleboeuf@univ-rennes1.fr, [c] tanguy.rouxel@univ-rennes1.fr

Keywords: scratch, fracture, glass, indentation, deformation, normal, anomalous, densification.

Abstract. Grinding and polishing are widely used for glass machining with fine finished surfaces. These processes result from abrasion due to repeated contacts between hard sliding particles and the glass surface. The study of contact mechanics problem is of fundamental interest to understand the process of material removal in glasses.

In order to get insight into this problem, an experimental set up was designed which allows a monotonic loading of the indenter combined with a controlled sliding of the specimen to simulate a slow abrasive machining process. In addition, the experiments are conducted with an in-situ video monitoring that allows for the observation of the different fracture phenomena beneath the indenter. Fracture surfaces were also studied using SEM and AFM for multi-scale investigation.

Fracture analysis was carried on a standard float glass, four different SLS glasses and a fused silica glass. The observed phenomena were discussed in the light of the influence of the normal load and the chemical composition.

Introduction

The study of the scratch resistance of soda-lime-silica (SLS) glasses is of great interest to better understand material removal in glasses as well as the causes for optical losses and for the fracture of windows or lenses due to surface damage in service. Some previous studies investigated the relationships between the composition of oxide glasses and their physical and thermo-mechanical properties such as density, coefficient of thermal expansion, elastic moduli, Poisson's ratio, hardness [1] and toughness [2]. The understanding of the mechanisms of fracture during scratching is not clearly established yet and few papers only were published so far, to the knowledge of the authors and justify plainly the present exploratory work. Some new experimental results concerning the scratch behavior and its dependence on chemical composition were obtained in the present study, using an original experimental setup. This study is mainly focused on the understanding and explanation of damages that occur during scratching of soda-lime silica glasses and the influence of the glass composition on the surface damage. The role of the load is also characterized.

Common damages are well known in glass during static indentation [3]. Similar observations have been carried out in the case of scratching [4-7] but this field remains to be further explored. The chevron cracks as defined by [4], the lateral cracks propagation described by [5-6] and the chipping process given by [7] need some more investigation. Observation of the surface damage leads to detailed results of the radial, lateral and chip formation and will be given in the *results* part.

The glass compositions were defined in such a way that with regard to their indentation behaviour, the studied glasses cover the range from typical normal glasses to near so-called *anomalous* glasses [8]. According to Peter [9], oxide glasses become normal when the modifier content exceeds 15-20 mol. %. Normal glasses are characterized by the absence or a minor contribution of densification process in the area beneath an applied contact stress. Indentation experiments showed that in this case irreversible deformation occurs by *plastic* rearrangement, or shear flow, as suggested by the presence of slip lines in the elastic-plastic contact zone [10]. On the contrary, a flow-densification process shows up in anomalous glasses, and the ability of glasses with relatively high silica content to densify under sharp contact loading has a great influence on the indentation and on the scratch damage features, and is thus of primary interest.

Experimental procedure

Experimental setup. An apparatus allowing for a variable loading cycle during a single experiment was designed. The horizontal displacement of the indenter (to produce a groove) is obtained by a bearing slide, while the vertical movement is controlled by a piezoelectric actuator. Both the penetration and the tangential forces are continuously monitored. The main characteristics of the apparatus are a maximal normal load of less than 5 N with an accuracy of 0.02 N, a vertical penetration displacement limited to 100 µm, and a bearing slider allowing for a displacement accuracy better than 1 µm and a maximum speed of 5 mm/s. The displacement of the bearing slider is computer controlled, and displacements and environmental parameters are continuously monitored.

Materials. A commercially available soda-lime-silica glass[1] and was studied. 40x15x4 mm^3 specimens were cut using diamond-type cutting tools from a pane annealed at 560 °C in air during 1 hours and cooled at 2 °C.min^{-1}. In addition, different glasses were synthesized[2] in the Na_2O-CaO-SiO_2 phase diagram. These glasses are referred as SLS (1 to 4), and were obtained by substituting SiO_2 for (Na_2O+CaO) while keeping Na_2O/CaO ratio constant and equal to 1.52. The glass compositions are given in the **Table 1**. These glasses were annealed for half an hour at T_g (measured by DSC) and slowly cooled at a rate equal to 1 °C.min^{-1}. Note that the same samples were used for all measurements. Glasses from the SLS series were cut and their surfaces were polished carefully up to 1 µm grid. A fused silica glass was also studied. Glass specimens were kept in a dried atmosphere to avoid moisture pollution before testing.

[% mol.]	Planilux	SLS1	SLS2	SLS3	SLS4	Fused Silica
SiO_2	70.8	71.0	74.0	77.0	80.0	100.0
Na_2O	12.8	17.5	15.7	13.9	12.1	-
MgO	5.9	-	-	-	-	-
CaO	10.2	11.5	10.3	9.1	7.9	-
AL_2O_3	0.4	-	-	-	-	-

Table 1. Chemical composition of studied glasses.

Performed tests. Three different types of run were conducted on the 6 glasses : i) scratching with a Vickers penetrator under predetermined constant loads in the range 0.2 N up to 3 N at an horizontal

---

[1] Planilux™, Saint-Gobain

[2] done by S. Deriano – see [15] for details

displacement rate of 0.01 mm/s ; ii) scratching with a Vickers penetrator under a 0-4 N load slope on 3 mm at an horizontal displacement rate of 0.01 mm/s ; and iii) indentation under loads in the range 0.2 N up to 3 N.

All the tests were performed in an atmosphere at 65 % of humidity. The Vickers penetrator (inverse pyramidal, 136° face to face angle) was used with a leading edge orientation and cleaned with ethanol before each test as well as the sample. Three different grooves were made on each glass to ensure a good reproducibility of the results. AFM measurements were performed (non-contact mode) on the scratched surfaces immediately after testing, so that the possible incidence of fatigue-corrosion phenomena is about the same for all the specimens. At last, the samples were observed by SEM after being coated with a thin layer of gold-palladium estimated to 12nm of thickness.

Results

Load dependence of the scratch behavior. During an indentation experiment performed with a Vickers indenter on a SLS glass, cracks are known to occur during loading or unloading, and depend strongly on the load level [11]. In a scratching experiment, the scratch pattern also strongly depends on the level of the normal load, and for low loads the different kinds of micro-cracks which form during, or with the scratch process and are namely : i) the median cracks, ii) the radial cracks and iii) the lateral cracks.

Monotonic loading/unloading cycles were conducted in order to screen all the possible damage events in a single scratch experiment. Following Ahn [6] and Bulsara [5], three different regimes are typically observed and are schematically drawn in **Fig. 1**: i) the first one is associated with a permanent groove with possible formation of sub-surface lateral cracks under the plastic track, and corresponds to a micro-ductile regime, ii) the second one, so-called micro-cracking regime, is characterized by an important damage by micro-cracking (lateral cracks intersecting the surface and radial cracks) and iii) the third one is a micro-abrasive regime and gives birth to many debris, with sometimes small lateral cracks along the track.

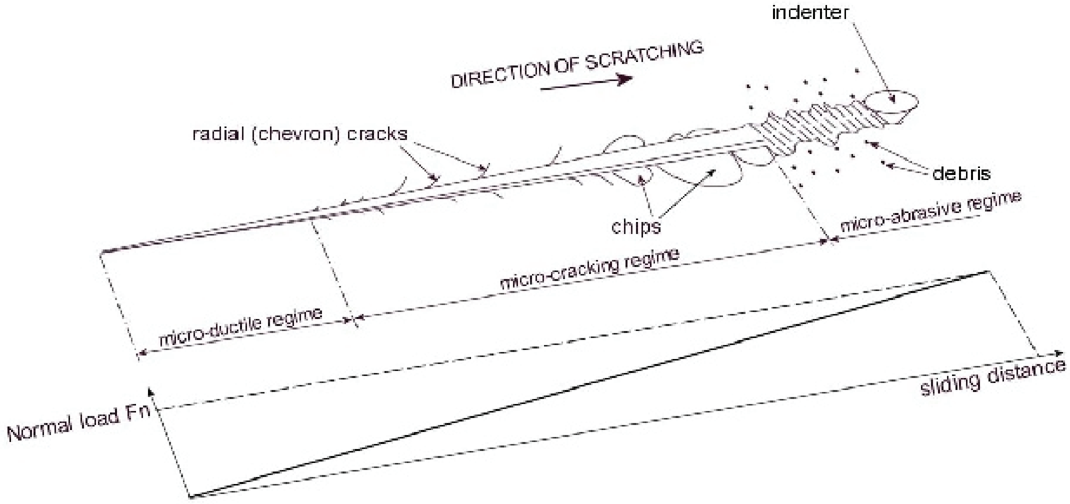

Fig. 1. Typical scratch pattern made on the surface of the SLS glass by a Vickers penetrator (leading edge) during a monotonic loading cycle (see load below the schematic drawing).

The micro-ductile regime. The micro-ductile regime in SLS glasses consists in a permanent scratch track without damage on each side and debris visible. This definition does not exclude damage inside and under the track, as long as they stay localised this way and they do not modify dramatically the scratch track appearance. To get insight into the comprehension of this regime, a lot of accurate observations were performed in SEM. Among these numerous observations, two were selected and reported in **Fig. 2** and **3**. The **Fig. 2** represents a "classical" scratch track on the SLS glass. Few slight cracks inside the track are visible. Their occurence doesn't match with the frequency due to the relative compliance of the machine (potential "stick-slip" effect of the indenter on the surface). The **Fig. 3** is far less classical. It shows a detail of a scratch track created at 0.4N, close to the transition load of the micro-ductile/cracking regimes. The particularity of this picture is that the considered sample exhibits a side of its track pulled up while the other remain intact. There is even a part of the scratch that is left attached by a ligament located in the middle of the track. This suggests that the removal process inside the track goes from the border toward the middle of the plastic imprint. This picture illustrates in an unusual point of view the damage that takes place under a plastic track, composed of a rough surface with perpendicular fracture orientation that disappears as it approaches the middle of the track.

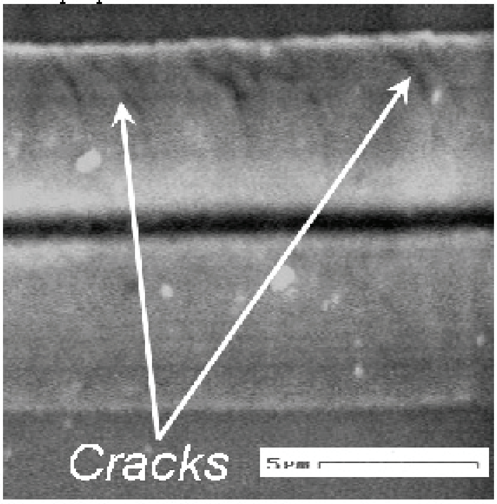

Fig. 2. Detail (S.E.M.) of the micro-plastic regime on the surface of a standard float glass.

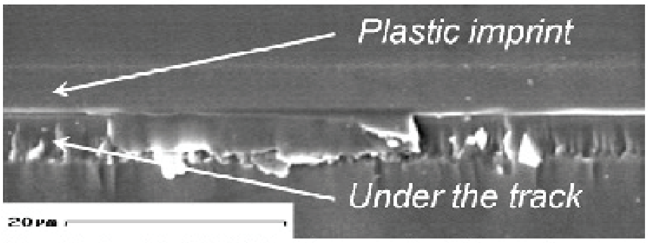

Fig. 3. Detail (S.E.M.) of a standard float glass scratched by a Vickers indenter in the micro-plastic regime. The plastic imprint and the damage under the scratch track are visible.

The cracking regime. According to [4], the cracking regime is composed of different damage phenomena : i) median cracks that propagate deeply in the material, ii) lateral cracks that take place under the indenter in the depth of the sample corresponding to the limit of the so-called plastic zone as introduced by Cook et al. [3], iii) radial as known as chevron cracks that occur on the surface and iv) chipping. This part consists in the description of the three last quoted damage mechanisms (radials, laterals and chipping) during the scratching of a glass with added fractographic considerations.

At high magnification, the radial cracks resulting from the scratch process don't look exactly as those described by Ahn [12]. These cracks are significantly inclined toward the sliding direction, and propagate in a curved shape usually ending perpendicular to the scratch direction as illustrated in **Fig. 1**, when there is no combination with another damage phenomenon (i.e. lateral cracks as we will see further). A crush scratch track appears at high loads (typically $F_n > 0.8$ N), and many debris are present. The **Fig. 4** shows the initiation and beginning of propagation of a chevron crack. It clearly initiates at the leading edge of the Vickers indenter and soon propagate from a direction parallel to the scratch track to a curved shape that tends to get perpendicular to the track. The crack reach out from the track with an angle marked θ on **Fig. 4** that probably depends on the friction coefficient and the environmental parameters. The crack initiation and propagation at the earliest steps is usually not visible in the track as it is probably *erased* by the moving indenter. Note that the non uniformity of the coating around the damage on the surface of the sample make the SEM observation underline the different cracks as they charge of electrons. Thus, damages are more visible but the drawback is that the potential magnification with the SEM is smaller. It usually looks as if the crack initiates on the border of the track with the angle θ from the scratch. Then, the chevron crack remain really close to the tip of the indenter at the contact, even maybe inside the imprint. This propagation can be qualified as semi-stable: i) after the initiation, it rapidly curves either on the right or on the left of the track ; this choice is purely statistic and constitute the unstable part of the propagation of the crack, ii) the advance speed of the crack suggests a stable propagation . Then, the semi-stable character gives account for both the stable propagation of the crack and the instability in the very first direction of the crack.

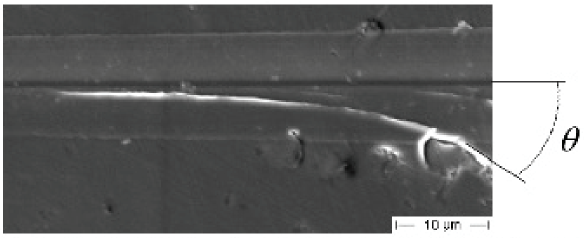

Fig. 4. Initiation and propagation of a radial (chevron) crack on the surface of a standard float glass (S.E.M.).

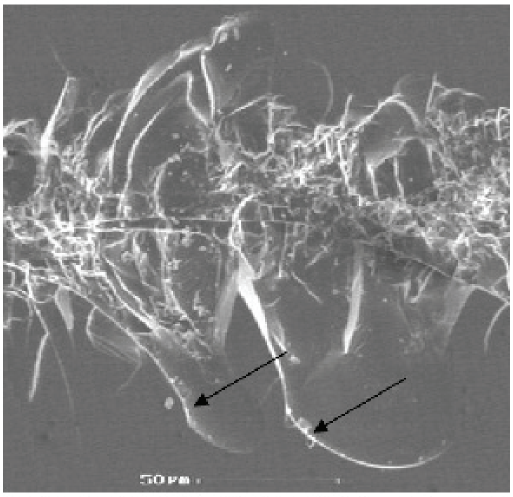

Fig. 5. Interaction between radial and lateral cracks without complete chip creation (SLS 1 - S.E.M.).

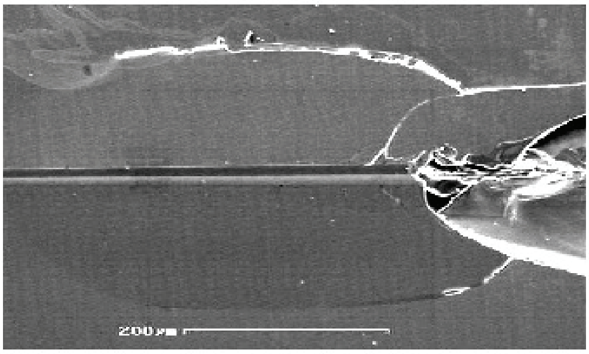

Fig. 6. chipping by propagation of a lateral crack – absence of radial cracks (SLS 4 - S.E.M.).

As explained by Le Houérou et al. [7], the interaction of radial and lateral damages gives rise to chipping when the load is high enough. The **Fig. 5** illustrates clearly this mechanism that is underlined by the two black arrows : the radials interact with the lateral crack that reaches out to the surface with an inflexion of the shape on the surface at the intersection. Under the hypothesis that sufficient energy is involved, the last step of the chip formation should be, for the radial/lateral couple on the left of **Fig. 5** for instance, the propagation of the lateral crack toward the surface until it reaches the neighbouring radial crack.

In the absence of radial cracks (case by low hygrometry for example [7]), chipping can also occur if enough energy is spent into the formation and the propagation of the lateral cracks toward the surface. The **Fig. 6** shows a lateral crack that begins to create a chip as it almost reaches the surface.

Fig. 7 shows the surface below a chip with its detail. Note that the chip was removed by cleaning process before coating for SEM observation. Twist hackle [13] is clearly visible on the fracture surface. It suggests that the fracture is driven mainly in mode I combined with a weak mode III component. The river lines pattern indicates the direction of propagation of the crack that initiate under the track and propagate far from the track, usually perpendicular to the scratching direction. The river lines are approximatively equally spaced well below 1 µm that is in good agreement with results reported in the literature [14].

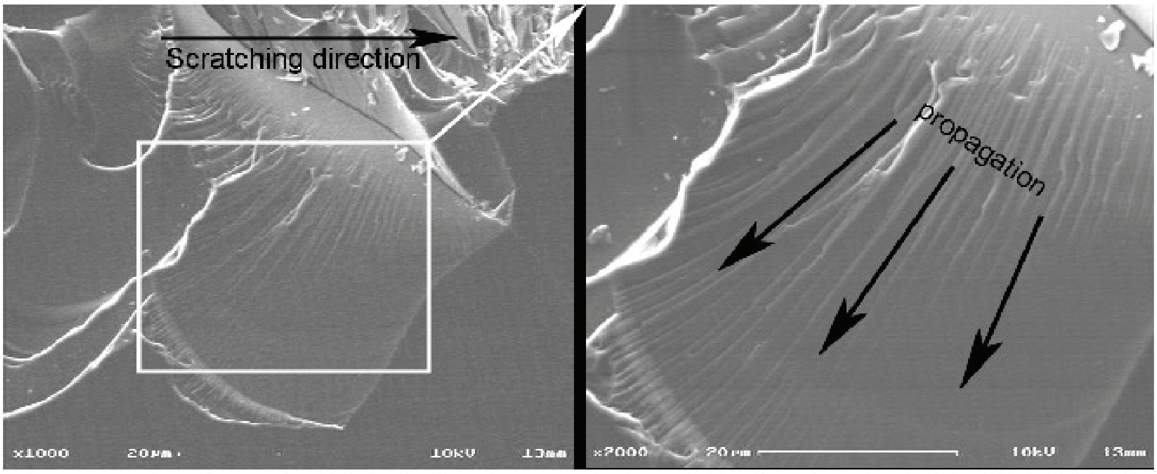

Fig. 7. Chip and its detail. River lines give the direction of propagation of the lateral crack (SLS 4 - S.E.M.).

Chemical composition. The scratchability is greatly affected by the chemical composition as already reported in the literature [7,15]. Standard float glass, SLS1 and 2 are sensitive to chipping as a direct consequence of their normal character that mainly allows cracks to form by local shearing [7] due to weak percolation paths [16]. SLS 3, 4 and fused silica with silica-like networks appear to be much more resistant to both crack propagation and chipping during scratch experiments as a consequence of their anomalous character [7] that accommodates the deformation by network rearrangement (densification) without breaking bonds [8].

As a result of these literature reminders, the normal glasses are more prone to pile-up due to the tendency to deform at constant volume (i.e. *plastically*) while the anomalous glasses are prone to sink-in as they densify. These two tendencies in behaviour of the normal/anomalous glasses under load are illustrated by the **Fig. 8** that shows AFM pictures of a detail of a Vickers indentation on both SLS 1 and SLS 4. Pile-up can be seen on the left of the SLS 1 imprint (the cutting section is around the middle of the face of the indenter) with several small cracks in the imprint while a sink in is visible on the SLS 4 imprint.

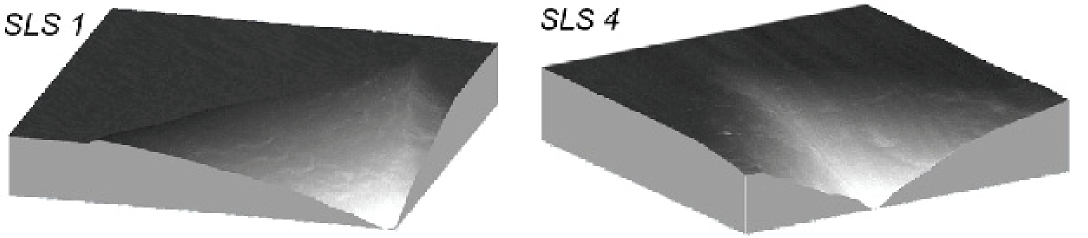

Fig. 8. Detail of AFM pictures of indentation on SLS 1 & 4 (scan area: 5x5 µm^2 - load: 0.6 N - maximum depth: 700 nm for SLS 1 and 625 nm for SLS 4).

This kind of behaviour considerations linked to the chemical composition can also be applied to fractographic analysis. For instance, **Fig. 9** shows parts of micro-cracking regime with their details of the standard float glass and the SLS 4 glass. Even if the global shape of the damage remains the same between the two materials in form of large chips (note that the cracking regime does not occur at the same load), the detail of the scratching track is totally different. In the case of the standard float glass, the scratch track exhibits small damages. The potential slipping sites in the structure of the glass are randomly located. Then, the shear bands can potentially make the rupture bifurcate and leads to a “fine” tortured fracture pattern like shown on the detail of **Fig. 9**. In the case of the anomalous SLS 4 glass, the scratch track is composed of fractures that can be qualified as *quasi-cleavage* pattern as described by Hull [14]. The homogeneity of the structure permits cleavage on relatively large surface due to the equal strength of bonds that are met by the tip as the crack propagates.

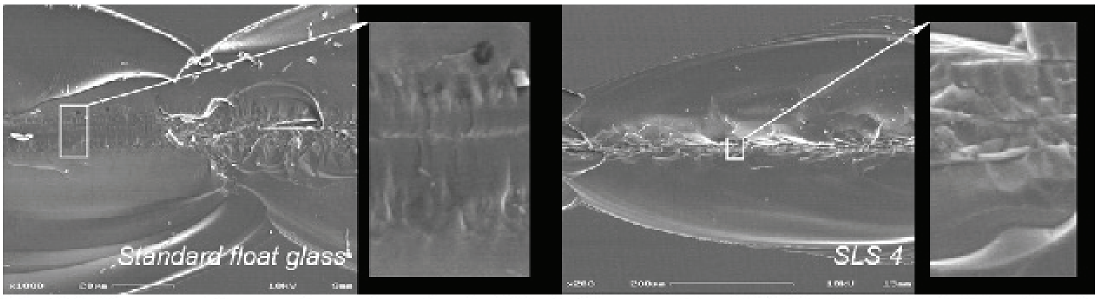

Fig. 9. Micro-cracking regime of a standard float glass and the SLS 4 glass and details of their scratch tracks (S.E.M.).

Lastly, the observation of the damage in the abrasive regime in function of the glass composition leads also to consistent conclusions with respect to sensitivity of the glasses to normal/anomalous behaviour. The **Fig. 10** shows details of abrasive regimes in the cases of fused silica, the SLS 3 and the standard float glass. The fused silica exhibits the less tortured track as expected in the light of previous conclusions ; the SLS 3 shows large chipping process all along the track with quasi-cleavage patterns due to a higher trend to potential shearing in comparison to fused silica ; under the sliding indenter the standard float glass produces long cracks and very fine and tortured damages inside the track, comparable to the ones visible in the cracking regime.

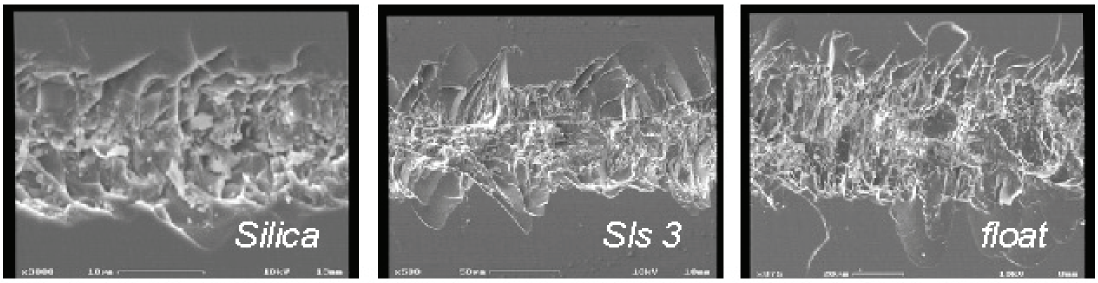

Fig. 10. Details of the micro-abrasive regime of a fused silica glass, the SLS 3 glass and a standard float glass (S.E.M.).

Conclusion

Scratching tests have been carried out on six different SLS glasses. According to the literature, distinct damage regimes have been identified with respect to the normal load : i) micro-plastic regime, micro-cracking regime and micro-abrasive regime.

Observations in SEM permit to identify the damages that occur under the scratch track in the micro-plastic regime.

Initiation and propagation of the *chevron* cracks have been studied. Their interaction with the lateral cracks that lead to chips formation has been illustrated and discussed. The chipping without radial cracks has also been evoked and commented. Twist hackle has been identified as fractographic pattern in the formation of chips.

The influence of the chemical composition of the glasses on the scratching behaviour have been investigated. Normal/anomalous behaviour of the SLS glasses is reported in the literature as glasses with a relatively high quantity of modifiers in their network are prone to deform by local shearing and glasses with silica-like network (i.e. glasses with high-silica content) have tendency to densify under load. With respect to these behaviour considerations, fractographic patterns of the micro-cracking regime have been discussed. Consistent similar conclusions have been shed to light for the micro-abrasive regime that occurs during the scratching process.

Aknowledgments

The authors would like to thank S. Dériano for providing the SLS glasses and his contribution to this work, and J. Michler for providing some of the technical resources used in this study.

References

[1] H. Scholze, Le verre nature structure et propriétés, 2nd Ed. Institut du Verre, Paris, 1974.
[2] E. Vernaz, F. Larche and J. Zarzycki, J. Non-Cryst. Solids 37 (1980) 359.
[3] R.F. Cook and G.M. Pharr, J. Am. Ceram. Soc., 73 [4] (1990) 787.
[4] R.W. Rice and J.J. Mecholsky, Special publication 562, National Bureau of Standards (1965) 351.
[5] V.H. Bulsara, PhD thesis, Perdue University, USA, 1997.
[6] Y. Ahn, PhD thesis, Perdue University, USA, 1997.
[7] V. Le Houérou, J.-C. Sangleboeuf, S. Dériano, T. Rouxel and G. Duisit, J. Non-Cryst. Solids 316 (2003) 54.
[8] A. Arora, D.B. Marshall, B.R. Lawn, M.V. Swain, J. Non-Cryst. Solids 31 (1979) 415.
[9] K.W. Peter, J. Non-Cryst. Solids 5 (1970) 103.
[10] J.T. Hagan, J. Mater. Sci. 15 (1980) 1417.
[11] K. Niihara, R. Morena, D.P.H. Hasselman, J. Am. Ceram. Soc. 65 (1982) C116.
[12] Y. Ahn, T.N. Farris, S. Chandrasekar, Mech. Mater. 29 (1998) 143.
[13] Ceramics and Glasses, Engineered materials handbook volume 4, ASM International, 1991 (636).
[14] D. Hull, Fractography: observing, measuring and interpreting fracture surface topography, Cambridge University Press, 1999.
[15] S. Dériano, PhD thesis, University of Rennes 1, France, 2002.
[16] G.N.Greaves, J. Non-Cryst. Solids 71 (1985) 203.

RÉSUMÉ

Ce travail de thèse traite de la résistance au rayage des verres silico-sodo-calciques (notés SLS) en fonction de considérations environnementales, de leur composition chimique, de l'histoire du chargement, des contraintes résiduelles et de la géométrie de l'indenteur.

Une étude phénoménologique détaillée permet d'identifier les fissures et les régimes d'endommagement mis en œuvre pendant le rayage des verres considérés. L'influence de la composition chimique est discutée à la lumière de considérations structurales et d'observations fractographiques à l'échelle microscopique. La notion de compétition densification/cisaillement dans la déformation de ces verres semble être le paramètre clé pour comprendre leur comportement à l'indentation/rayure.

Un modèle mécanique a alors été envisagé pour prédire les endommagements identifiés pendant les essais expérimentaux. L'approche de Ahn* donnant une solution analytique au problème du rayage par un indenteur conique (dérivé de celui de Yoffe° pour une indentation statique) est dans cette étude généralisée. Le développement réside en deux extensions principales: i) l'extension à la géométrie de l'indenteur Vickers grâce à un modèle par éléments finis 3D de l'indentation statique par un Vickers et ii) l'extension aux verres de la famille SLS en étudiant la compétition densification/cisaillement (par des considérations expérimentales couplées à des mesures par AFM) qui contrôle principalement leur comportement à l'indentation.

Les résultats du modèle sont corrélés par les résultats phénoménologiques et les observations expérimentales. Le comportement à la rayure des différents verres au regard de leur caractère normal/anormal est également discriminé par le modèle.

ABSTRACT

This work deals with the scratch resistance of soda-lime silica (SLS) glasses with regard to environmental considerations, chemical composition of glass, load history, residual stresses and indenter geometry.

A detailed phenomenology investigation allows identifying the cracks and the damage regimes that occur during micro-scratching on the considered glasses. The influence of the chemical composition is discussed through structure considerations and fractographic observations at the micro-scale. The notion of densification/shear competition in the deformation process of these glasses (related to their normal/anomalous character) appears as the key factor in the understanding of their indentation/scratch behavior.

A mechanical modeling was considered to predict the damage which was identified during scratch experiments. The approach of Ahn* of an analytical solution of a scratch performed on a glass by a conical indenter (derived from Yoffe's° model for a static indentation) is extended to the present study. The development lies in two main extensions: i) the extension to the Vickers indenter geometry with the help of a 3D Finite Elements model of a Vickers static indentation, and ii) the extension to the SLS glass series by studying the densification/shear competition (experimental considerations conjugated to AFM measurements) that mainly control their indentation behavior.

The results of the model are correlated to the phenomenology results obtained by experimental observations. The scratch behavior of the different glasses with regard to their normal/anomalous character is also discriminated by the model.

---

* Y Ahn, *Deformation about sliding indentation in ceramics and its application to lapping*. 1992, Perdue University: (USA).

° E.H. Yoffe, *Elastic stress field caused by indenting brittle materials,* Philosophical Magazine A, **46** (4), (1982), p. 617-628.